

Sheffield Hallam University

Novel Experimental Characterisation of Hyperelastic Materials

AHMED, Shakeel

Available from the Sheffield Hallam University Research Archive (SHURA) at:

<http://shura.shu.ac.uk/24584/>

A Sheffield Hallam University thesis

This thesis is protected by copyright which belongs to the author.

The content must not be changed in any way or sold commercially in any format or medium without the formal permission of the author.

When referring to this work, full bibliographic details including the author, title, awarding institution and date of the thesis must be given.

Please visit <http://shura.shu.ac.uk/24584/> and <http://shura.shu.ac.uk/information.html> for further details about copyright and re-use permissions.



Materials and Engineering Research Institute

Shakeel Ahmed

**Novel Experimental Characterisation of Hyperelastic
Materials**

Thesis submitted in partial fulfilment of the requirements of
Sheffield Hallam University
For the degree of Doctor of Philosophy

July 2018

Table of Contents

Table of Contents.....	ii
Preface	viii
Nomenclature.....	ix
List of figures.....	xi
List of Appendix Figures	xxi
List of Tables.....	xxiii
Abstract.....	xxv
1. Introduction.....	1
1.1 What is Latex?.....	2
1.2 Processing latex gloves	4
1.2.1 Cleaning the Glove Formers	4
1.2.2 Former Dipping into Chemicals and Latex Coagulant	6
1.2.3 Vulcanizing the Rubber and Leaching.....	7
1.2.4 Lip Rolling and Stripping Latex Gloves off.....	8
1.2.5 Checking for Defects using Air and Water Tests.....	10
1.2.6 Packing the Exam Gloves in Boxes	11
1.3 Characterizing a Thin Polymer Sheet	11
1.4 Modelling a Thin Polymer Sheet.....	15
1.5 Aims and Objectives	16

2.	Literature Review	17
2.1	Hyper Elastic Material Models	18
2.1.1	Introduction.	18
2.1.2	Basics of Continuum Mechanics	22
2.1.3	Phenomenological Models based upon Invariants of Strain I_i	24
2.1.4	Phenomenological Models based upon Principal Stretch Ratios λ_i	28
2.1.5	Molecular Statistical Network based Models	29
2.1.6	Conclusive remarks about Hyperelastic Models.....	34
2.1.7	Curve Fitting a Phenomenological Hyperelastic Material Model ...	36
2.2	Characterizing Hyperelastic Materials	39
2.2.1	Introduction	39
2.2.2	Uniaxial Tension Test.....	40
2.2.3	Biaxial Extension Test	41
2.2.4	Nanoindentation	42
2.2.5	Bulge Test.....	43
2.3	Summary	51
3.	The Experimental Setup	52
3.1	Bulge Hardware Setup.....	53

3.1.1	The Bulge Chamber Assembly.....	54
3.1.2	The Pressure Sensor	57
3.1.3	The Syringe Pump System.....	58
3.1.4	The Control System.....	59
3.1.5	The Height Measurement System	61
3.2	The Tensile test setup.....	63
3.2.1	Strain Measurement.....	64
3.2.2	Tensile Test Fixture (Retrofitted Syringe Pump)	65
3.2.3	Loadcell Assembly	68
3.2.4	Loadcell Calibration.....	68
3.2.5	ADC Calibration	69
4.	3D DIC with a Commercial System.....	71
4.1	Introduction	72
4.2	The Working Principle of DIC.....	72
4.3	Hardware Setup.....	74
4.4	Preparing the Samples	75
4.5	DIC Calibration	76
4.6	Profiles Acquisition	79

4.7	Calculations	80
4.7.1	Relative to First	82
4.7.2	Sum of Differential and Differential.....	82
4.8	Extracting Data	83
4.8.1	Rectangular Bulge Window	83
4.8.2	Circular Bulge Window	86
4.8.3	Tensile Test.....	87
4.9	Export	87
5.	Processing DIC Data and Extracting Material Parameters	88
5.1	Introduction	89
5.2	Subset Size Convergence and Sensitivity	90
5.3	Smoothing the Bulge-Profile:	95
5.4	The Bulge-Profile Approximations	99
5.4.1	Rectangular Bulge Window	99
5.4.2	Circular Bulge Window	104
5.5	Zero Pressure Height Correction	105
5.6	Fitting Curve to the Rectangular Bulge Data:.....	106
5.7	Fitting Curve to the Circular Bulge Data:.....	109

5.8	Stabilization and Hysteresis.....	111
5.9	Unusable Results of some Rectangular Samples.....	114
5.10	Material Characterized Properties from Bulge Test.....	117
5.10.1	Variation of Plane-strain Modulus (M_r).....	118
5.10.2	Variation of Biaxial Modulus (M_c).....	121
5.10.3	Variation of Young's Modulus (E).....	123
5.10.4	Variation of Residual Stress (σ_0).....	124
5.11	Measuring Isotropy of the Material with Tensile Test.....	126
5.11.1	Poisson's ratio (ν) measured by Tensile Test.....	127
5.11.2	Poisson's ratio (ν) Calculated from Characterized Parameters.....	128
5.11.3	Young's Modulus (E) measured by Tensile Test.....	131
5.12	Calibrating a Hyperelastic Material Model using a commercial FEA Software.....	132
5.13	Discussion of Results.....	136
5.13.1	DIC Subset size.....	136
5.13.2	Alternate Methods of Calculating some Material Parameters ..	137
5.13.3	Aspect Ratio of Rectangular Bulge Tests.....	139
5.13.4	Poisson's Ratio and Isotropy of the Material.....	140

6. Conclusions	145
6.1 Conclusions and key Contributions to the Knowledge	146
6.2 Future Work	147
References	148
Appendix A. Geometrical Considerations of Cylindrical Bulge Shape	154
Appendix B. Hyperelastic Models calibration data (ANSYS)	157
Appendix C. Key Plots of Data	172
Appendix D. Drawings	181
Appendix E. Matlab Codes	190
Appendix F. Publications and Posters.....	206

Preface

This dissertation titled “Novel Experimental Characterisation of hyperelastic materials” is submitted for the partial fulfilment of Doctor of Philosophy at Sheffield Hallam University, Sheffield, United Kingdom. This research described here has been conducted under Dr. David Thomas Asquith (Director of Studies) and Dr. Jacques Penders (Supervisor) between January 2013 and July 2018.

This work presented here, to the best of my knowledge, is my original work except where acknowledgements and references to others work are made. Neither this, nor any other substantially similar dissertation, in part or completely, has been or is being submitted for any other qualification at any other Institution or University anywhere in the world.

First, I would like to express extreme gratitude to both my supervisors without their support and motivation I would have lost the courage and esteem required for a doctorate degree. I am grateful to Lyuba Alboul for her kindness and support. I am thankful to Andrew Alderson for his time and efforts, and feedback he gave during a special session with him. I am grateful to Gary Robinson for his suggestions in designing and machining parts for my bulge test equipment. I would like to thank all my colleagues in MERI.

At last, I would like to thank my wife Sidrat for her support, patience and her love and my parents, especially my mother for her prayers and support.

Shakeel Ahmed,
July 2018,
Sheffield UK.

Nomenclature

List of Symbols

\mathbb{B}	- Left Cauchy-Green deformation tensor
\mathbb{C}	- Right Cauchy-Green deformation tensor
\mathbb{F}	- Deformation gradient tensor
$\lambda_{i=1,2,3}$	- Stretch ratio along an axis (x, y, z)
$I_{i=1,2,3}$	- Strain Invariants
σ	- Cauchy or True stress
σ_0	- Residual stress
σ_b	- Biaxial value of residual stress
σ_p	- Plane-strain value of residual stress
s	- Piola-Kirchhoff or Nominal stress
W	- Strain Energy function
p	- Hydrostatic pressure
P	Bulge pressure
N	- Number of network chains in a unit volume
k	- Boltzmann's constant
θ	- Absolute temperature; angle
C_{ij}	- Hyperelastic material model constants
E	- Young's modulus
μ_i	- Hyperelastic material model constant (Ogden model)
μ	- Shear modulus
α_i	- Hyperelastic material model constant (Ogden model)
\mathcal{L}^{-1}	- Inverse Langevin function (3-chain model)

w	- Weight factors
h	- Bulge height
h_0	- Maximum bulge height
a	- Half-width (radius) of rectangular (circular) thin film samples
b	- Half-length of rectangular thin film samples
t	- Thickness of polymer thin film samples
t_p	- Thickness of polymer thin film samples
ν	- Poisson's ratio
M_r	- Plane-strain modulus
e	- Nominal stress
R	- Bulge radius of spherical cap; Radius of cylindrical bulge
ε	- True strain or Hencky strain
$R_{i=1,2,3}$	- Rectangular bulge test samples of three different aspect ratios
ϕ	- Diameter of a circular die
$S_{i=1,2,3}$	- Polymer test samples
M_c	- Biaxial modulus
C20	- Circular bulge window of radius 20 mm.
L	- Longitudinal length of a line on tensile test sample
L_0	- Longitudinal length of a line (initial) on tensile test sample
W	- Lateral length of a line on tensile test sample
W_0	- Lateral length of a line (initial) on tensile test sample

List of figures

Figure 1-1 Multiple stages of cleaning aglove formers after a previous run. (a) formers taking a dip in a water tank (b) Formers are being cleaned in a chlorine tank (c) Revolving brushes scour the hard to reach ceramic-former surfaces (d) formers are being dried in air while doing a swivel motion. -----	5
Figure 1-2 Glove formers being dipped to form exam gloves -----	6
Figure 1-3 Hand formers with latex film entering over for curing (volcanizing)---	7
Figure 1-4 Latex gloves leached to clean gloves and to remove the chemical residues and protiens. -----	8
Figure 1-5 Workers Removing Latex Gloves From Formers -----	9
Figure 1-6 Worker testing gloves for holes using air test -----	10
Figure 1-7 Worker testing medical gloves for holes using water test. -----	11
Figure 2-1 A typical hyperealstic (latex polymer) material's "S" shaped response curve showing tensile stress vs tensile stretch ratio (λ) (Treloar, 1944). -----	19
Figure 2-2. A 3-chain model showing initial and deformed chains orientation (Steinmann et al., 2012).-----	30
Figure 2-3. An 8-chain model showing initial and deformed chains orientation (Steinmann et al., 2012).-----	31
Figure 2-4 Schematic representation of three tests. The arrows show stresses. In the absence of any symbols, the system is free to move along that direction (a) Uniaxial tension (b) Equibiaxial tension (c) Planar tension (or Pure shear), with triangles showing fixed supports. -----	36

Figure 2-5 A cruciform material sample for equibiaxial testing,. [Source: adopted from (Galliot & Luchsinger, 2011)]-----	41
Figure 2-6 Example of the evolution of the applied load vs. the penetration depth upon nanoindentation cycle (Poilane et al., 2000).-----	43
Figure 2-7 A rectangular sample (half section) under bulge and coordinate system.-----	44
Figure 2-8 Nomenclature of a rectangular thin film sample -----	46
Figure 2-9 A circular bulge sample geometry showing, the radius of the die hole (window) 'a', R is the radius of the bulged spherical cap, bulge pressure p and h_0 is the maximum bulge height. -----	50
Figure 3-1 A systematic overview of bulge setup with Digital Image Correlation (DIC) system. The syringe pump also houses the micro-controller in it.-----	53
Figure 3-2. The bulge chamber assembly, showing bulge chamber, sample mounting and holding configuration of a rectangular sample and pressure sensor. Insert shows the bulge Chamber assembled view @ 0.5 the scale of the exploded assembly.-----	54
Figure 3-3 sample platform and holder plate for circular bulge samples.-----	56
Figure 3-4 Three different rectangular sample windows (sample holder plates) nominal sizes (WxL mm).-----	56
Figure 3-5 The pressure sensor (IFM PN3097) attached to the bulge chamber with a rectangular bulge window mounted on the top. The lcd display unit are set to kPa.-----	57

Figure 3-6. The customised syringe pump system retrofitted with micro controller and stepper motor driver with feedback loop from pressure sensor. ----- 59

Figure 3-7. Microcontroller with a stepper motor driver (controller). Wirings are not shown to keep the presentation of the system tidy. ----- 60

Figure 3-8 (a) Bulge testing with Digital Image Correlation system by LaVision with various components mounted in the vertical position on a tripod (tripod not visible in the image). (b) A calibration plate 58x58x5.8 mm. ----- 62

Figure 3-9 Schematic of Tensile test setup. Note: the syringe pump is now acting as tensile fixture. ----- 64

Figure 3-10 Syringe pump modification to carry out a tensile test of the polymer specimen. ----- 65

Figure 3-11 an image from DaVis 8.3 showing three Tensile Test strips. The yellow lines are added to clearly show sample and three strips in it. ----- 66

Figure 3-12 Loadcell assembly containing a 3kg loadcell. The angle plate is attached onto the syringe pump, the loadcell is then attached to the angle plate on one end and sample clamping plates on the other. Lower left corner insert shows actual loadcell assembly. ----- 68

Figure 3-13 Loadcell calibration plot showing ~100% fit and linear equation relating applied force [N] (x) to the resulting Vdc (y) produced by the loadcell. 69

Figure 3-14 Arduino ADC calibration results showing a very good fit. ----- 70

Figure 4-1 Basic step of DIC where a speckle pattern is discretized into small subsets. [Source: LaVision's 'Strain Master' manual] ----- 73

Figure 4-2 Correlation peak for each facet (subset) and corresponding pattern displacement in 2D. [Source: adopted from LaVision's 'Strain Master' manual]73

Figure 4-3 A 3D stereoscopic DIC system with two cameras. Images L and R are recorded by left and right camera respectively. Displacements of each point (u, v) are calculated and mapped together to calculate 3D displacements. [source: adopted from LaVision's 'Strain Master' brochure]----- 74

Figure 4-4 Latex gloves used to cut samples from for testing with DIC. [Source of gloves: Premier Protector, Latex Examination Gloves (medium).] ----- 75

Figure 4-5 a circular latex sample is lightly spray painted with matt black paint (a commercially available spray bottle) to generate a random speckle pattern suitable for digital image correlation. ----- 76

Figure 4-6 Calibration window from DaVis showing calibration plate Type 7/ Type 058-5 fitted with a 3D mapping function.----- 77

Figure 4-7 A window showing fit parameters from DaVis 8.3.----- 78

Figure 4-8 A quadrilateral mask is applied to include the rectangular bulge window area. A seeding point is also placed to start discretization the masked area into subsets of N xN. A default value of 31x31 pixels for subset is shown in Figure 4-9 (a) ----- 81

Figure 4-9 More calculation settings. (a) Default settings of subset size and step sizes (b) time series settings controlling correlation modes. ----- 81

Figure 4-10 2D (top) view of vector field showing the rectangular window from the bulge test in DaVis. The rectangular vector field is not oriented along either of the DIC axes (X, Y). W-line is approximately along the width of the rectangle. ----- 84

Figure 4-11 Bulge-shape along a W-line when projected onto DIC axes (X, Y) and the corrected actual bulge-shape along the width of a rectangular bulge window in Matlab.----- 85

Figure 4-12 Bulge chamber rotation arrangements. The bulge chamber can be rotated the required angle approximately.----- 86

Figure 4-13 Circular bulge window with a line drawn across its diameter to extract the bulge shape. ----- 87

Figure 5-1 A 3D deformed surface as constructed in DaVis. A small roughness can be seen on the surface. These random surface imperfections are mainly a result of the speckle pattern not being uniform size and shape which results in a non-smooth surface. ----- 89

Figure 5-2 Variation of maximum bulge heights calculated using DIC from a single DIC recording of the bulge test with R1 bulge window as subset sizes are increased.----- 91

Figure 5-3 Variation of maximum bulge heights calculated using DIC from a single DIC recording of the bulge test with R2 bulge window as subset sizes are increased.----- 92

Figure 5-4 Variation of maximum bulge heights calculated using DIC from a single DIC recording of the bulge test with R3 bulge window as subset sizes are increased.----- 92

Figure 5-5 Variation of maximum bulge heights calculated using DIC from a single DIC recording of the bulge test with circular bulge window as subset sizes are increased.----- 93

Figure 5-6 Variation of longitudinal stretch ratio (λ_1) calculated using DIC from a single DIC recording of the tensile test as subset sizes are increased.----- 94

Figure 5-7 Variation of lateral stretch ratio (λ_2) calculated using DIC from a single DIC recording of the tensile test as subset sizes are increased. The value of λ_2 drops 0.1825% as subset size is increased from 27 to the default size of 31. - 95

Figure 5-8. (R1S3) the third sample of the Rectangular window (aspect ratio ~4) after and before smoothing.----- 96

Figure 5-9 (R2S2) the second sample of the Rectangular window (aspect ratio ~6) after and before smoothing.----- 97

Figure 5-10 (R3S3) the third sample of the Rectangular window (aspect ratio ~7) after and before smoothing.----- 97

Figure 5-11 (C20S3) the third sample of the circular bulge window of diameter 20mm. Smoothing diametrical bulge-profile using 'lowess' and a span of 0.2.- 98

Figure 5-12 (C20S4) the fourth sample of the circular bulge window of diameter 20mm. Smoothing diametrical bulge-profile using 'lowess' and a span of 0.2.- 98

Figure 5-13 (R1S4) a circular arc fit to the bulge-shape. The horizontal position of the centre of the arc remains at a mean of $x = 0.00$ mm and standard deviation of $s = 0.0082$ mm. The lowest arc represents the lowest pressure. ----- 99

Figure 5-14 The bulge-profile (R1S2) at a pressure of 1.44 kPa showing polynomial fits of 2nd, 3rd, 4th, 5th and 6th degrees along with their respective goodness of fit (adjusted R^2). All degrees of polynomials fit the bulge-profile very well. -----101

Figure 5-15. The bulge-profile (R1S2) at a pressure of 15.164 kPa showing polynomial fits of 2nd, 3rd, 4th, 5th and 6th degrees along with their respective adjusted R² of fit. Polynomial fits of degree 4 and higher degrees fit best at all pressures (upto ~15kPa) and maximum bulge heights (upto ~4mm).-----101

Figure 5-16 Variation of adjusted R² (goodness of fit) of a quadratic polynomial fit as maximum bulge height increases. R1, R2 and R3 are three different aspect-ratio-rectangular bulge windows. Each R window has many different samples and are designated by S1, S2 and so on. -----102

Figure 5-17 Variation of adjusted R² (goodness of fit) of a biquadratic polynomial fit as maximum bulge height increases. R1, R2 and R3 are three different aspect-ratio-rectangular bulge windows. Each R window has many different samples and are designated by S1, S2 and so on. -----103

Figure 5-18 Rectangular bulge setup showing optically inaccessible spots (1 and 2) which do not correlate well in DIC and result in distortions and excessive noise. -----104

Figure 5-19 C20S3, Circular bulge window of diameter 20mm and sample three. A circular arc fits reasonably well to bulge shape as shown by the values of adjR². -----105

Figure 5-20 Pressure and maximum bulge height (p-h0) response after height correction. Seven cycles are shown -----106

Figure 5-21 (R2S2) Quality of the linear fit of equation (45) for the five loading cycles. -----107

Figure 5-22. Linearization of experimental data for loading of the bulge test (R2S2) with line constants and an adjusted R² value of 81%. -----108

Figure 5-23 (C20S3) Quality of the linear-fit of equation (45) for the eight loading cycles. -----110

Figure 5-24. linearization of experimental data for loading of the circular bulge test (C20S3) with an adjusted R^2 value of 90%. -----111

Figure 5-25 (R3S4) Maximum bulge height and pressure plot of material with five cycles of loading (pressurizing) and unloading (de-pressurizing). The material response mainly stabilizes after the first cycle so that the following loading cycles give fairly consistent pressure and maximum bulge height response with hysteresis. -----112

Figure 5-26 (C20S3) stabilization in the material response curve under cyclic bulging with circular bulge window. The material response is mainly stable after the first cycle. -----112

Figure 5-27 Tensile sample with ten stretching cycles showing stabilization of longitudinal stress-stretch (σ_1 - λ_1) behaviour mainly after the first stretching cycle. -----113

Figure 5-28 (R2S1) A broken DIC correlation at the top of the bulged surface. The size of these missing patches (white colour) increased at higher strains (higher bulge pressure). The bulge-surface is colored with respect to the bulge height. -----114

Figure 5-29 (R2S1) Bulge-profile as exported from DaVis showing non-circular shape but actually observed (through naked-eye) bulge shape during the experiment is circular (cylindrical in 3D).-----115

Figure 5-30 Variation of plane-strain modulus (M_r) showing bad samples. Only R3S1 shows a very high value as compared to the rest of the samples with R2S1 not far from other values in R_2 group. -----116

Figure 5-31 Variation of residual (σ_0) stress showing bad samples. The two samples, R2S1 and R3S1 show very low values for residual stress. 'C' shows the results from circular bulge window of diameter 20 (C20). -----117

Figure 5-32 Variation of plane-strain modulus with rectangular bulge window as the aspect ratio is increased of various samples over cyclic loading. The first cycle of loading has not been shown as the material stabilizes during it. The error bars show a 95% confidence interval on the estimated values. -----118

Figure 5-33 Variation of plane-strain modulus with rectangular bulge window with increasing aspect ratio for many samples. Mean and standard deviation of plane-strain modulus to all cycles of a sample are shown. -----119

Figure 5-34 Variation of plane-strain modulus over three aspect ratios. Aspect ratio of rectangular bulge window show a clear increasing trend. The average value of this parameter for R2 is 1.171 ± 0.24 MPa.-----120

Figure 5-35 Variation of biaxial modulus as material goes through cyclic bulging for two samples. The first bulging cycle data are not shown as the material stabilizes during it. The error bars show a 95% confidence interval on the estimated values. -----122

Figure 5-36 Variation of Young's modulus (E) of the material with circular and rectangular bulge windows. -----123

Figure 5-37 Variation of residual stress of the material with rectangular and circular bulge windows. First cycle of loading has not been shown as the material stabilizes during it. The error bars show a 95% confidence interval on the estimated values. -----124

Figure 5-38 Variation of residual stress of the material with rectangular and circular bulge window geometries. -----125

Figure 5-39 Variation of residual stress value for circular (C) and three aspect ratios of rectangular (R) bulge windows.-----125

Figure 5-40 Gauge lines along length (L) and width (W) for used to calculate stretch ratios. These lines are not fiducial lines rather drawn during processing in DaVis.-----126

Figure 5-41 Values of ν measured at three angle orientations of samples. Samples from two gloves are cut at each orientation and the material is stretched many cycles before recording with the DIC. -----128

Figure 5-42 Variation of Poisson's ratio as calculated from plane-strain modulus and average biaxial modulus value plotted against samples of different geometry. -----129

Figure 5-43 Variation of Poisson's ratio as calculated from plane-strain modulus and biaxial modulus. All samples of one aspect ratio are grouped together. --130

Figure 5-44 Variation of Young's modulus calculated from the tensile test at three different orientations. -----131

Figure 5-45 Engineering stress-strain data for uniaxial tensile test, equibiaxial test (circular bulge test) and pure shear test (plane-strain bulge test). Initial gradients of these curves are also shown. -----133

Figure 5-46 comparison of experimental and modelled stress data for Mooney-Rivlin 9 parameters (MR9) hyperelastic model. MR9 is able to predict all three types of deformations better than all others.-----135

List of Appendix Figures

Figure C 1 Linearizatton result of R1S1 showing a 73% fit to the experimental data
-----172

Figure C 2 Linearizatton result of R1S2 showing a 77% fit to the experimental data
-----172

Figure C 3 Linearizatton result of R1S3 showing a 77% fit to the experimental data
-----173

Figure C 4 Linearizatton result of R1S4 showing a 75% fit to the experimental data
-----173

Figure C 5 Linearizatton result of R2S2 showing a 81% fit to the experimental data
-----174

Figure C 6 Linearizatton result of R2S3 showing a 76% fit to the experimental data
-----174

Figure C 7 Linearizatton result of R2S4 showing a 80% fit to the experimental data
-----175

Figure C 8 Linearizatton result of R2S5 showing a 81% fit to the experimental data
-----175

Figure C 9 Linearizatton result of R3S2 showing a 85% fit to the experimental data
-----176

Figure C 10 Linearization result of R3S3 showing a 87% fit to the experimental data -----	176
Figure C 11 Linearization result of R3S4 showing a 86% fit to the experimental data -----	177
Figure C 12 Linearization result of R3S5 showing a 86% fit to the experimental data -----	177
Figure C 13 Linearization result of C20S3 showing a 90% fit to the experimental data -----	178
Figure C 14 Linearization result of C20S4 showing a 80% fit to the experimental data -----	178
Figure C 15 The transverse strain vs. longitudinal strain for 2 nd cycle for two samples (S2 and S3) -----	179
Figure C 16 The transverse strain vs. longitudinal strain for 3 rd cycle for two samples (S2 and S3) -----	179
Figure C 17 Variation of Young's Modulus with longitudinal stretch for the two samples and three orientations (00°, 45°, and 90°) for 2 nd stretching cycle. ---	180
Figure C 18 Variation of Young's Modulus with longitudinal stretch for the two samples and three orientations (00°, 45°, and 90°) for 3 rd stretching cycle ----	180

List of Tables

Table 1 Different types of materials and geometries generally tested using a bulge test.-----	45
Table 2 Three different rectangular window geometries with their respective aspect ratios (AS) and actual dimensions. All dimensions are in mm. -----	56
Table 3 Varius techniques used for height measurement in a bulge test.-----	61
Table 4 Percentage decrease in maximum bulge height calculated using average height of subset sizes of 15, 21, 27 and 31 pixels when compared to the height calculated from a subset size of 111 pixels. -----	91
Table 5 Showing values of initial and final gradients of three stress-strain curves -----	132
Table 6 showing thirteen ANSYS hyperelastic models calibrated using stress strain data from this study. These models have been ranked with respect to normalized error of fit (residual)-----	134

List of Appendix Tables

Table B 1 Values of the Mooney-Rivlin 5 parameters hyperelastic material constants.-----	157
Table B 2 Values of Yeoh 3 rd Order hyperelastic material constants. -----	159
Table B 3 Values of the Mooney-Rivlin 3 parameters hyperelastic model constants.-----	160
Table B 4 Values of Yeoh 2 nd Order hyperelastic material constants.-----	161
Table B 5 Values of Ogden 1st Order hyperelastic material constants. -----	162

Table B 6 Values of Mooney-Rivlin 2 Parameters hyperelastic material constants.	163
Table B 7 Values of Neo Hookean hyperelastic material constants.	164
Table B 8 Values of Yeoh 1 st Order hyperelastic material constants.	165
Table B 9 Values of Arruda-Boyce hyperelastic material constants.	166
Table B 10 Values of Ogden 3 rd Order hyperelastic material constants.	167
Table B 11 Values of Ogden 2 nd Order hyperelastic material constants.	169
Table B 12 Values of Gent hyperelastic material constants.	171

Abstract

A History Channel modern marvels broadcast aired in 2004 opened with this statement ‘*Our four most important natural resources are air, water, petroleum, and rubber*’. In this list, the last element surprised everyone. No wonder the natural rubber latex is an essential material in today’s modern world. An important application of natural rubber is medical gloves. Reducing thickness of gloves to match the natural feel of human hands is always a challenge while maintaining structural integrity.

A simple testing methodology is required to understand the mechanical behaviour of the thin latex sheets. A uniaxial test and a bulge test with circular and rectangular bulge windows is a simple combination to characterize the mechanical behaviour of this polymer sheet. Poisson’s ratio is directly measured from simple tensile test using Digital Image Correlation (DIC).

The value of Poisson’s ratio is used to critique the bulge test results and underlying assumptions of bulge test analytical models. A bulge test with a sufficiently long rectangular bulge window creates a plane-strain condition, which simplifies the analytical treatments, and an analytical model of bulge pressure and maximum bulge height gives plane-strain modulus. Similarly, a circular bulge window creates a state of equibiaxial strain and a similar analytical model gives biaxial modulus. Both analytical models of the bulge test also give residual stress.

Material samples from gloves (thickness 125 μm) have been characterized with biaxial modulus of $1.863 \pm 0.11 \text{ MPa}$, plane-strain modulus of $1.171 \pm 0.24 \text{ MPa}$ and a biaxial residual stress of $0.292 \pm 0.052 \text{ MPa}$. The value of Poisson’s ratio a mean value of 0.385 ± 0.003 .

Tensile test samples have been cut along three different directions and tensile data shows that the material is isotropic and an interesting relationship between biaxial data and plane-strain data is developed to calculate the anisotropy.

Finally, stress-strain data from these three tests is used to calibrate hyperelastic material models in ANSYS.

1. Introduction

This chapter includes a brief introduction to latex and processing of latex products. It also includes a brief about characterizing and modelling a thin latex polymer film.

1.1 What is Latex?

Natural rubber is widely used in many aspects of life on a daily basis. It possesses some very distinct properties, which put it into a special position among other types of rubber, biopolymers and other materials. The important qualities of rubber are listed below: (Kohjiya et al., 2014)

1. It is the only bio-synthesised (biomass) rubber by a tropical plant, *Hevea brasiliensis*. By means of tapping into the trunk of this tree, a milky liquid called Latex is collected into a container that is hung in a suitable position around the trunk of the tree.
2. It is the only polymeric hydrocarbon among biopolymers, i.e. *cis*-1, 4-polyisoprene that is composed of carbon and hydrogen atoms alone. All other biopolymers contain other covalently bonded elements as opposed to impurities. The covalently bonded elements include nitrogen, oxygen and sulphur, in addition to carbon and hydrogen.
3. Although many different types of synthetic rubbers (biopolymers) have been developed industrially, natural rubber has not yet been chemically synthesised.
4. Being an agricultural product, natural rubber is renewable and carbon neutral. It begins with carbon dioxide as the starting material and decomposes to carbon dioxide at the end of its life cycle. Hence, it does not contribute to global warming.
5. It is the elasticity of natural rubber, which makes it scientifically important. It is an essential material for automobile tyres, among other things.

In 1839, Charles Goodyear developed 'vulcanisation of rubber' (Goodyear, 1839). Vulcanisation is the process of cross-linking the rubber molecules with sulphur to give a stable network structure. This process made relatively less useful material into an industrially important material that transformed manufacturing especially during times of war.

However, the following points must be taken into consideration while trying to understand the mechanical behaviour of this natural material.

1. Since it is agricultural product, the exact percentage of different constituents vary from tree to tree.
2. Geographic location and hence the weather of the area where the rubber tree is grown affects the chemical composition of the natural latex.
3. Processing techniques have been improved over decades of research and development to improve stability, mechanical behaviour, aesthetic properties, durability etc.

Therefore, it is usual to see some variation in the characterized mechanical behaviour of the natural latex material.

For a more detailed and very recent (2014) discussion on Natural Rubber Latex (NRL), the reader is referred to a book (Kohjiya et al., 2014) authored by over a dozen experts from all over the world and topics include:

1. Natural sources and different types of raw materials used in the production
2. Details of biosynthesis, processing and composition
3. Improvements in the sustainable production and recycling and reusing of this strategic material

To help understand the mechanical behaviour and characterization of latex gloves, it is important to understand the processing of latex gloves in a glove manufacturing industry.

1.2 Processing latex gloves

Even though most of the manufacturing process of medical gloves is automated by machines, it is still fairly labor intensive process. For instance, the exam gloves are typically packaged into boxes by hand. For this reason, the cost of labor play a significant role in determining where medical exam gloves are manufactured to ensure the glove factory remains competitive in the global market.

The key element in the glove manufacturing factories is the quality and types of formers used. Therefore, it is not uncommon for some glove factories to produce medical examination gloves as well as industrial gloves, surgical gloves and even condoms.

All images in this section are from science channel's how it is made - rubber-gloves TV program (Channel, 2013)

1.2.1 Cleaning the Glove Formers

Quality production of exam gloves include making sure the environment throughout the glove factory is clean. This also means formers must be cleaned to ensure there are no dirt or debris anywhere. Not cleaning the glove formers would cause the final product to possibly have defects like holes. Exam glove-formers are molds in the shape of a hand made from ceramic material. To clean the glove formers, an acid bath is used by dipping the formers in them and then rinsing with clean water. The formers are then dipped into an alkaline bath to neutralize the

acid, and again rinsed in clean water. Afterwards, the formers are brushed to ensure the surface of the formers are consistent. This is an important step. Factories brush the formers to eliminate pin holes on the latex gloves. All these cleaning stages are shown the Figure 1-1.

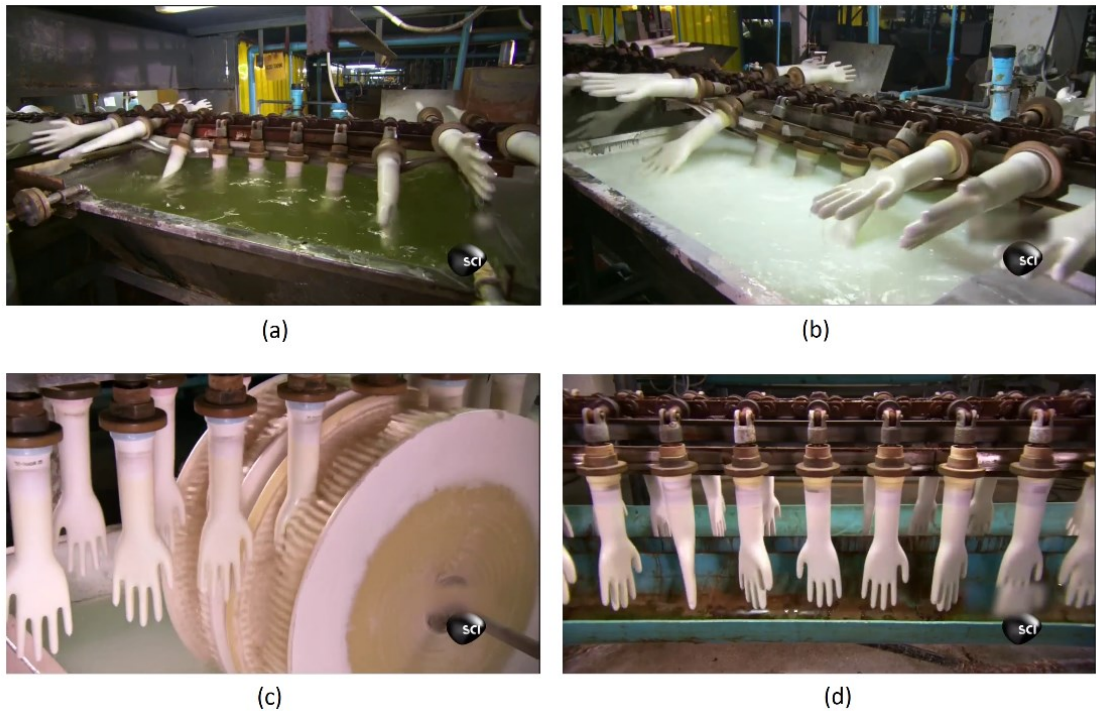


Figure 1-1 Multiple stages of cleaning aglove formers after a previous run. (a) formers taking a dip in a water tank (b) Formers are being cleaned in a chlorine tank (c) Revolving brushes scour the hard to reach ceramic-former surfaces (d) formers are being dried in air while doing a swivel motion.

Glove factories have multiple production lines that produce batches of disposable gloves. A dirty former can result in the manufacturer being forced to trash the entire batch of exam gloves. For this reason, glove formers are regularly inspected and cleaned before the molds are dipped into coagulant tanks.

1.2.2 Former Dipping into Chemicals and Latex Coagulant

Once cleaned, the glove formers are first dipped into a chemical bath. This chemical forms a film onto the formers and it is critical stage, as latex will not adhere to the ceramic formers otherwise.

Next, the ceramic formers are given a bath in a coagulant tank (Figure 1-2) to help the latex mixture adhere to the formers and help ensure the latex is distributed evenly. The coagulant tank stage determines the thickness of the latex exam glove. The thicker the requirements for the disposable gloves are, the longer the formers will travel in the coagulant tank.



Figure 1-2 Glove formers being dipped to form exam gloves

1.2.3 Vulcanizing the Rubber and Leaching

After the formers are dipped into the latex mixture, they eventually travel through a series of ovens to dry the gloves. This process is known as vulcanization (Figure 1-3). Vulcanization gives the rubber latex its strength and elasticity. This process modifies the polymer by forming bridges (cross-links) between individual polymer chains.

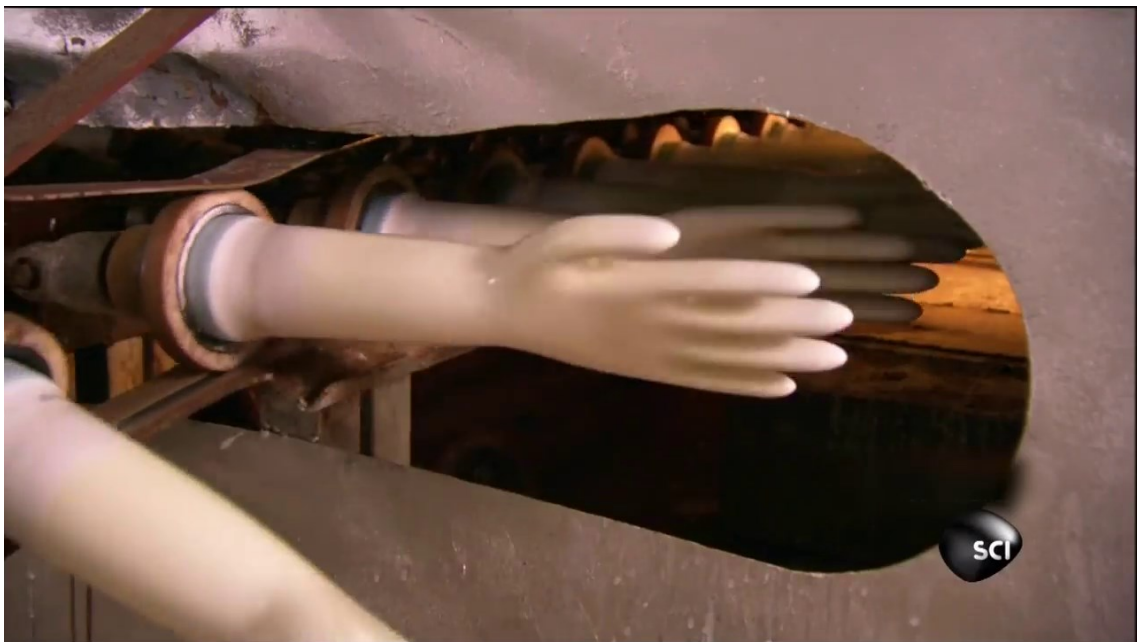


Figure 1-3 Hand formers with latex film entering over for curing (vulcanizing)

After drying the latex mixture, the gloves are put through a leaching line to remove residual chemicals and proteins from the surface of the gloves. A good leaching line should be long, so latex proteins can be more effectively washed out. The water should also be hot and fresh to dissolve proteins better. This step is crucial to minimize the occurrence of latex sensitivity. The key to making a good medical glove is to have a good leaching line. Factories that have bad leaching lines will probably be dirty in addition to the leaching line being short.



Figure 1-4 Latex gloves leached to clean gloves and to remove the chemical residues and proteins.

The glove leaching stage is one area factories will vary depending on the quality of exam gloves that are produced. Implementing a long leaching stage is expensive because there is an opportunity cost in the number of disposable gloves the production line can produce. The best factories will constantly circulate fresh water adding to the cost of making exam gloves marginally more expensive.

1.2.4 Lip Rolling and Stripping Latex Gloves off

Lips (or beads) are rolled on the top of the gloves to facilitate the removal of gloves from formers. These lips also help to put the gloves on and off.



Next, the latex gloves are stripped off the formers. Note that in the Figure 1-5, the workers wear exam gloves and hair coverings so the medical exam gloves being manufactured do not become contaminated.



Figure 1-5 Workers Removing Latex Gloves From Formers

1.2.5 Checking for Defects using Air and Water Tests

One of the quality tests factories will use to meet AQL (Acceptable Quality Level) standards for manufacturing latex exam gloves is the air test. The factories will inflate the latex gloves with air to visually detect any defects placing close attention to the fingers. Air testing the exam gloves is quite effective because the workers can see how the latex material spreads as the glove inflates.



Figure 1-6 Worker testing gloves for holes using air test

The FDA (Food and Drug Authority) requires the testing of medical exam gloves for pinholes, which can best be detected in a water test (Figure 1-7). Each exam glove is filled with 1000 ml of water and examined for leaks.



Figure 1-7 Worker testing medical gloves for holes using water test.

1.2.6 Packing the Exam Gloves in Boxes

The final step in manufacturing latex gloves is to pack the exam gloves in boxes. Factories who are meticulous about quality will pack the exam gloves flat, one on top of the other. This reduces waste, makes gloves easier to take out of the box, and minimizes the bare human hand's touch. Think of how easy it is to dispense tissue from a tissue box. The same idea is applied to exam glove box dispensers. Reputable companies will make sure that every exam glove is packaged using the layered technique.

1.3 Characterizing a Thin Polymer Sheet

Natural rubber is still preferred for many applications, probably because of its unique ability of strain-induced crystallisation (Kohjiya et al., 2014). Stretching a piece of natural rubber at room temperature turns the amorphous rubber into a semi-crystalline material. These crystallites are highly oriented along the tensile direction and, acting like filler particles or crosslinks, tremendously increase the tensile strength (Yeh & Hong, 1979).

Developing an understanding of mechanical properties of thin latex sheets is vital in predicting their response under various kinds of loading conditions, which these thin sheets experience commonly during their applications. The mechanical properties of thin latex sheets have been improved mainly because of secret combinations of ingredients and processing techniques over the past couple of decades. The main drive behind these developments is ever increasing demand of natural latex rubber based products.

Natural latex rubber is extensively used in different medical devices. One of the main medical use of this material is as medical gloves. Apart from helping to mitigate the spread of germs from touching by bare hand, the natural feel of human hand contact with body parts and other tools and objects, called the tactile performance, is another important requirement. The thickness of the medical gloves plays a crucial role when considering tactile performance. The thinner the medical gloves the better, but without compromising the mechanical strength and structural integrity. Therefore, there are many commercially available glove brands, which use a commercially confidential combination of additive ingredients and/or processing techniques to gain competitive advantage in the market. The mechanical properties of thinner material deviates from that of the bulk materials, because of the sample dimensions are in an order of magnitude where physical effects like dislocation motion, takes place (Arzt, 1998).

In light of the above discussion, it almost becomes imperative after a decade or so to characterize the mechanical behaviour of thin latex films used in products where tactile performance is vital besides structural integrity.

Through an in depth review of the literature on polymers thin film characterization methods (discussed in section 2.1.8), a bulge test is chosen. A bulge test is also reported by some other names in the literature; like bubble inflation test (Galliot & Luchsinger, 2011) or bubble-inflation-technique (Reuge, Schmidt, Maoult, M.Rachik, & Abbe, 2001) and pressurized blistering test (Williams, 1997). The bulge test has been developed based upon the seminal work by Beams (Beams, 1959). It is a well-developed technique and performing the experiment is relatively easy. Many common bulging geometries, called bulge windows, can be used with the same bulge experimental setup by changing only a few parts of the bulge test setup. A state of plane-strain (width-height plane) can be achieved by using a sufficiently long rectangular bulge window (Vlassak & Nix, 1992) and a state of equibiaxial stress and strain is achieved at the centre of the bulge-surface from a circular bulge window (Reuge et al., 2001). Analytical solutions involving bulge pressure and maximum bulge height for infinitely long rectangular and circular windows give plane-strain modulus and biaxial modulus through curve fitting.

Residual stress can be introduced in thin films including polymer thin films through volume changes, which may take place in association with crosslinking or crystallization mainly due to:

1. Temperature changes
2. Variation of atmospheric moisture contents
3. Processing techniques

Therefore, both analytical models (rectangular and circular bulge-windows) of bulge pressure and maximum bulge height ($p - h_0$) mentioned above include a compensation term for residual stress and are similarly evaluated through curve fitting.

Therefore, the whole reliability of a bulge test's results depends upon accurate measurements of bulge pressure and maximum bulge height. Accurate pressure measurement is not a big challenge but the accurate measurements of out of plane bulge height is not as simple. Several methods to measure the bulge height have been reported in the literature:

1. Interferometers: (Huang, Lou, Tsai, Wu, & Lin, 2007; Huston, Sauter, Bunt, & Esser, 2001; Maier-Schneider, Maibach, & Obermeier, 1995; Tsakalakos, 1981; Wu, Fang, & Yip, 2004; Xiang & Chen, 2005; Y. H. Xu et al., 2000; Zheng et al., 2000)
2. Atomic force Microscope (AFM): (Schweitzer & Göken, 2007)
3. Microscope: (Kalkman, Verbruggen, Janssen, & Groen, 1999; J. Neggers, Hoefnagels, Hild, Roux, & Geers, 2014; Orthner, Rieth, & Solzbacher, 2010; Pan, Lin, Maseeh, & Senturia, 1990)
4. Moiré Deflectometry: (D. Xu & Liechti, 2010)
5. Mechanical Profilometers: (Jan Neggers, Hoefnagels, Hild, Roux, & Geers, 2013)
6. 3D Digital Image Correlation (3D DIC): (Machado, Favier, & Chagnon, 2012)

3D DIC is one of the techniques used to measure maximum bulge height. It not only measures maximum bulge height but also the full deformed shape. A commercially available 3D DIC system from LaVision will be used in bulge tests and tensile tests throughout this study.

Another important mechanical property of material is Poisson's ratio. It is the negative ratio of lateral and longitudinal strains. A tensile test is a simple way to investigate the Poisson's ratio and using the DIC makes it simple to setup.

1.4 Modelling a Thin Polymer Sheet

Polymers belong to the class of materials called hyperelastic materials. Hyperelastic materials are better known for their ability to sustain large strains (several hundred percent). Several dozen material models have been developed to capture this behaviour (Boyce & Arruda, 2000; Marckmann & Verron, 1999). Hyperelastic material models are developed either based upon their polymer chain structures, called Micromechanical models, or based upon the physical material behaviour without any reference to its chain structure, called Phenomenological models.

Phenomenological hyperelastic models are commonly incorporated into commercial Finite Element Analysis softwares like ANSYS and ABAQUS. ANSYS has been picked up for its built-in hyperelastic model and its geometric modelling capabilities. ANSYS will be used to fit a phenomenological hyperelastic model using various types of engineering stress-strain data (uniaxial, plane and equibiaxial) produced from multiple material characterization tests.

1.5 Aims and Objectives

Aim:

This research will try to characterize a sample of Latex obtained from commercially available gloves using current state-of-the measurement technology. This data will be used in conjunction with existing hyperelastic models to produce viable numerical simulations through simple mechanical testing.

The average thickness of these glove samples is 125 microns. The term thin film has been used throughout this document to refer to latex samples obtained from a specific brand of commercially available gloves measuring 125 microns in thickness.

Objectives:

1. Identify a suitable set of test methods and procedures to capture the mechanical behaviour of the latex polymer under various types of deformation.
2. Characterize typical latex polymer glove samples using above methods.
3. Identify hyperelastic material models that can predict stress-strain behaviour of this polymer.

2. Literature Review

This chapter discusses the modelling of hyperelastic materials. The hyperelastic materials are classified into two categories i.e. Micro-mechanical network based models, and Phenomenological models. There are many hyperelastic models based upon these two approaches, the most common of these models are presented in this chapter.

Most common characterizing techniques employed to hyperelastic materials will also be discussed in this chapter.

2.1 Hyperelastic Material Models

A brief review of common Hyperelastic material models will be presented in this chapter ending with a brief explanation of how some common material characterization tests that are used to curve fit hyperelastic material models.

2.1.1 Introduction.

Rubber materials, also known as hyperelastic materials, are made up of long chains of macromolecules. These macromolecule chains are essentially randomly oriented and made up of cross-linked molecules with weak molecular interactions. The word elastomer is derived from elastic and polymer and is often used interchangeably with rubber because rubber is elastic and made up of long molecular polymer chains. This molecular network structure enables these materials to undergo large strain by changing their random configuration into a stretch-oriented direction that governs the stress-strain behaviour of these polymers (Figure 2-1).

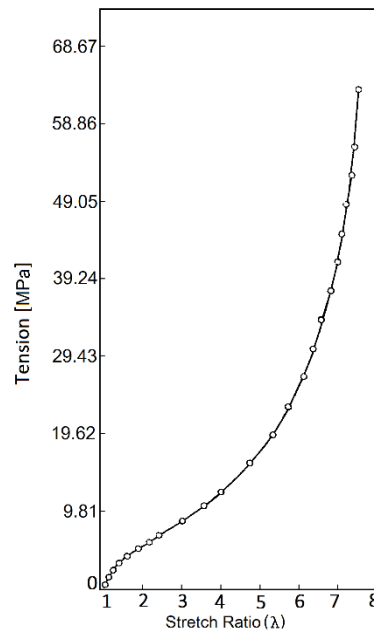


Figure 2-1 A typical hyperelastic (latex polymer) material's "S" shaped response curve showing tensile stress vs tensile stretch ratio (λ) (Treloar, 1944).

The behaviour of a rubber band when stretched many times its original length and, when released, recovering its original size quickly is a common matter of everyday experience. To study this large strain behaviour of rubber-like materials numerous hyperelastic material models have been proposed in the literature. These models are classified by (Treloar, 1978) into two main categories:

1. Micro-mechanical network based hyperelastic models, and
2. Phenomenological models

A wide range of polymers can be modelled satisfactorily using statistical mechanical treatments (micro-mechanical) and continuum mechanics treatments (phenomenological models). Some polymers can withstand more orders of magnitude of stretch (and therefore strain) than others, and some polymers are slightly more compressible than others are, but they mainly exhibit non-linear elastic material behaviour.

Phenomenological models are not derived from any micro-mechanical physical behavioural considerations and usually lack relations to the molecular structure of the material. They are based upon the strain energy potential functions derived using macroscopic continuum mechanics formulations using strain invariants or principle stretches generally having polynomial form while still able to model overall behaviour. Natural latex rubber is assumed isotropic in elastic behaviour (Rivlin, 1948) and very nearly incompressible (Rivlin, 1948). This assumption of incompressibility simplifies the phenomenological materials models greatly. Phenomenological models are commonly implemented in commercial Finite Element Analysis (FEA) packages like ANSYS and ABAQUS. The primary reason for this is the fact that these hyperelastic material models can be calibrated easily with a set of mechanical tests. Calibrating phenomenological hyperelastic models will be discussed further later in this chapter.

Micro-mechanical network models, on the other hand, are based upon underlying physical mechanisms of the material's individual chains. These models relate the applied deformation to the individual chain stretches. For a complete review of statistical mechanics treatment of rubber elasticity and related topics, the reader is advised to see Treloar, (Treloar, 1975).

The performance of a hyperelastic model is based upon its ability to describe the complete behaviour of the material under different loading conditions i.e. Uniaxial or Biaxial and simple or pure shear. Therefore, better models will be those which can predict experimental data satisfactorily under different types of loading conditions (Marckmann & Verron, 1999). An efficient hyperelastic material model can be defined by four qualities (Chagnon, Marckmann, & Verron, 2004).

1. It should be able to accurately reproduce the whole “S” shaped response of rubbers cf. Figure 2-1.
2. The change of deformation modes should not be problematic, i.e. if the model behaves satisfactorily in uniaxial tension, it should also be quite accurate in simple shear or in equibiaxial extension.
3. The number of relevant material parameters must be as small as possible, in order to reduce the number of experimental tests needed for their identification.
4. The mathematical formulation has to be quite simple to render possible numerical implementation of the model.

Therefore, it is imperative to develop a basic understanding of continuum mechanics necessary to model a hyperelastic material model.

2.1.2 Basics of Continuum Mechanics

In the following, the basics of continuum mechanics needed to model hyperelastic materials are presented. This is in no way a complete discussion of continuum mechanics. For more detailed and basic descriptions of the modelling of large strain the reader is advised to read for instance (Ward & Sweeney, 2012).

Several rotation-independent deformation tensors are used in mechanics, the most common are the left and the right Cauchy-Green deformation tensors given by $\mathbb{B} = \mathbb{F}\mathbb{F}^t$ and $\mathbb{C} = \mathbb{F}^t\mathbb{F}$ respectively where \mathbb{F}^t represents the transpose of the deformation gradient tensor \mathbb{F} . The left Cauchy-Green deformation tensor, \mathbb{B} is also known as Finger deformation tensor named after Joseph Finger (1894). Both deformation tensors have the same invariants, I_1, I_2 and I_3 . These strain invariants are given by:

$$\begin{aligned} I_1 &= \lambda_1^2 + \lambda_2^2 + \lambda_3^2 \\ I_2 &= \lambda_1^2\lambda_2^2 + \lambda_2^2\lambda_3^2 + \lambda_1^2\lambda_3^2 \\ I_3 &= \lambda_1^2\lambda_2^2\lambda_3^2 \end{aligned} \quad (1)$$

When dealing with large strains it is convenient to define a stretch ratio instead of strain. A stretch ratio is defined as the ratio of stretched length and original length in each of three mutually normal axes i.e. $\lambda = \frac{L}{L_{original}}$. Hence, stretch ratio

(λ) and engineering strain ($e = \frac{L-L_{original}}{L_{original}}$) are related as:

$$\lambda = 1 + e \quad (2)$$

Hyperelastic material models start by defining a strain energy potential function, W (strain energy per unit undeformed volume). This strain energy potential function is defined either in terms of principal stretch ratios ($\lambda_1, \lambda_2, \lambda_3$) or one or more of the strain invariants, I_1, I_2 and I_3 .

As mentioned earlier most polymers (except foam-like ones) are considered incompressible for most applications thus,

$$I_3 = 1 \quad (3)$$

There are two types of stresses classically defined: the true or Cauchy stress σ and the nominal or first Piola-kirchhoff stress s . Once the strain energy function $W = w(I_1, I_2)$ has been defined, the principle stresses σ_{ii} (σ_{11}, σ_{22} and σ_{33}) can be found using the following relation (Ward & Sweeney, 2012):

$$\sigma_{ii} = 2 \left\{ \lambda_i^2 \frac{\partial W}{\partial I_1} - \frac{1}{\lambda_i^2} \frac{\partial W}{\partial I_2} \right\} - p, \quad i = 1, 2, 3 \quad (4)$$

In equation (4), the term p represents an arbitrary hydrostatic pressure that does not produce any deformation and can be found by applying conditions of equilibrium and/or loading boundary conditions. For example in a uniaxial test σ_{22} (or σ_{33}) can be set equal to zero and an expression for p can be derived.

The nominal stress, s , in terms of the principal stretches and principal strain invariants can be found (Holzapfel, 2000) using the following relations:

$$s_i = \frac{\partial W}{\partial \lambda_i} - \frac{1}{\lambda_i} p, \quad i = 1, 2, 3 \quad (5)$$

$$s_i = \frac{\partial W}{\partial I_1} \frac{\partial I_1}{\partial \lambda_i} + \frac{\partial W}{\partial I_2} \frac{\partial I_2}{\partial \lambda_i} - \frac{1}{\lambda_i} p, \quad OR \quad (6)$$

$$s_i = 2 \left\{ \lambda_i \frac{\partial W}{\partial I_1} - \frac{1}{\lambda_i^3} \frac{\partial W}{\partial I_2} \right\} - p \frac{1}{\lambda_i}$$

Equation (6) can be easily derived from equation (5) using chain rule and the fact that $W = w(I_1, I_2)$ and $I_{1,2} = f(\lambda_i)$. Therefore, values of the nominal stress, s , can be derived from the solution of system of equations (6) by applying loading and boundary condition as explained earlier in this section.

2.1.3 Phenomenological Models based upon Invariants of Strain (I_i)

It is common in the literature to form a strain energy potential function using the continuum mechanics approach in terms of strain invariants. Some more common models are presented here.

2.1.3.1 Polynomial Model

Some of the common hyperelastic models based upon statistical mechanical treatment (phenomenological) take the general polynomial form (ANSYS, 2013):

$$W = \sum_{i+j=1}^N C_{ij}(I_1 - 3)^i (I_2 - 3)^j + \sum_{k=1}^N \frac{1}{d_k} (I_3 - 1)^{2k} \quad (7)$$

The above equation is based upon generalized Mooney strain energy function (Mooney, 1940), constants C_{ij}, d_k are material parameters and determined by curve fitting to experiment data from one or more tests from uniaxial, biaxial, pure shear and volumetric tests. The term involving d_k accounts for strain energy resulting from material compression and if the material is incompressible ($I_3 = 1$), this term is dropped and the equation (7) simplified to the following equation:

$$W = \sum_{i+j=1}^N C_{ij}(I_1 - 3)^i (I_2 - 3)^j \quad (8)$$

In general, there is no upper limit on the value of N and a higher value of N improves fit to an exact solution but it creates computational difficulty. Special cases of equation (8) with values of N upto three give the Neo-Hookean and Mooney-Rivlin models as discussed below.

2.1.3.2 The Neo-Hookean Model (1943):

The Neo-Hookean model is the simplest model. If we retain only the first term of equation (8) we get,

$$W = C_{10}(I_1 - 3) \quad (9)$$

The shear modulus of the material is related to the constant $\mu = 2C_{10}$.

This is equivalent to the Gaussian model, which is based upon a micro-mechanical formulation and takes into account molecular chain statistical considerations

with, $C_{10} = \frac{1}{2}Nk\theta$

where:

N = number of network chains in a unit volume

k = Boltzmann's constant

θ = absolute temperature

Treloar (Treloar, 1944) while investigating carbon black-filled natural rubber found the value of this constant $C_{10} = 0.2 \text{ MPa}$ and showed that this model is able to predict the uniaxial, biaxial and simple shear experimental test data satisfactorily upto 50%.

2.1.3.3 The Mooney Model (1940)

Mooney (Mooney, 1940) observed the linear response of rubber under simple shear loading conditions. This model is actually first two terms of the polynomial model equation (8). He was able to define a strain energy potential function of the form:

$$W = C_{10}(I_1 - 3) + C_{01}(I_2 - 3) \quad (10)$$

where C_{10} and C_{01} are material constants. This model is only suitable for only moderate strains (under 200%).

2.1.3.4 The Mooney-Rivlin Model (1948):

The Mooney-Rivlin model is an improvement of the previous Mooney model by considering more terms of reduced polynomial equation (8). This model has been extensively utilized in the study of polymers and it captures the shortcomings of Neo-Hookean model mainly by considering terms involving the second invariant, I_2 (Steinmann, Hossain, & Possart, 2012).

The series is often truncated to include fewer terms otherwise the unknowns in the equation will rise significantly for example third degree truncation will require 9 material constants. The three-term Mooney-Rivlin strain energy function is given as:

$$W = C_{10}(I_1 - 3) + C_{01}(I_2 - 3) + C_{11}(I_1 - 3)(I_2 - 3) \quad (11)$$

At different deformation states this model can grossly overestimate stresses at moderate to large strains (Boyce & Arruda, 2000).

A two term Mooney-Rivlin model performs well in the moderate strain range *i.e.* 200-250% (Marckmann & Verron, 1999)

2.1.3.5 The Rivlin and Saunders Model (1951):

Rivlin and Saunders (Rivlin & Saunders, 1951) used a biaxial tensile test and obtained experimental conditions to set I_1 or I_2 constant and they observed the following:

- $\frac{\partial W}{\partial I_1}$ is independent of I_1 and I_2 and is constant.
- $\frac{\partial W}{\partial I_2}$ depends inversely upon I_2 .

Based upon the above observations they proposed the following strain energy function:

$$W = C_{01}(I_1 - 3) + f(I_2 - 3) \quad (12)$$

where function f has to be determined using experimental data.

2.1.3.6 The Yeoh Model (1990):

The Yeoh model (Yeoh, 1990, 1993) is another form of reduced polynomial strain energy function with $i = 3$ and $j = 0$ as follow:

$$W = \sum_{i=1}^3 C_{i0}(I_1 - 3)^i \quad OR \quad (13)$$

$$W = C_{10}(I_1 - 3) + C_{20}(I_1 - 3)^2 + C_{30}(I_1 - 3)^3$$

The use of higher order terms of only I_1 in the Yeoh's strain energy function are useful in capturing different modes of deformation i.e. Uniaxial, Biaxial and Shear, at moderate to large strains (Boyce & Arruda, 2000).

2.1.3.7 The Gent Model (1996):

It is a relatively sophisticated model proposed by (Gent, 1996). It is similar to Yeoh as it is also based only upon I_1 but it also includes I_m which limits the maximum finite chain extensibility.

$$W = -\frac{E}{6} \ln \left[1 - \frac{I_1 - 3}{I_m - 3} \right] \quad (14)$$

where E is Young's modulus of the material. As proved by Arruda and Boyce (Arruda & Boyce, 1993a), their 8-chain model (will be discussed in section 2.1.5.2) can be proved equivalent to Gent's model. The logarithm terms can be expanded into polynomial form as follows:

$$W = \sum_{i=1}^n C_i (I_1^i - 3^i) \quad (15)$$

where C_i are material constants. The highest value of n is usually three.

2.1.4 Phenomenological Models based upon Principal Stretch Ratios

(λ_i)

One obvious advantage of using hyperelastic material models based upon principal stretch ratios is that they are directly measurable.

2.1.4.1 The Ogden Model (1972):

The Ogden Model is a sophisticated class of models used in simulation of hyperelastic materials, proposed by R. W. Ogden (Ogden, 1972). The strain energy function is the sum of real powers of principal stretches:

$$W = \sum_{i=1}^N \frac{\mu_i}{\alpha_i} (\lambda^{\alpha_{i_1}} + \lambda^{\alpha_{i_2}} + \lambda^{\alpha_{i_3}} - 3) \quad (16)$$

Here μ_i and α_i are material constants and may assume any real values and are subjected to following stability criteria:

$$\mu_i \alpha_i > 0 \quad \forall i = 1, N \quad (17)$$

This model is most widely used to model large strain because of its ability to be tailored to fit a variety of data but this flexibility comes at the cost of computational difficulty. This model has been shown to fit excellently by the author to the Treloar's (Treloar, 1944) experimental data with $N = 3$ (which requires six material parameters).

This model is particularly popular in FEA but the only possible disadvantage is the six material parameters, which requires large amounts of data for calibration.

2.1.5 Molecular Statistical Network based Models

These hyperelastic material models are founded upon micro-mechanical behaviour of a rubber-like material consisting of network chains. Since the polymer network chains are made up of identical repeat units, called monomers, therefore, the overall response under any loading condition is a collective result of the individual deformations of this network structure. The statistical mechanical based approach begins by assuming a structure of randomly oriented large macromolecules where each chain is regarded as an assemblage of n number of links of length l each.

The simplest model is based upon a Gaussian statistical distribution, also known as the Neo-Hookean model, which has already been discussed previously.

2.1.5.1 The 3-chain Model (1943, 1952):

The 3-chain model is an improvement of the Gaussian model through the use of non-Gaussian network flexible chain theory (Wang & Guth, 1952). In this model, the chains are located along the eigenvectors of the right Cauchy-Green strain tensor using arbitrarily chosen principal axes (Figure 2-2). The chain deforms in an affine manner (transformation that maps parallel lines to parallel lines and finite points to finite points) along these directions giving principal stretch ratios.

The resulting strain energy function is noted as follows:

$$W = \frac{\mu}{3} \sqrt{n} \sum_{i=1}^3 \left[\lambda_i \beta_i + \sqrt{n} \ln \left(\frac{\beta_i}{\sinh \beta_i} \right) \right] \quad (18)$$

where, $\beta_i = \mathcal{L}^{-1} \left(\frac{\lambda_i}{\sqrt{n}} \right)$ for $i = 1, 2, 3$ and \mathcal{L}^{-1} is called the inverse Langevin function

defined by:

$$\mathcal{L}(\beta) = \coth \beta - \frac{1}{\beta} \text{ and}$$

$\mu = Nk\theta$ is shear modulus

N = number of network chains in a unit volume

k = Boltzmann's constant, and

θ = absolute temperature.

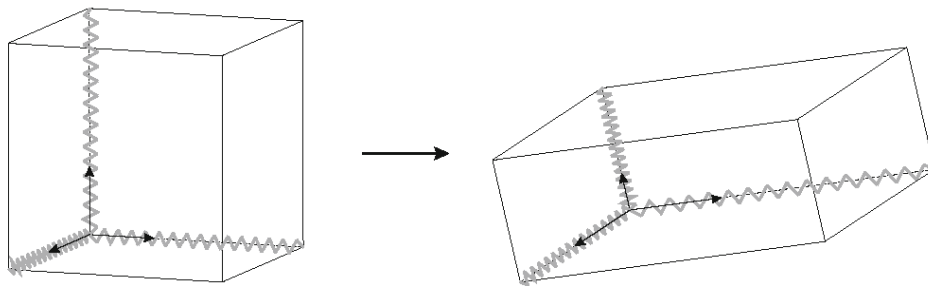


Figure 2-2. A 3-chain model showing initial and deformed chains orientation (Steinmann et al., 2012).

2.1.5.2 The 8-chain Model (1993):

Arruda and Boyce (Arruda & Boyce, 1993b) proposed a model similar to the 3-chain model but is an 8-chain model where it is idealized in a cuboid, Figure 2-3. Each network chain is assumed oriented along a half diagonal of the cuboid. Due to symmetry of the chain structure, the central interior junction point remains at the centre during the deformation. Therefore, the stretch of each chain in the structure is the root-mean square of the applied stretches:

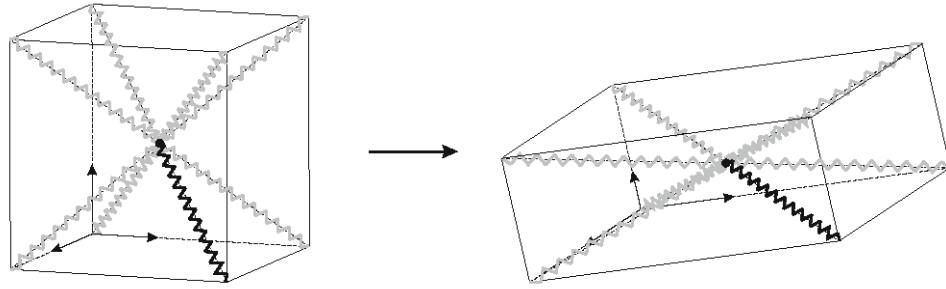


Figure 2-3. An 8-chain model showing initial and deformed chains orientation (Steinmann et al., 2012).

$$\lambda_{chain} = \sqrt{\frac{1}{3}(\lambda_1^2 + \lambda_2^2 + \lambda_3^2)} = \sqrt{\frac{I_1}{3}} \quad (19)$$

The strain energy function is given by the following:

$$W = Nk\theta\sqrt{n} \left[\lambda_{chain}\beta_{chain} + \sqrt{n} \ln \left(\frac{\beta_{chain}}{\sinh \beta_{chain}} \right) \right] \quad (20)$$

where, $\beta_{chain} = \mathcal{L}^{-1} \left(\frac{\lambda_{chain}}{\sqrt{n}} \right)$.

2.1.5.3 The Tube Model (1997):

This model was developed by G. Heinrich and M. Kaliske (Heinrich & Kaliske, 1997) and it proposes that the polymer chains remain in a tube-like structure while surrounded by other chains. This model is based upon the fact that rubber network chains are highly entangled. Therefore, there is always a topology restoring potential in the rubber chain network and this potential is based upon statistical mechanics. The strain potential energy function contains one term accounting for strain energy due to cross-linking and another term for strain energy due to limited chain extensibility of its network chains. The strain energy potential function is given by:

$$W = G_c I^*(2) - \frac{2G_e}{\beta} I^*(-\beta) \quad (21)$$

where $I^*(\alpha)$ is the first invariant of the generalized (Lagrangian) α -order strain tensor, $e_i(\lambda_i; n) = \frac{\lambda_i^n - 1}{n}$, β is an empirical parameter ($0 \leq \beta \leq 1$), and G_c and G_e are cross-link network modulus and constrained (or extensibility) network modulus respectively. Initial shear modulus is given by $G = G_c + G_e$. This model is equivalent to Ogden 2nd order with $\alpha_1 = 2, \alpha_2 = -\beta, \mu_1 = G_c$ and $\mu_2 = -2G_e/\beta$. This model is only suitable for moderate strains (200~250%) and cannot accommodate strain hardening.

2.1.5.4 The Extended-Tube Model (1999)

The same authors (Kaliske & Heinrich, 1999) of the tube model tried to overcome the limitation of their model by replacing the underlying Gaussian distribution by a non-Gaussian distribution. They formulated a new strain energy function by introducing an extensibility parameter δ .

$$W = \frac{G_c}{2} \left[\frac{(1 - \delta^2)(I_1 - 3)}{1 - \delta^2(I_1 - 3)} + \ln\{1 - \delta^2(I_1 - 3)\} \right] + \frac{2G_e}{\beta^2} \sum_{i=1}^3 (\lambda_i^{-\beta} - 1) \quad (22)$$

where I_1 is the first invariant of strain tensor and the other constants used have the same meaning as described in the tube model.

2.1.5.5 The Non-Affine Micro-Sphere Model (2004):

Recently, Miehe et al (C. Miehe, S. Göktepe, 2004) developed an approach based upon many previous models including 3-chains and 8-chains in which individual polymer network chains are considered to be oriented radially from the centre of a unit sphere to its surface. The authors suggested that a discretization of 21 directions over a half sphere are sufficient to approximate a uniform distribution of the chains over the sphere surface, which ensures isotropic behaviour of the local chains. The strain energy function is as follows:

$$W = Nk\theta n \sum_{i=1}^{21} w_i \left[\frac{\lambda_i \beta_i}{\sqrt{n}} + \ln \left(\frac{\beta_i}{\sinh \beta_i} \right) \right] \quad (23)$$

where, w_i are weight factors.

2.1.6 Conclusive remarks about Hyperelastic Models

M. Johlitz et al. (Johlitz & Diebels, 2011) have simulated and compared uniaxial and biaxial tensile stretch experiments data for silicon rubber ELASTOCIL[®] RT 265 using Neo-Hookean, Mooney-Rivlin and Yeoh hyperelastic models. They found that Neo-Hookean model is only sufficient to model a uniaxial test data. Whereas, a Mooney-Rivlin hyperelastic model can simulate both types of test data satisfactorily upto a stretch of 60%.

E. Verron & G. Marckmann have extensively studied the inflation of rubber balloons and bubble inflating flat thin rubber sheets and performed numerical simulations of this problem using various hyperelastic models. At first, (Verron & Marckmann, 2003b) they have used a two-terms Mooney-Rivlin model to do a numerical study of inflation of two connected (where air can move between them) rubber balloons. They concluded that the equilibrium of the connected balloons is complicated and more complex hyperelastic constitutive equations, such as Ogden's models, are needed to model the hyperelastic behaviour.

Later on the same year, E. Verron & G. Marckmann (Verron & Marckmann, 2003a) have numerically simulated the same problem of inflating rubber balloons using Network constitutive models. They have compared classical neo-Hookean model with 3-chain, 8-chain and full network (which later became micro-sphere model) hyperelastic models. They concluded that classical Neo-Hookean hyperelastic model does not account for the strain hardening which influences the shape of inflated hyperelastic material.

Carbon black rubber at moderate engineering strain (~25%) have been simulated using Yeoh model in a commercial FEA code (ANSYS™) by Mathew Wadham-Gagnon et al (Wadham-Gagnon et al., 2006). They calibrated the Yeoh model and used it to experimentally validate the model by performing an experimental test on a cantilevered rubber plate subjected to a bending load at the free end of the plate.

M. Afandi (Mohammed, 2014) has shown that the gluten can be modelled as a finite viscoelastic material using extended tube model. The extended tube model when calibrated using uniaxial tension and compression, agrees reasonably well with the experimental results except for tension results of strain more than 0.7.

It can be clearly seen from the above discussion that suitability of a particular hyperelastic model to perform a numerical simulation is based upon the results of calibration of these models with test data (Uniaxial, Biaxial and Pure shear). A hyperelastic model with relatively small error of fit is deemed best. Therefore, a suitable hyperelastic model to perform a numerical simulation of a bulge test will be selected based upon the lowest value of error of fit while calibrating.

2.1.7 Curve Fitting a Phenomenological Hyperelastic Material Model

Curve fitting a particular phenomenological hyperelastic material model, which finds the coefficients of the strain energy potential function (W) requires engineering stress-strain data from one or more of the following type of tests:

3. Uniaxial tension or compression test
4. Biaxial tension or compression test
5. Pure Shear test (planar test)

Although fine-tuning a hyperelastic model with only a uniaxial test will give reasonably accurate results for simple low strain (~50%) applications, for more complex modes of deformation and higher strains, more than one type of test data is required. A volumetric test can also be performed when fitting a hyperelastic model to simulate a compressible hyperelastic material, generally a foam.

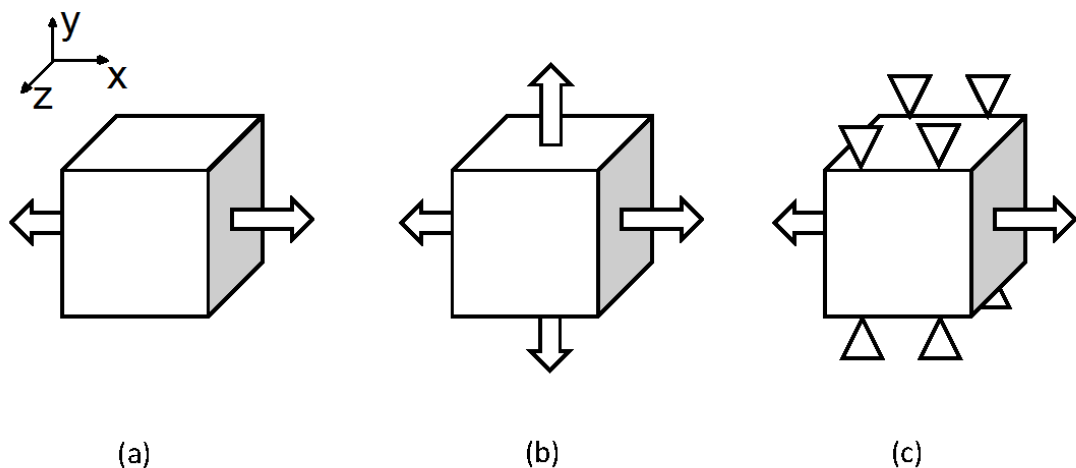


Figure 2-4 Schematic representation of three tests. The arrows show stresses. In the absence of any symbols, the system is free to move along that direction (a) Uniaxial tension (b) Equibiaxial tension (c) Planar tension (or Pure shear), with triangles showing fixed supports.

2.1.7.1 Uniaxial Test

In a uniaxial test, the material sample is stretched (or compressed) in the longitudinal dimension only, therefore the stretch ratios for an incompressible material and state of stress defining the deformation state and stress state respectively are as follow:

$$\lambda_1 = \lambda \text{ and } \lambda_2 = \lambda_3 = \frac{1}{\sqrt{\lambda}} \quad (24)$$

Using these values of λ and the facts that for a thin material uniaxial tensile test $s_3 = 0$, equation (6) can be used to drive the following relation for nominal stress, s_1 .

$$s_1 = 2 \left(1 - \frac{1}{\lambda^3} \right) \left(\lambda \frac{\partial W}{\partial I_1} + \frac{\partial W}{\partial I_2} \right) \quad (25)$$

2.1.7.2 Biaxial Test

The biaxial test is another commonly used test. A special type of biaxial test is an equibiaxial test. In an equibiaxial test, a material sample, usually square shape, is stretched equally in two dimensions (both dimension are equal) and hence the name equibiaxial. Therefore, the stretch ratios and state of stress defining the deformation state and stress state respectively are as follow:

$$\lambda_1 = \lambda_2 = \lambda \text{ and } \lambda_3 = \frac{1}{\lambda^2} \quad (26)$$

Using these values of λ and the facts that for a biaxial test $s_1 = s_2$ and $s_3 = 0$, equation (6) can be used to drive the following relation for nominal stresses s_1 and s_2 .

$$s_1 = s_2 = 2 \left(\lambda - \frac{1}{\lambda^5} \right) \left(\frac{\partial W}{\partial I_1} + \lambda^2 \frac{\partial W}{\partial I_2} \right) \quad (27)$$

2.1.7.3 Planar Tensile Test (or Pure Shear Test)

In a planar test, one dimension of the test sample (at least ten times more than the one being stretched) is held fixed ($\lambda_2 = 1$) while the other dimension is stretched like a tensile test. Therefore, the stretch ratios and state of stress defining the deformation state and stress state respectively are as follow:

$$\lambda_1 = \lambda, \quad \lambda_2 = 1 \text{ and } \lambda_3 = \frac{1}{\lambda} \quad (28)$$

Using these values of λ and the facts that for a biaxial test $s_1 = s_2$ and $s_3 = 0$, equation (6) can be used to drive the following relation for nominal stresses s_1 .

$$s_1 = 2 \left(\lambda - \frac{1}{\lambda^3} \right) \left(\frac{\partial W}{\partial I_1} + \frac{\partial W}{\partial I_2} \right) \quad (29)$$

Once engineering stress-strain data is on hand, the simplest approach as taken by many researchers is to use a commercial FEA software like, ANSYS or ABAQUS (Daly, Prendergast, Dolan, & Lee, 2000; Gong & Riyad, 2002; Wadham-Gagnon et al., 2006) to find the coefficients of the strain energy potential functions.

ANSYS provides a simple drag and drop functionality when a new material is defined, one of the hyperelastic models can be dragged on to the new material's properties box. Similarly, a set of material tests can subsequently be dragged and dropped onto the properties box and values of stress and strain can be pasted into the table of the respective test.

2.1.8 Characterizing Hyperelastic Materials

In this section, common technology and tests employed to characterize hyperelastic thin materials will be presented.

2.1.8.1 Introduction

Hyperelastic materials are generally characterized by non-linear elastic behaviour with large, mostly recoverable, elastic deformations. Their mechanical behaviour also strongly depends upon temperature and strain rates.

C. Poilane et al (Poilane, Delobelle, Lexcellent, Hayashi, & Tobushi, 2000) have used nanoindentation, bulge test and point membrane deflection to characterize thin film of polyurethane shape memory polymer and compared these three non-conventional characterizing techniques. They have obtained similar values of Young's modulus and residual stress with the three charactering techniques i.e. nanoindentation, bulging and point membrane deflection.

C.K. Huang et al (Huang et al., 2007) have characterized Polymethyl methacrylate (PMMA)-based polymer using bulge tests with square and rectangular bulge windows. They have also studied the effect of different thicknesses on the value of Young's modulus and concluded that slight thickness variations have no significant effect on Young's modulus. They have also concluded that a bulge test measures average values as compared to a nanoindentation test.

Galliot & Luchsinger (Galliot & Luchsinger, 2011) have characterized Ethylene Tetra Fluoro Ethylene (ETFE) foils using uniaxial tensile tests, biaxial extension of cruciform specimen and bubble inflation (bulge test) tests.

Therefore, from the above discussion, the most common experimental measurement techniques (tests) employed to characterize the mechanical behaviour of thin hyperelastic materials are uniaxial tension and biaxial extension tests, nanoindentation and bulge tests.

2.1.8.2 Uniaxial Tension Test

The uniaxial tension test or simply the tensile test is the most common type of test in material science because of the relatively simple construction of its testing device. It typically gives the load-deflection profile along the longitudinal direction. It can also be used to calculate Poisson's ratio, another important property. Measurement of Poisson's ratio requires strain to be measured in the transverse direction. With the advancements of optical measurement techniques (like Digital Image Correlation), it is comparatively easy to measure strains in longitudinal and lateral sample directions. Therefore, a tensile test can measure Poisson's ratio directly; alternatively, Poisson's ratio can be estimated from a combination of other tests data.

2.1.8.3 Biaxial Extension Test

The biaxial extension test is another common test performed to characterize hyperelastic materials. A biaxial extension test, as compared to a simple tensile test, is more versatile but requires a more complex setup. A common geometry of sample is a cruciform which facilitates gripping but uses more material and sometimes test samples start tearing from corners which limits the maximum strain (Galliot & Luchsinger, 2011).

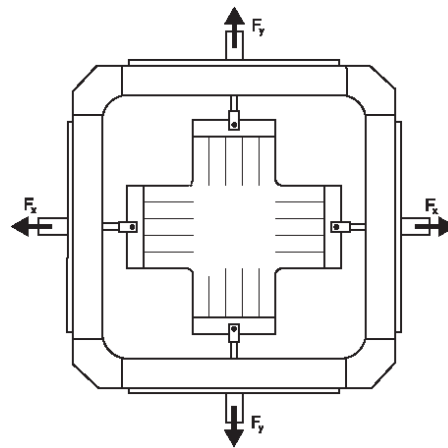


Figure 2-5 A cruciform material sample for equibiaxial testing. [Source: adopted from (Galliot & Luchsinger, 2011)]

Others have used more complex grips which are attached all around the edges to maintain equibiaxial loads (Johlitz & Diebels, 2011; Kim et al., 2012; Meng et al., 2015).

However, a biaxial tension test setup is worth the effort as it captures a large part of possible deformation states mainly because of its ability to stretch samples in two orthogonal independent directions at the same time. Therefore, it is easier to perform simple tension and pure shear tests (planar test) using the biaxial test

setup. Sometimes the term biaxial is used synonymous with equibiaxial. Engineering stress-strain data obtained from equibiaxial test is then used to fit hyperelastic material models discussed in section 2.1.6.

2.1.8.4 Nanoindentation

Nanoindentation is a thin film characterization technique similar to the hardness tests commonly used for bulk material. A nanoindentation test uses an indentation instrument (a diamond Berkovich type indenter), which measures the penetration depth and load during the loading and unloading continuously (Oliver & Pharr, 1992).

The indentation depth is related to the area of contact between the indenter and the test material. This is done by making the indentation with a well-controlled force while continuously monitoring and measuring the displacement of the indenter, Figure 2-6. A nanoindentation test typically gives hardness and Young's modulus of the material.

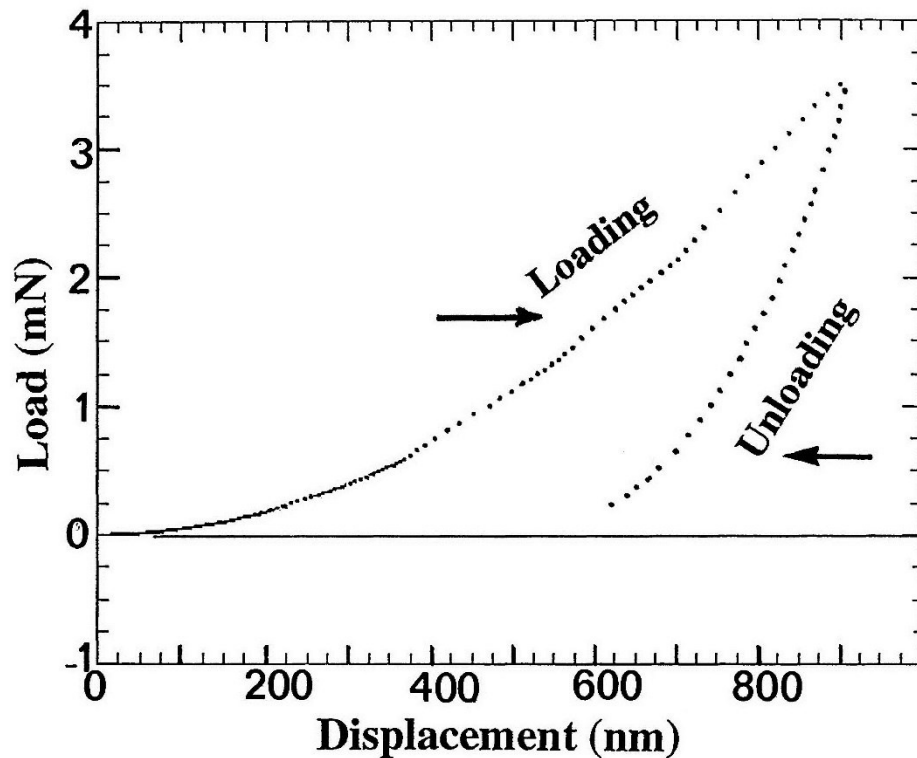


Figure 2-6 Example of the evolution of the applied load vs. the penetration depth upon nanoindentation cycle (Poilane et al., 2000).

2.1.8.5 Bulge Test

The bulge test is a versatile characterization method capable of determining a complete set of material properties of thin films under various controlled conditions i.e. temperature, pressure and humidity (Tsakalakos, 1981). Hardware setup is relatively simple and mounting samples is quick and easy. Following the original work (Beams, 1959), this technique was used by many researchers with many innovative improvements.

A bulge test is based on the precise measurement of the maximum bulge height of the centre of a thin film, h_0 under a uniform applied pressure, p . This $p - h_0$ behaviour depends upon the geometry of the bulge sample. Figure 2-7 shows a rectangular bulge geometry.

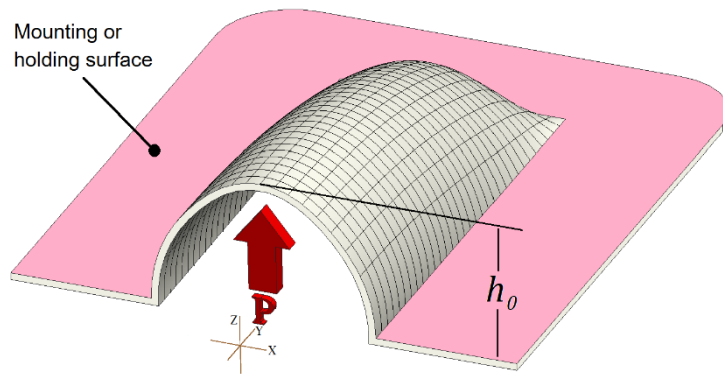


Figure 2-7 A rectangular sample (half section) under bulge and coordinate system.

Bulge test has been successfully used to characterize thin films of a variety of materials (metals, ceramics, semiconductors and polymers) and bulge geometries, summarized in Table 1.

Table 1 Different types of materials and geometries generally tested using a bulge test.

Material tested	Reference	Bulge geometry
Low pressure chemical vapour deposited Silicon Nitride (LPCVD Si ₃ N ₄)	(Kalkman et al., 1999; Maier-Schneider et al., 1995; Schweitzer & Göken, 2007; Vlassak & Nix, 1992; Youssef, Ferrand, Calmon, Pons, & Plana, 2010)	Square, Rectangular
Silicon Carbide (SiC)	(Huston et al., 2001; Wu et al., 2004)	Square, Rectangular, Circular
Silicon (Si)	(Huston et al., 2001; Youssef et al., 2010)	Square, Rectangular
Cu, Cu-Ni, Al-Cu	(Kalkman et al., 1999; Schweitzer & Göken, 2007; Tsakalacos, 1981)	Rectangular, Circular
Poly-arylethers (PAE)	(Y. H. Xu et al., 2000; Zheng et al., 2000)	Square
Polyethylene terephthalate (PET)	(D. Xu & Liechti, 2010)	Rectangular, Circular
Ethylene tetra fluoro ethylene (ETFE)	(Galliot & Luchsinger, 2011)	Circular
Silicon based elastomer (RTV 141)	(Machado et al., 2012)	Rectangular

Therefore, the commonly investigated bulge window geometries are rectangular and circular.

2.1.8.5.1 Bulge Test with Rectangular Thin Film Samples

The crux of this test is the correlation between bulge pressure, p and maximum bulge height h_0 . Figure 2-8 shows the basic geometry of a rectangular film sample.

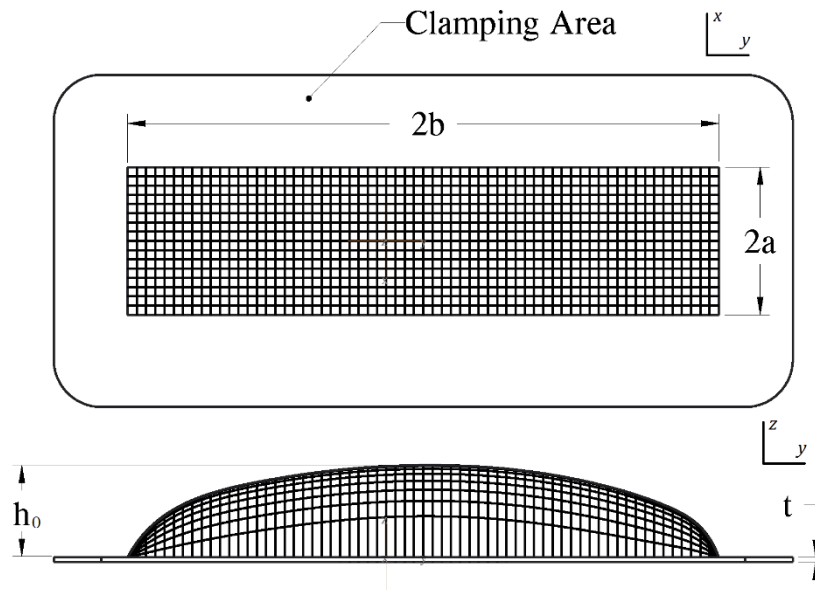


Figure 2-8 Nomenclature of a rectangular thin film sample

A well-established correlation is given by (Pan et al., 1990) for a rectangular film sample as follows:

$$p = C_1 \frac{\sigma_0 t}{a^2} h_0 + C_2 \frac{Et}{a^4(1-\nu)} h_0^3 \quad (30)$$

Where, p is the applied differential pressure, t is the undeformed thickness, h_0 is the maximum height at the centre of the thin film, E is the elastic modulus, ν is the Poisson's ratio, a is the characteristic lateral dimension of the thin film measured from centre, and σ_0 is the residual stress with C_1 and C_2 as dimensionless constant functions. The value of C_1 depends upon the aspect ratio $\left(\frac{b}{a}\right)$ of a square or a rectangular sample. The value of C_1 for a square film sample is 3.393 and

for a rectangular sample, it approaches a value of 2.0 as the aspect ratio approaches 4.0 (Vlassak & Nix, 1992). C_2 , on the other hand, depends upon Poisson's ratio, ν and the aspect ratio $\left(\frac{b}{a}\right)$ of the rectangular sample and its value becomes independent of aspect ratio as aspect ratio exceeds a value of 4.0 (Vlassak & Nix, 1992). Therefore, for a sufficiently long rectangular sample ($b \geq 4a$), C_2 is $\frac{4}{3(1+\nu)}$. Herein the term 'long rectangular film' will mean ($b \geq 4a$). Therefore, for a sufficiently long rectangular film sample, the state of strain becomes plane-strain as strain in the length direction (y -axis) of the film is negligible. The only strain is in width-height plane (xz -plane)

$$p = \frac{4M_r t}{3a^4} h_0^3 + \frac{2\sigma_0 t}{a^2} h_0 \quad (31)$$

Where $M_r = \frac{E}{1-\nu^2}$ is known as plane-strain modulus.

2.1.8.5.2 Stress and Strain in Rectangular Thin Film Bulge Samples

In a long rectangular film under uniform pressure, the shape of the bulge is cylindrical. If $h_0 \ll a$, then the measured $p - h_0$ data can directly translate into the nominal stress and nominal strain using the following relations (derivation in Appendix A)

$$s_x = \frac{pa^2}{2h_0 t}, \quad e_x = \frac{a^2}{6R^2} = \frac{2h_0^2}{3a^2} \quad (32)$$

where R is the radius of bulged-cylindrical surface. Deflection (h) of the thin film is a polynomial function but for very low bulge heights in long rectangular samples the bulge-shape can be modelled as a parabola satisfactorily (Kalkman et al., 1999).

Equation (32) will be used to calculate nominal stress-strain data to calibrate hyperelastic models.

Using true strain $\varepsilon = \ln\left(\frac{\text{Stretched length}}{\text{Original length}}\right)$ and considering incompressible material:

$$\varepsilon_x + \varepsilon_y + \varepsilon_z = 0 \quad (33)$$

The plane-strain assumption dictates that $\varepsilon_y = 0$, then the thickness of material at the pole of the bulged surface can be approximated using the following equation with $\varepsilon_x = \varepsilon$:

$$t_p = t \cdot \exp^{-\varepsilon} \quad (34)$$

The true stress is calculated using the reduced (actual) thickness and is given by:

$$\sigma_x = \frac{p(a^2 + h_0^2)}{2h_0 t_p} \quad (35)$$

It is easy to calculate the stretched length of the sample along the x (or y) axis and hence the stretch ratio (λ). Using the basic relation to calculate the stretched arc length along the width axis of the rectangular bulge window and dividing the stretched arc length by its original width, in this case the half-width of rectangular bulge window ' a ' gives the stretch ratio. (Appendix A)

$$\lambda = \frac{R}{a} \sin^{-1}\left(\frac{a}{R}\right) \quad (36)$$

Therefore, the true strain is calculated as follows:

$$\varepsilon = \ln(\lambda) = \ln\left[\frac{R}{a} \sin^{-1}\left(\frac{a}{R}\right)\right] \quad (37)$$

2.1.8.5.3 Bulge Test with Circular Thin Film Samples

A general correlation between applied differential pressure (p) and the resulting radius of curvature (R) is given as (D. Xu & Liechti, 2010):

$$p = \frac{M_c t a^2}{3} \left(\frac{1}{R}\right)^3 + 2\sigma_0 t \left(\frac{1}{R}\right) \quad (38)$$

where $M_c = \frac{E}{1-\nu}$ and is known as biaxial modulus.

But there is a discrepancy in equation (38) between the strain energy and work done by pressure, to compensate this difference, a mean strain is introduced by (Wan, Guo, & Dillard, 2003) as follows:

$$\varepsilon_e = \frac{3}{4} \varepsilon = \frac{a^2}{8R^2} \quad (39)$$

This mean strain has also been derived by Williams (Williams, 1997) based upon general elasticity.

So equation (38) becomes,

$$p = \frac{M_c t a^2}{4} \left(\frac{1}{R}\right)^3 + 2\sigma_0 t \left(\frac{1}{R}\right) \quad (40)$$

2.1.8.5.4 Stress and Strain in Circular Thin Film Bulge Samples

The true biaxial state of stress exists at the centre of the bulged surface (called pole) as depicted in Figure 2-9. The biaxial true stress at the pole of the spherical cap is given by:

$$\sigma_x = \sigma_y = \frac{pR}{2t_p} \quad (41)$$

where,

p = bulge pressure

R = bulge radius or radius of curvature

t_p = thickness of the bulge sample at the pole

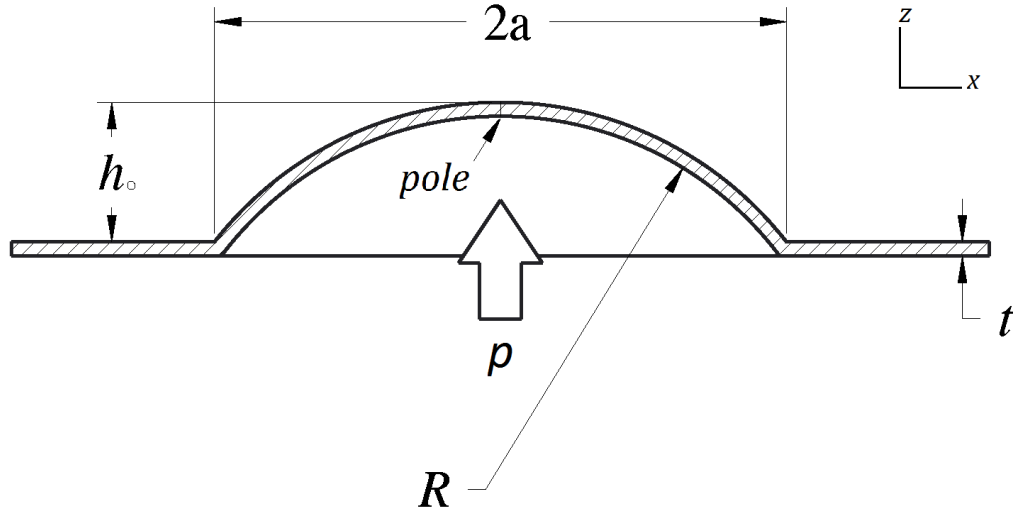


Figure 2-9 A circular bulge sample geometry showing, the radius of the die hole (window) 'a', R is the radius of the bulged spherical cap, bulge pressure p and h_0 is the maximum bulge height.

Thickness of the thin polymer can be approximated using equibiaxial true strains along x and y -axes. Since the polymer is assumed incompressible, it results in the following equation:

$$\varepsilon_z = -\varepsilon_x - \varepsilon_y \quad (42)$$

Since $\varepsilon_z = \ln\left(\frac{t_p}{t}\right)$ and $\varepsilon_x = \varepsilon_y = \varepsilon$, therefore

$$t_p = t \cdot e^{-2\varepsilon} \quad (43)$$

The stretch ratio (λ) is calculated using equation (36) and the true strain is calculated from equation (37):

2.1.9 Summary

Polymers belong to a type of material called hyperelastic materials. Hyperelastic materials are modelled either using phenomenological or based upon molecular statistical networks. The choice of a particular model depends upon, how good the model can fit various types of tests data (Uniaxial, biaxial, pure shear).

Bulge test is well-developed thin films characterization technique, able to determine important mechanical properties. Using long rectangular and circular bulge windows and fitting their corresponding analytical models, Young's modulus (given Poisson's ratio) of the material can also be calculated besides biaxial modulus and plain-strain modulus.

A tensile test with means to measure lateral strain can be used to measure Poisson's ratio.

Therefore, a bulge test with rectangular and circular bulge geometries and a tensile test will be performed to characterize the polymer samples.

3. The Experimental Setup

This chapter details the customised hardware setup design of the bulge and the tensile tests. The bulge test has two variants with slight modification to its sample holding fixture; one to hold a circular, \varnothing 20 mm sample, and another to hold a rectangular sample.

A tensile test setup is built by modifying the bulge hardware setup. The same syringe pump used to apply bulge pressure is used to perform the tensile tests.

3.1 Bulge Hardware Setup

The bulge testing system (Figure 3-1) is made-up of many sub-systems as follows:

1. A bulge chamber assembly with the provision of sample mounting and a buffer chamber.
2. A pressure sensor with electrical signal output.
3. A source of compressed air (a retrofitted syringe pump)
4. A control system: a non-PC based microcontroller system (Arduino)
5. and a bulge height measurement system (3D DIC by LaVision)

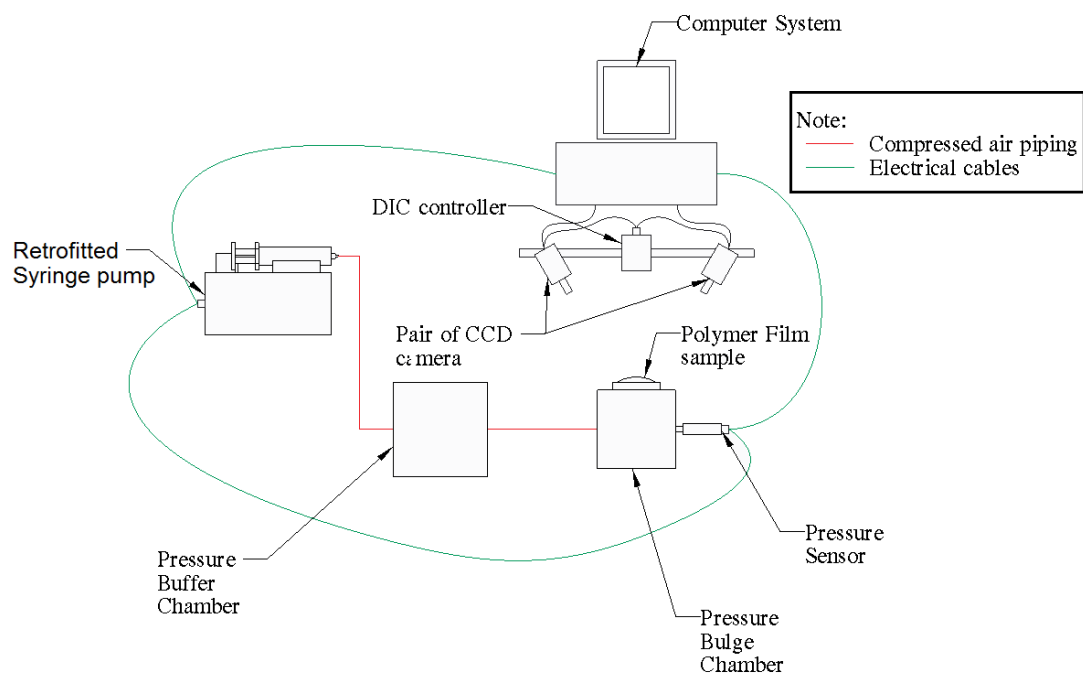


Figure 3-1 A systematic overview of bulge setup with Digital Image Correlation (DIC) system. The syringe pump also houses the micro-controller in it.

3.1.1 The Bulge Chamber Assembly

A cylindrical hole is drilled in a solid circular stock of steel of outer diameter $\varnothing 75$ mm. The top side of the bulge chamber, Figure 3-2, was machined to provide a standard groove for an O-ring to seal the bulge chamber and sample platform. Several other side holes are necessary for compressed air inlet/outlet and for pressure sensor attachment. An extra side hole, which was originally drilled for an exhaust controller that was needed in case of a desktop compressor was used, is plugged. The size of the bulge test geometry dimensions is limited by the maximum dimensions of the nearly flat samples, which can be obtained from the palm area of the gloves.

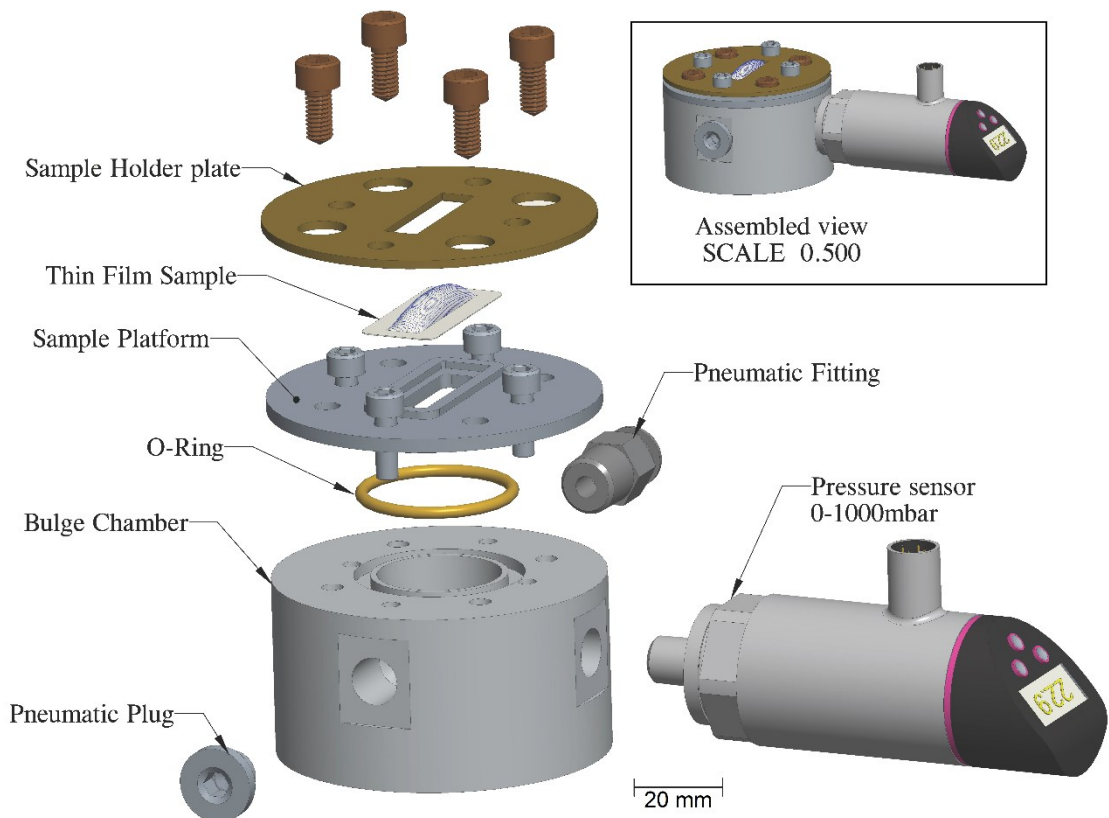


Figure 3-2. The bulge chamber assembly, showing bulge chamber, sample mounting and holding configuration of a rectangular sample and pressure sensor.

Insert shows the bulge Chamber assembled view @ 0.5 the scale of the exploded assembly.

A sample platform is machined and bolted on top of the pressure chamber. This platform with sample holder plate mainly serves two purposes:

1. Provide a uniform surface for mounting the sample.
2. It can be changed, along with the sample holder plate, to accommodate different aspect ratios of rectangular and circular samples without changing the whole bulge chamber.

The polymer sample is sealed onto the sample platform with a sample holder plate, which is bolted into the bulge chamber body through the sample platform. The pressure is applied through a buffer chamber. The buffer chamber is not shown in Figure 3-2, as it is the same as the bulge chamber but with only inlet and outlet side-holes for compressed air and the top sealed through an O-ring. The purpose of the buffer chamber is to add some stability by smoothing out any pressure fluctuations during loading and unloading cycles. Figure 3-3 shows the sample platform and sample holder plate as seen in a CAD package (PTC Creo).

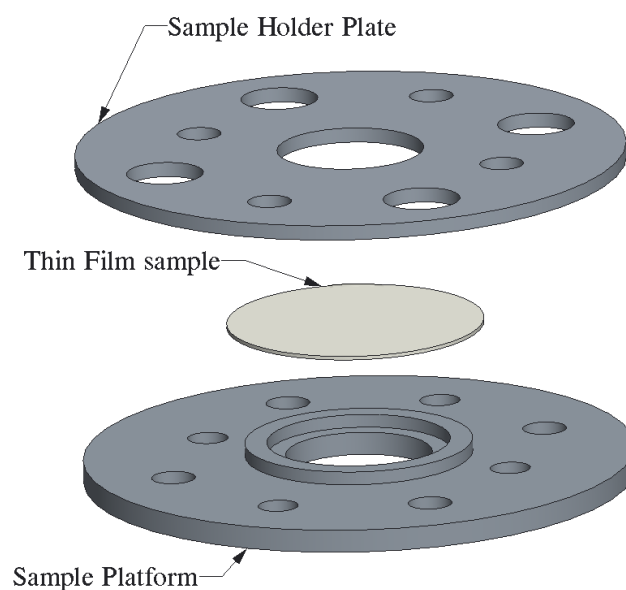


Figure 3-3 sample platform and holder plate for circular bulge samples.

The diameter of the circular bulge geometry is $\varnothing = 20\text{mm}$.

Three different aspect ratios of rectangular geometries have been used as shown in Figure 3-4 and Table 2.

Table 2 Three different rectangular window geometries with their respective aspect ratios (AS) and actual dimensions. All dimensions are in mm.

#	Name [Nominal size]	Width (2a)	Length (2b)	AS (b/a)
1	R1 [8x32]	7.93	31.93	4.03
2	R2 [6x36]	5.85	36.03	6.16
3	R3 [5x35]	4.83	34.93	7.23

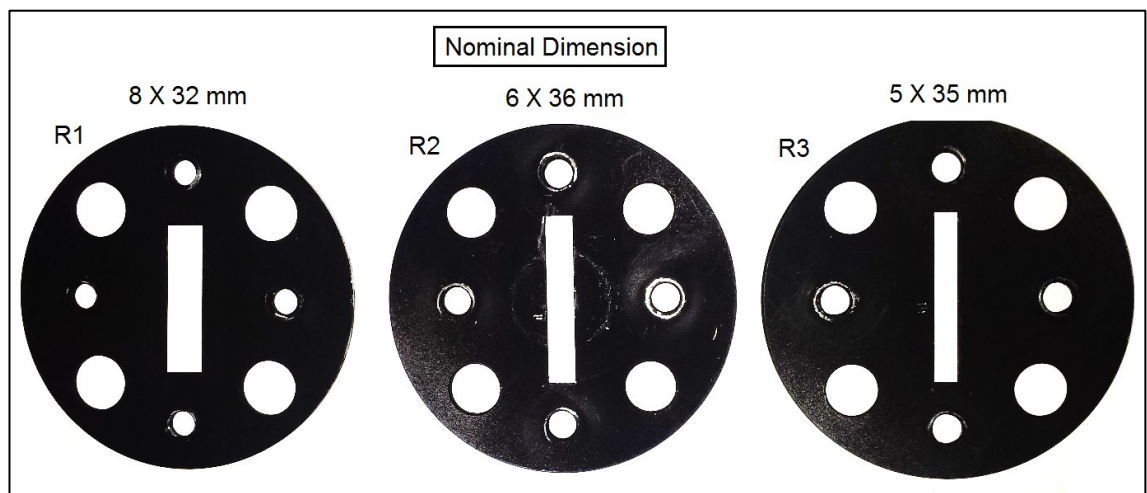


Figure 3-4 Three different rectangular sample windows (sample holder plates) nominal sizes (WxL mm).

3.1.2 The Pressure Sensor

The pressure sensor from IFM (PN3097) has a working range of 0-101kPa. This pressure sensor also has an LCD display for reference purposes. The pressure sensor analogue current output is 0-20 mA and Vdc is 0-10 volts.



Figure 3-5 The pressure sensor (IFM PN3097) attached to the bulge chamber with a rectangular bulge window mounted on the top. The lcd display unit are set to kPa.

This voltage can be recorded into the DIC system through its built-in analogue-to-digital convertor (ADC) of the 'Strain Master' Controller (LaVision™) but it is only passive recording without any means of controlling the pressure.

The pressure has to be controlled during the experiment to maintain the same maximum pressure during loading cycles. The solution is to use an external control system, which can also control the pressure while storing pressure ADC data.

In this case, the pressure sensor output signals were stored in the control system. The control system used is an Arduino Nano general purpose board (version 3.0).

3.1.3 The Syringe Pump System.

A syringe pump system has been modified, only its hardware has been used after removing all the electronic circuitry. The hardware used includes the body, a syringe holding fixture, leadscrew with v-grooved belt-pulley assembly and a stepper motor. The leadscrew receives the torque through a drive belt, which reduces the speed of the motor to half. There is no need to physically remove the keypad and LCD screen since it is disconnected (seen in Figure 3-6).

The stepper motor is a six wire centre-tapped and takes 200 steps per revolution, thus giving 1.8° per step. A simple resistance measurement method with the help of a digital multimeter was used to identify the common terminals of the centre-tapped-6-wired stepper motor. Further trial and error revealed the complete order of the step sequence to run the stepper with any desired steps, speed, and direction. The maximum speed at no load is found to be not more than 120 revolutions per minute (RPM). The stepper motor have been programmed to run at 60 RPM for all bulge experiments. Therefore, the leadscrew rotates at half the speed, 30 RPM. The pitch of the leadscrew has been measured to be 0.5 mm. At the current parameters, the platform attached to the leadscrew travels linearly with a speed of 15 mm/min.

A 100ml syringe has been used throughout the bulge tests; Figure 3-6 shows the complete syringe pump with control system inside the pump body.

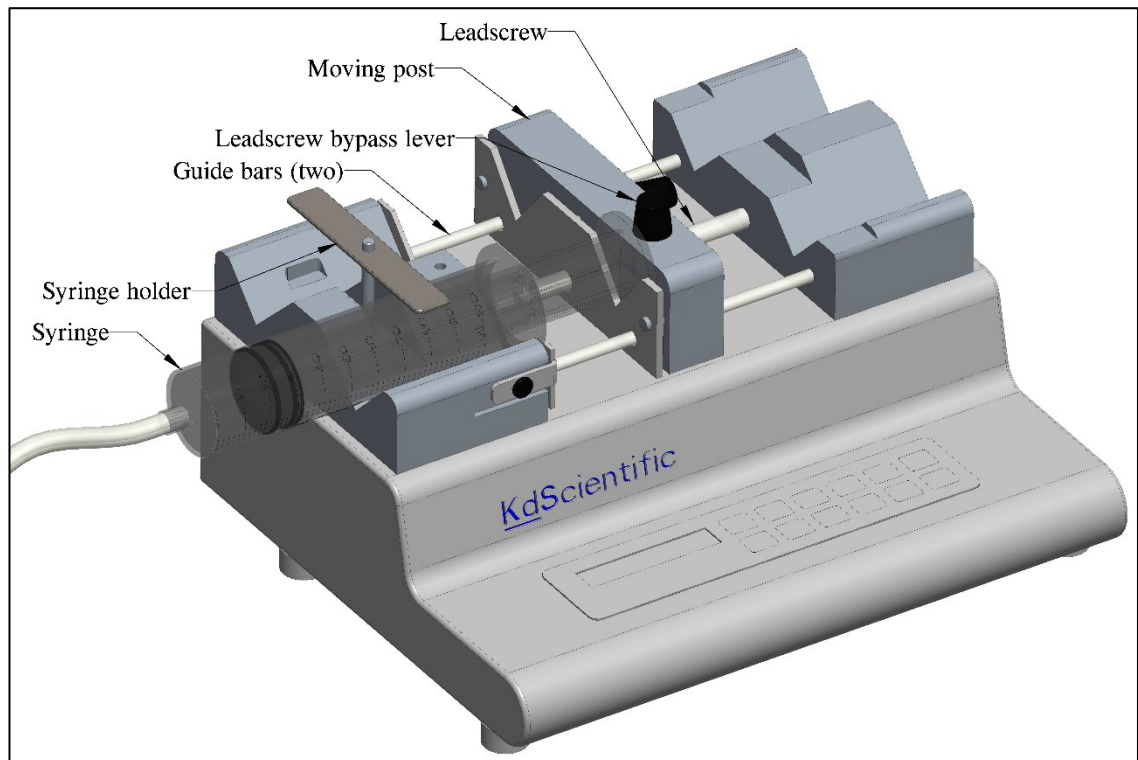


Figure 3-6. The customised syringe pump system retrofitted with micro controller and stepper motor driver with feedback loop from pressure sensor.

The 100ml syringe (internal diameter $\phi 33\text{mm}$) when plunged with a linear speed of 15 mm/min gives a volume flow rate of 0.2138 ml/sec.

3.1.4 The Control System

The control system is the brain of the experimental setup. A commercially available general-purpose microcontroller board is used to coordinate the whole experiment. The microcontroller performs the following functions as the master:

1. Read the pressure sensor analogue voltage through ADC (Analogue-to-digital converter). This microcontroller has a 10-bit ADC.
2. Control the maximum pressure by controlling the syringe pump during loading and unloading cycles.
3. Store pressure readings in a log file using a free serial/TCP software.

4. Trigger the DIC system to capture a profile.

Since the microcontroller board analogue input pins are only 5 volts (DC) tolerant, the pressure analogue signal (0-10VDC) should be halved using a voltage divider circuit as seen in Figure 3-7 if the working maximum pressure is higher than 50kPa (5 VDC). However, for these bulge tests the maximum pressure has been under this value. Therefore, the pressure analogue signal has been directly input to the microcontroller.

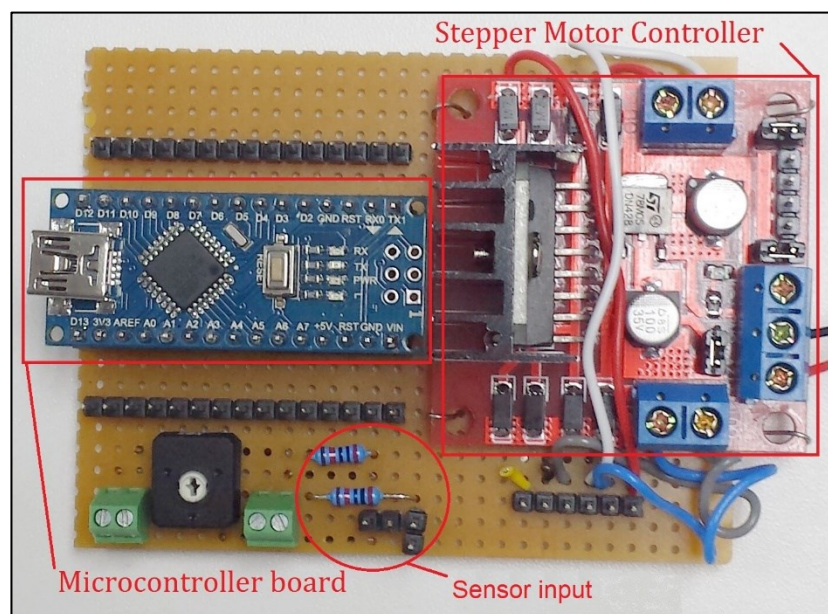


Figure 3-7. Microcontroller with a stepper motor driver (controller). Wirings are not shown to keep the presentation of the system tidy.

The minimum pressure with this arrangement that can be read from the bulge experiment comes from ADC and the pressure sensor. The 10-bit ADC can read a minimum of $\frac{50,000 \text{ Pa}}{2^{10}} = 48.8 \text{ Pa}$ and pressure sensor's accuracy, as given in its technical notes, is 0.5% full scale (101 kPa) that is 505 Pa. Therefore, the accuracy of the bulge pressure measurement system is 0.5 kPa.

3.1.5 The Height Measurement System

There are many different height measurement techniques reported in the literature used in a bulge test. Table 3 summarizes the bulge height measurement techniques. The most common method of measuring a bulge height is laser interferometer. However, a laser interferometer can only measure a maximum of few hundreds of micrometers. It is clear from Table 3 that to be able measure a bulge height in mm range a 3D DIC system is needed.

Table 3 Varius techniques used for height measurement in a bulge test.

Height measurement technique	Bulge heights (min.-max.)	References
Laser Interferometer	4-200 μm	(Huston et al., 2001; Schweitzer & Göken, 2007; Vlassak & Nix, 1992; Wu et al., 2004; Y. H. Xu et al., 2000; Zheng et al., 2000)
Scanning laser beam	50 μm	(Kalkman et al., 1999)
Michelson type interferometer	25 μm	(Huang et al., 2007)
Fringe projection	200 μm	(Poilane et al., 2000)
Optical profilometer	20 μm	(Youssef et al., 2010)
3D DIC	Upto 180 mm	(Çakmak, Kallaí, & Major, 2014; Galliot & Luchsinger, 2011; Machado et al., 2012)

Therefore, using a 3D DIC system, it not only calculates the bulge height but also calculates the 3D bulged-shape, which helps to justify analytical models developed, based upon assumptions of certain bulged shapes (cylindrical and spherical cape).

A commercially available 3D Digital Image Correlation (3D DIC) system (LaVision GmbH) has been used to measure the 3D bulged shape and hence determine the maximum bulge height. The DIC system (Figure 3-8) consists of the following:

1. Two digital CCD cameras for recording low noise, grey-scaled images.
2. Two sets of white LED light units
3. 'Strain Master' controller: the main unit, which coordinates cameras, LED lights and other external signals (trigger and analogue signals inputs).
4. A tripod to hold the cameras, LED lights and 'Strain Master' controller.
5. Calibration plates (various sizes).

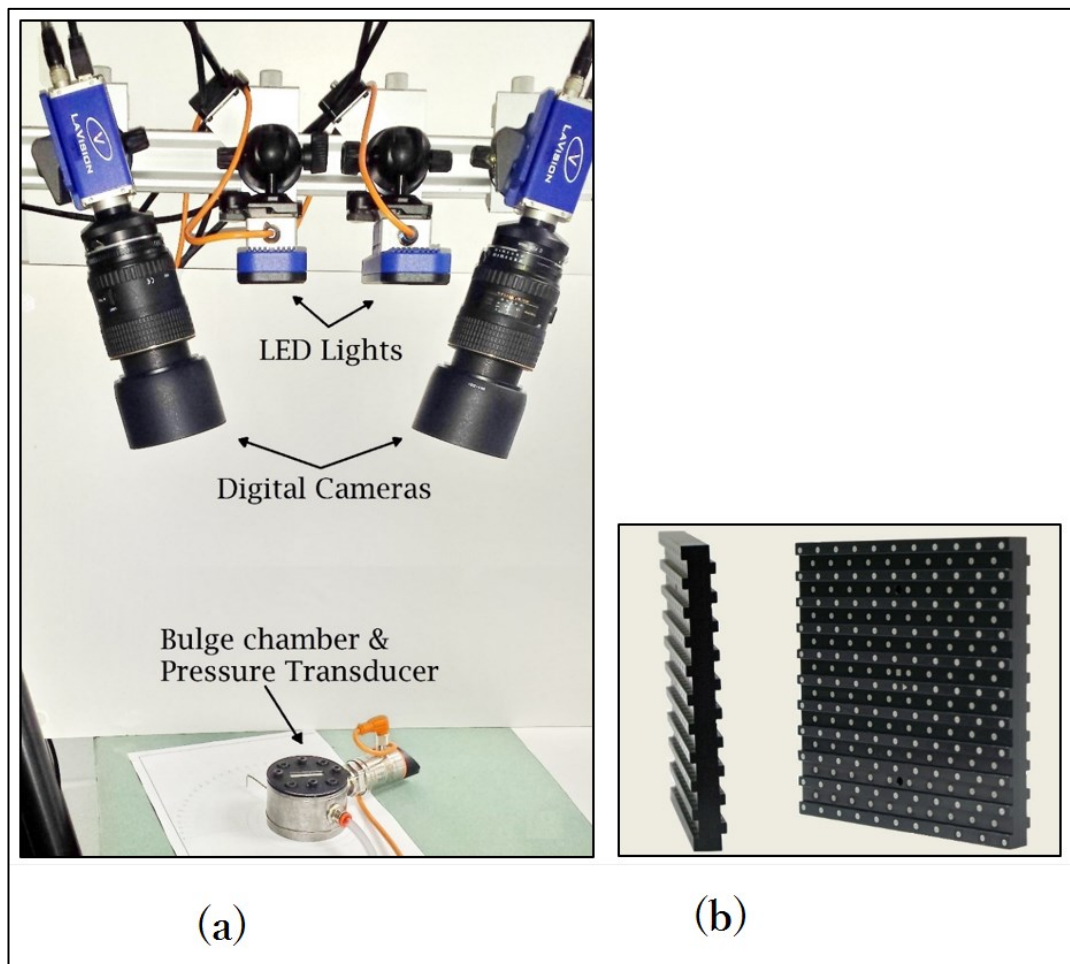


Figure 3-8 (a) Bulge testing with Digital Image Correlation system by LaVision with various components mounted in the vertical position on a tripod (tripod not visible in the image). (b) A calibration plate 58x58x5.8 mm.

3.2 The Tensile test setup

The tensile test is a very useful and basic test. The uniaxial stress-strain data it produces can be used to fine-tune a hyperelastic model for simple loading conditions.

A very simple tensile test setup is required as samples are very small and the tensile force requirements are very low as the polymer material is small dimensions (45x15 mm). This material can be stretched very easily even with a gentle pull.

The syringe system from the bulge test has been modified to build a miniature stepper-motor electric frame. It is sufficiently stiff and provides appropriate displacement control.

The tensile test set up consists of the following main components as shown in Figure 3-9.

1. A syringe pump to act as main tensile test platform with custom control system to act as master controlling stepper motor of the syringe pump, storing data from the Loadcell and triggering the DIC system.
2. Two grips to hold the tensile test sample one on the fixed post side and the other on the moving post of the tensile fixture (syringe pump). The fixed grip is attached to the tensile fixture through the load cell.
3. DIC system to calculate strain in the tensile strips.

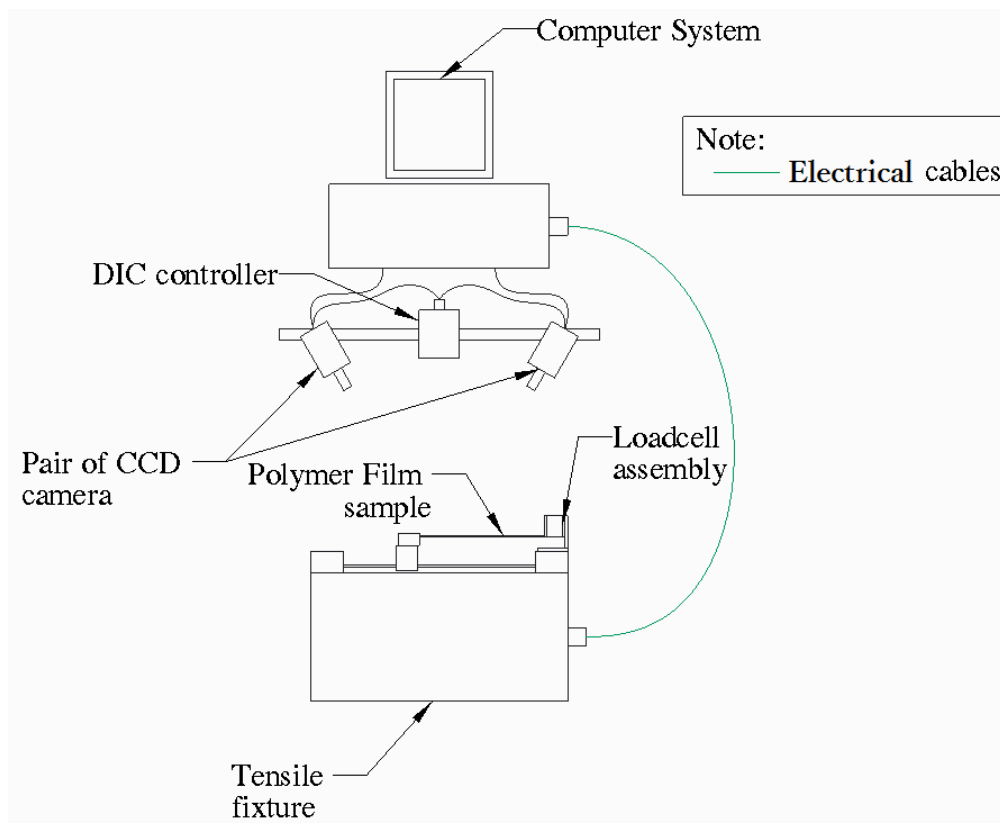


Figure 3-9 Schematic of Tensile test setup. Note: the syringe pump is now acting as tensile fixture.

3.2.1 Strain Measurement

A conventional tensile test only measures elongation (hence strain) along longitudinal direction only. A wide variety of techniques exists for measuring strain in a tensile test; namely the strain gauges, extensometers, stress and strain determined by machine crosshead motion, optical strain measurement techniques and others (Motra, Hildebrand, & Dimmig-Osburg, 2014). None of the techniques given above is able to measure lateral strain in polymers as required in Poisson's ratio calculations except optical strain measurement. A bulge tests always involve a multi-direction loading, therefore, a tensile test is required to estimate the Poisson's ratio (ν). Strain gauges are practically impossible to attach to flexible polymer samples going through a large strain.

Therefore, using the same DIC system as used with the bulge test is most appropriate technique of measuring longitudinal and lateral strains.

3.2.2 Tensile Test Fixture (Retrofitted Syringe Pump)

The syringe pump from the bulge test as described in 3.1.3 with slight modifications has been used to perform the tensile test as shown in Figure 3-10. This is simple and suitable for very small force tensile test.

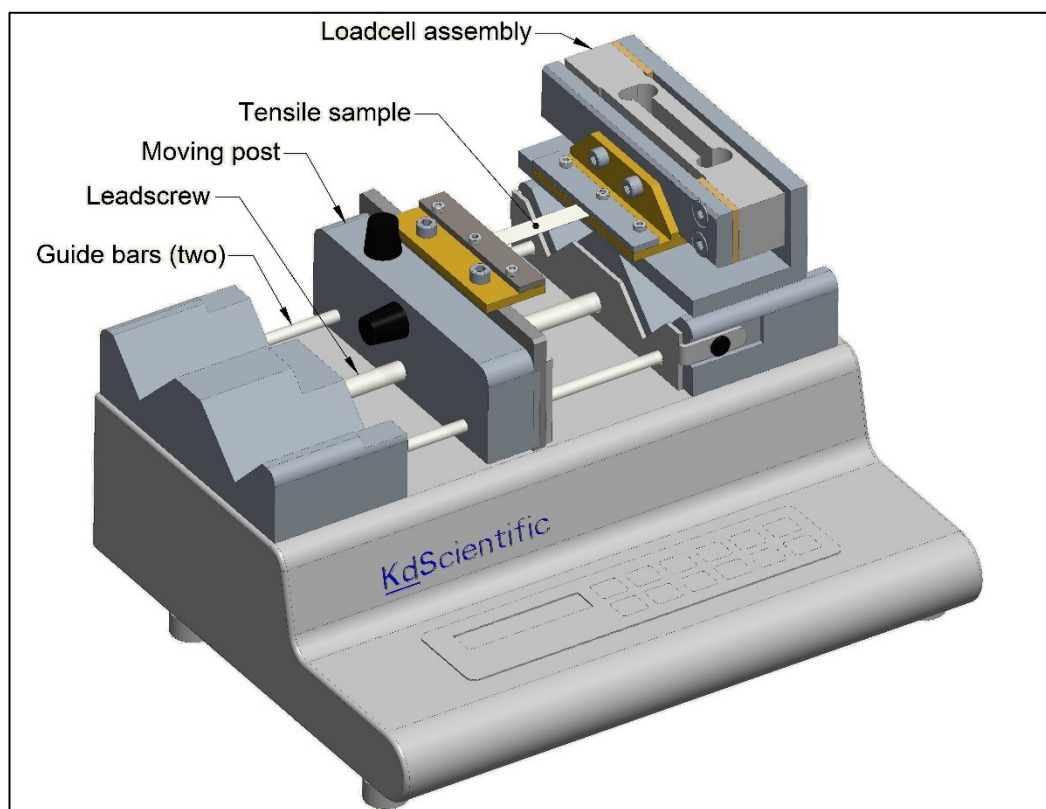


Figure 3-10 Syringe pump modification to carry out a tensile test of the polymer specimen.

The loadcell assembly has been mounted on the non-moving side of the syringe pump to minimize inertia effects and the moving post, attached to the leadscrew, grips the other end of the tensile sample.

Since travel of the moving post is limited due to small size of the syringe pump, the dimensions of the tensile sample must be kept small.

Following a technique reported by Selvadurai (Selvadurai, 2006), a specimen with large nominal dimensions and integral cuts was used. This produces three individual test specimens in a single test with the overall measured data being the sum of the individual specimen response. The combined specimen has a nominal size of 45 mm in length and 30 mm in width. The three test specimens within this have nominal cross-sectional dimensions of $10.0\text{ mm} \times 0.125\text{ mm}$. This specimen design enables a larger grip area, reducing slip, but still provides minimal transverse constraint allowing the specimen to deform without warping. To further minimise slip or damage to the specimen, an additional piece of latex was glued to the grip regions of the test specimen

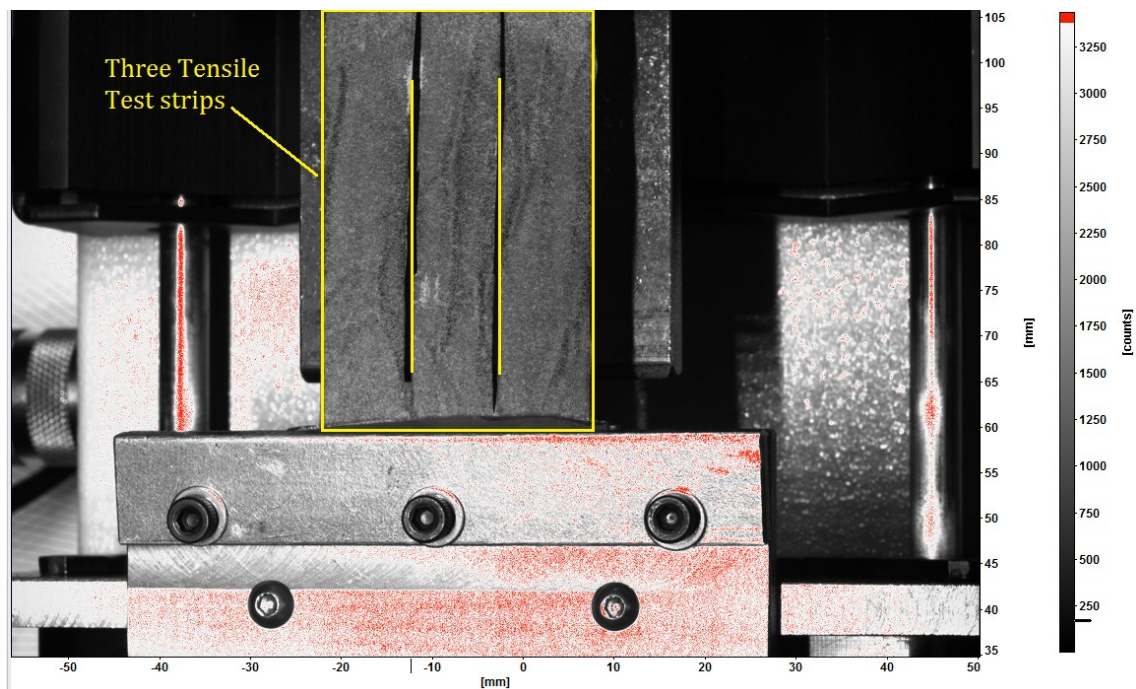


Figure 3-11 an image from DaVis 8.3 showing three Tensile Test strips. The yellow lines are added to clearly show sample and three strips in it.

Another benefit of using three tensile test strips is that the error in the sample dimensions will also be averaged over the three tensile strips instead of just one tensile strip.

3.2.3 Loadcell Assembly

A load cell (max load 3kg, TEDEA-HUNTLEIGH) with a Load cell amplifier unit (LAU 73.1, Sensor Techniques Limited) is used to measure tensile force (Figure 3-12).

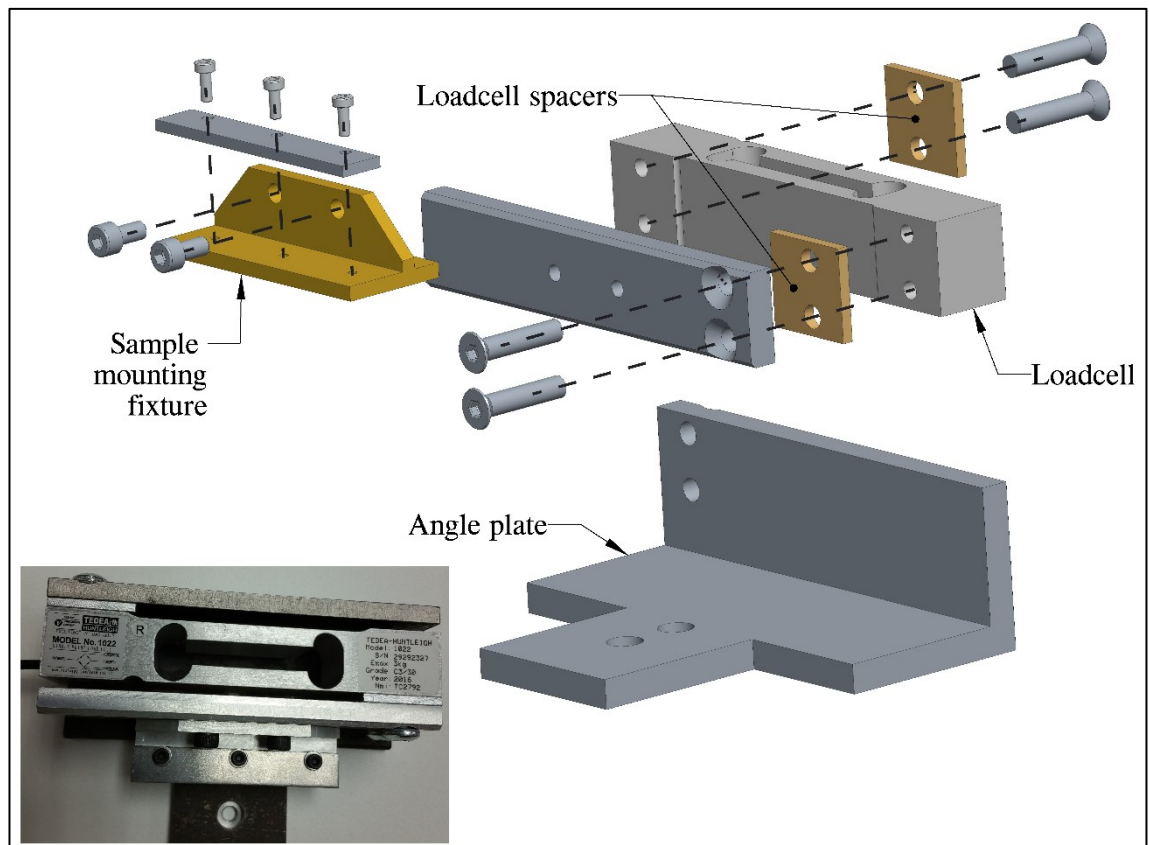


Figure 3-12 Loadcell assembly containing a 3kg loadcell. The angle plate is attached onto the syringe pump, the loadcell is then attached to the angle plate on one end and sample clamping plates on the other. Lower left corner insert shows actual loadcell assembly.

3.2.4 Loadcell Calibration

The Loadcell has been calibrated with a digital force-measuring instrument (Sauter FK100) with a maximum capacity of 100N in 0.05N steps. The force meter has been attached to the Loadcell assembly through a tensile spring. The

Loadcell assembly is bolted to the syringe pump, the force meter is pulled slightly and held static at its position, and Vdc output from the Loadcell is measured with a multimeter. Figure 3-13 shows the calibration result. No hysteresis has been observed during repeated cycles of loading and unloading of the Loadcell.

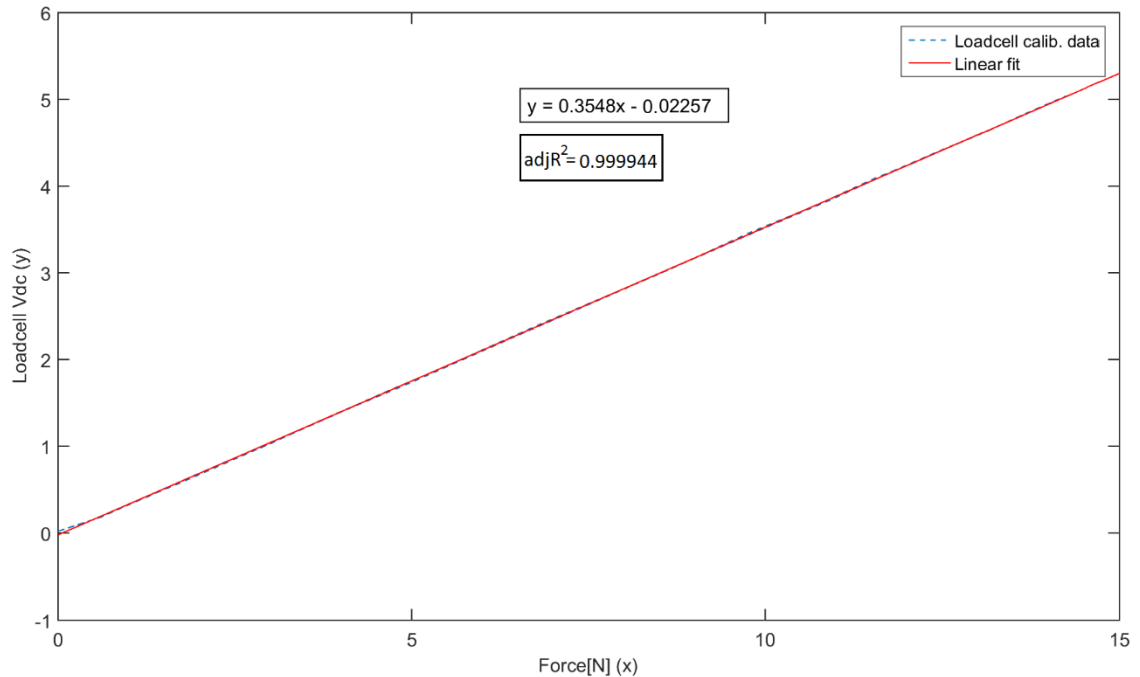


Figure 3-13 Loadcell calibration plot showing ~100% fit and linear equation relating applied force [N] (x) to the resulting Vdc (y) produced by the loadcell.

3.2.5 ADC Calibration

The ADC (10-bits) of the controller is also calibrated with the help of a power supply (TTi QL355T) and digital multimeter (Agilent 34405A). A known voltage is applied to an analogue pin of the controller and the corresponding ADC values are noted. The process have been repeated several times for increasing and decreasing applied voltages.

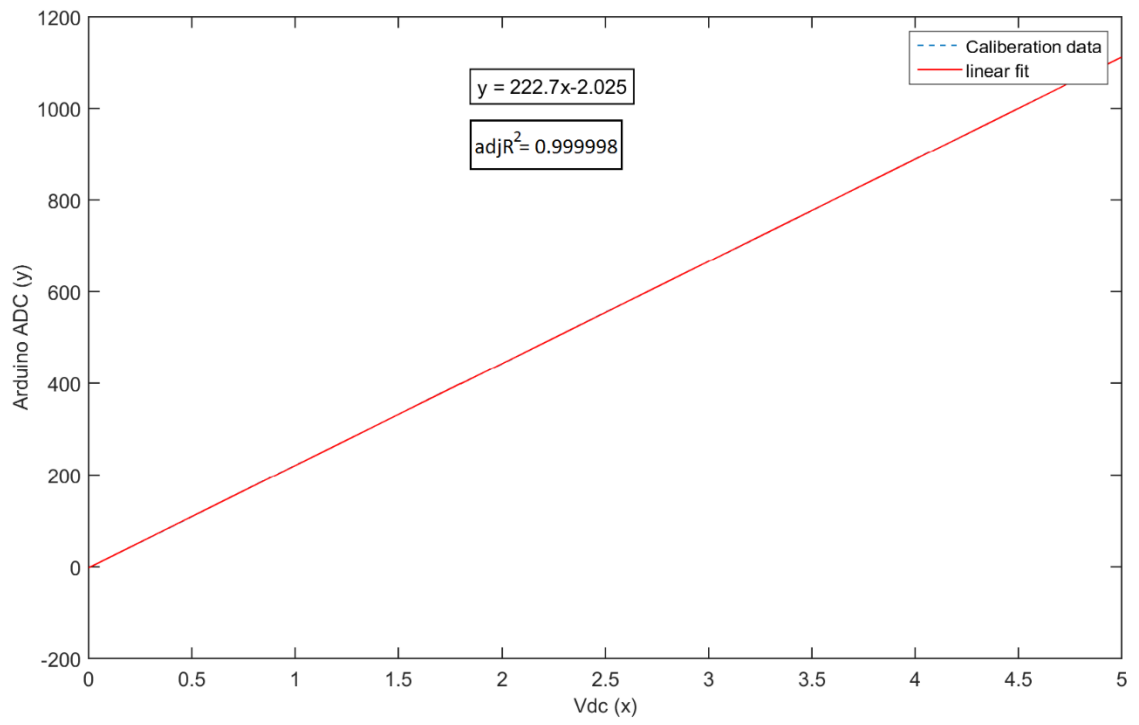


Figure 3-14 Arduino ADC calibration results showing a very good fit.

4. 3D DIC with a Commercial System

In this chapter, a brief review of the working principle of DIC will be presented. All software manuals are accessible from the DIC software used in this study.

4.1 Introduction

Digital Image Correlation (DIC) is a non-contact, non-invasive measurement technique. It is an optical method that only requires visual access to the experimental surface (Chu, Ranson, & Sutton, 1985). The sample surface to be recorded needs to have some identifiable surface pattern or texture. Some surfaces have a natural identifiable pattern but in some cases where the surface is smooth and shiny, an artificial speckle pattern should be created by spray paint or any other means.

An optical mouse is a very common example of motion detection below its surface using DIC while illuminated with a light source.

This technique tracks the changes of grey value pattern in a small area of $N \times N$ pixels called a subset during deformation or rigid body motion. This can be used to measure both displacement and deformation.

4.2 The Working Principle of DIC

The working principle of DIC system is similar for 2-D and 3-D measurement environments. A camera takes a series of grey-scale images of a deforming surface and compares them to a reference image (the first or previous image), Figure 4-1. In 2D, a mapping function is calculated from one or more images of a known dot pattern. This mapping is known as calibration, discussed in detail in section 4.4.

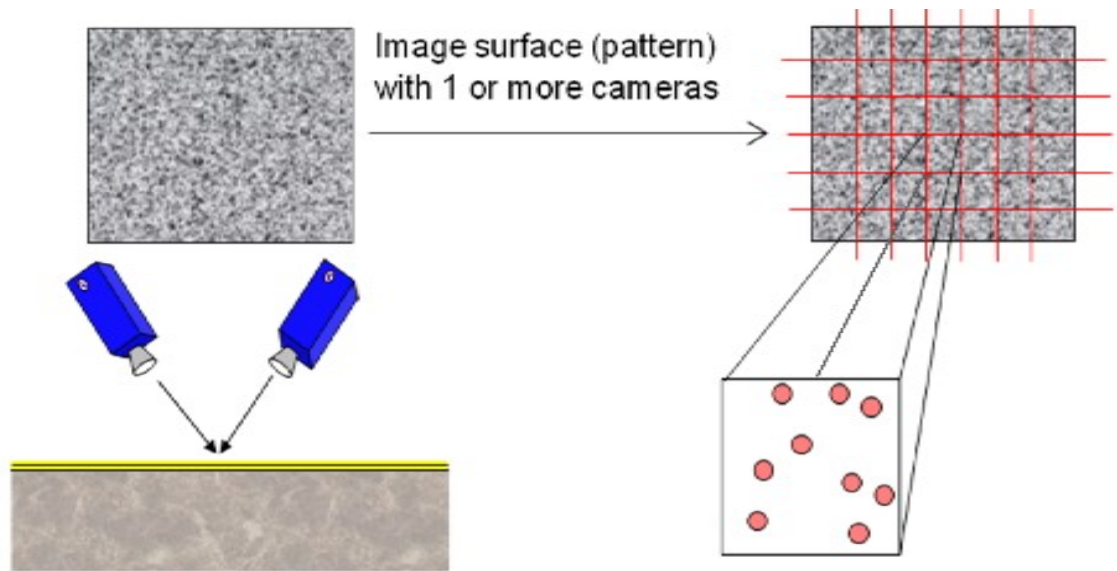


Figure 4-1 Basic step of DIC where a speckle pattern is discretized into small subsets. [Source: LaVision's 'Strain Master' manual]

The images are discretized into small squares of pixels, called subsets. The subset at time t is compared to another subset at the same location in the next image (at time $t+dt$). During the comparison the subset is moved slightly (step over) to find the best match that gives the displacement vector for each subset, Figure 4-2.

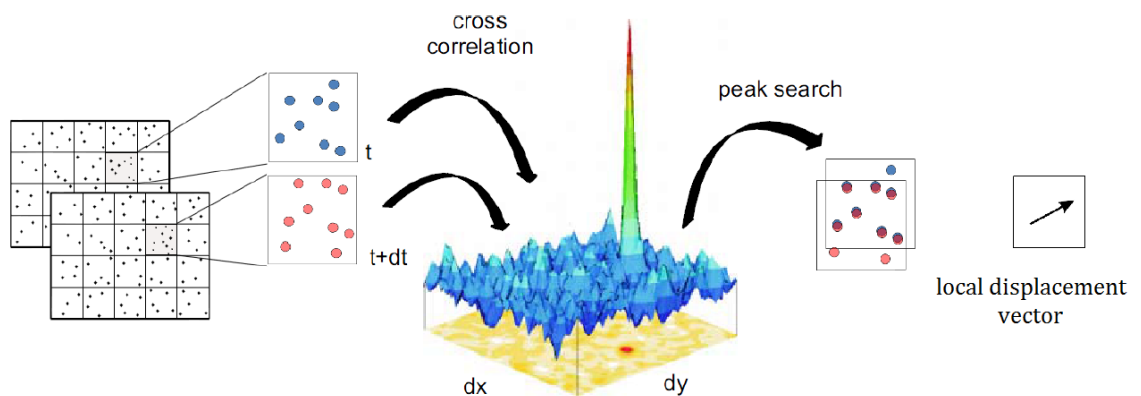


Figure 4-2 Correlation peak for each facet (subset) and corresponding pattern displacement in 2D. [Source: adopted from LaVision's 'Strain Master' manual]

In a 3D stereoscopic DIC system, two cameras see the same specimen surface being recorded (Figure 4-3). The DIC system is calibrated and a 3D mapping function is calculated to transform the local coordinate system of both cameras into world space. Each camera matches the pattern as explained in Figure 4-2 and the set of displacements from each camera is combined using the 3D mapping function to build a 3D surface.

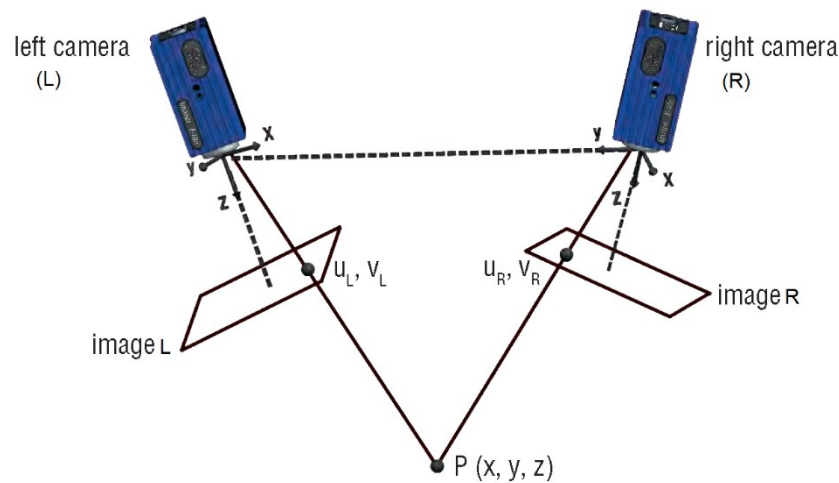


Figure 4-3 A 3D stereoscopic DIC system with two cameras. Images L and R are recorded by left and right camera respectively. Displacements of each point (u, v) are calculated and mapped together to calculate 3D displacements. [source: adopted from LaVision's 'Strain Master' brochure]

This study uses a LaVision DIC system that comes with its own software (DaVis V8.3) to perform the DIC algorithm.

4.3 Hardware Setup

The system is supplied complete with tripod, associated mounts for camera, and LED lighting system. The system is setup in a vertical orientation so that the two cameras have been arranged and focused to see vertically down the same area

of the bulge setup where polymer samples are mounted as shown in Figure 3-8
(a)

Once the hardware setup is complete and all connections are made, it is ready to launch the Davis softwares and acquire images for calibration.

4.4 Preparing the Samples

Latex material samples are cut from commercially available gloves (Figure 4-4). The average thickness of the gloves has been measured as 125 ± 1.4 with the help of a digital micrometre with a resolution of $\pm 1 \mu\text{m}$.



Figure 4-4 Latex gloves used to cut samples from for testing with DIC. [Source of gloves: Premier Protector, Latex Examination Gloves (medium).]

The colour of these glove samples gives a good contrast when spray painted with black matt paint as shown in Figure 4-5. The other samples for the bulge test are also cut in a similar manner from relatively flat areas of gloves, back and front of the glove around the palm area.

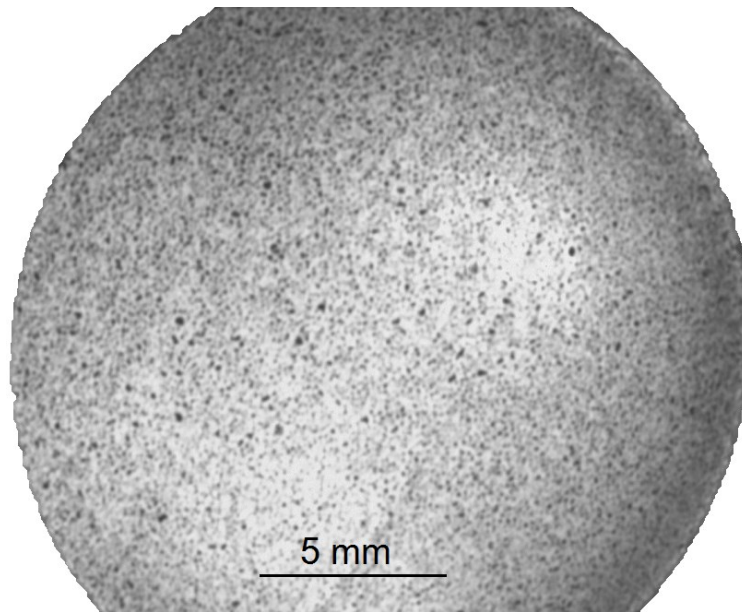


Figure 4-5 a circular latex sample is lightly spray painted with matt black paint (a commercially available spray bottle) to generate a random speckle pattern suitable for digital image correlation.

After the samples are prepared, they are ready for DIC experiments as outlined in the next sections.

4.5 DIC Calibration

A calibration must be performed for every new experiment or a new sample and if the system is left unattended for long time. The LaVision DIC system comes with various sized calibration plates for 2D and 3D. For the experiments carried out in this work a calibration plate measuring 58 x 58 x 5.8 mm (Type 7) is used. This plate type is suitable for 3D calibration as it has 1mm height steps on both sides. Figure 4-6 shows the calibration window from DaVis showing recognised fiducial features.

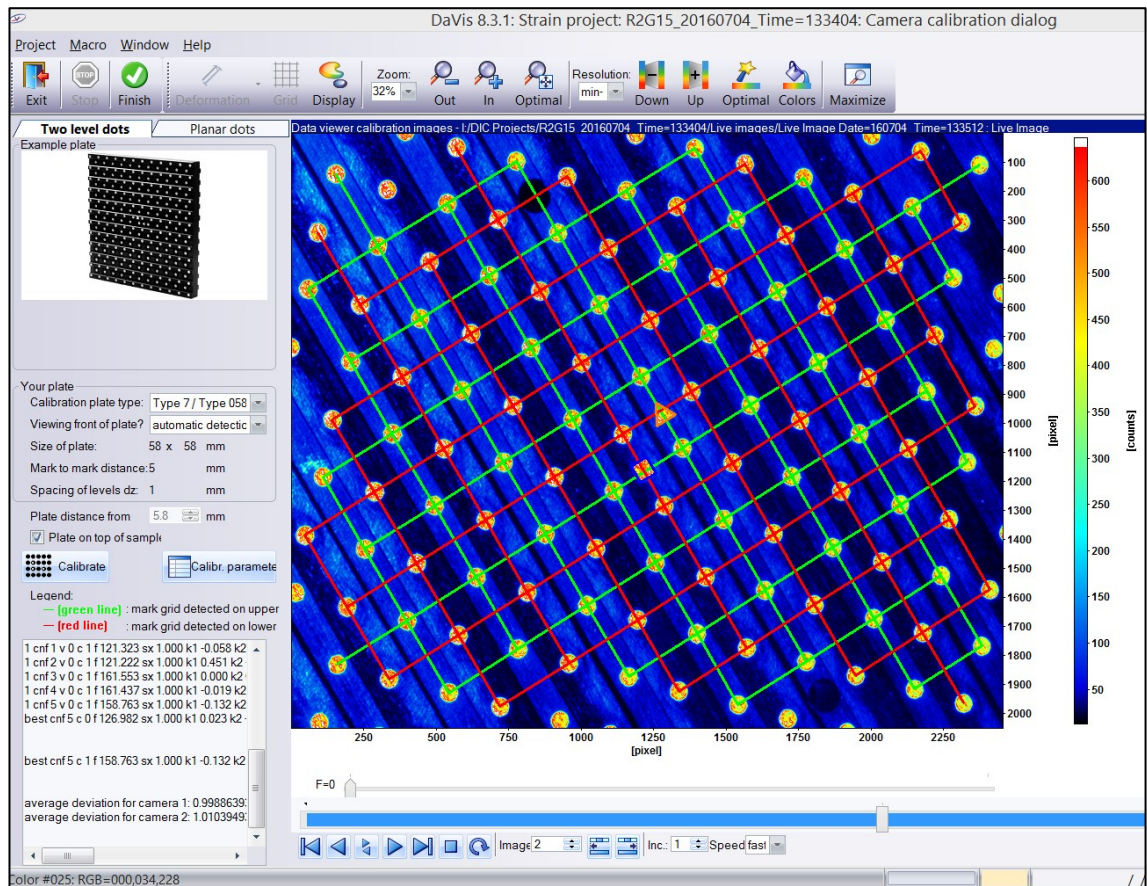


Figure 4-6 Calibration window from DaVis showing calibration plate Type 7/ Type 058-5 fitted with a 3D mapping function.

A few images (three are sufficient) of the calibration plate are taken while placed on the sample and rotated slightly between the consecutive images. Then the calibration process is initiated and a 3D mapping function is calculated (Figure 4-7). The reader is advised to read the manual ‘Strain Master’, available through help menu in DaVis, for a step-by-step calibration procedure.

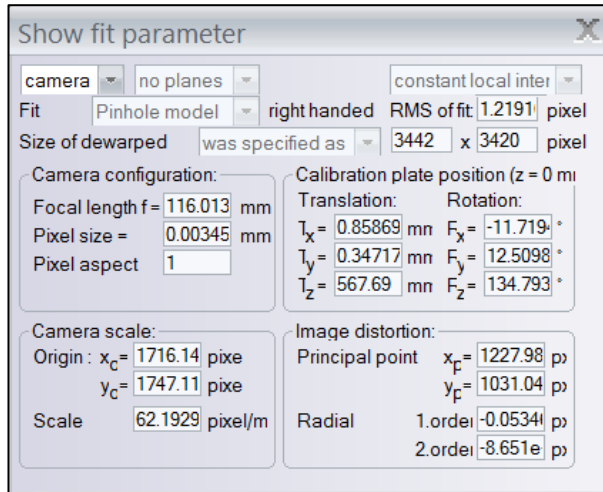


Figure 4-7 A window showing fit parameters from DaVis 8.3.

An important parameter is the root mean square of fit (RMS of fit). It is mentioned by LaVision in the 'strain Master' manual that for a 2 mega pixel camera an RMS fit value lower than 1 pixel is good, a value lower than 0.3 pixel is excellent, values higher than 2 pixel are questionable. These limits on values of pixels increase with higher resolution cameras. The cameras employed in this study are 5 megapixels. Therefore, an RMS of fit of value 1.2 (Figure 4-7) will be considered good.

4.6 Profiles Acquisition

Once the DIC system is calibrated, the next step is to acquire DIC data from the experiment. The important parameters to be set before recording are:

1. Exposure time: duration of time during which light is allowed to reach the camera sensor. It is adjusted until there is no light saturation in the recorded images and it depends on the lighting level surrounding the surface being recorded. A typical value between 15,000 – 50,000 microseconds (μs) is used in these experiments. If exposure time is too short (7000 ns at one time), then contrast will be very low and the surface speckle pattern will not be clearly visible. DIC correlation will either fail or give very noisy results.
2. Recording frequency: this is selected based upon the speed of the experiment. The approximate time for one loading cycle is noted and then using the number of cycles planned and the frequency, the total number of images is calculated. An upper limit of frequency, other than the DIC hardware (controller and cameras) exists because of the value of the exposure time. For example, with a 50,000 μs exposure time the maximum frequency permitted is 20 images per second

The term 'profile' is used for the set of images taken by cameras while each camera image is called a frame of the profile in DaVis.

There are two ways to synchronize the start of recording of profiles in DaVis and the start of stretching or pressure bulging.

1. Start the experiment and the recording in DIC system at about the same time manually.

2. Put the DIC system on standby from DaVis and trigger it externally. A microcontroller has been used to drive a stepper motor that drives the retrofitted syringe pump. The microcontroller triggers the DIC system when the syringe pump has been stopped for 500 milliseconds. DIC is triggered during this time to avoid any blurring due to motion. When the DIC system takes the set number of profiles, it stops or recording is cancelled early in any situation (say sample damage).

The second method has been used in all experiments. After acquisition of DIC profiles, the digital image correlation is run to calculate displacements.

There is a specific colour scheme in DaVis to check if there is any light saturation in the recording DIC profiles (images). The areas of saturation will be highlighted in red. If there is saturation in the recorded DIC profiles, the DIC correlation will not converge. Therefore, exposure time and

4.7 Displacement Calculations

In this step, DIC profiles are cross-correlated and resulting displacements and deformed surfaces are built. A combination of masks can be used to add and /or subtract areas of interest.

As explained in 4.2, the image is divided into subsets starting from one or more seeding points selected in the masked area as shown in Figure 4-8.

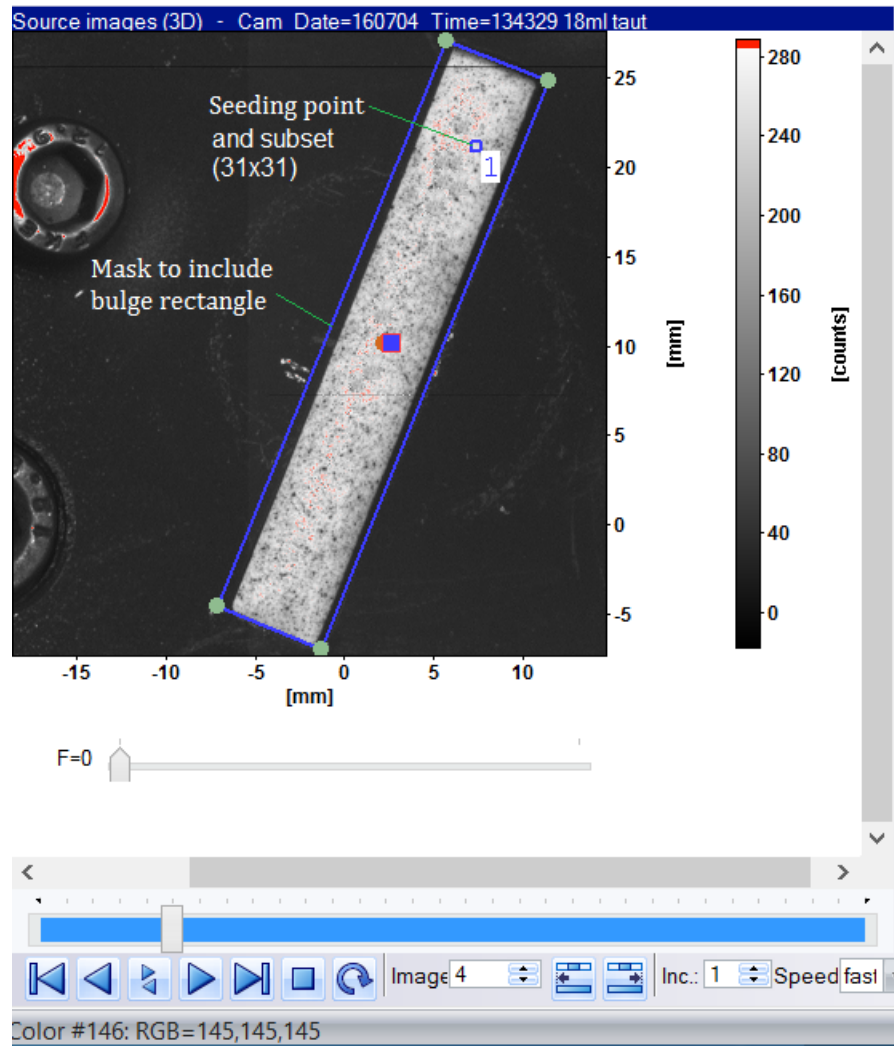


Figure 4-8 A quadrilateral mask is applied to include the rectangular bulge window area. A seeding point is also placed to start discretization the masked area into subsets of $N \times N$. A default value of 31×31 pixels for subset is shown in Figure 4-9 (a)

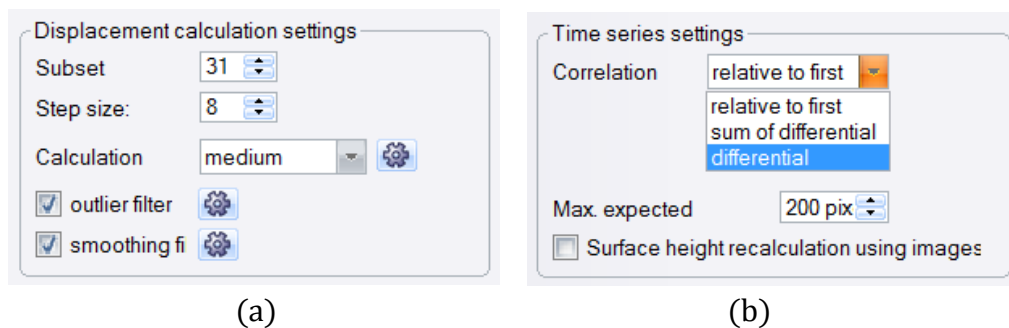


Figure 4-9 More calculation settings. (a) Default settings of subset size and step sizes (b) time series settings controlling correlation modes.

The value of subset size affects the displacements calculated. Therefore, an optimal subset size will be selected from a convergence study for each new experiment.

There are three time series settings that control how to digitally correlate the profiles as shown in Figure 4-9 (b). These three settings are briefly summarized below:

4.7.1 Relative to First

For small strains, as typical in metals (say 10%~20%), displacements are calculated by correlating all subsequent profiles always to the first profile. Since the total strain is small, the relative displacements between two consecutive profiles will be very small depending upon the recording frequency. Therefore, LaVision suggests using 'relative to first' time series setting when dealing with small strains.

4.7.2 Sum of Differential and Differential

For experiments involving large strains, typically for polymers, where strain is in typically three figures percentage, sum of differential or differential time setting is recommended by LaVision. In these modes of displacement calculations, two consecutive profiles are correlated as opposed to all profiles 'relative to first'. These differential displacements are either added up as in 'sum of differential' case or just left unadded. If there are some less important areas (usually extreme sides) with more noise in them, the 'sum of differential' option does not always converge. In this situation, the 'differential' time series setting is used and the displacement data are processed outside DaVis.

In this study the 'Sum of differential' setting is used for all experiments.

4.8 Extracting Data

Once all profiles in a recording have been correlated, DaVis provides many different tools in which useful information can be extracted from the vector field built from the calculated displacements.

In the bulge test, only the bulge-profile along certain directions is important depending upon the bulge window geometry as described in the next section.

4.8.1 Rectangular Bulge Window

As discussed in section 0, for a long rectangular window, bulge-shape is only relevant in the width direction.

The orientation of the displacement vector field (and deformed surface) is a combination of placement and orientation of the bulge chamber beneath the cameras and relative positions of the two cameras. Therefore, to be able to see the actual bulge-shape along the width, the local coordinate system has to be rotated.

The projection of bulge height onto the DIC axes is shown in Figure 4-10

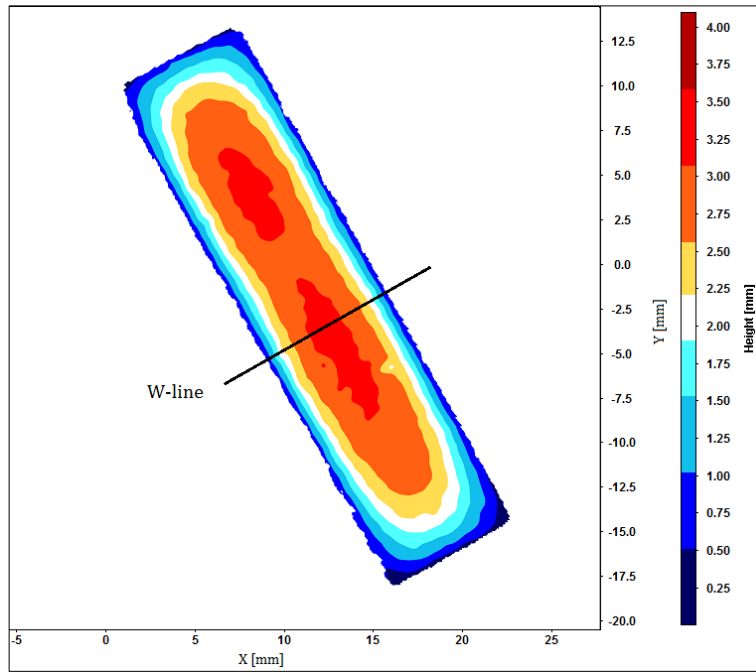


Figure 4-10 2D (top) view of vector field showing the rectangular window from the bulge test in DaVis. The rectangular vector field is not oriented along either of the DIC axes (X, Y). W-line is approximately along the width of the rectangle.

The bulge height along the W-line is projected onto the DIC x-axis and then along the y-axis as shown. The bulge-shapes along the DIC axes and along the W-line are presented in Figure 4-11.

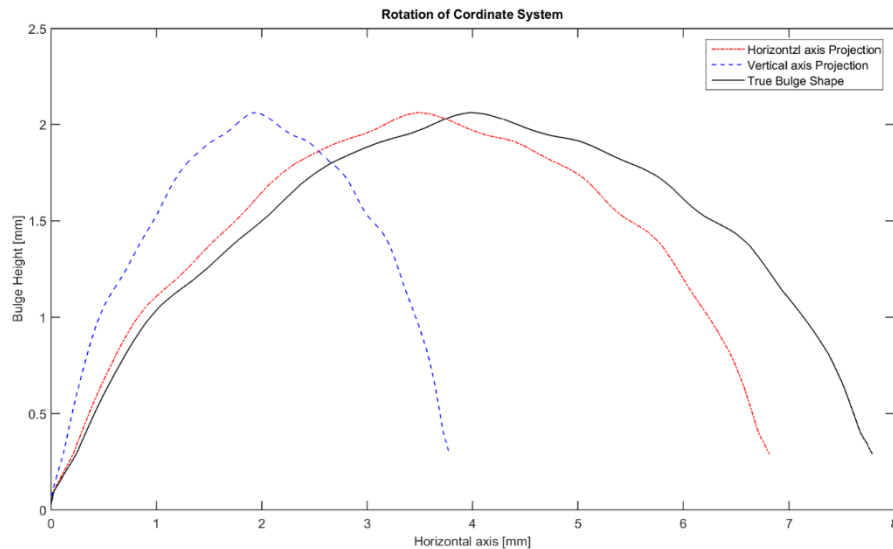


Figure 4-11 Bulge-shape along a W-line when projected onto DIC axes (X, Y) and the corrected actual bulge-shape along the width of a rectangular bulge window in Matlab.

An alternate approach of getting the actual bulge-shape along the width of the rectangle is to rotate the bulge chamber after calibration but before recording the bulge experiment a certain number of degrees clockwise or anti-clockwise so that the resulting displacement vector field is either approximately horizontal or vertical.

It is a time taking process requiring trial and error. After calibrating the DIC system, two profiles are recorded and correlated. An image of the vector field similar to the one shown in Figure 4-10 is taken and angle of rotation is measured from either DIC axes. The angle of rotation is measured in a free windows application called 'ImageJ'. The bulge chamber is rotated about its axis of rotation avoiding any translation (Figure 4-12). After every rotation the resulting rotation of vector field in the DaVis software is measured. This process is repeated until an approximate horizontal or vertical displacement vector field is obtained.

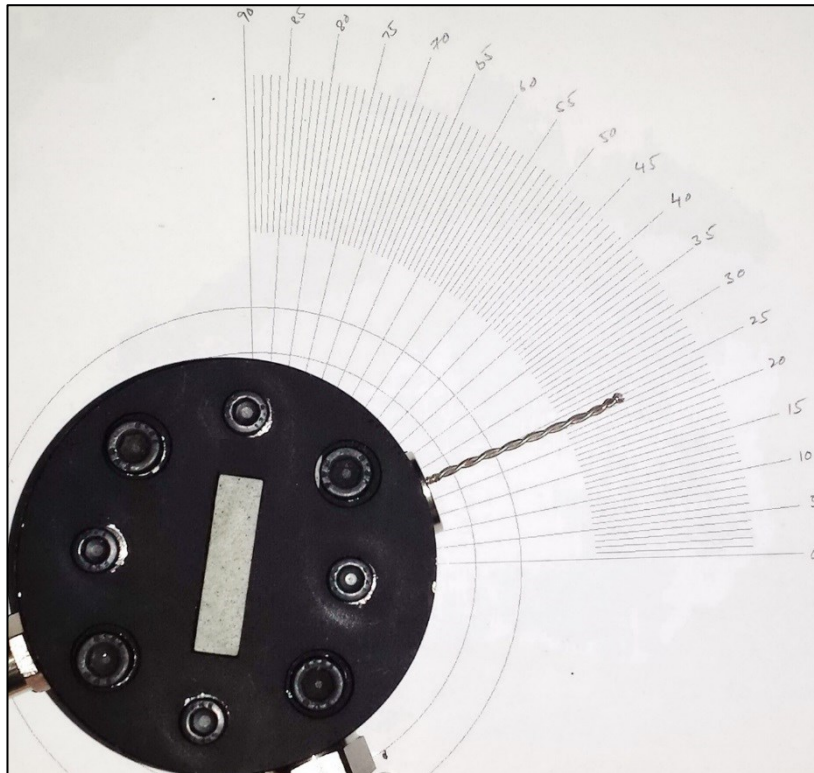


Figure 4-12 Bulge chamber rotation arrangements. The bulge chamber can be rotated the required angle approximately.

The average number of rotations per bulge test recording is five. This second approach has been used in most of the bulge test recordings.

4.8.2 Circular Bulge Window

The bulge shape from the circular bulge window should be extracted such that it contains the maximum bulge height point, the centre point. The following procedure is adopted to locate the centre of the circular bulge.

A vertical line close to the centre of the bulge is first drawn and the DIC y-axis value of maximum bulge height is noted from DaVis. Then a horizontal line through the 'noted value' is drawn and bulge-shape is extracted in DaVis as shown in Figure 4-13.

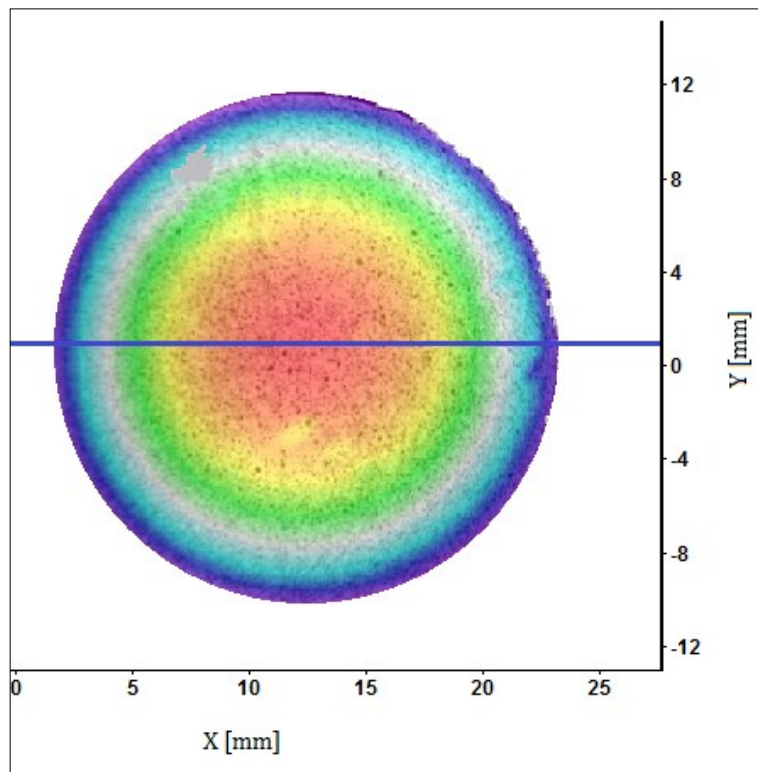


Figure 4-13 Circular bulge window with a line drawn across its diameter to extract the bulge shape.

4.8.3 Tensile Test

The tensile test does not involve any 3D shape although the 3D DIC system is used to record it. The data required from DIC of the tensile test is strain along two mutually perpendicular lines. DaVis has a functionality of calculating strain along a line called the 'Gauge Line'. Therefore, lines are drawn along longitudinal and lateral and longitudinal directions and strain along these lines is calculated using the 'Gauge Line' function.

4.9 Export

Once the bulge-shape or strain of all profiles are extracted, they are exported as a data file format (*.dat).

5. Processing DIC Data and Extracting Material Parameters

All experimental results are presented in this chapter. The processing of experimental data collected from experiments in MatLab is presented first then the shape of bulge is approximated with a polynomial and a circular arc. Material parameters are extracted through curve fitting of analytical models into the experimental data. Poisson's ratio is calculated from tensile test results and compared to the value of Poisson's ratio calculated from the material parameters obtained from the bulge tests.

5.1 Introduction

DIC constructs a full 3D deformed surface by adding 3D displacements calculated from every two consecutive profiles (Figure 5-1). Each of the two cameras are used to capture an image at the same time and their images are combined into a profile using the mapping function calculated by DaVis during the calibration process. However, differential cumulative error also accumulates as differential displacements are added to construct the deformed surface.

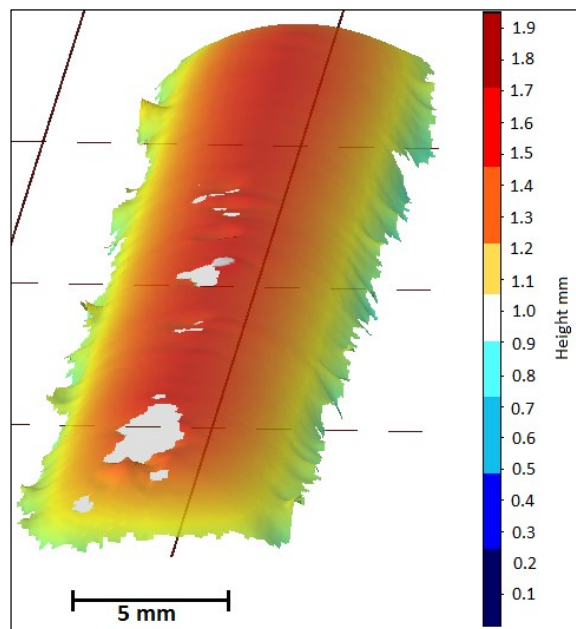


Figure 5-1 A 3D deformed surface as constructed in DaVis. A small roughness can be seen on the surface. These random surface imperfections are mainly a result of the speckle pattern not being uniform size and shape which results in a non-smooth surface.

The bulge-profiles data are read along different lines of interest in DaVis as outlined in 4.8.1 and exported as data files (*.dat extension). These data files are read in MatLab using a script file (*.m) and stored in MatLab data files (*.mat) ready for further processing as described in the next sections. All MatLab code files are attached in Appendix E.

5.2 Subset Size Convergence and Sensitivity

Subset size in '*displacement calculations settings*' as discussed in section 4.7 is an important parameter, which effects the DIC result. A subset-size convergence study is used to select an appropriate subset size for all different bulge test geometries as well as tensile tests.

Figure 5-2, Figure 5-3, and Figure 5-4 show variations in the maximum bulge heights as the subset size in '*DIC settings*' is increased for a particular DIC recording of the rectangular bulge test. It has been noted that as the nominal width size of rectangular bulge window is decreased in R1, R2 and R3, the maximum bulge height calculated by DIC also decreases gradually as the subset size is increased to 111 pixels (Table 4). It is clear from these figures that a default subset size of 31 pixels is suitable for DIC settings for rectangular bulge windows.

Table 4 Percentage decrease in maximum bulge height calculated using average height of subset sizes of 15, 21, 27 and 31 pixels when compared to the height calculated from a subset size of 111 pixels.

Name [nominal width (mm)]	%age decrease in heights
R1 [8]	5.31
R2 [6]	8.87
R3 [5]	12.78

A subset size of smaller than 15 pixels in the DIC settings did not converge showing that an average speckle size is in the order of 15 pixels.

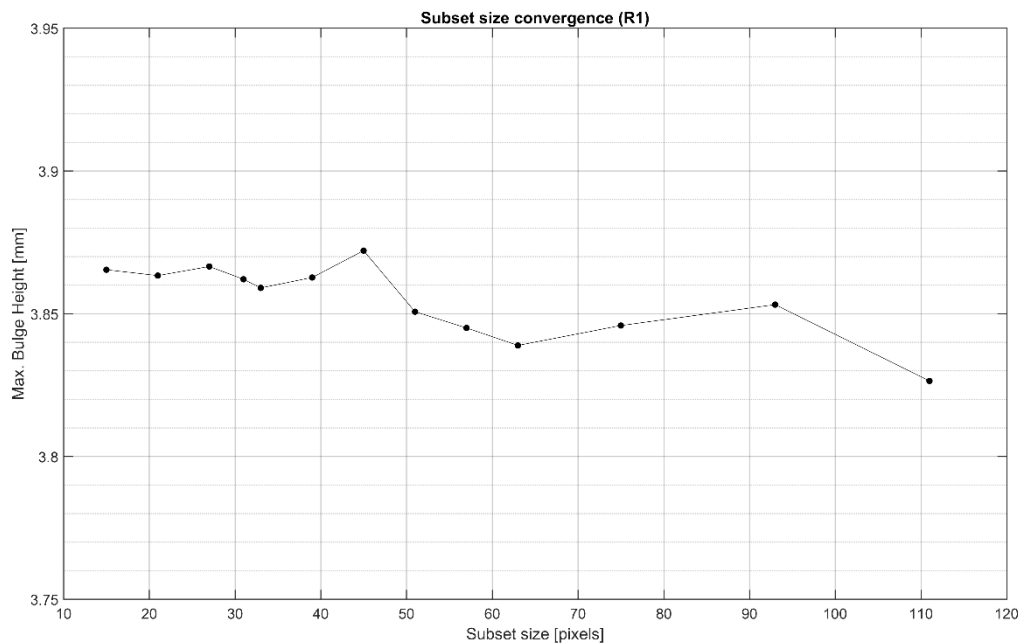


Figure 5-2 Variation of maximum bulge heights calculated using DIC from a single DIC recording of the bulge test with R1 bulge window as subset sizes are increased.

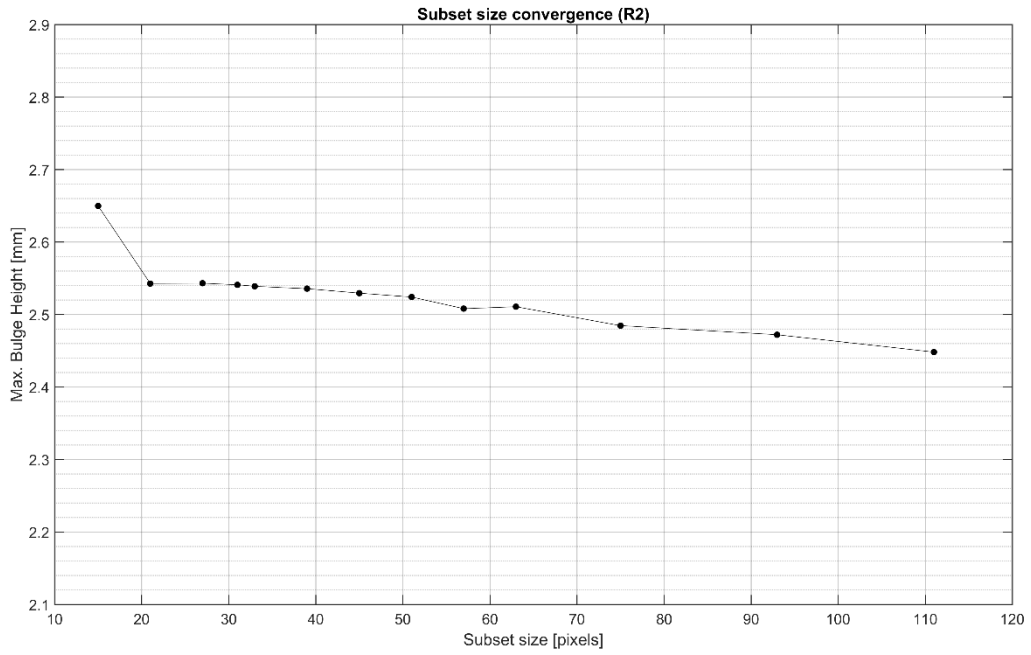


Figure 5-3 Variation of maximum bulge heights calculated using DIC from a single DIC recording of the bulge test with R2 bulge window as subset sizes are increased.

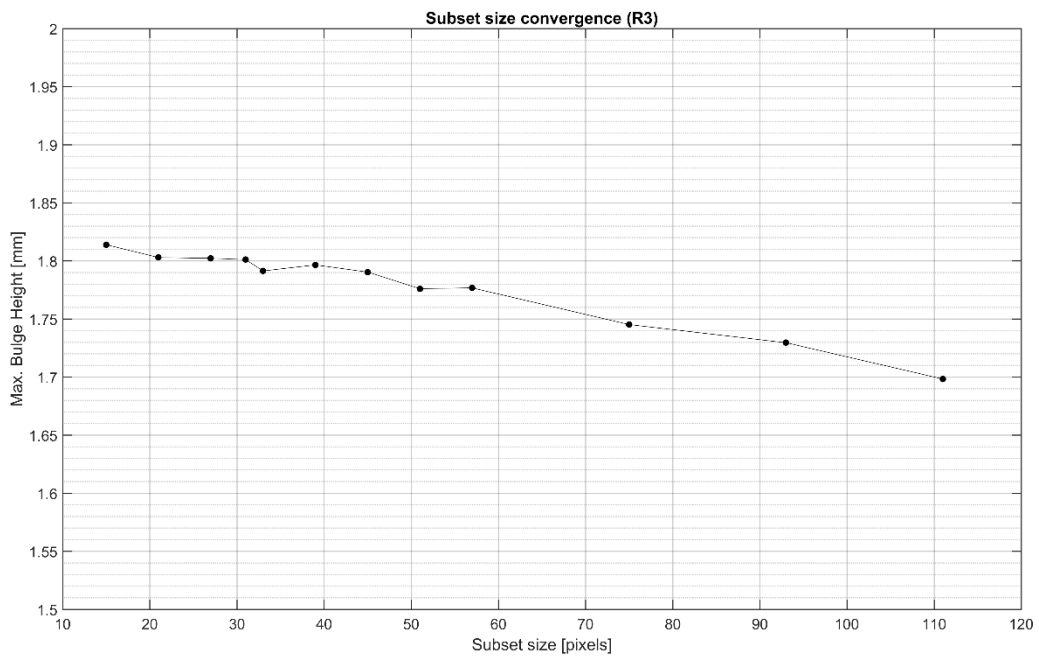


Figure 5-4 Variation of maximum bulge heights calculated using DIC from a single DIC recording of the bulge test with R3 bulge window as subset sizes are increased.

Figure 5-5 shows subset size effect on the maximum bulge height of the circular bulge window. The maximum bulge height calculated with subset size of 111 pixels drops 6.17% from the average maximum bulge height calculated from the subset sizes of 15, 21, 27 and 31 pixels. Therefore, a default subset size is suitable for strain calculations for a circular bulge window.

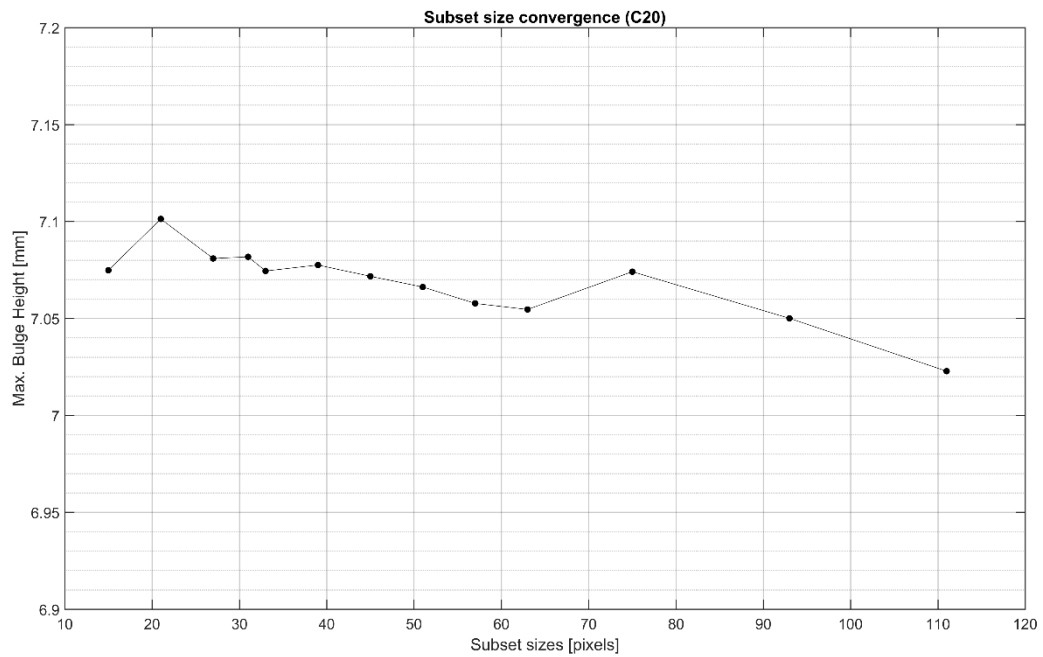


Figure 5-5 Variation of maximum bulge heights calculated using DIC from a single DIC recording of the bulge test with circular bulge window as subset sizes are increased.

The most interesting phenomenon is observed while changing subset size for a tensile test. There is no significant effect ($205.8 \pm 0.082\%$) on the longitudinal stretch ratio (λ_1) for the selected subset sizes shown in Figure 5-6. On the other hand, the lateral stretch ratio (λ_2) is very sensitive to the subset size changes (Figure 5-7). The calculated λ_2 remains constant upto a subset size of 27 and only falls $\sim 0.2\%$ when the subset size is increased to the default size of 31. The calculated λ_2 fall nearly linearly as the subset size is increased, as shown in Figure 5-7. Therefore, a subset size of 27 is used to calculate stretch ratios from the tensile tests.

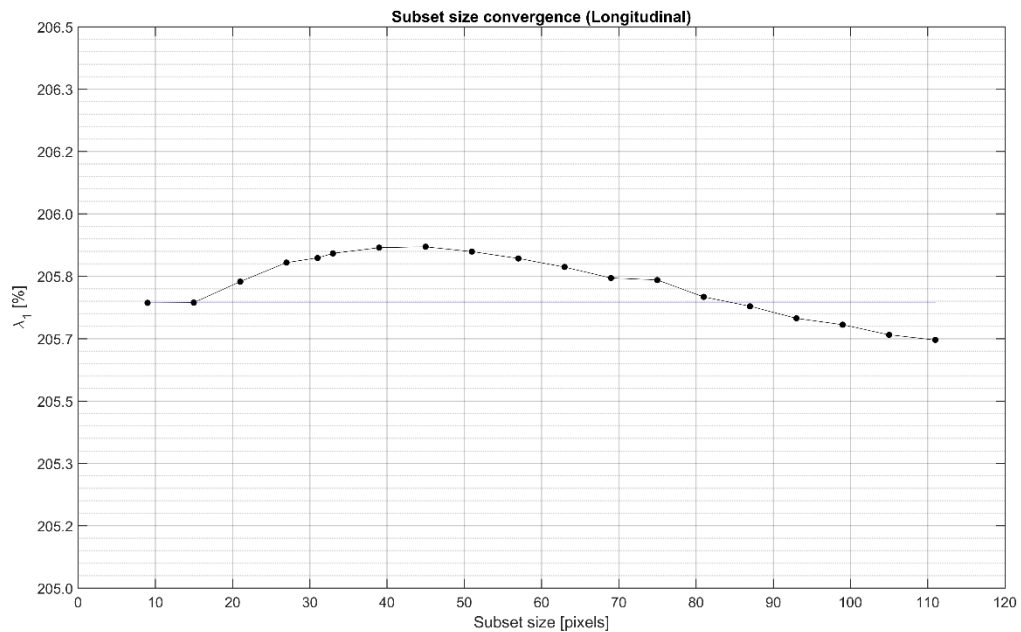


Figure 5-6 Variation of longitudinal stretch ratio (λ_1) calculated using DIC from a single DIC recording of the tensile test as subset sizes are increased.

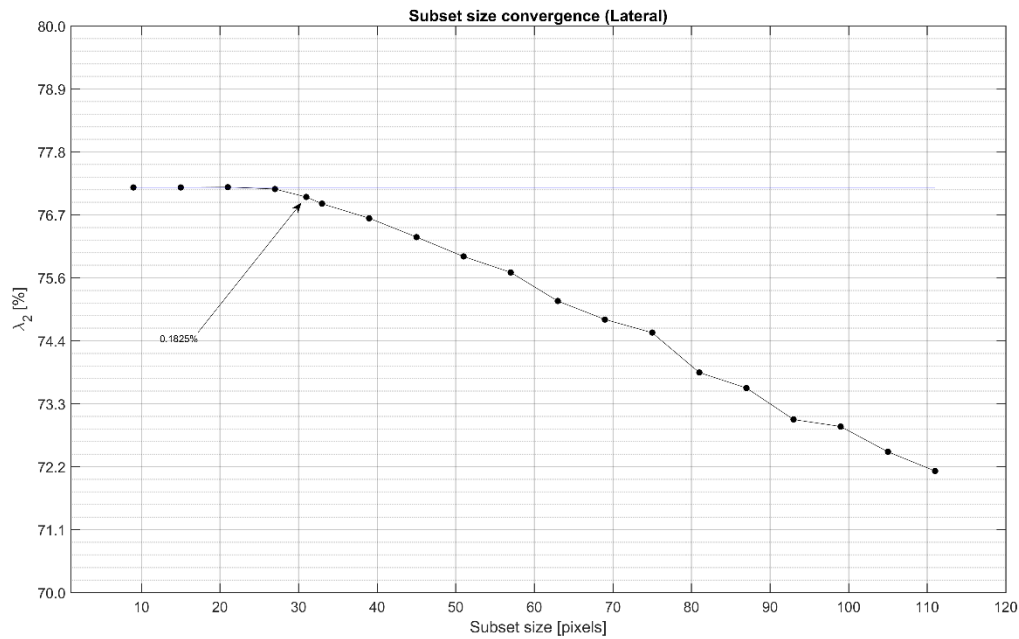


Figure 5-7 Variation of lateral stretch ratio (λ_2) calculated using DIC from a single DIC recording of the tensile test as subset sizes are increased. The value of λ_2 drops 0.1825% as subset size is increased from 27 to the default size of 31.

As seen from Figure 5-2 to Figure 5-7, the general trend is an underestimation of the displacements at higher subset sizes. The most variation is observed in lateral stretch (λ_2) during the tensile test as subset size, is increased.

5.3 Smoothing the Bulge-Profile:

The bulge-profile data from DaVis have small fluctuations and require some smoothing. These small random variations are mainly the result of the sprayed speckled pattern. A very bad speckle pattern results in correlation breakdowns, but there are other less important factors like material discontinuities, sample thickness variations and experimental errors, which are harder to quantify.

A MatLab function for smoothing data called *smooth* is used. The smoothing function takes one of the many methods available i.e. 'moving average (default)', 'lowess', 'loess', 'spgolay', 'rloess', and 'rloess'. Therefore a method called 'lowess'

(local regression using weighted linear least squares and a 1st degree polynomial) with 0.2 (20%) span is used after trying all other methods available in MatLab. The sampling span is a trade-off between deviation from original (raw) data and the noise in the DIC profile's shapes, as seen in the raw data in Figure 5-8 to Figure 5-12. Each figure shows few bulge profiles to make the figures clearer. Higher bulge heights show a higher bulge pressure. The reader is referred to the MatLab documentation (MathWorks, 2016) for a complete review of *smooth* function.

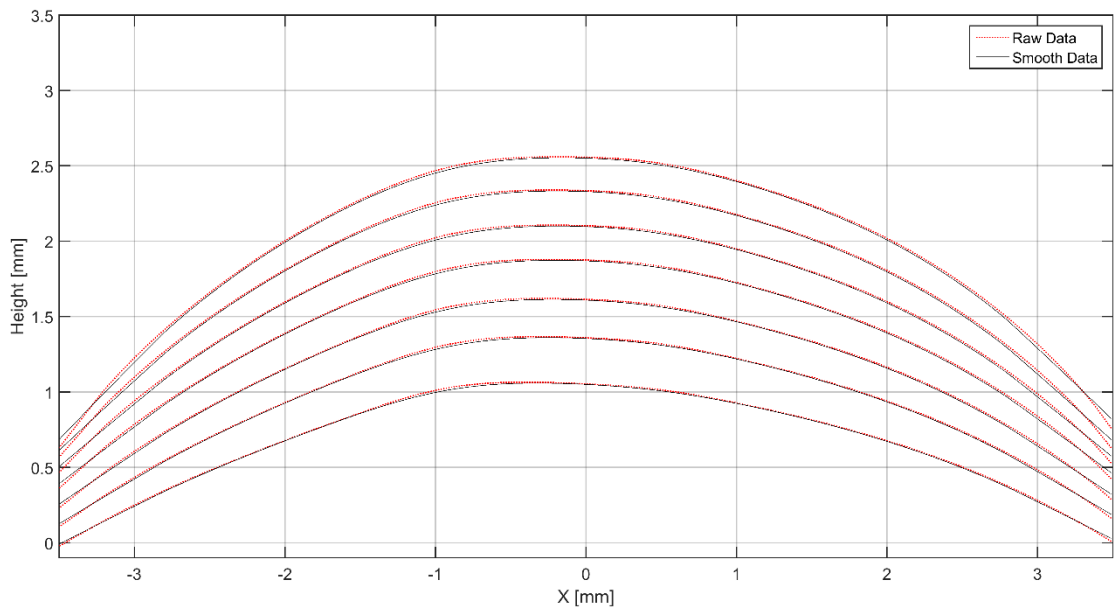


Figure 5-8. (R1S3) the third sample of the Rectangular window (aspect ratio ~ 4) after and before smoothing.

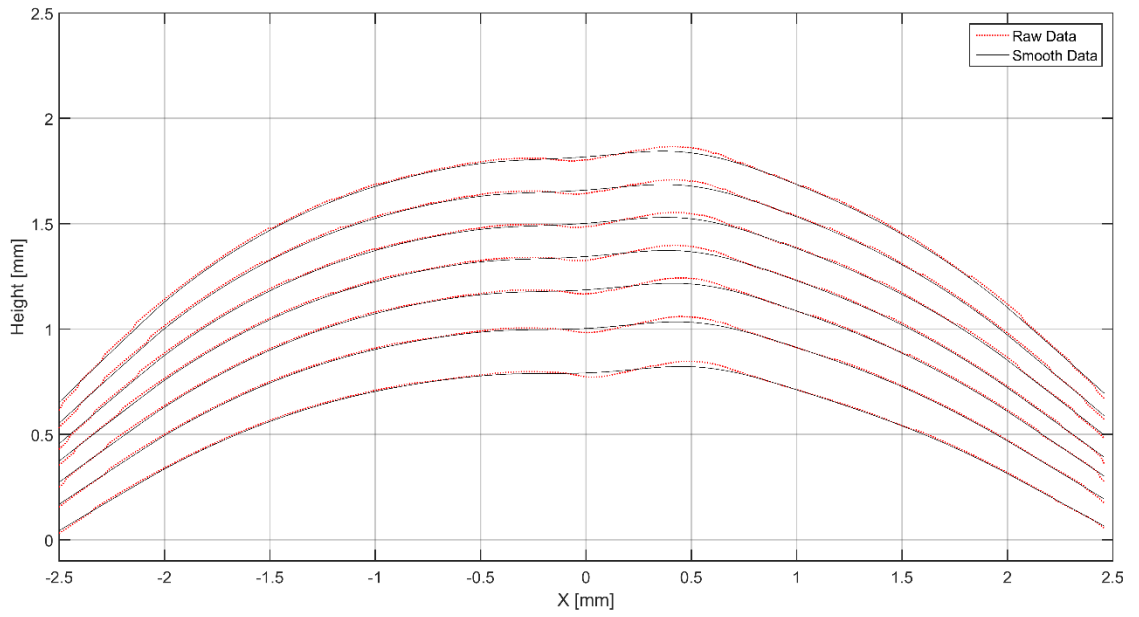


Figure 5-9 (R2S2) the second sample of the Rectangular window (aspect ratio ~6) after and before smoothing.

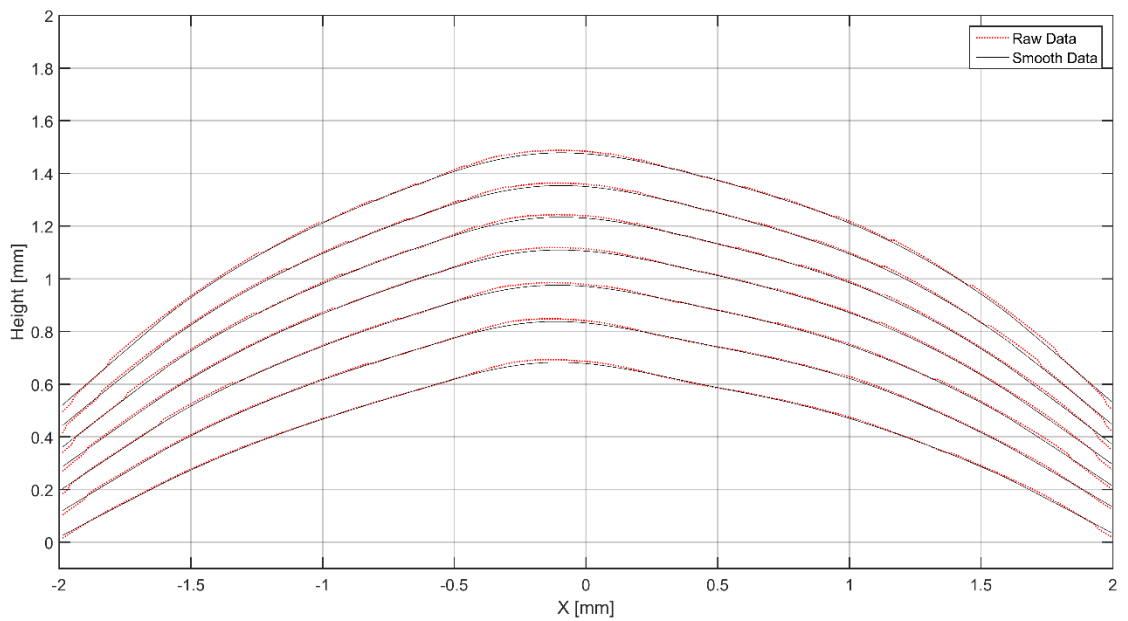


Figure 5-10 (R3S3) the third sample of the Rectangular window (aspect ratio ~7) after and before smoothing.

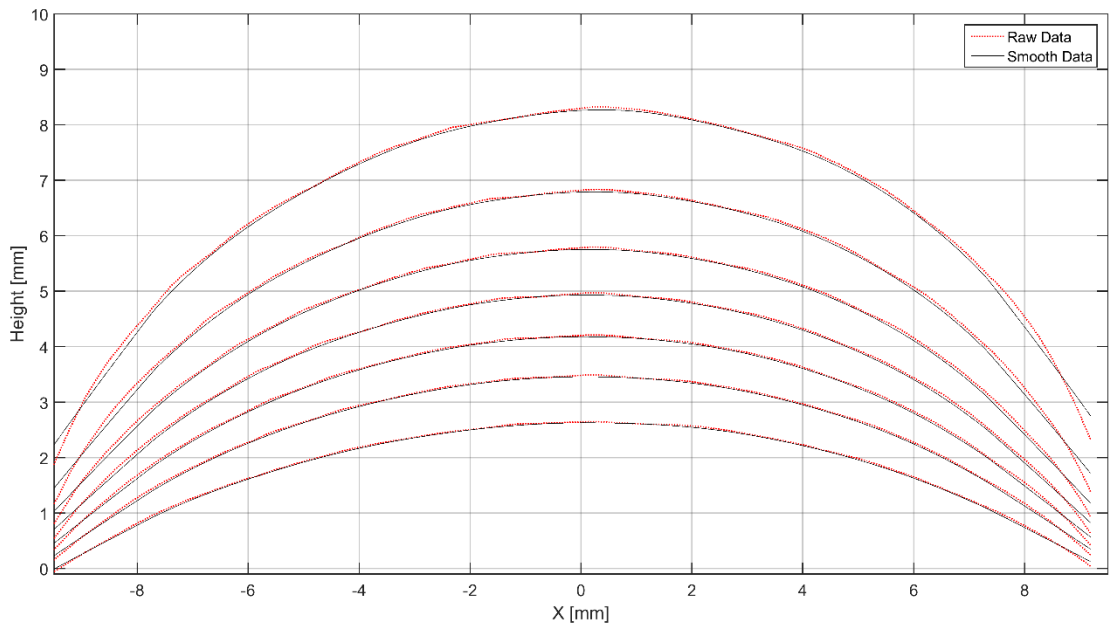


Figure 5-11 (C20S3) the third sample of the circular bulge window of diameter 20mm. Smoothing diametrical bulge-profile using 'lowess' and a span of 0.2.

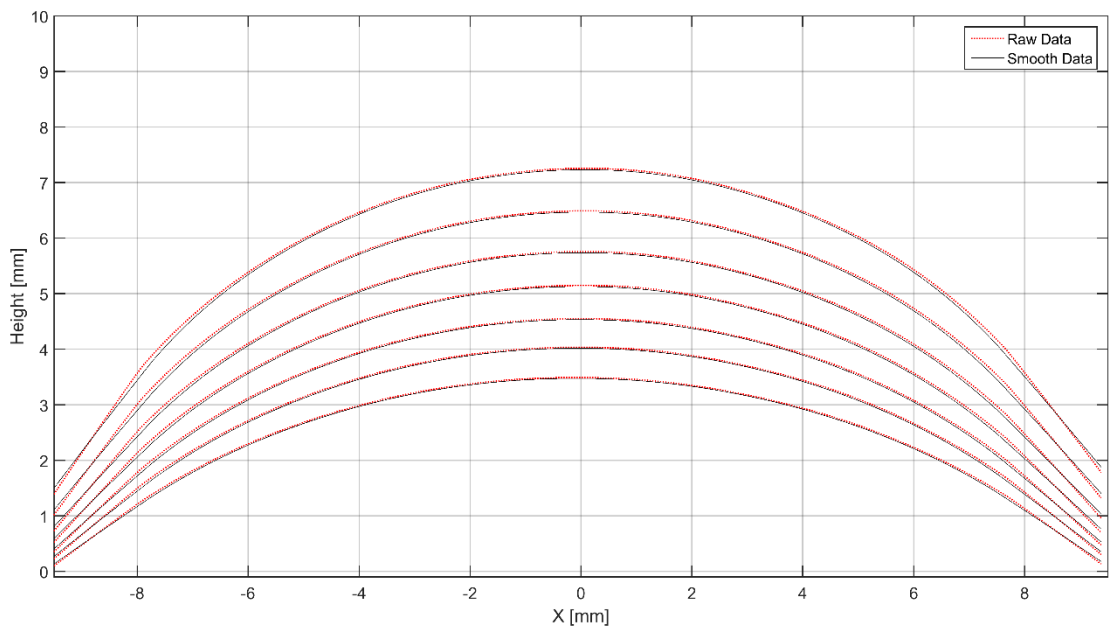


Figure 5-12 (C20S4) the fourth sample of the circular bulge window of diameter 20mm. Smoothing diametrical bulge-profile using 'lowess' and a span of 0.2.

5.4 The Bulge-Profile Approximations

The thin polymer film takes a certain shape depending upon the bulge window geometry. A sufficiently long rectangular bulge window becomes a cylindrical surface while and a circular bulge window becomes a spherical surface.

5.4.1 Rectangular Bulge Window

The bulge-profile (bulge-shape) is cylindrical as a circular arc can fit very well as shown in Figure 5-13. The centre of the bulge-arc moves only vertically and radius of the circular arcs decreases (from 5.55mm to 3.96mm) as the bulge pressure is increased. The horizontal position of centre of the arc fluctuates very slightly with a standard deviation of 0.0082 mm .

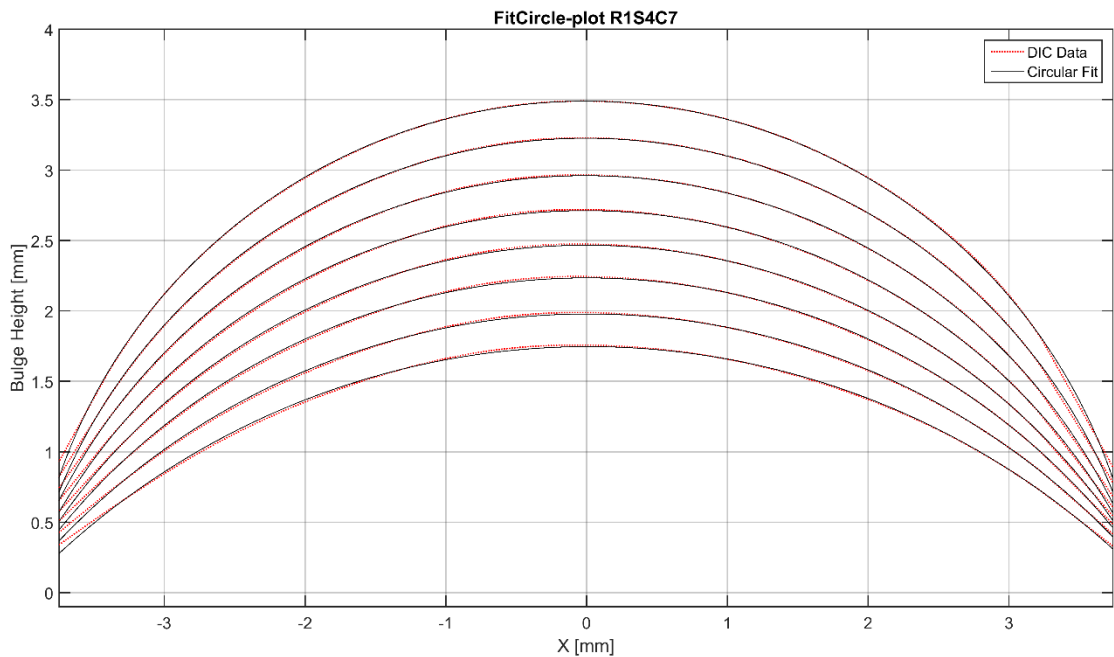


Figure 5-13 (R1S4) a circular arc fit to the bulge-shape. The horizontal position of the centre of the arc remains at a mean of $\bar{x} = 0.00\text{ mm}$ and standard deviation of $s = 0.0082\text{ mm}$. The lowest arc represents the lowest pressure.

The shape of the bulge can also be approximated by a polynomial. For a small bulge height, the shape of the bulge is a parabola as also noted by Kalkman (Kalkman et al., 1999) and as seen in Figure 5-14. For higher bulge heights (and pressures), the bulge-shape can be better fit with a 4th degree polynomial (Pratt & Johnson, 1993), shown in Figure 5-15.

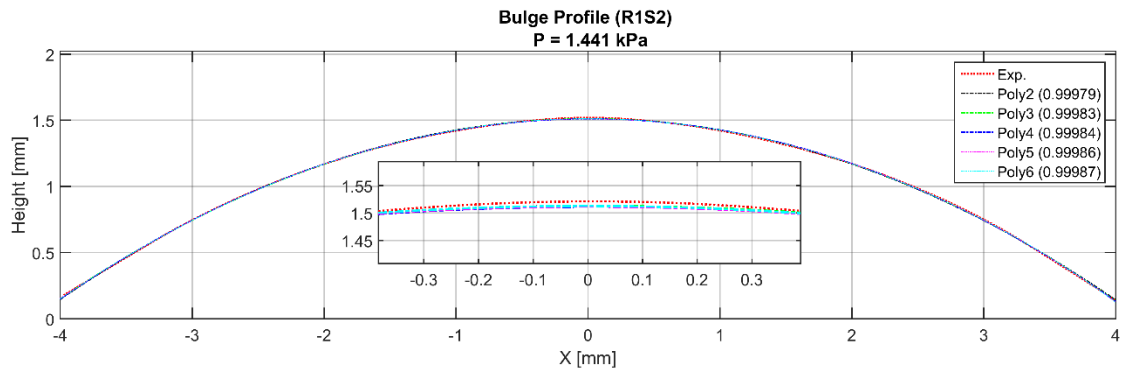


Figure 5-14 The bulge-profile (R1S2) at a pressure of 1.44 kPa showing polynomial fits of 2nd, 3rd, 4th, 5th and 6th degrees along with their respective goodness of fit (adjusted R²). All degrees of polynomials fit the bulge-profile very well.

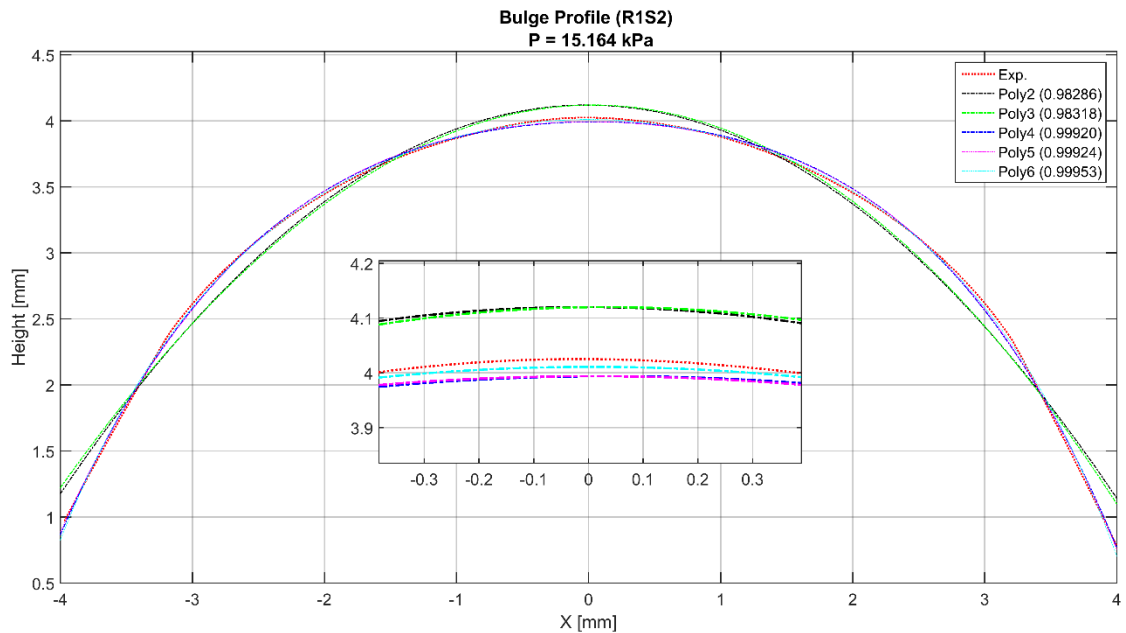


Figure 5-15. The bulge-profile (R1S2) at a pressure of 15.164 kPa showing polynomial fits of 2nd, 3rd, 4th, 5th and 6th degrees along with their respective adjusted R² of fit. Polynomial fits of degree 4 and higher degrees fit best at all pressures (upto ~15kPa) and maximum bulge heights (upto ~4mm).

A 4th degree polynomial fit to the bulge-profile is very good and increasing the degree of polynomial further (fifth, sixth etc.) gives no significant improvement as shown in Figure 5-15.

It has also been observed that with quadratic fit, the goodness of fit degrades as bulge height is increased past 2 mm in the case of R1 and R2, and in the case of R3, the same is observed post 1.25 mm bulge height.

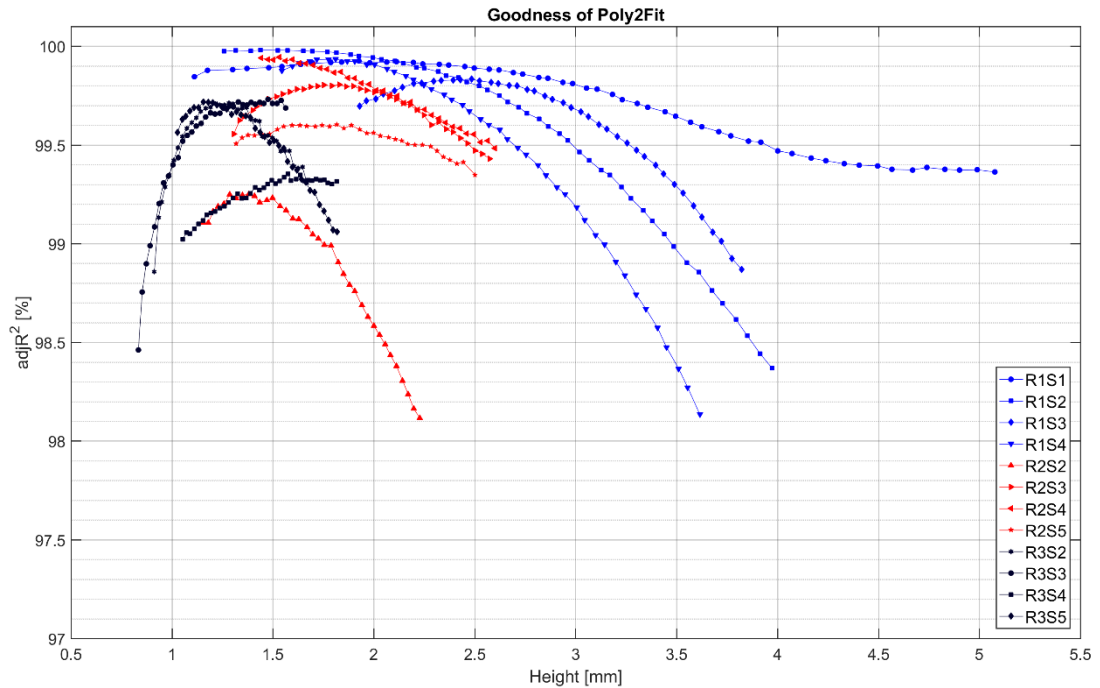


Figure 5-16 Variation of adjusted R^2 (goodness of fit) of a quadratic polynomial fit as maximum bulge height increases. R1, R2 and R3 are three different aspect-ratio-rectangular bulge windows. Each R window has many different samples and are designated by S1, S2 and so on.

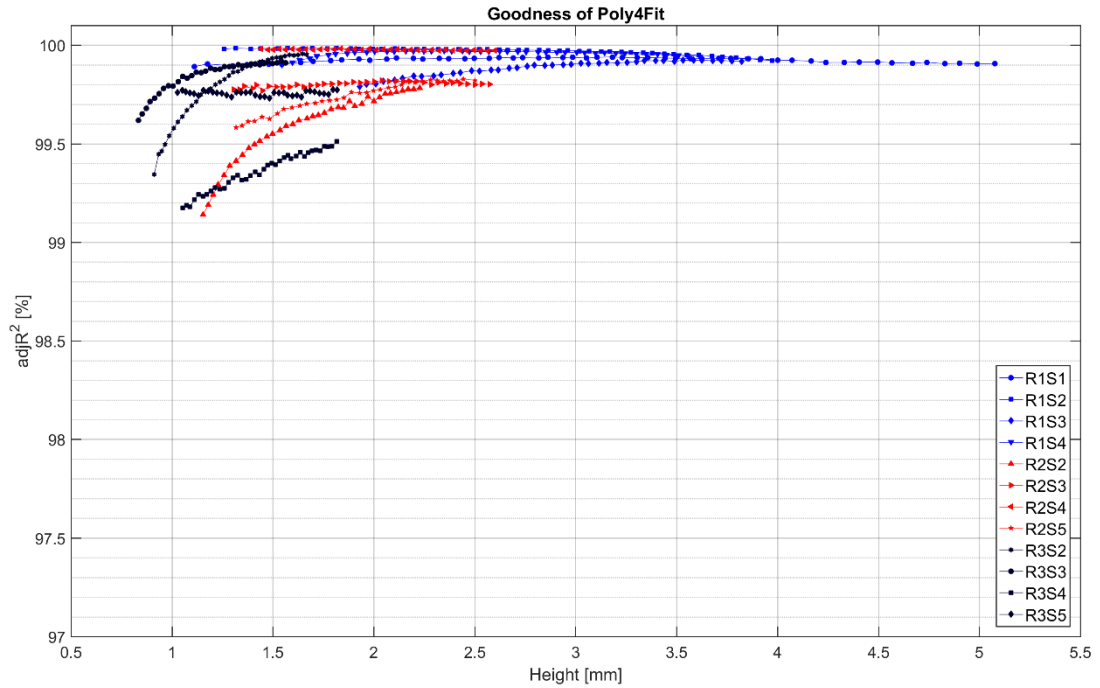


Figure 5-17 Variation of adjusted R^2 (goodness of fit) of a biquadratic polynomial fit as maximum bulge height increases. R1, R2 and R3 are three different aspect-ratio-rectangular bulge windows. Each R window has many different samples and are designated by S1, S2 and so on.

The benefit of fitting a polynomial curve is to be able to calculate the curve length, the new stretched length of the sample and hence the stretched ratios along the width and length of rectangular samples, λ_1 and λ_2 but polynomial curve is more susceptible to noise near edges as optical access is not very good.

The arc length method will be used in this study, as it is better in dealing with the noise in the bulge-profile near the edges. The sample holder plate is 2mm thick and the when bulge height is about the same or more than the sample holder plate thickness, it obstructs the view of one or both DIC cameras as shown in Figure 5-18.

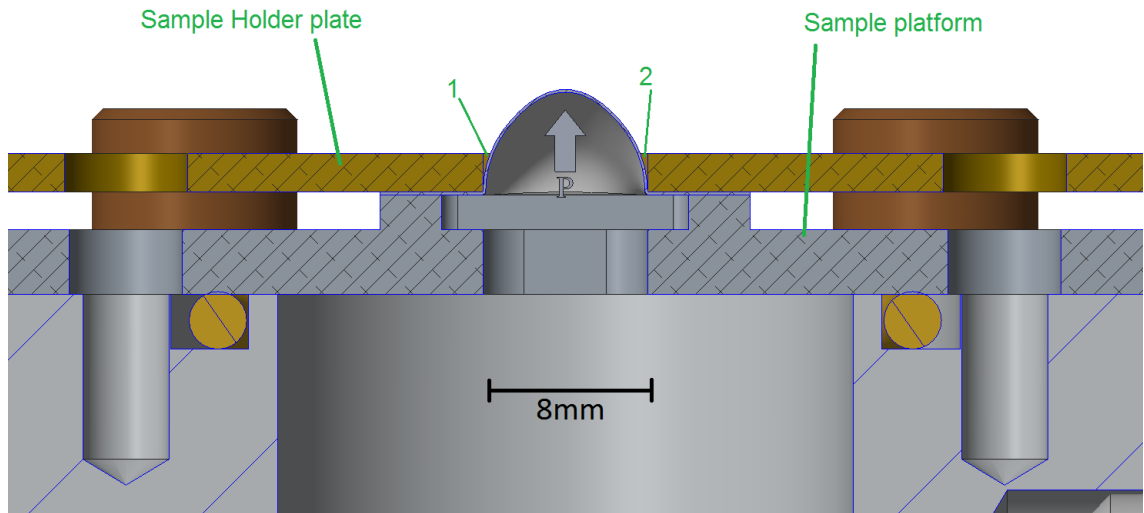


Figure 5-18 Rectangular bulge setup showing optically inaccessible spots (1 and 2) which do not correlate well in DIC and result in distortions and excessive noise.

Therefore, if bulge radius is used to calculate the stretched length of the bulge-profile, it bypasses the noise related problem in dealing with the polynomial curve length.

5.4.2 Circular Bulge Window

When the bulge-profile is extracted from a diametric line on the deformed 3D geometry as explained in 4.8.2, a circular arc can be fitted to the bulge-shape with very reasonable accuracy as shown in Figure 5-19.

The bulge-shape produced by a circular window is a spherical cap. This assumption of a spherical cap remains only valid upto a hemispherical cap as also noted by (Reuge et al., 2001).

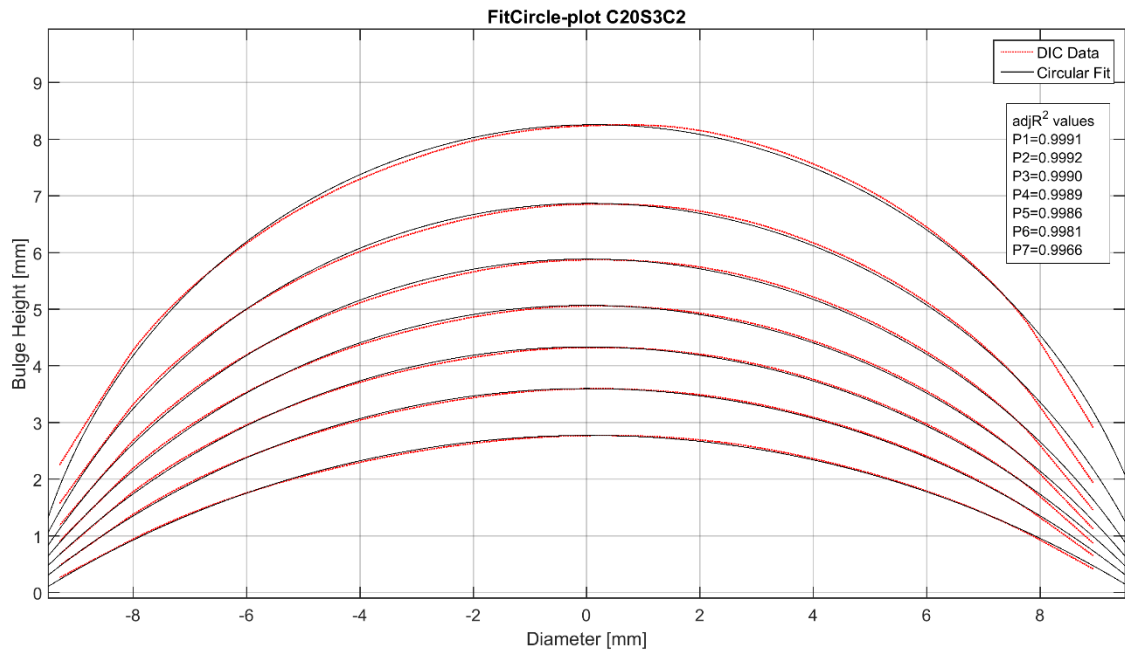


Figure 5-19 C20S3, Circular bulge window of diameter 20mm and sample three. A circular arc fits reasonably well to bulge shape as shown by the values of adjR^2 .

5.5 Zero Pressure Height Correction

It is necessary to compensate the maximum bulge height with pressure if the sample surface is not flat at the beginning due to wrinkles (Kalkman et al., 1999; Schweitzer & Göken, 2007; Xiang & Chen, 2005; Yang, Long, Ma, & Wang, 2014). A non-zero pressure is required to keep the thin polymer film from collapsing and wrinkling. If the sample film collapsed and/or wrinkled, it would block the optical access of the DIC cameras to the sample surface. Another reason is that material samples are taken from gloves that are not completely flat which have a non-zero bulge height.

Therefore, it is very important to compensate and correct the bulge heights of the first cycle. After the first cycle of bulging, the material has some temporary plastic stretch that is due to hysteresis and need not be corrected.

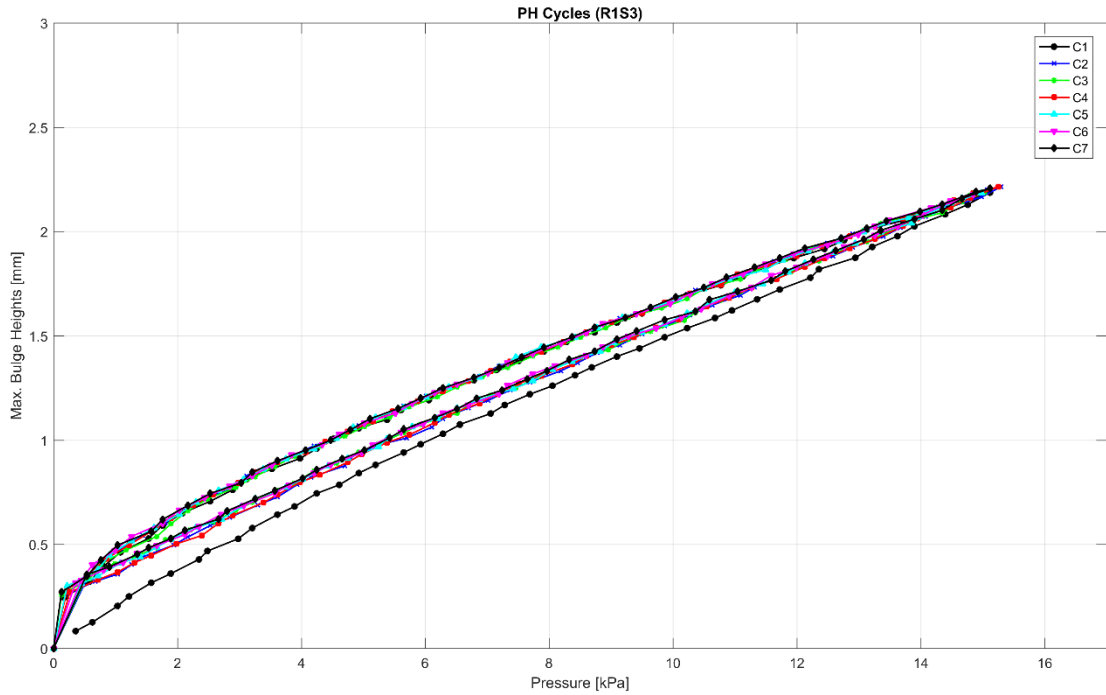


Figure 5-20 Pressure and maximum bulge height ($p - h_0$) response after height correction. Seven cycles are shown

The starting two pressure values for the first cycle are taken and linear backward extrapolation is used to estimate the bulge height corresponding to a zero pressure. This value is subtracted from all bulge height values before curve fitting.

5.6 Fitting Curve to the Rectangular Bulge Data:

A well-established correlation between bulge pressure (p) and bulge height (h_0), as discussed in section 2.1.8.5.1 equation (31), is as follows: (Vlassak & Nix, 1992)

$$p = 2 \frac{\sigma_0 t_0}{a^2} h_0 + \frac{4M_r t_0}{3a^4} h_0^3$$

This relation can be linearized as follows (Yang et al., 2014; Youssef et al., 2010):

$$\frac{p}{h_0} = A + B h_0^2 \quad (44)$$

Once $p - h_0$ data have been extracted from the bulge test results, best straight-line fit can be obtained using the equation:

$$Y = A + BX \tag{45}$$

where,

$$Y = p/h_0$$

$$X = h_0^2$$

$A =$ the $Y -$ intercept

$B =$ the gradient of the best fit straight line

Figure 5-21 shows the quality of straight-line fit of equation (45). The mean value adjusted R^2 is 0.79 ± 0.020 .

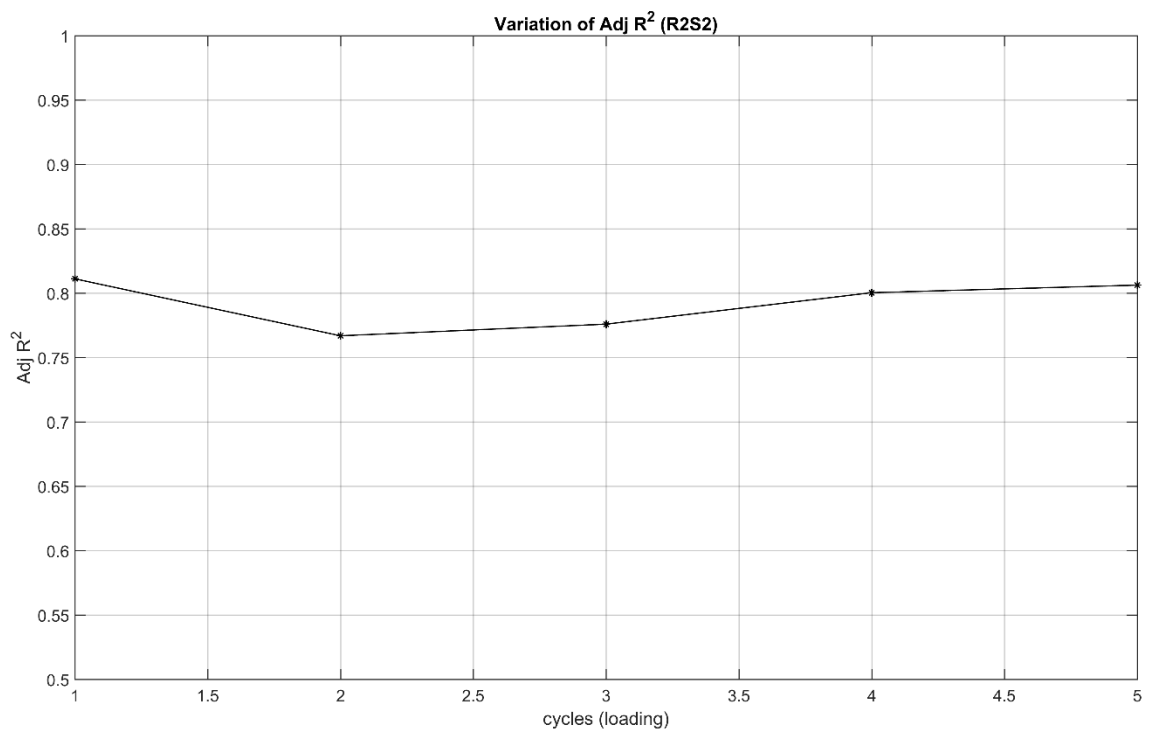


Figure 5-21 (R2S2) Quality of the linear fit of equation (45) for the five loading cycles.

Using a MatLab[®] script, the curve fit parameters A and B are found. The (X, Y) plot together with the value of constants of equation (45) is depicted in Figure 5-22, which shows a reasonable correlation.

Using the values of constants A and B , the two material constants $\sigma_0 = \frac{Aa^2}{2t_0}$ and $M_r = \frac{3Ba^4}{4t_0}$, given $2a$ for their respective rectangular windows (R1, R2 and R3) and thickness of samples ($t_0 = 125 \mu m$), are found.

Note that a non-zero minimum pressure is required to keep the thin sheet taught and stop it from wrinkling and falling down because of its own weight.

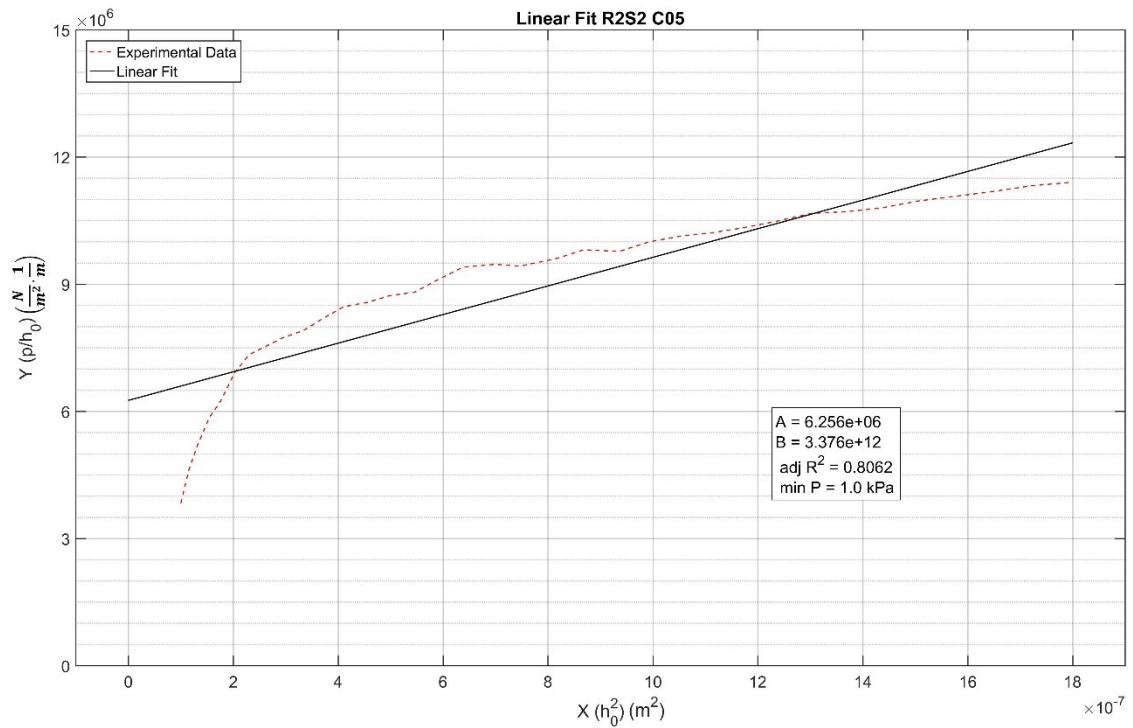


Figure 5-22. Linearization of experimental data for loading of the bulge test (R2S2) with line constants and an adjusted R^2 value of 81%.

5.7 Fitting Curve to the Circular Bulge Data:

A correlation between bulge pressure (p) and bulge radius of curvature (R), as discussed in section 2.1.8.5.3 and given in equation (40), is as follows:

$$P = \frac{M_c t a^2}{4} \left(\frac{1}{R}\right)^3 + 2\sigma_0 t \left(\frac{1}{R}\right)$$

Similarly, this relation can be linearized as follows:

$$pR = A + B \left(\frac{1}{R}\right)^2 \quad (46)$$

Once $p - R$ data have been extracted from bulge test results. A best straight-line fit can be obtained using the linearization equation (45) with new values of X and Y:

$$Y = pR$$

$$X = \frac{1}{R^2}$$

Figure 5-23 shows the quality of straight-line fit to linearized equation (45). The mean adjusted R^2 is 0.90 ± 0.01 .

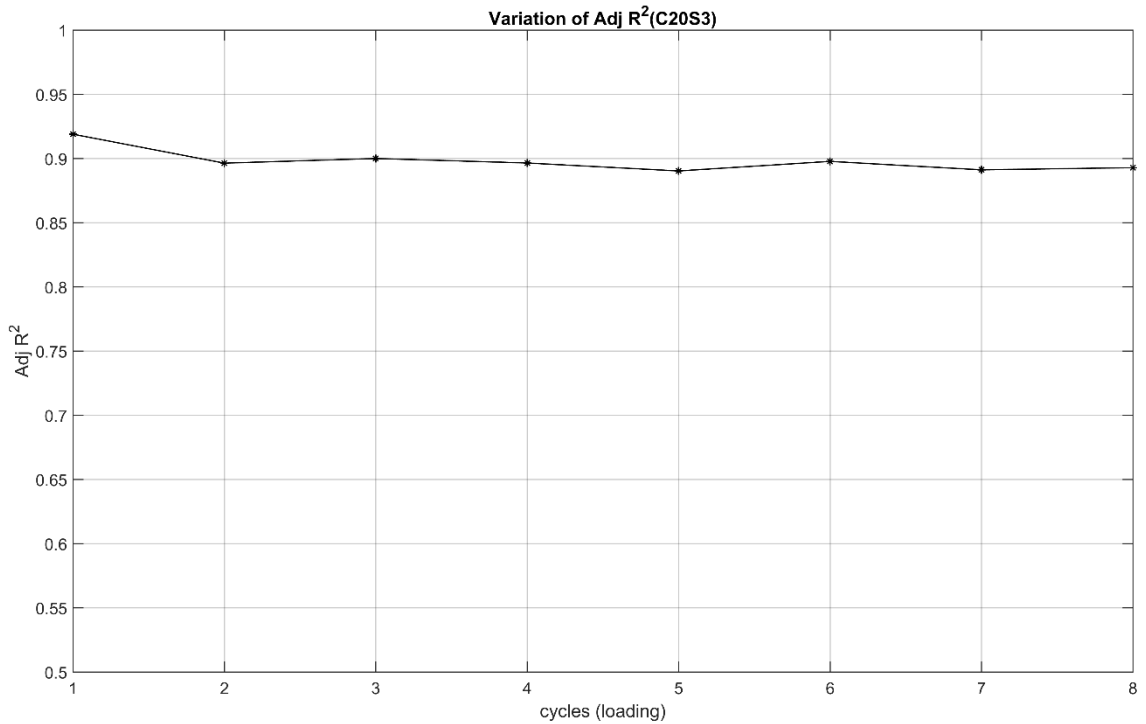


Figure 5-23 (C20S3) Quality of the linear-fit of equation (45) for the eight loading cycles.

The (X, Y) plot together with the value of constants of equation (45) is depicted in Figure 5-24.

Using the values of constants A and B , the two material constants $\sigma_0 = \frac{A}{2t_0}$ and $M_c = \frac{4B}{t_0 a^2}$, given the radius of circular bulge window a ($\frac{20}{2} = 10mm$), and thickness of the sample t_0 , are found.

Note that a non-zero minimum pressure is required to keep the thin sheet taught and stop it from wrinkling and falling down because of its own weight.

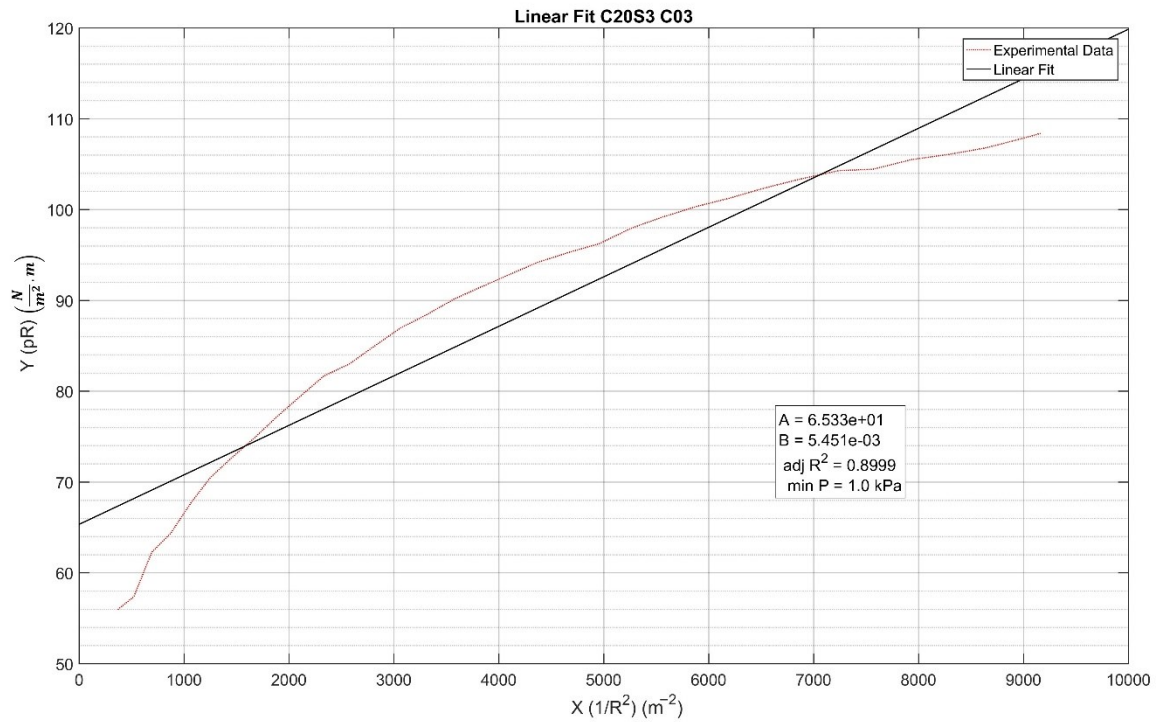


Figure 5-24. linearization of experimental data for loading of the circular bulge test (C20S3) with an adjusted R^2 value of 90%.

5.8 Stabilization and Hysteresis

It has been observed with all samples that the material ($p - h_0$) response mostly stabilizes after the first cycle of loading and unloading (or inflating and deflating), Figure 5-25. The same effect has been observed with all samples of all three aspect ratios (R1, R2 and R3) as well as circular window bulge samples (Figure 5-26). A similar material response has also been observed in the tensile test results (Figure 5-27). Figure 5-27

Therefore, all results from the first cycles of all experiments have been omitted from further presentation and use, to present stable results from which material behaviour can be determined.

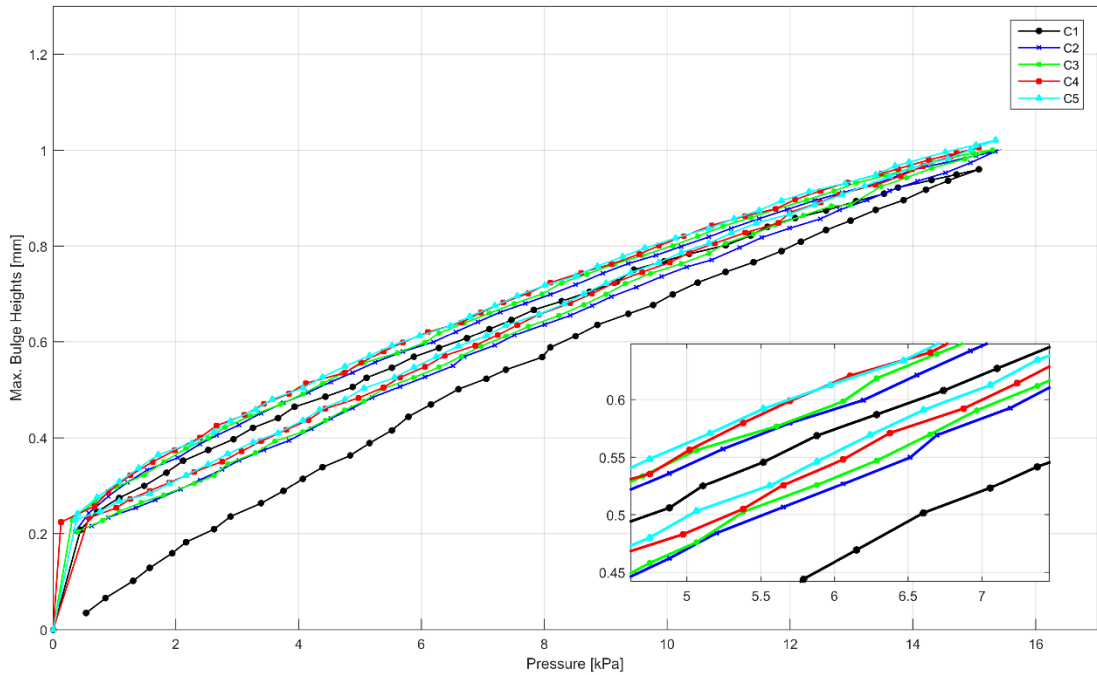


Figure 5-25 (R3S4) Maximum bulge height and pressure plot of material with five cycles of loading (pressurizing) and unloading (de-pressurizing). The material response mainly stabilizes after the first cycle so that the following loading cycles give fairly consistent pressure and maximum bulge height response with hysteresis.

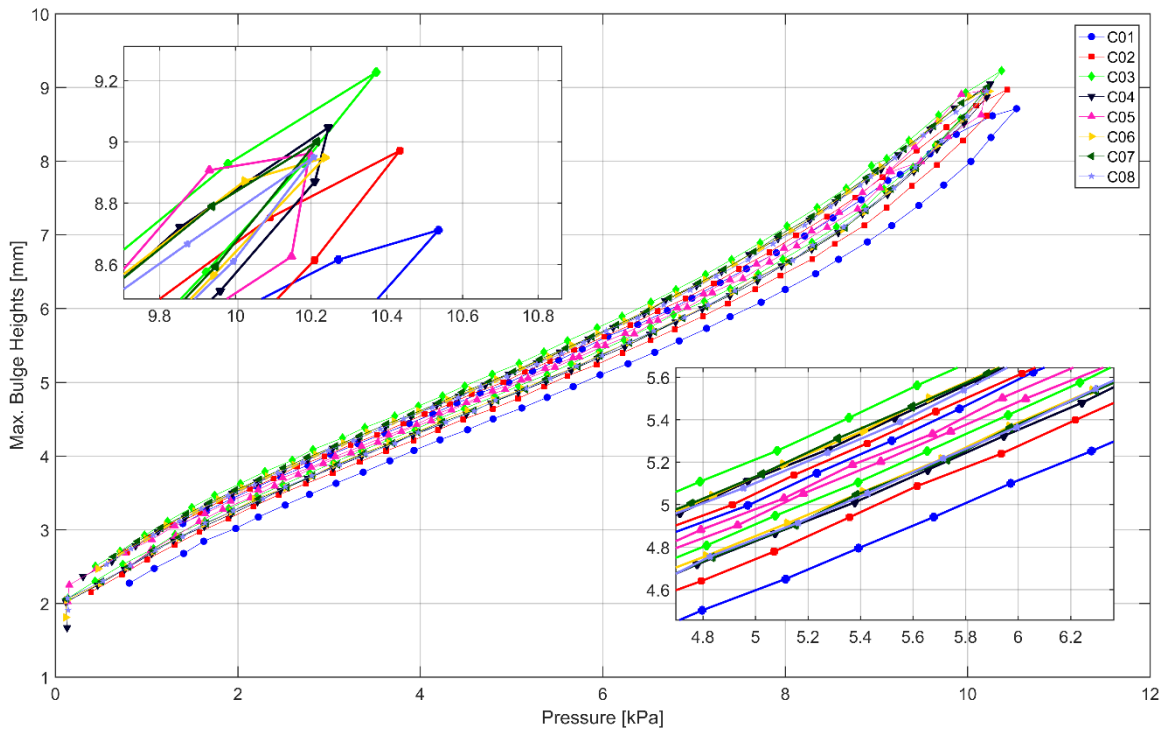


Figure 5-26 (C20S3) stabilization in the material response curve under cyclic bulging with circular bulge window. The material response is mainly stable after the first cycle.

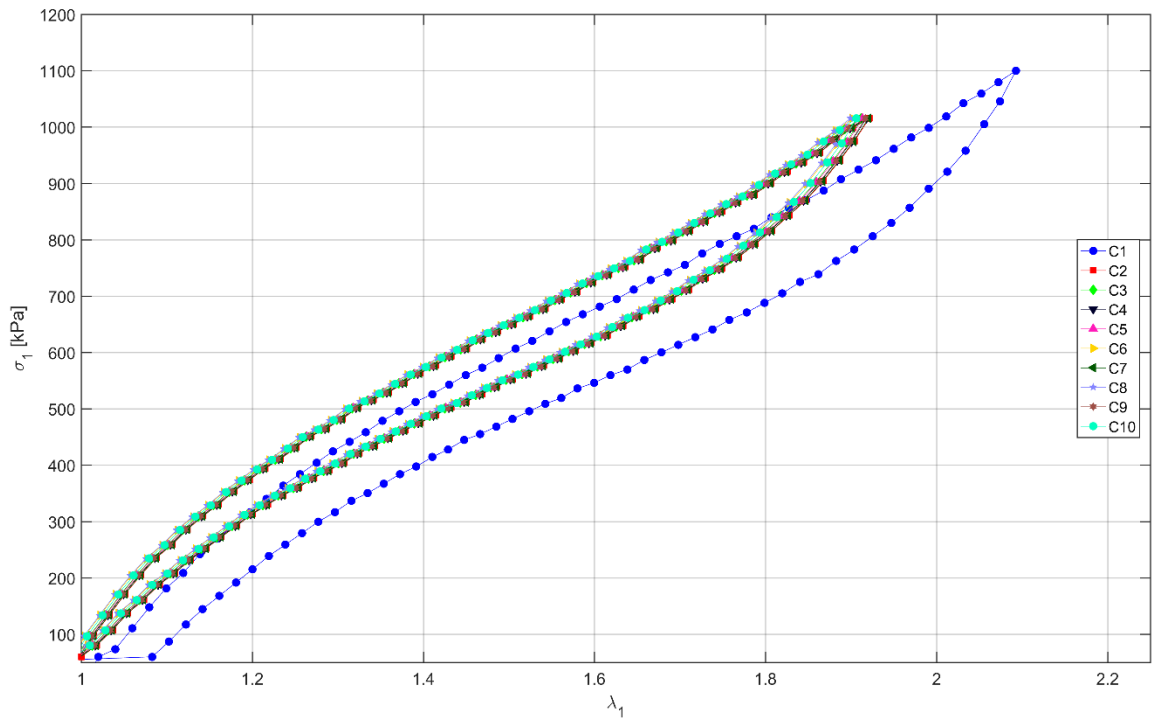


Figure 5-27 Tensile sample with ten stretching cycles showing stabilization of longitudinal stress-stretch ($\sigma_1 - \lambda_1$) behaviour mainly after the first stretching cycle.

The stress-stretch data presented in the Figure 5-27 has been aligned to origin for presentation, therefore, it is not suitable for reading Young's modulus values.

This stabilization effect is known as 'Mullins effect' and is attributed to strain-induced softening of a polymer chain material due to repeated strain cycles (Göktepe & Miehe, 2005).

5.9 Unusable Results of some Rectangular Samples

During the course of experiments, two rectangular samples (R2S1 and R3S1) were found unsuitable for further consideration. It was noted that during construction of the deformed 3D shape, the bulged surface had missing surface patches especially from the top area (mid-width) because of reflection of light when the bulged surface had high curvature. These missing surface patches are due to a bad speckle-pattern (not unique) which results in the DIC correlation process to break down.

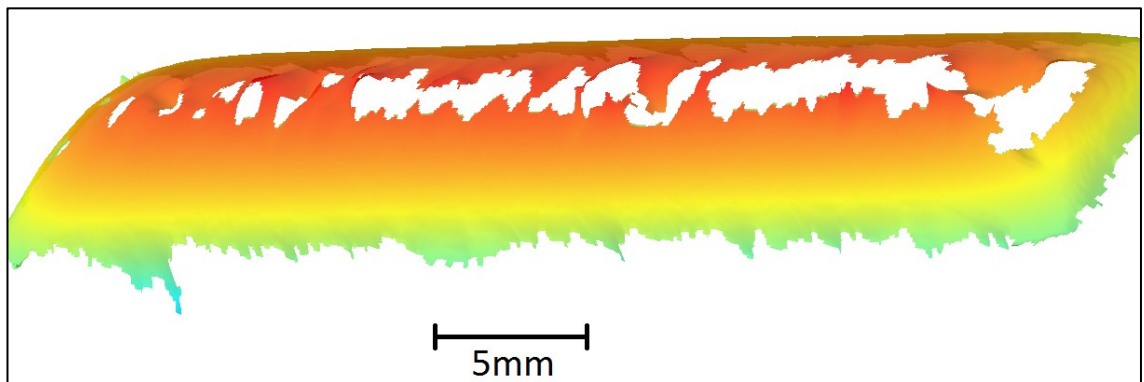


Figure 5-28 (R2S1) A broken DIC correlation at the top of the bulged surface. The size of these missing patches (white colour) increased at higher strains (higher bulge pressure). The bulge-surface is colored with respect to the bulge height.

Therefore, when the slice of the bulge shape is taken as described in section 4.8, the bulge-profile does not represent the actual bulge shape observed during the experiment as shown in Figure 5-29.

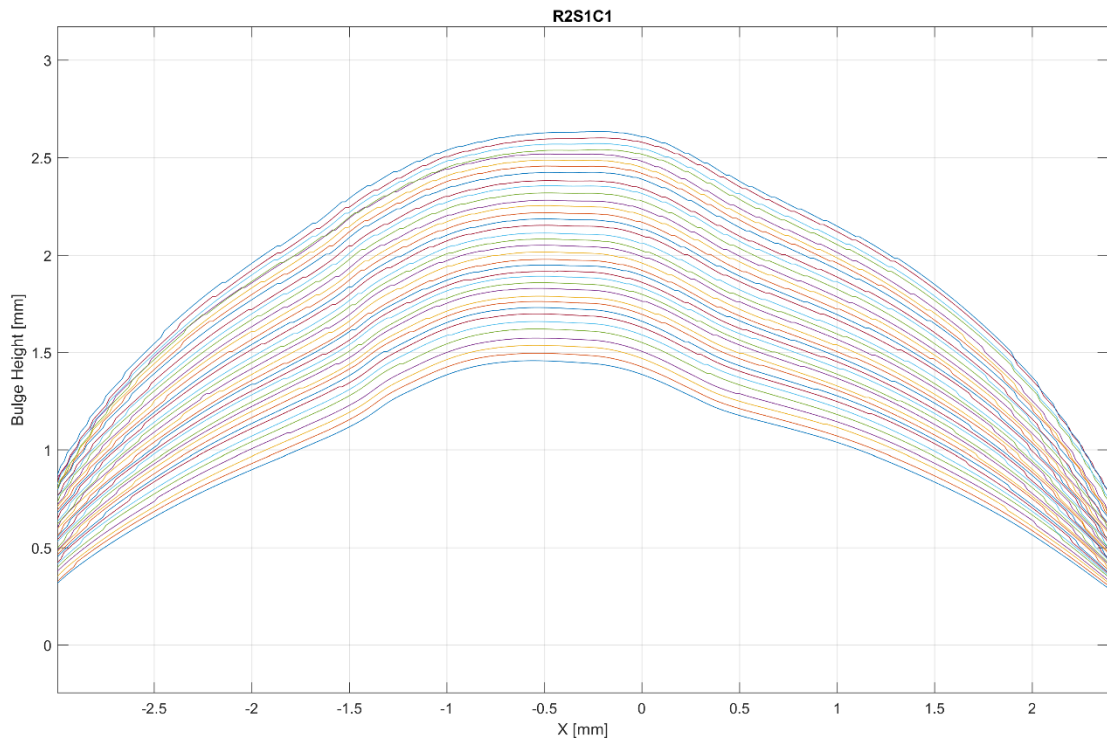


Figure 5-29 (R2S1) Bulge-profile as exported from DaVis showing non-circular shape but actually observed (through naked-eye) bulge shape during the experiment is circular (cylindrical in 3D).

Two such samples have been identified to be unsuitable.

1. R2S1: Second rectangular bulge window and first sample.
2. R3S1: Third rectangular bulge window and first sample

The material constants estimated from these two samples are also far from that of the material constants from other samples of the same geometry (Figure 5-30 and Figure 5-31).

The other sample with abnormal material parameters is R3S1. There is no problem with its 3D deformed surface but there is an excessive slack in the bulge after the first cycle. It is probable that the sample has not been mounted firmly, which resulted in slippage at high pressure. Therefore, no characterized material parameters are discussed/presented further from these two samples.

Figure 5-30 shows values of plane-strain modulus (M_r), the value of M_r for R3S1 ($2.64 \pm 0.08 \text{ MPa}$) is 41% higher than the average value of other four samples of R3. However, the same value for R2S1 is not far from the other four samples in R2 though.

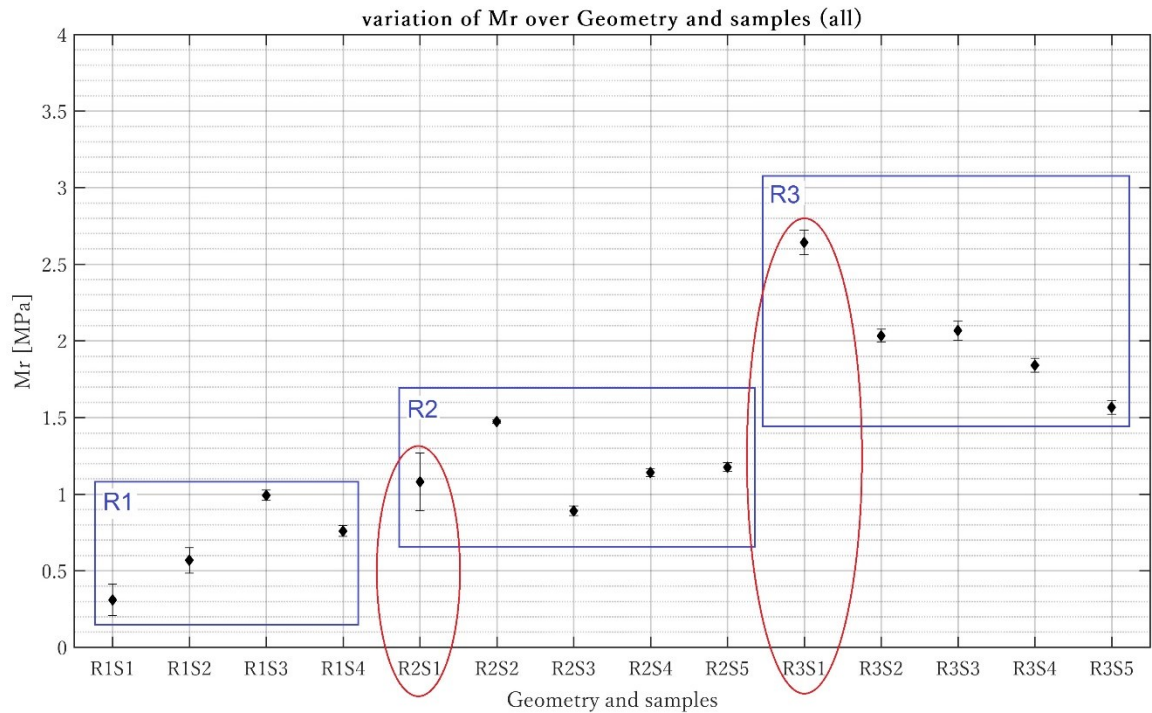


Figure 5-30 Variation of plane-strain modulus (M_r) showing bad samples. Only R3S1 shows a very high value as compared to the rest of the samples with R2S1 not far from other values in R₂ group.

Figure 5-31 shows the values of residual stress (σ_0) for both bad samples. The values are far below the other values in their respective aspect ratio categories, R₂ & R₃ respectively.

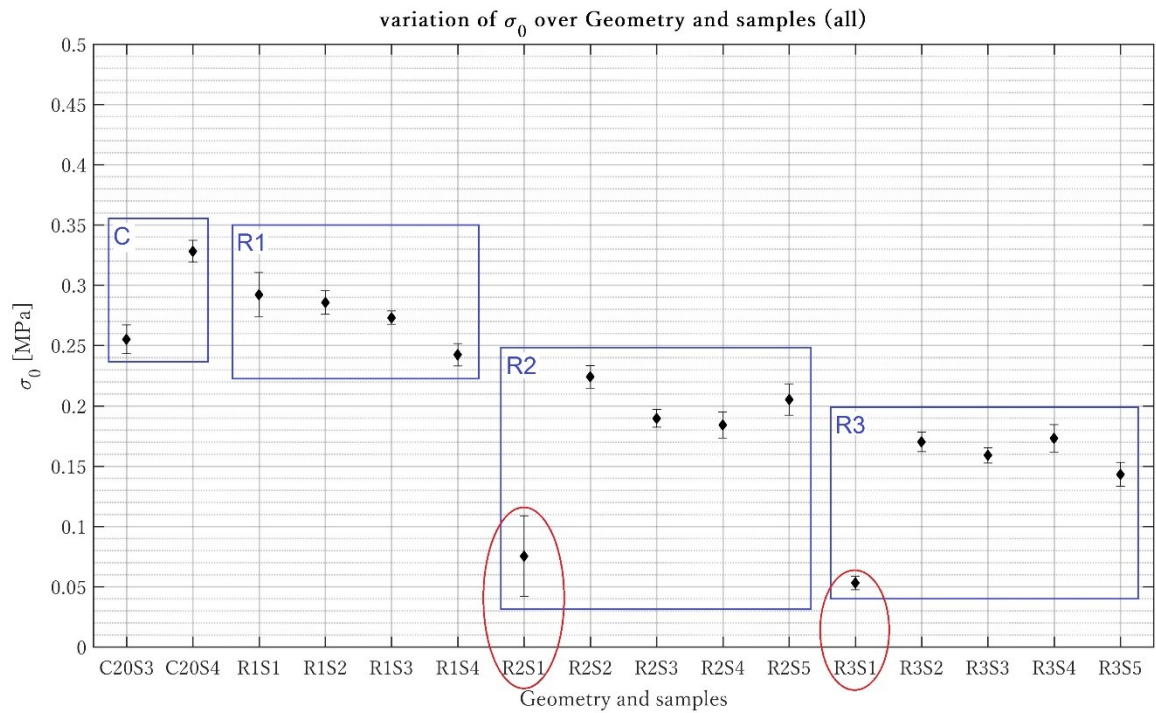


Figure 5-31 Variation of residual (σ_0) stress showing bad samples. The two samples, R2S1 and R3S1 show very low values for residual stress. 'C' shows the results from circular bulge window of diameter 20 (C20).

5.10 Material Characterized Properties from Bulge Test

Bulge test analytical models for a rectangular and a circular bulge window geometry give these three material properties:

1. Plane-strain modulus (M_r) from a long rectangular bulge window
2. Biaxial modulus (M_c) from a circular bulge window
3. Young's Modulus (E) derived from M_r and M_c .
4. Residual stress (σ_0) from both bulge window geometries.

These characterized material properties are presented in the next sections.

5.10.1 Variation of Plane-strain Modulus (M_r)

The values of plane-strain modulus have been estimated from curve fitting into equation (31). The next three figures present the variations in the values of plane-strain modulus highlighting effects of loading cycles, samples and geometry (aspect ratio) respectively.

Figure 5-32 presents variations in the values of M_r , arising from three factors: loading cycles of a sample, samples of same geometry and aspect ratio of the rectangular bulge window. The data presented in the figure is only one point for each cycle; therefore, the error bars represent a 95% confidence interval on the estimated material parameters. The same can also be said about Figure 5-35 and Figure 5-37 presented in the next sections.

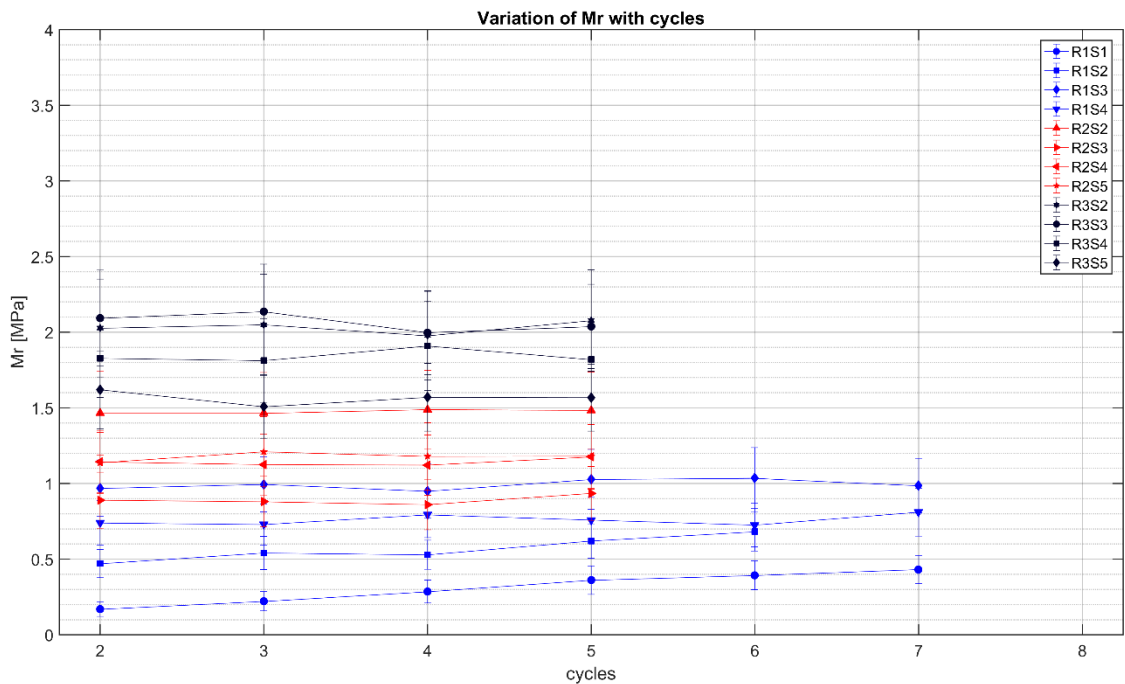


Figure 5-32 Variation of plane-strain modulus with rectangular bulge window as the aspect ratio is increased of various samples over cyclic loading. The first cycle of loading has not been shown as the material stabilizes during it. The error bars show a 95% confidence interval on the estimated values.

Figure 5-33 shows the mean and standard deviation in M_r of cycles plotted against four samples of each geometry. Figure 5-34 depicts the mean value of M_r averaged over loading cycles and samples.

Firstly, there is no regular pattern of variations in the value of M_r over loading cycles and the variation is small probably due to experimental variations and post statistically processing of DIC data in MatLab. The maximum standard deviation (10%) from the sample average value of M_r is in the cycles of R1S1 (Figure 5-33). In general, there is slightly more random variation in samples of R1 than R2 and R3. Therefore, the material response under cyclic loading is deemed consistent as compared to other variations as discussed in the following paragraphs.

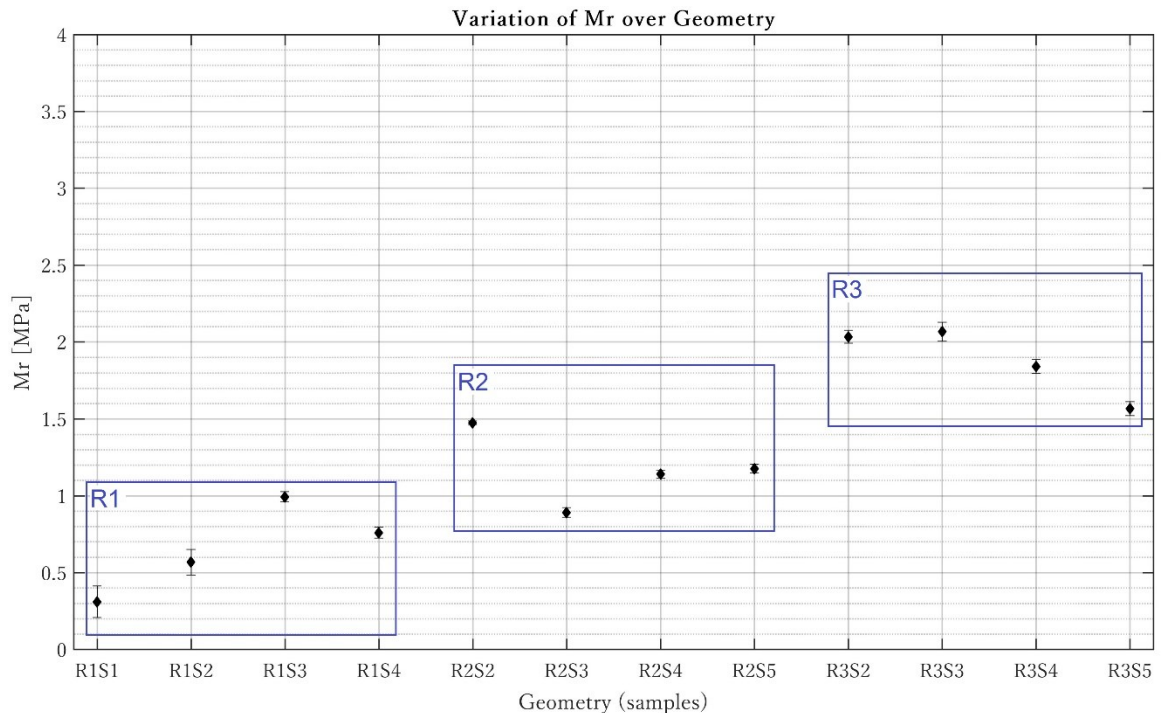


Figure 5-33 Variation of plane-strain modulus with rectangular bulge window with increasing aspect ratio for many samples. Mean and standard deviation of plane-strain modulus to all cycles of a sample are shown.

Secondly, different samples with the same aspect ratio show more variation (Figure 5-33) as compared to the variations due to loading cycles (Figure 5-32). This variation can be explained by variations in the natural rubber material composition. As explained in section 1.1, properties of natural latex rubber vary based upon many factors. Therefore, it is likely that the two samples obtained from two gloves have slight difference in material composition. Even two samples from the same glove may have some variations in the thicknesses and initial curvatures. The initial curvatures in the bulge tests have been corrected through zero pressure height corrections (section 5.5). In addition, the variations in the DIC data of each sample due to inhomogeneity in spraying on the samples to produce a speckle pattern for DIC should not be ignored.

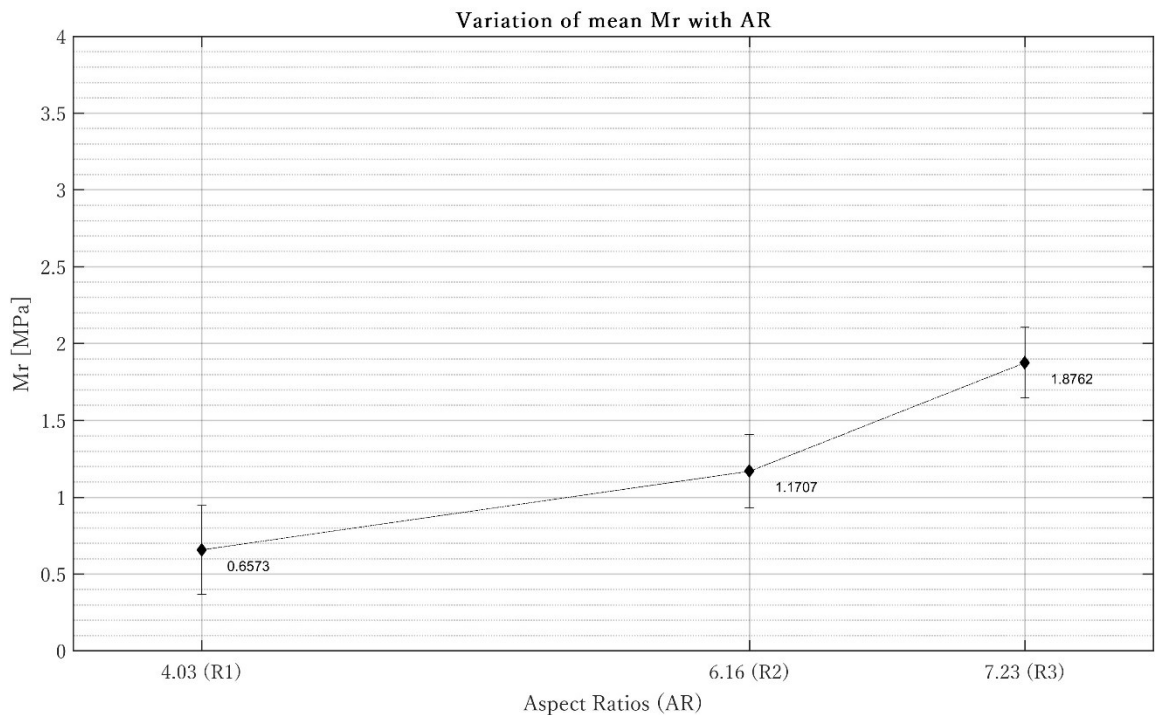


Figure 5-34 Variation of plane-strain modulus over three aspect ratios. Aspect ratio of rectangular bulge window show a clear increasing trend. The average value of this parameter for R2 is 1.171 ± 0.24 MPa.

Third and finally, there is clear a trend in the value of M_r with aspect ratio (Figure 5-34). The value of M_r increases as aspect ratio increases. It is also observed that the consistency in the value of M_r has also slightly improved with increasing aspect ratio.

The average value of M_r for R2 is $1.171 \pm 0.24 \text{ MPa}$.

5.10.2 Variation of Biaxial Modulus (M_c)

The value of the biaxial modulus (M_c) is calculated through curve fitting the equation (40) in MatLab as discussed in section 5.7.

The variation in the value of the biaxial Modulus (M_c) over cyclic loading of two samples is shown in Figure 5-35. The variations in the value of M_c over cycles is negligible and between the two samples is small. The average value of this parameter is $1.863 \pm 0.11 \text{ MPa}$.

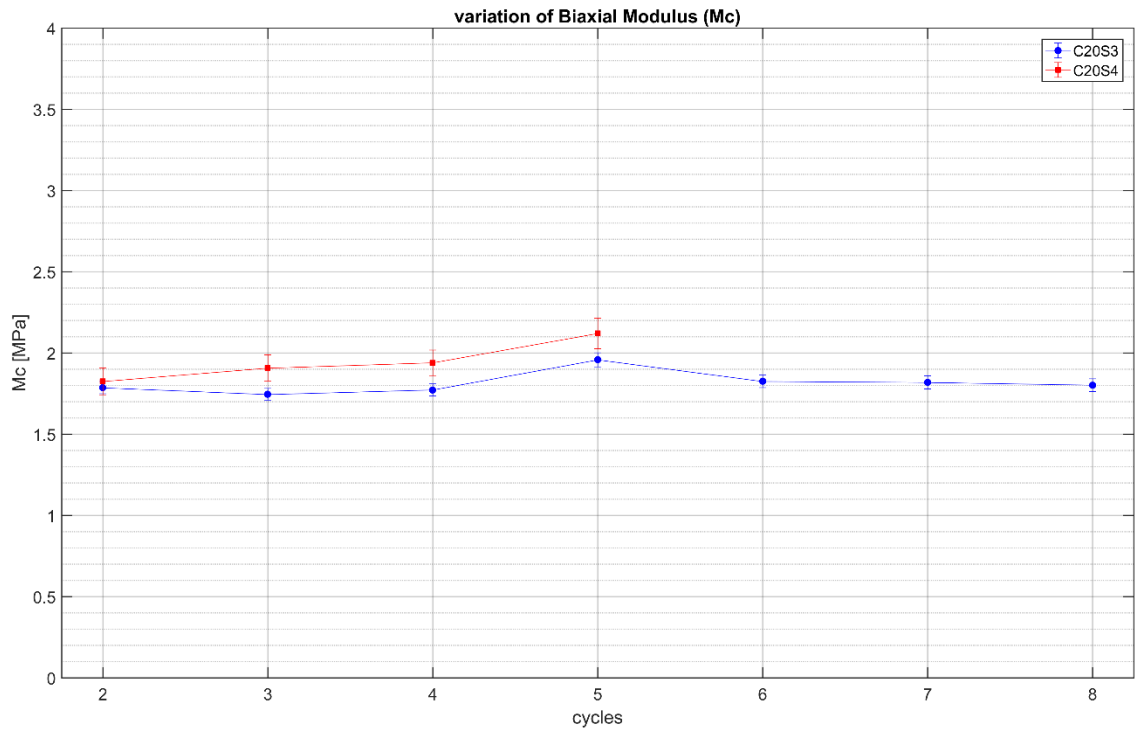


Figure 5-35 Variation of biaxial modulus as material goes through cyclic bulging for two samples. The first bulging cycle data are not shown as the material stabilizes during it. The error bars show a 95% confidence interval on the estimated values.

5.10.3 Variation of Young's Modulus (E)

Plane-strain modulus ($M_r = \frac{E}{1-\nu^2}$) and biaxial modulus ($M_c = \frac{E}{1-\nu}$) can be used to calculate Young's modulus (E). The mean value of Poisson's ratio $\nu = 0.385$ from tensile test is used to calculate the value of E . The value of E for R2 is $0.997 \pm 0.18 \text{ MPa}$ and the value of E for C (biaxial bulging with circular bulge window) is $1.145 \pm 0.18 \text{ MPa}$ as shown in Figure 5-36. The values of E from other two aspect ratios (R1 and R3) are either too low or too high.

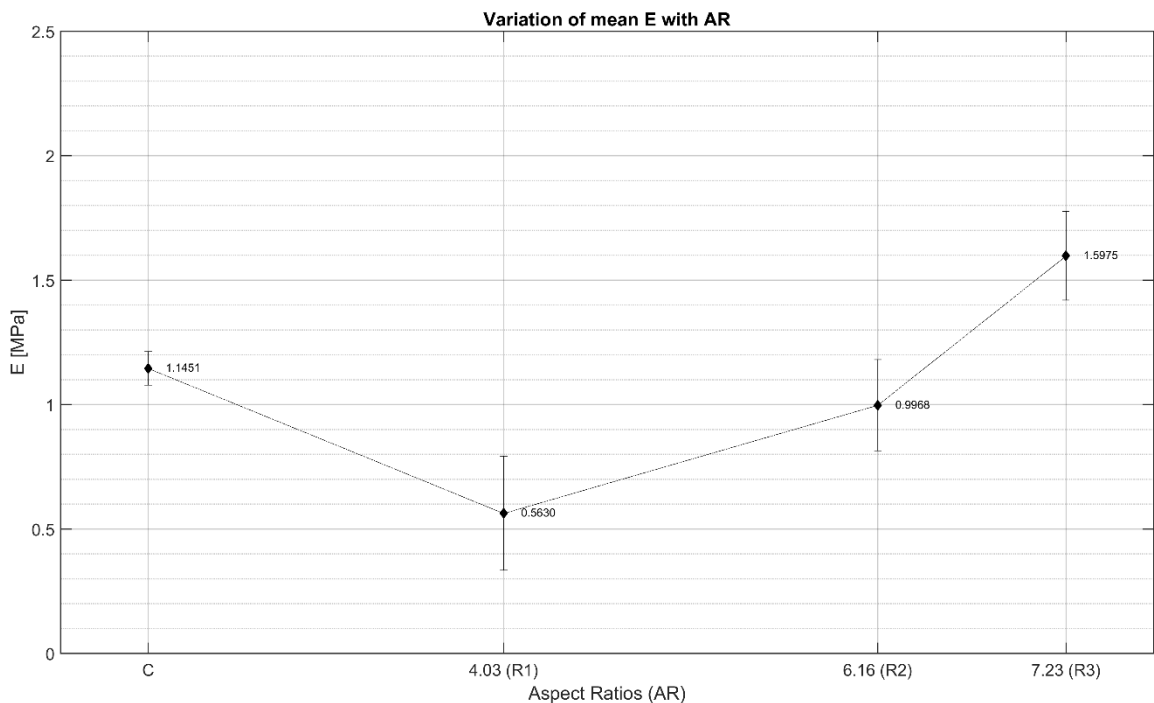


Figure 5-36 Variation of Young's modulus (E) of the material with circular and rectangular bulge windows.

5.10.4 Variation of Residual Stress (σ_0)

The value of residual stress (σ_0) does not vary significantly over cycles in a sample as shown in Figure 5-37, as the other material parameters discussed above.

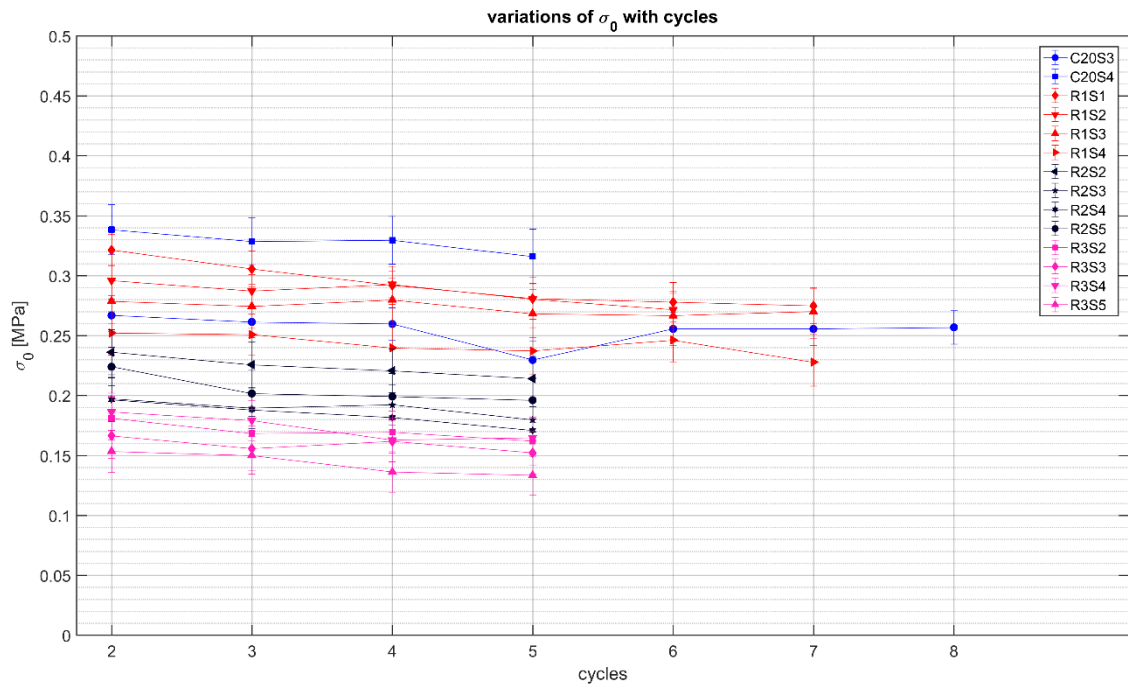


Figure 5-37 Variation of residual stress of the material with rectangular and circular bulge windows. First cycle of loading has not been shown as the material stabilizes during it. The error bars show a 95% confidence interval on the estimated values.

The sample-to-sample variations (Figure 5-38) can be attributed similarly to the same factors outlined in the discussion of plane-strain modulus (M_r) in section 5.10.1.

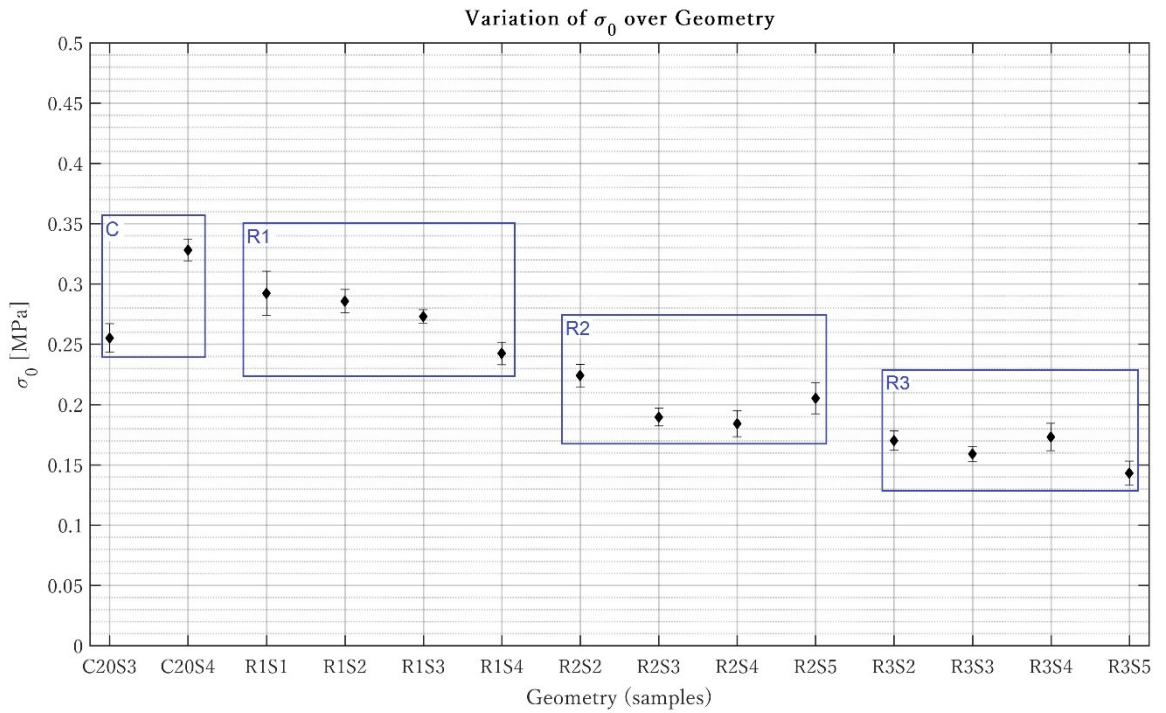


Figure 5-38 Variation of residual stress of the material with rectangular and circular bulge window geometries.

The biaxial and plane-strain values of σ_0 are $0.292 \pm 0.052 \text{ MPa}$ and $0.201 \pm 0.018 \text{ MPa}$ respectively.

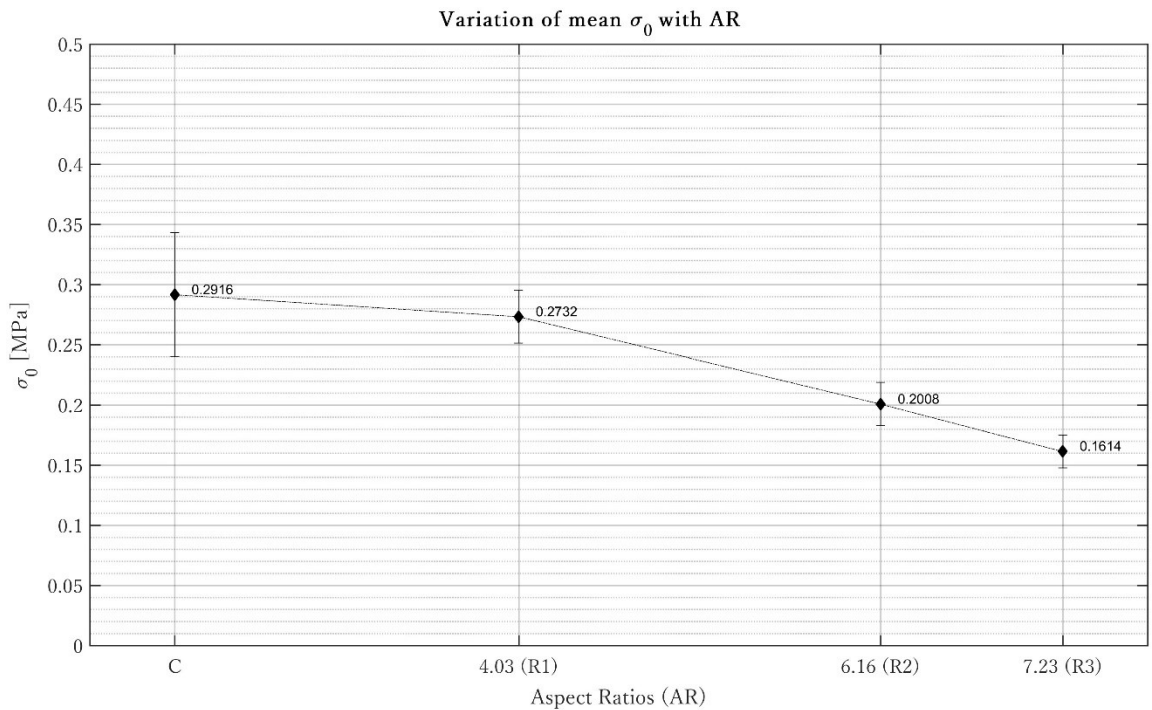


Figure 5-39 Variation of residual stress value for circular (C) and three aspect ratios of rectangular (R) bulge windows.

The value at 'C' represents biaxial value (from circular bulge) and as the aspect ratio increases the state of σ_0 moves towards a true plane-strain value.

However, the most significant trend in the values of σ_0 is observed over aspect ratio. As a state of plane-strain is achieved, the value of σ_0 calculated represents only a component of the actual biaxial value of σ_0 in a thin polymer sheet of constant area. This will be discussed in details in the discussion of the results section 5.13.

5.11 Measuring Isotropy of the Material with Tensile Test

The lengths of two orthogonal gauge lines (Figure 5-40), drawn on the sample in the DaVis software during processing of the tensile test data, as the tensile sample undergoes one-dimensional stretching, are exported from DaVis and are read in MatLab[®]. Material samples of latex are stretched and un-stretched several times before recording with the DIC system to accommodate the stabilization effects.

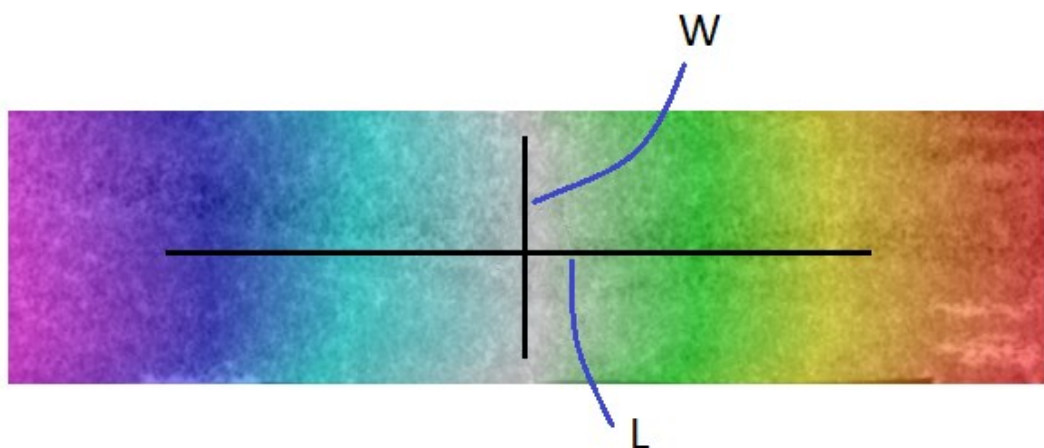


Figure 5-40 Gauge lines along length (L) and width (W) for used to calculate stretch ratios. These lines are not fiducial lines rather drawn during processing in DaVis.

Stretch ratios are calculated in longitudinal (L) and lateral (W) directions as follow:

$$\lambda_1 = \frac{L}{L_0}, \quad \lambda_2 = \frac{W}{W_0} \quad (47)$$

Where L_0 and W_0 are un-stretched lengths while L and W are stretched lengths in the two principal directions as shown on Figure 5-40. The stretching force is also recorded during the experiment. The tensile test data will be processed to yield poisson's ratio and young's modulus.

5.11.1 Poisson's ratio (ν) measured by Tensile Test

It is important to investigate the isotropy of the material. For this purpose, samples are cut from gloves at three different orientations. The three orientations used are 0° , 45° and 90° measured from axis of the glove along the fingers.

Poisson's ratio (ν) is defined as the negative of the ratio of lateral strain and longitudinal strain. When dealing with large strains, as in polymers, Hencky (or true) strain is preferably used (Starkova & Aniskevich, 2010). Therefore, the following relation gives the Poisson's ratio:

$$\nu = -\frac{\text{Ln}(\lambda_2)}{\text{Ln}(\lambda_1)} \quad (48)$$

Figure 5-41 shows the variation of the value of ν averaged from two samples for each of the orientations.

The mean value of PR is 0.385 ± 0.003 (Figure 5-41). The variation in the measured value of PR in three selected directions is minimal supporting the claim that the material is isotropic.

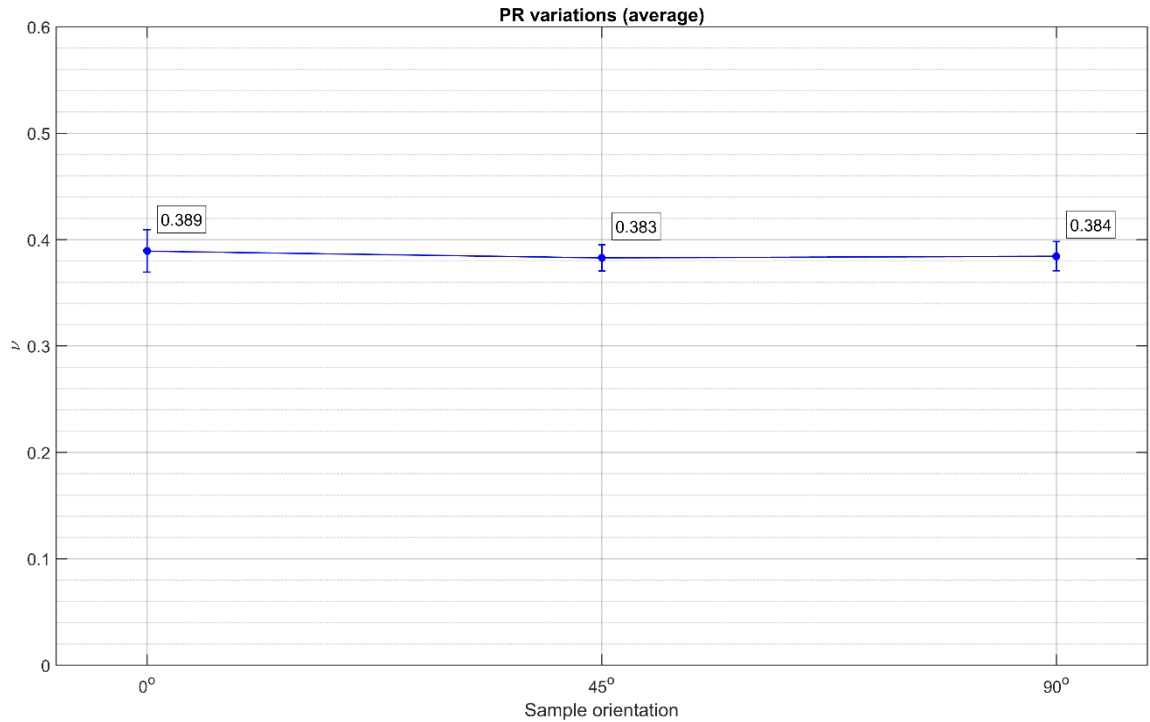


Figure 5-41 Values of ν measured at three angle orientations of samples. Samples from two gloves are cut at each orientation and the material is stretched many cycles before recording with the DIC.

5.11.2 Poisson's ratio (ν) Calculated from Characterized Parameters

The value of ν can also be calculated from the values of plane-strain modulus

($M_r = \frac{E}{1-\nu^2}$) and biaxial modulus ($M_c = \frac{E}{1-\nu}$) as follows:

$$\nu = \frac{M_c}{M_r} - 1 \quad (49)$$

The average value of biaxial modulus ($M_c = 1.863 \pm 0.11 \text{ MPa}$) is used to calculate the values of ν in Figure 5-42 and Figure 5-43. Note that the individual values of M_r presented in Figure 5-33 are used but not the average values of M_r shown in Figure 5-34 for the calculations of PR. Most spread is seen in the values of ν for R1, specially the value of R1S1, which is 226% higher than the average value of ν for other samples (S2, S3 and S4) of R1. In either case, all calculated values of ν in R1 are unrealistic. In the category of R2, the only value a bit off is R2S3.

The mean value of ν comes very close to 0.5 ($\nu = 0.49$) when the value of ν calculated from R2S3 is not considered. For R3, the PR is near zero and marginally negative which is likely unrealistic. The derived value of PR from R2 are most consistent with the value of PR typical of incompressible rubber ($\sim +0.5$).

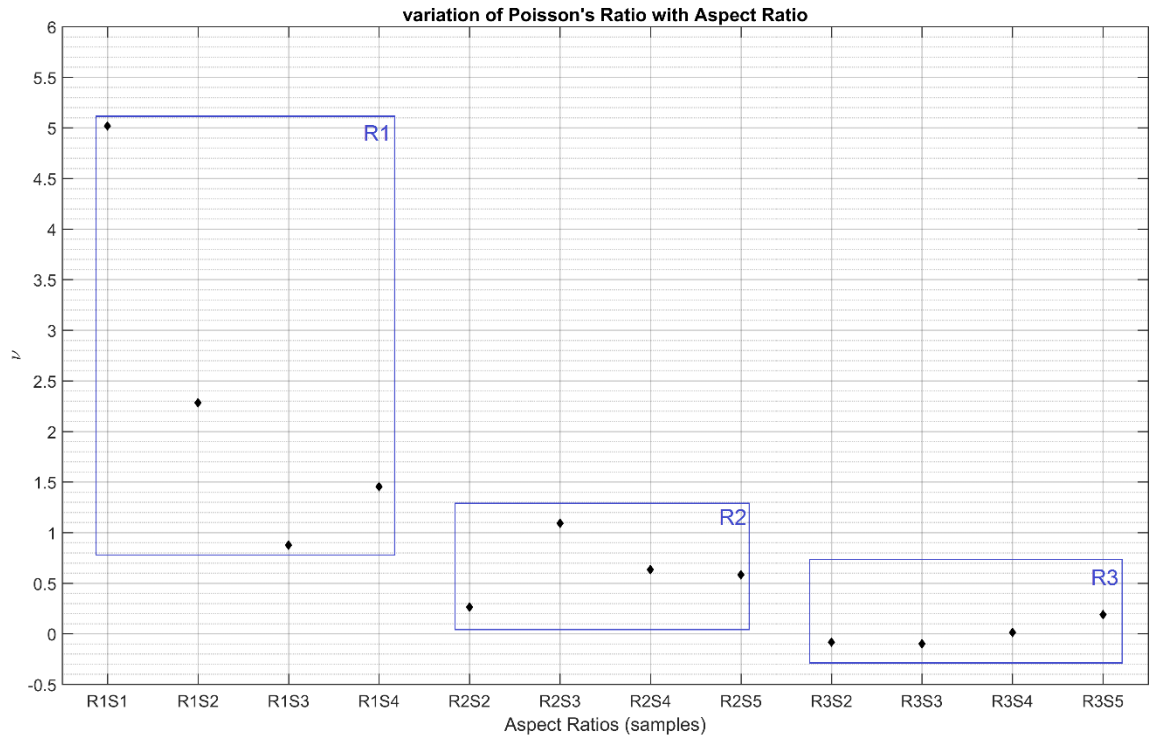


Figure 5-42 Variation of Poisson's ratio as calculated from plane-strain modulus and average biaxial modulus value plotted against samples of different geometry.

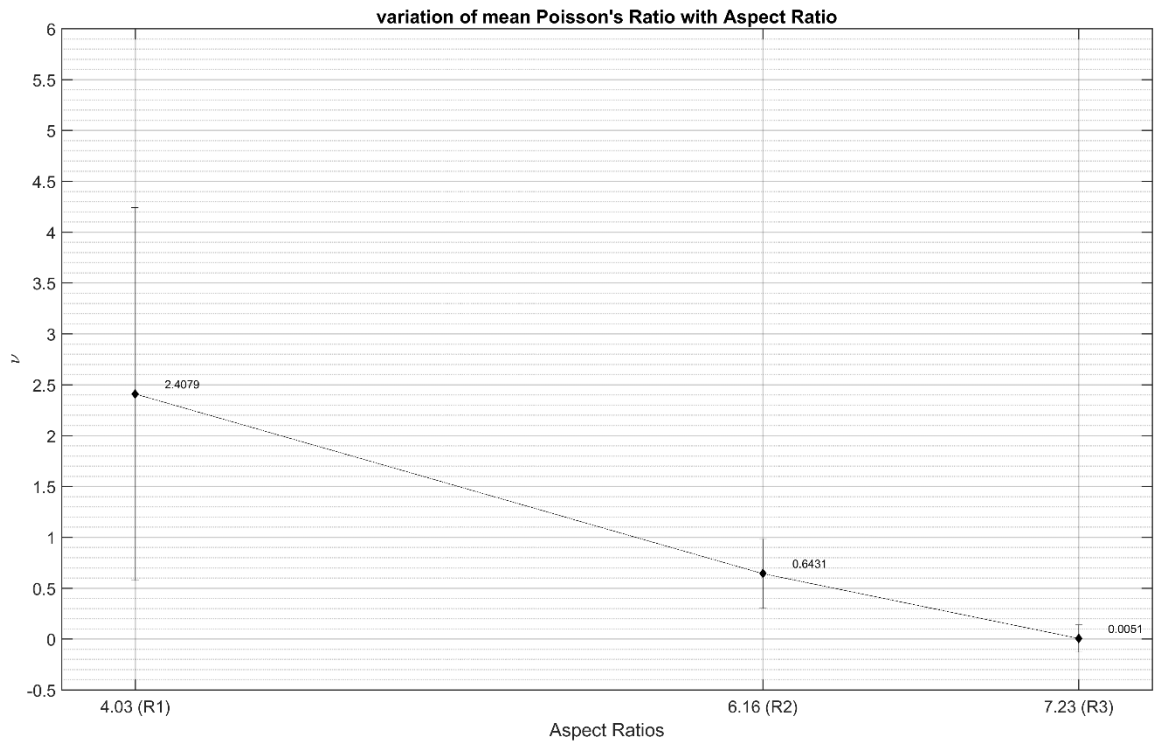


Figure 5-43 Variation of Poisson's ratio as calculated from plane-strain modulus and biaxial modulus. All samples of one aspect ratio are grouped together.

5.11.3 Young's Modulus (E) measured by Tensile Test

It is simple to extract Young's modulus (E) from a tensile test. It is the ratio of the tensile stress (σ) and the tensile engineering strain (e), $E = \frac{\sigma}{e}$. Figure 5-44 shows the variation in the value of Young's modulus measured from a tensile test from samples cut at three different orientations. It has been observed that the value of Young's modulus also varies slightly over the stretch ratio, λ_1 . Therefore, the values of Young's modulus have been averaged over the range of the stretch ratios. The mean value of E , hence calculated is $1.066 \pm 0.24 \text{ MPa}$.

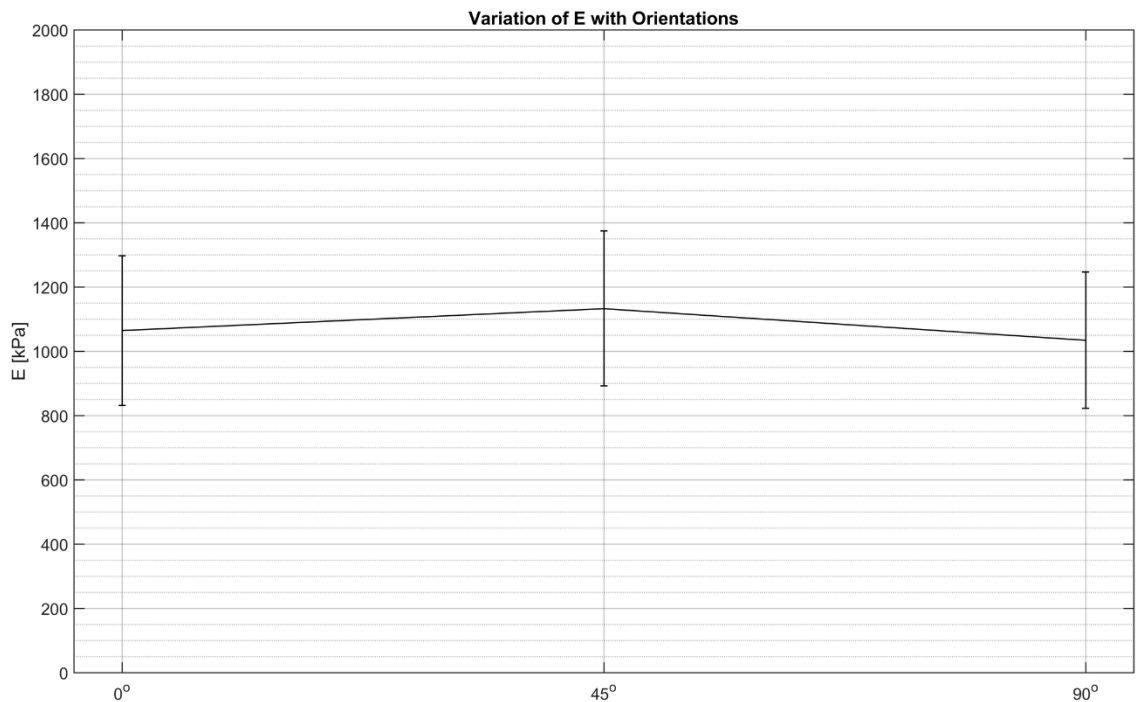


Figure 5-44 Variation of Young's modulus calculated from the tensile test at three different orientations.

5.12 Calibrating a Hyperelastic Material Model using a commercial FEA Software

ANSYS is one of the commercial FEA softwares available. It provides many hyperelastic material models for FEA simulations. These models can be easily calibrated using at least one or more of the uniaxial tensile test, pure shear test and equibiaxial test. Figure 5-45 shows stress-strain data of these three tests. The order in which the three types of loading curve are shown in the figure is consistent with the same curves reported in the literature (Steinmann et al., 2012).

The Figure 5-45 also shows the initial gradients of these stress-strain curves, which show initial values of Young's modulus (E), plane-strain modulus (M_r) and biaxial modulus (M_c) of their respective curves. It is clear from the figure that these three stress-strain curves are nonlinear. The least nonlinear (almost straight) being the tensile curve and the most nonlinear being the equibiaxial curve whereas the pure shear curve is in the middle. Therefore, it is not surprising to see that the initial value of Young's modulus (1.192 MPa) is very close to its value calculated from circular bulge test (1.145 MPa). The other parameters values (M_r and M_c) lie in the range between initial and final gradients of stress-strain curves (Table 5).

Table 5 Showing values of initial and final gradients of three stress-strain curves

Loading Type	Initial Value [MPa]	Final Value [MPa]
Tensile	1.192	0.509
Pure Shear	2.266	0.419
Equibiaxial	3.350	0.112

A circular bulge test creates a true state of equibiaxial stress at the centre of the bulged surface. Therefore, this stress-strain data can be used to fine-tune a hyperelastic model in ANSYS instead of a biaxial extension test.

A state of plane-strain is achieved in a bulge test with a long rectangular window along the width axis of the rectangle. The state of plane-strain resembles a pure shear test. Therefore, stress-strain data from plane-strain test can similarly be used to fine-tune a hyperelastic model in ANSYS instead of a shear test.

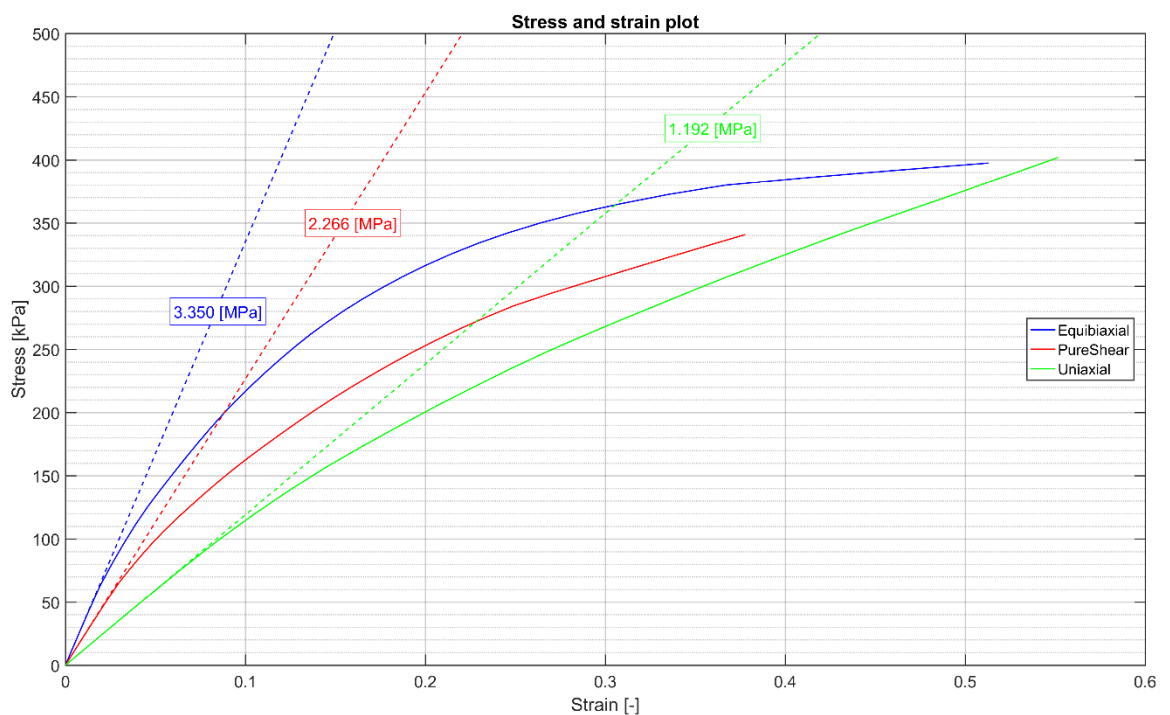


Figure 5-45 Engineering stress-strain data for uniaxial tensile test, equibiaxial test (circular bulge test) and pure shear test (plane-strain bulge test). Initial gradients of these curves are also shown.

Several ANSYS hyperelastic models have been fitted to the experimental data (Appendix B). The quality of a model is based upon the value of normalised error of fit (residual).

Table 6 showing thirteen ANSYS hyperelastic models calibrated using stress strain data from this study. These models have been ranked with respect to normalized error of fit (residual)

#	Model names	residual
1	MR9	0.36
2	MR5	0.70
3	Yeoh 3rd Order (Y3)	0.83
4	Yeoh 2nd Order (Y2)	1.16
5	MR3 Parameters	1.23
6	MR2 Parameters	2.30
7	Ogden 1st Order (O1)	2.31
8	Neo-Hookean (NH)	2.52
9	Yeoh 1st Order (Y1)	2.52
10	Arruda-Boyce (AB)	2.52
11	Ogden 2nd Order (O2)	77.20
12	Ogden 3rd Order (O3)	77.50
13	Gent (Ge)	79.38

Mooney-Rivlin models with nine and five parameters (MR9 and MR5) and the Yeoh 3rd order models have the first three lowest values (below one) of residual error of fit.

Figure 5-46 shows Mooney-Rivlin model with nine parameters (MR9). It is clear that it is only the biaxial stress strain data, which is responsible for most of the residual value otherwise MR9 predicts other types of stress strain data reasonably well.

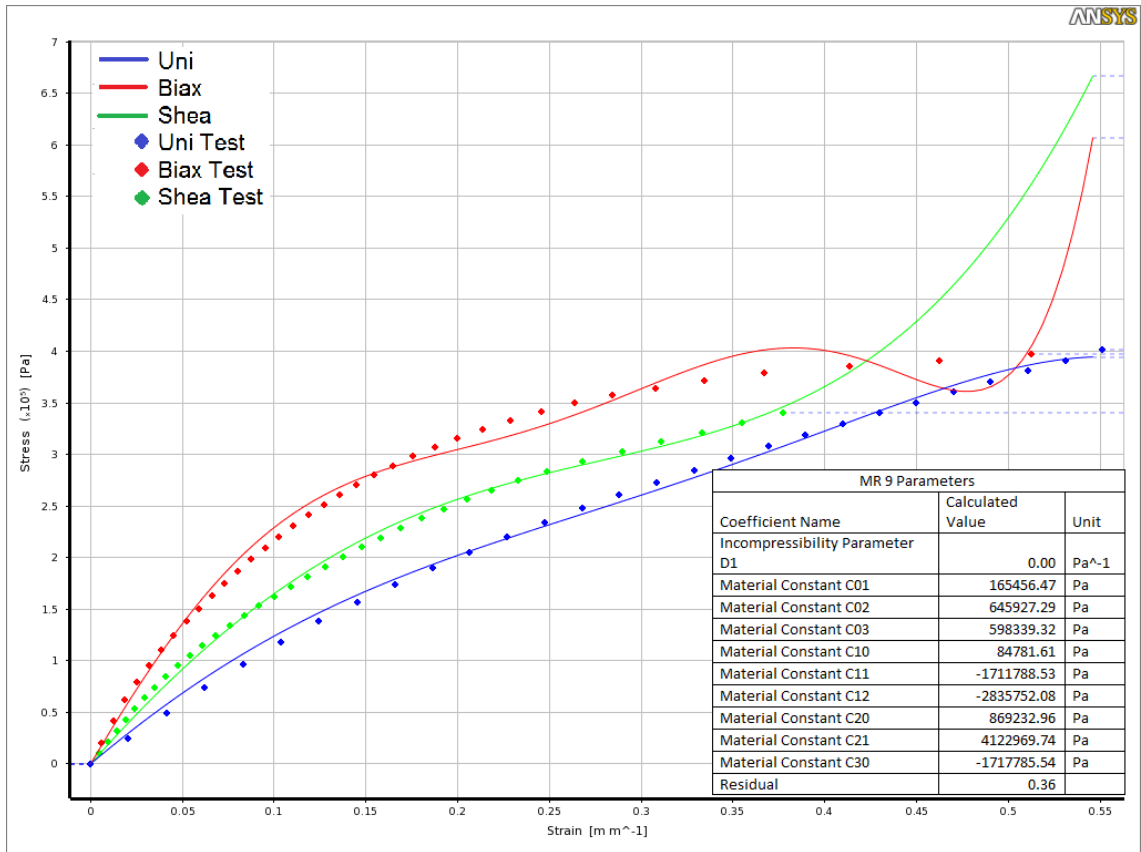


Figure 5-46 comparison of experimental and modelled stress data for Mooney-Rivlin 9 parameters (MR9) hyperelastic model. MR9 is able to predict all three types of deformations better than all others.

5.13 Discussion of Results

Natural rubber is a strategic and key material for many applications because of its unique ability of strain-induced crystallisation (Kohjiya et al., 2014). Stretching a sample of natural rubber at room temperature turns the amorphous rubber into a semi-crystalline material. These crystallites become highly oriented along the tensile direction and increase the tensile strength (Yeh & Hong, 1979).

It is important to re-examine of mechanical properties of thin latex sheets after decades of developments in processing techniques and improved combinations of secret ingredients to produce high quality products to get a competitive advantage. By precisely knowing the mechanical properties of the products, the manufacturers can better control the quality and performance of their products.

Measuring strain of hyperelastic material is specially challenging because these material are soft and a non-contact measurement method is more suitable for strain measurements. DIC is one of the non-contact strain measurement techniques. It not only measures maximum bulge height at a point but also the full deformed shape. Use of DIC is especially beneficial when used to measure strain in a tensile test because it can measure longitudinal and lateral strains easily. These strains are used to calculate poisson's ratio of the material.

5.13.1 DIC Subset size

The speckle pattern and the speckle size are crucial for the proper working of a DIC system. DIC algorithms will not converge if a speckle pattern is not unique and distinguishable. The same speckled surface can give different pixel sizes when calibrated based upon focused area of the surface, which in turn will affect

the subset size used in the displacement calculations settings. If a coarse subset size is used it tends to under estimate displacements due to averaging of displacement vectors but reduces computational efforts. On the other hand, if a finer subset size is used and the DIC algorithm converges, then the displacements calculated tends to be noisier and the DIC becomes computationally very expensive. A default subset size of 31×31 pixels, as recommended by LaVision works fine in most cases but a quick (if not a full) subset size convergence study around the default subset size should be performed to see if default size is appropriate.

5.13.2 Alternate Methods of Calculating some Material Parameters

The key material parameters calculated are plane-strain modulus M_r , biaxial modulus M_c , Young's Modulus, E and poisson's ratio ν . The two variants of bulge testing i.e. rectangular and circular, through curve fitting of their respective analytical models, have given M_r and M_c respectively. The tensile test, on the other hand, has allowed a direct measurement of E and PR, ν in the direction of the sample.

Using a combination of material characterization tests to measure a set of required mechanical properties are often employed. C. K. Huang (Huang et al., 2007) have measured Poisson's ratio and Young's modulus of Poly(methyl methacrylate)-based thermoplastic polymer thin film using bulge test with long rectangular and square bulge windows. Galliot (Galliot & Luchsinger, 2011) have used a combination of uniaxial tension, biaxial extension of cruciform samples and bubble inflation (bulge) test with circular bulge window to characterize ETFE (Ethylene Tetra Fluoro Ethylene (ETFE) foils and compared the results. Xu (D. Xu &

Liechti, 2010) have also measured Young's modulus and Poisson's ratio of Polyethylene terephthalate (PET) film using bulge test with circular and rectangular bulge windows.

The value of Young's modulus E has been derived from the values of M_r and M_c using ν from tensile test. The value of E from R1 and C (Figure 5-36) is lies in the range of $0.813 - 1.212 \text{ MPa}$ whereas the values from R1 and R3 are relatively outside of ballpark of values of E . The range of values of E calculated from the tensile test is $0.826 - 1.306 \text{ MPa}$. Similar values of Young's modulus of natural rubber and related materials using various filler materials and processing methods have been reported in the literature. A value of Young's modulus in the range $0.49 - 1.99 \text{ MPa}$ is reported by Kohjiya (Kohjiya et al., 2014).

The initial gradient from tensile stress strain data (Figure 5-45) also gives initial value of 1.192 MPa for E . This value is in good agreement with the values from bulge test generally and the circular and R2 specifically. R1 does not represent true state of plane-strain; therefore, its value is expected to reach a true plane-strain value when AR increases to R2 and R3. The value of E from R3 will be discussed in the next section.

The value of PR has been derived from the measured values of M_r and M_c . For R1 the values are grossly overestimated and on the opposite end the values of PR from R3 are near zero and marginally negative which are both likely unrealistic. The value of R2 appears to be most consistent with the values calculated from tensile test and typically considered for incompressible rubber ($\sim+0.5$).

5.13.3 Aspect Ratio of Rectangular Bulge Tests.

The aspect ratio of the rectangular bulge window in a bulge test plays a key role in the estimation of plane-strain modulus. The values of these bulge parameters are not independent of aspect ratio at four (R1) as reported by (Schweitzer & Göken, 2007). It has been noted in this study that values of these material parameters vary significantly when aspect ratio increases from four to six. An increasing trend in the values of plane-strain modulus and a decreasing trend in the values of residual stress have been observed.

The value of aspect ratio is increased by reducing the width of the rectangular bulge window and at the same time increasing its length, if possible. (Nominal sizes, R1: 8x32, R2: 6x36 and R3: 5x35). The analytical model equation

5.13.4 Poisson's Ratio and Isotropy of the Material

The values of ν estimated from bulge parameters (M_r and M_c) can be used to draw important conclusions about the material's bulge parameters themselves. The only sensible value of ν presented in Figure 5-43, is 0.643 ± 0.34 calculated from the value of M_r with aspect ratio of R2. The value of ν from R1 is too high and similarly that of R3 is too low and marginally negative as compared to the values of ν computed from tensile test data. The only reasonable explanation for this is that R1 does not represent a true state of plane-strain and at the aspect ratio of R3; the width of the rectangle is too small and possibly the bending stiffness has an effect in the bulging. The bulge analytical models are derived based upon the assumption of negligible bending stiffness. If bending stiffness plays a non-negligible role in the bulging then it will tend to make the material parameters over stiff like observed in the values of M_r (and hence E) from R3.

From the above discussion of ν , it can be concluded that the best value of plane-strain modulus is calculated from the rectangular bulge test with an aspect ratio of ~ 6 (R2).

If σ_b represents the biaxial value of σ_0 from a circular bulge and σ_p represents the plane-strain value of σ_0 , for an isotropic material, the two residual stresses are connected through the following relation:

$$\sigma_b = \sqrt{2}\sigma_p \quad (50)$$

Equation (50) is derived assuming two components of σ_b have the same magnitudes of σ_p and are directed orthogonally along the width and length axes of the rectangular bulge samples.

If the nominal value of σ_0 is taken 0.201 MPa (R2 from Figure 5-39) then the calculated value from equation (50) is $\sigma_p = 0.284$ MPa which is only 2.61% lower than the biaxial value (0.292) of σ_b from the bulge test (C from Figure 5-39).

The same treatment is also applied to the values of the biaxial and plane-strain moduli. If M_b stands for biaxial modulus and M_p for plane-strain modulus, then using the value of $M_p = 1.171$ MPa (R2 from Figure 5-34) gives the value of $M_b = 1.656$ MPa which is 11.14% lower than the biaxial value of M_b (1.863 ± 0.11 MPa) from the bulge test.

The errors outlined above can be improved by performing bulge test on larger dimensions of rectangular and circular bulge windows.

Therefore, equation (50) validates the previously made assumptions of the material being isotropic and that the stress field in a circular bulge sample is equibiaxial. This concept can also be used to study properties of anisotropic materials. For an anisotropic thin material of uniform thickness, the relation can be generalized be as follows:

$$X_b = \sqrt{X_1^2 + X_2^2} \quad (51)$$

where X_1 and X_2 are values of a material property along the two orthogonal directions (excluding the thickness axis) and X_b is the value measured under biaxial conditions.

5.13.5 Hyperelastic models

Hyperelastic models are selected based upon their ability to best-fit the material's mechanical response under various loading conditions i.e. Uniaxial, Planar, Biaxial tests. The common practice to curve-fit is to use built-in curve-fit tools in commercial finite element analysis code (Ansys®, Abaqus®, Comsol®, etc.). Shahzad (Shahzad et al., 2015) have tested an indigenously developed rubber and curve-fit the test data using Abaqus® and ranked various hyperelastic material models as shown in Table 7. They did not use higher order Mooney-Rivlin models (MR5 and MR9) but none the less, Y3 was the best model to simulate the rubber material.

Table 7 Hyperelastic material models with their respective goodness of fit identified in Abaqus®.

Models	R ²
Y3	0.9962
AB	0.9902
O3	0.9896
MR2	0.9881
NH	0.9710

In a similar study by Sasso et al. (Sasso, Palmieri, Chiappini, & Amodio, 2008) have characterized a type rubber using uniaxial tension and biaxial tension (a bulge test) and done an FEA simulation (using Abaqus®) and identified the most appropriate hyperelastic material models. They concluded that MR5 (second order MR model) and Ogden (O3) hyperelastic models are most accurate with least RMS values.

5.14 Uncertainties in experimental data from a bulge test

Experiments of bulging include several uncertainties. Some are due to the sensors precision like the measurements of the internal bulge pressure. This uncertainty has been overcome by selecting a precise pressure sensor. The pressure sensor used (ifm PN3097) has an accuracy of 0.5 kPa, as discussed in section 3.1.4.

There may be other uncertainties due to the experimental devices such as dimensional inaccuracies of the bulge geometries (rectangular and circular) being tested. Again, this uncertainty has been overcome by careful machining and measurements of the bulge geometries. The main uncertainties in a bulge test generally come from the measurements of the bulge heights when using digital image correlation, DIC.

This study has used a commercially available DIC system from LaVision that has been developed with an experience of over two decades. The accuracy of measurement using this system depends upon the following parameters:

1. Calibration of the system
2. Correlation control parameters

The user manual for this system provides guidance for using the calibration plates and the calibration process as described in section 4.5. Therefore, reasonably good calibration results were achieved following the calibration guidelines. The maximum RMS of fit achieved during calibration is two pixels and a typical scale of 62.1929 pixels/mm (Figure 4-7). Using these two values, we get a maximum error of 32 μm in bulge height calculations.

The other important parameters, which affect the accuracy of the DIC system, are settings controlling the displacement calculations as described in section 4.7. A convergence study on effect of subset size variations (section 5.2) has been used to select an optimal subset size to minimize the uncertainties in DIC calculations.

6. Conclusions

A brief chapter detailing conclusions and key contributions to the knowledge. It also contains a brief discussion about the future work.

6.1 Conclusions and key Contributions to the Knowledge

1. A new methodology to characterize a hyperelastic material using bulge and tensile testing have been developed and demonstrated to work. A tensile test is a simple test and less prone to measurement errors and does not involve many assumptions as compared to a bulge test. Therefore, underlying assumptions of a bulge test has been examined employing a tensile test.
2. Material samples from gloves have been characterized with biaxial modulus of $1.863 \pm 0.11 \text{ MPa}$, plane-strain modulus of $1.171 \pm 0.24 \text{ MPa}$ and biaxial residual stress of $0.292 \pm 0.052 \text{ MPa}$. The material response has been proved nearly incompressible and isotropic with poisson's ratio 0.385 ± 0.003 .
3. A simple relation has been proposed and shown to work reasonably well; connecting a biaxial material parameter measured from two orthogonally cut material samples. This interesting and simple relation can be used to study anisotropy.
4. Stress-stain data from uniaxial tension test and bulge tests have been used to calibrate ANSYS hyperelastic material models. This calibration shows that relatively simple hyperelastic material models with three or fewer parameters are generally not able to fit satisfactorily to the calibration data.

6.2 Future Work

The same material should be studied using a similar methodology but using much larger dimensions of samples to look into the effect of aspect ratio in more details. The tensile tests should be carried out on larger samples and stretched upto their breaking point to observe the variations in martial parameters in more details.

The method developed to measure properties of anisotropic materials biaxial modulus and residual stress is based upon stress-strain data for a plane-strain condition and from an equibiaxial data. This method requires further evaluation for other materials, specifically anisotropic materials.

References

- ANSYS. (2013). ANSYS Mechanical APDL Material Reference. Retrieved from [http://148.204.81.206/Ansys/150/APDL Material Reference.pdf](http://148.204.81.206/Ansys/150/APDL%20Material%20Reference.pdf)
- Arruda, E. M., & Boyce, M. C. (1993a). A three-dimensional constitutive model for the large stretch behavior of rubber elastic materials. *Journal of the Mechanics and Physics of Solids*, 41(2), 389–412. [https://doi.org/10.1016/0022-5096\(93\)90013-6](https://doi.org/10.1016/0022-5096(93)90013-6)
- Arruda, E. M., & Boyce, M. C. (1993b). Evolution of plastic anisotropy in amorphous polymers during finite straining. *International Journal of Plasticity*, 9(6), 697–720. [https://doi.org/http://dx.doi.org/10.1016/0749-6419\(93\)90034-N](https://doi.org/http://dx.doi.org/10.1016/0749-6419(93)90034-N)
- Arzt, E. (1998). Size Effects in Materials Due To Microstructural and Dimensional Constraints : a Comparative Review. *Acta Materialia*, 46(16), 5611–5662. [https://doi.org/10.1016/S0957-5820\(99\)70836-0](https://doi.org/10.1016/S0957-5820(99)70836-0)
- Beams, J. W. Mechanical properties of thin films of gold and silver (1959). New York: Wiley. Retrieved from <http://catalog.hathitrust.org/Record/001479700>
- Boyce, M. C., & Arruda, E. M. (2000). Constitutive Models of Rubber Elasticity: A Review. *Rubber Chemistry and Technology*, 73, 504–523. <https://doi.org/10.5254/1.3547602>
- C. Miehe, S. Göktepe, F. L. (2004). A micro-macro approach to rubber-like materials?Part I: the non-affine micro-sphere model of rubber elasticity. *Journal of the Mechanics and Physics of Solids*, 52(11), 2617–2660. <https://doi.org/10.1016/j.jmps.2004.03.011>
- Çakmak, U. D., Kallai, I., & Major, Z. (2014). Temperature dependent bulge test for elastomers. *Mechanics Research Communications*, 60, 27–32. <https://doi.org/10.1016/j.mechrescom.2014.05.006>
- Chagnon, G., Marckmann, G., & Verron, E. (2004). A comparison of the hart-smith model with arruda-boyce and gent formulations for rubber elasticity. *Rubber Chemistry and Technology*, 77(4), 724–735. <https://doi.org/10.5254/1.3547847>
- Channel, S. (2013). *How it is made - Rubber Gloves*. USA. Retrieved from https://www.imdb.com/title/tt2822418/?ref_=ttep_ep1
- Chu, T. C., Ranson, W. F., & Sutton, M. A. (1985). Applications of digital-image-correlation techniques to experimental mechanics. *Experimental Mechanics*, 25(3), 232–244. <https://doi.org/10.1007/BF02325092>
- Daly, S., Prendergast, P., Dolan, F., & Lee, T. (2000). Use of finite element analysis to simulate the hyperelastic behaviour of cardiovascular tissue. *12th Conference of the ...*, (Fig 1), 2000. Retrieved from <http://ansys.net/ansys/papers/cardiovascular.pdf>
- Galliot, C., & Luchsinger, R. H. (2011). Uniaxial and biaxial mechanical properties of ETFE foils. *Polymer Testing*, 30(4), 356–365. <https://doi.org/10.1016/j.polymertesting.2011.02.004>
- Gent, A. N. (1996). A New Constitutive Relation for Rubber. *Rubber Chemistry and Technology*, 69(1), 59–61. <https://doi.org/10.5254/1.3538357>

- Göktepe, S., & Miehe, C. (2005). A micro-macro approach to rubber-like materials. Part III: The micro-sphere model of anisotropic Mullins-type damage. *Journal of the Mechanics and Physics of Solids*, *53*(10), 2259–2283. <https://doi.org/10.1016/j.jmps.2005.04.010>
- Gong, X. Y., & Riyad, M. O. E. (2002). *On stress analysis for a hyperelastic material*. Retrieved from <http://ansys.net/ansys/papers/Hyper.pdf>
- Goodyear, C. (1839). Gum-Elastic and Its Varieties, with a Detailed Account of Its Application and Uses and of the Discovery of Vulcanization.
- Heinrich, G., & Kaliske, M. (1997). Theoretical and numerical formulation of a molecular based constitutive tube-model of rubber elasticity. *Computational and Theoretical Polymer Science*, *7*(3–4), 227–241. [https://doi.org/10.1016/S1089-3156\(98\)00010-5](https://doi.org/10.1016/S1089-3156(98)00010-5)
- Holzapfel, G. A. (2000). *Nonlinear Solid Mechanics: A Continuum Approach for Engineering*. Wiley. Retrieved from https://books.google.co.uk/books?id=_ZkeAQAIAAJ
- Huang, C. K., Lou, W. M., Tsai, C. J., Wu, T. C., & Lin, H. Y. (2007). Mechanical properties of polymer thin film measured by the bulge test. *Thin Solid Films*, *515*(18), 7222–7226. <https://doi.org/10.1016/j.tsf.2007.01.058>
- Huston, D. R., Sauter, W., Bunt, P. S., & Esser, B. (2001). Bulge testing of single and dual layer thin films. *Proceedings of SPIE - The International Society for Optical Engineering*, *4344*, 673–681. Retrieved from <http://www.scopus.com/inward/record.url?eid=2-s2.0-0034761523&partnerID=40&md5=c10a50af7c59d8ac204bc5d4ee73c014>
- Johlitz, M., & Diebels, S. (2011). Characterisation of a polymer using biaxial tension tests. Part I: Hyperelasticity. *Archive of Applied Mechanics*, *81*(10), 1333–1349. <https://doi.org/10.1007/s00419-010-0480-1>
- Kaliske, M., & Heinrich, G. (1999). An Extended Tube-Model for Rubber Elasticity: Statistical-Mechanical Theory and Finite Element Implementation. *Rubber Chemistry and Technology*, *72*(4), 602–632. <https://doi.org/10.5254/1.3538822>
- Kalkman, a. J., Verbruggen, a. H., Janssen, G. C. a. M., & Groen, F. H. (1999). A novel bulge-testing setup for rectangular free-standing thin films. *Review of Scientific Instruments*, *70*(10), 4026. <https://doi.org/10.1063/1.1150029>
- Kim, B., Lee, S. B., Lee, J., Cho, S., Park, H., Yeom, S., & Park, S. H. (2012). A comparison among Neo-Hookean model, Mooney-Rivlin model, and Ogden model for chloroprene rubber. *International Journal of Precision Engineering and Manufacturing*, *13*(5), 759–764. <https://doi.org/10.1007/s12541-012-0099-y>
- Kohjiya, S., Palosuo, T., Ikeda, Y., Isayev, A. I., Fukahori, Y., Hashim, A. S., ... Palosuo, T. (2014). *Chemistry, Manufacture and Applications of Natural Rubber*. (S. Kohjiya & Y. Ikeda, Eds.), *Chemistry, Manufacture and Applications of Natural Rubber*. Woodhead Publishing. <https://doi.org/http://dx.doi.org/10.1533/9780857096913.1.68>

- Machado, G., Favier, D., & Chagnon, G. (2012). Membrane Curvatures and Stress-strain Full Fields of Axisymmetric Bulge Tests from 3D-DIC Measurements. Theory and Validation on Virtual and Experimental results. *Experimental Mechanics*, *52*, 865–880. <https://doi.org/10.1007/s11340-011-9571-3>
- Maier-Schneider, D., Maibach, J., & Obermeier, E. (1995). A New Analytical Solution for the Load-Deflection of Square Membranes. *Journal of Microelectromechanical Systems*, *4*(4), 238–241. <https://doi.org/10.1109/84.475551>
- Marckmann, G., & Verron, E. (1999). Comparison of Hyperelastic Models for Rubber-Like Materials. *Rubber Chemistry and Technology*, *79*(5), 835–858. <https://doi.org/10.5254/1.3547969>
- MathWorks. (2016). MATLAB Release 2016b, The MathWorks, Inc., Natick, Massachusetts, United States. Retrieved from https://www.mathworks.com/help/curvefit/smooth.html?s_tid=srchtitle
- Meng, L. pu, Lin, Y. fei, Xu, J. li, Chen, X. wei, Li, X. yu, Zhang, Q. lei, ... Li, L. bin. (2015). A Universal equipment for biaxial stretching of polymer films. *Chinese Journal of Polymer Science (English Edition)*, *33*(5), 754–762. <https://doi.org/10.1007/s10118-015-1623-1>
- Mohammed, M. A. P. (2014). Visco-hyperelastic model for soft rubber-like materials. *Sains Malaysiana*, *43*(3), 451–457.
- Mooney, M. (1940). A theory of large elastic deformation. *Journal of Applied Physics*, *11*(9), 582–592. <https://doi.org/10.1063/1.1712836>
- Motra, H. B., Hildebrand, J., & Dimmig-Osburg, A. (2014). Assessment of strain measurement techniques to characterise mechanical properties of structural steel. *Engineering Science and Technology, an International Journal*, *17*(4), 260–269. <https://doi.org/10.1016/j.jestch.2014.07.006>
- Neggers, J., Hoefnagels, J., Hild, F., Roux, S., & Geers, M. (2013). Global digital image correlation for pressure deflected membranes. *Conference Proceedings of the Society for Experimental Mechanics Series*, *6*, 135–140. https://doi.org/10.1007/978-1-4614-4436-7_20
- Neggers, J., Hoefnagels, J. P. M., Hild, F., Roux, S., & Geers, M. G. D. (2014). Direct Stress-Strain Measurements from Bulged Membranes Using Topography Image Correlation. *Experimental Mechanics*, *54*(JUNE), 717–727. <https://doi.org/10.1007/s11340-013-9832-4>
- Ogden, R. W. (1972). Large Deformation Isotropic Elasticity - On the Correlation of Theory and Experiment for Incompressible Rubberlike Solids. *Proceedings of the Royal Society of London. Series A, Mathematical and Physical Sciences*, *326*(1567), 565–584. Retrieved from <http://www.jstor.org/stable/77930>
- Oliver, W. C., & Pharr, G. M. (1992). An improved technique for determining hardness and elastic modulus using load and displacement sensing indentation experiments. *Journal of Materials Research*, *7*(6), 1564–1583. <https://doi.org/10.1557/JMR.1992.1564>

- Orthner, M. P., Rieth, L. W., & Solzbacher, F. (2010). High speed wafer scale bulge testing for the determination of thin film mechanical properties. *Review of Scientific Instruments*, *81*(5), 055111. <https://doi.org/10.1063/1.3427493>
- Pan, J. Y., Lin, P., Maseeh, F., & Senturia, S. D. (1990). Verification of FEM analysis of load-deflection methods for measuring mechanical properties of thin films. In *Solid-State Sensor and Actuator Workshop, 1990. 4th Technical Digest., IEEE* (pp. 70–73). <https://doi.org/10.1109/SOLSEN.1990.109823>
- Poilane, C., Delobelle, P., LExcellent, C., Hayashi, S., & Tobushi, H. (2000). Analysis of the mechanical behavior of shape memory polymer membranes by nanoindentation, bulging and point membrane deflection tests. *Thin Solid Films*, *379*(1–2), 156–165. [https://doi.org/10.1016/S0040-6090\(00\)01401-2](https://doi.org/10.1016/S0040-6090(00)01401-2)
- Pratt, R. I., & Johnson, G. C. (1993). Mechanical Characterization of Thin Films Using Full-Field Measurement of Diaphragm Deflection. In *Symposium M1 – Thin Films: Stresses and Mechanical Properties IV* (Vol. 308, pp. 115–120). <https://doi.org/10.1557/PROC-308-115>
- Reuge, N., Schmidt, F., Maoult, Y. Le, M. Rachik, & Abbe, F. (2001). Elastomer Biaxial Characterization Using Bubble Inflation Technique. I: Experimental Investigations. *Polymer Engineering and Science*, *41*(3), 522–531.
- Rivlin, R. S. (1948). Large Elastic Deformations of Isotropic Materials. I. Fundamental Concepts. *Philosophical Transactions of the Royal Society of London A: Mathematical, Physical and Engineering Sciences*, *240*(822), 459–490. Retrieved from <http://rsta.royalsocietypublishing.org/content/240/822/459.abstract>
- Rivlin, R. S., & Saunders, D. W. (1951). Large Elastic Deformations of Isotropic Materials. VII. Experiments on the Deformation of Rubber. *Philosophical Transactions of the Royal Society of London A: Mathematical, Physical and Engineering Sciences*, *243*(865), 251–288. <https://doi.org/10.1098/rsta.1951.0004>
- Sasso, M., Palmieri, G., Chiappini, G., & Amodio, D. (2008). Characterization of hyperelastic rubber-like materials by biaxial and uniaxial stretching tests based on optical methods. *Polymer Testing*, *27*(8), 995–1004. <https://doi.org/10.1016/j.polymertesting.2008.09.001>
- Schweitzer, E. W., & Göken, M. (2007). In situ bulge testing in an atomic force microscope: Microdeformation experiments of thin film membranes. *Journal of Materials Research*, *22*(10), 2902–2911. <https://doi.org/10.1557/JMR.2007.0373>
- Selvadurai, a. P. S. (2006). Deflections of a rubber membrane. *Journal of the Mechanics and Physics of Solids*, *54*(6), 1093–1119. <https://doi.org/10.1016/j.jmps.2006.01.001>
- Shahzad, M., Kamran, A., Siddiqui, M. Z., Farhan, M., Materials, A., & Highway, I. (2015). Mechanical Characterization and FE Modelling of a Hyperelastic Material, *18*(5), 918–924.
- Starkova, O., & Aniskevich, A. (2010). Poisson's ratio and the incompressibility relation for various strain measures with the example of a silica-filled SBR rubber in uniaxial tension tests. *Polymer Testing*, *29*(3), 310–318. <https://doi.org/10.1016/j.polymertesting.2009.12.005>

- Steinmann, P., Hossain, M., & Possart, G. (2012). Hyperelastic models for rubber-like materials: Consistent tangent operators and suitability for Treloar's data. *Archive of Applied Mechanics*, *82*(9), 1183–1217. <https://doi.org/10.1007/s00419-012-0610-z>
- Treloar, L. R. G. (1944). Stress-strain data for vulcanised rubber under various types of deformation. *Trans. Faraday Soc.*, *40*(0), 59–70. <https://doi.org/10.1039/TF9444000059>
- Treloar, L. R. G. (1975). *The Physics of Rubber Elasticity* (3rd ed.). Oxford University Press. Retrieved from <https://global.oup.com/academic/product/the-physics-of-rubber-elasticity-9780198570271?cc=gb&lang=en&#>
- Treloar, L. R. G. (1978). Dilation of rubber on extension. *Polymer*, *19*(12), 1414–1420. [https://doi.org/10.1016/0032-3861\(78\)90093-9](https://doi.org/10.1016/0032-3861(78)90093-9)
- Tsakalagos, T. (1981). The bulge test: A comparison of the theory and experiment for isotropic and anisotropic films. *Thin Solid Films*, *75*(3), 293–305. [https://doi.org/10.1016/0040-6090\(81\)90407-7](https://doi.org/10.1016/0040-6090(81)90407-7)
- Verron, E., & Marckmann, G. (2003a). Inflation of elastomeric circular membranes using network constitutive equations. *International Journal of Non-Linear Mechanics*, *38*, 1221–1235.
- Verron, E., & Marckmann, G. (2003b). Numerical analysis of rubber balloons. *Thin-Walled Structures*, *41*(8), 731–746. [https://doi.org/10.1016/S0263-8231\(03\)00023-5](https://doi.org/10.1016/S0263-8231(03)00023-5)
- Vlassak, J. J., & Nix, W. D. (1992). A new bulge test technique for the determination of Young's modulus and Poisson's ratio of thin films. *Journal of Materials Research*, *7*(12), 3242–3249. <https://doi.org/10.1557/JMR.1992.3242>
- Wadham-Gagnon, M., Hubert, P., Semler, C., Paidoussis, M. P., Vezina, M., & Lavoie, D. (2006). Hyperelastic modeling of rubber in commercial finite element software (ANSYS™). Retrieved from https://people.mcgill.ca/files/pascal.hubert/2006_SAMPE_51_Wadham-Gagnon.pdf
- Wan, K. T., Guo, S., & Dillard, D. A. (2003). A theoretical and numerical study of a thin clamped circular film under an external load in the presence of a tensile residual stress. *Thin Solid Films*, *425*(1–2), 150–162. [https://doi.org/10.1016/S0040-6090\(02\)01103-3](https://doi.org/10.1016/S0040-6090(02)01103-3)
- Wang, M. C., & Guth, E. (1952). Statistical Theory of Networks of Non-Gaussian Flexible Chains. *The Journal of Chemical Physics*, *20*(7), 1144–1157. <https://doi.org/10.1063/1.1700682>
- Ward, I. M., & Sweeney, J. (2012). The Behaviour in the Rubber-Like State: Finite Strain Elasticity. In *Mechanical Properties of Solid Polymers* (pp. 31–59). John Wiley & Sons, Ltd. <https://doi.org/10.1002/9781119967125.ch3>
- Williams, J. G. (1997). Energy Release Rates for the Peeling of Flexible Membranes and the Analysis of Blister Tests. *International Journal of Fracture*, *87*(1), 265–288. <https://doi.org/10.1023/A:1007314720152>

- Wu, C., Fang, W., & Yip, M. (2004). Measurement of Mechanical Properties of Thin Films Using Bulge Test. *Microelectronics Design Technology and Packaging Iii*. Retrieved from <http://sem-proceedings.com/04s/sem.org-SEM-X-Int-Cong-s022p05-Measurement-Mechanical-Properties-Thin-Films-Using-Bulge-Test.pdf>
- Xiang, Y., & Chen, X. (2005). Plane-strain bulge test for thin films. *Journal of Materials Research*, *20*(09), 2360–2370. <https://doi.org/10.1557/JMR.2005.0313>
- Xu, D., & Liechti, K. M. (2010). Bulge Testing Transparent Thin Films with Moire Deflectometry. *Experimental Mechanics*, *50*(2), 217–225. <https://doi.org/10.1007/s11340-009-9291-0>
- Xu, Y. H., Tsai, Y., Zheng, D. W., Tu, K. N., Wo Ong, C., Choy, C. L., ... Brongo, M. (2000). Measurement of mechanical properties for dense and porous polymer films having a low dielectric constant. *Journal of Applied Physics*, *88*(10), 5744–5750. <https://doi.org/10.1063/1.1287756>
- Yang, L., Long, S., Ma, Z., & Wang, Z. (2014). Accuracy analysis of plane-strain bulge test for determining mechanical properties of thin films. *Transactions of Nonferrous Metals Society of China*, *24*(10), 3265–3273. [https://doi.org/10.1016/S1003-6326\(14\)63466-X](https://doi.org/10.1016/S1003-6326(14)63466-X)
- Yeh, G. S. ., & Hong, K. Z. (1979). Strain-Induced Crystallization, Part 111: Theory. *Polymer Engineering and Science*, *19*(6), 395–400.
- Yeoh, O. H. (1990). Characterization of Elastic Properties of Carbon-Black-Filled Rubber Vulcanizates. *Rubber Chemistry and Technology*, *63*(5), 792–805. <https://doi.org/10.5254/1.3538289>
- Yeoh, O. H. (1993). Some Forms of the Strain Energy Function for Rubber. *Rubber Chemistry and Technology*, *66*(5), 754–771. <https://doi.org/10.5254/1.3538343>
- Youssef, H., Ferrand, a., Calmon, P., Pons, P., & Plana, R. (2010). Methods to improve reliability of bulge test technique to extract mechanical properties of thin films. *Microelectronics Reliability*, *50*(9–11), 1888–1893. <https://doi.org/10.1016/j.microrel.2010.07.013>
- Zheng, D. W., Xu, Y. H., Tsai, Y. P., Tu, K. N., Patterson, P., Zhao, B., ... Brongo, M. (2000). Mechanical property measurement of thin polymeric-low dielectric-constant films using bulge testing method. *Applied Physics Letters*, *76*(15), 2008. <https://doi.org/10.1063/1.126237>

Appendix A. Geometrical Considerations of Cylindrical Bulge Shape

Consider a cylindrical bulge-profile symmetrical about y-axis plane in Figure A1
 'a' is the radius of circular bulge die (window).

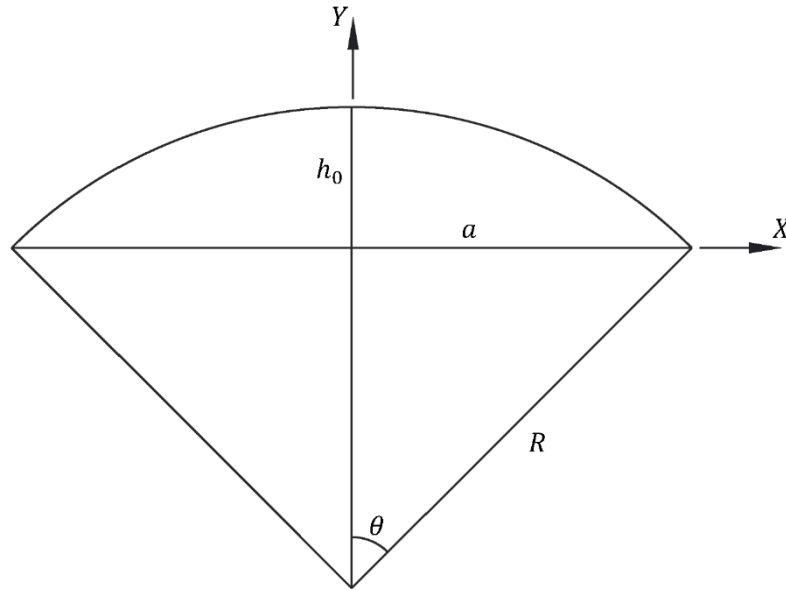


Figure A1 Circular bulge-profile for derivation of geometric strain e .

Considering Hoop stress in the cylindrical bulge shape, gives.

$$s_x = \frac{pR}{t} \quad (A1)$$

Consider a right-angle triangle in Figure A1,

$$R^2 = (R - h_0)^2 + a^2 \quad (A2)$$

$$\Rightarrow R = \frac{h_0^2 + a^2}{2h_0} \quad (A3)$$

From Eq. (A3) put in (A1), we have

$$s_x = \frac{p(a^2 + h_0^2)}{2h_0t} \quad (\text{A4})$$

An expression for strain can be derived based upon pure geometric considerations: ratio of stretched arc length ($R\theta$) and half-width of rectangle (a):

$$e = \frac{R\theta - a}{a} = \frac{R\theta}{a} - 1 \quad (\text{A5})$$

From Figure A1, $\sin \theta = \frac{a}{R} \Rightarrow \theta = \arcsin\left(\frac{a}{R}\right)$ and putting value of R from equation (A3).

$$e = \frac{R}{a} \arcsin\left(\frac{a}{R}\right) - 1 = \frac{h_0^2 + a^2}{2ah_0} \arcsin\left(\frac{2ah_0}{h_0^2 + a^2}\right) - 1 \quad (\text{A6})$$

From Figure A1, $\sin \theta = \frac{a}{R}$ and using Taylor series,

$$\Rightarrow \theta = \arcsin\left(\frac{a}{R}\right) = \left(\frac{a}{R}\right) + \frac{1}{6}\left(\frac{a}{R}\right)^3 + \frac{3}{40}\left(\frac{a}{R}\right)^5 + \dots \quad (\text{A7})$$

Ignoring higher power terms of $\left(\frac{a}{R}\right)$

$$\Rightarrow e = \frac{a^2}{6R^2} \quad (\text{A8})$$

Putting value of R ,

$$e = \frac{2a^2h_0^2}{3(a^2 + h_0^2)^2} \quad (\text{A9})$$

Now if $h_0 \ll a$ which makes $a^2 + h_0^2 \cong a^2$ and stress-strain relations simplify to the following relation:

$$s_x = \frac{pa^2}{2h_0t} \quad (\text{A10})$$

$$e = \frac{2h_0^2}{3a^2} \tag{A11}$$

Appendix B. Hyperelastic Models calibration data (ANSYS)

Table B 1 Values of the Mooney-Rivlin 5 parameters hyperelastic material constants.

MR 5 Parameters		
Coefficient Name	Calculated Value	Unit
Incompressibility Parameter D1	0.00	Pa ⁻¹
Material Constant C01	83965.66	Pa
Material Constant C02	109364.25	Pa
Material Constant C10	150332.01	Pa
Material Constant C11	-308795.15	Pa
Material Constant C20	133484.82	Pa
Residual	0.70	

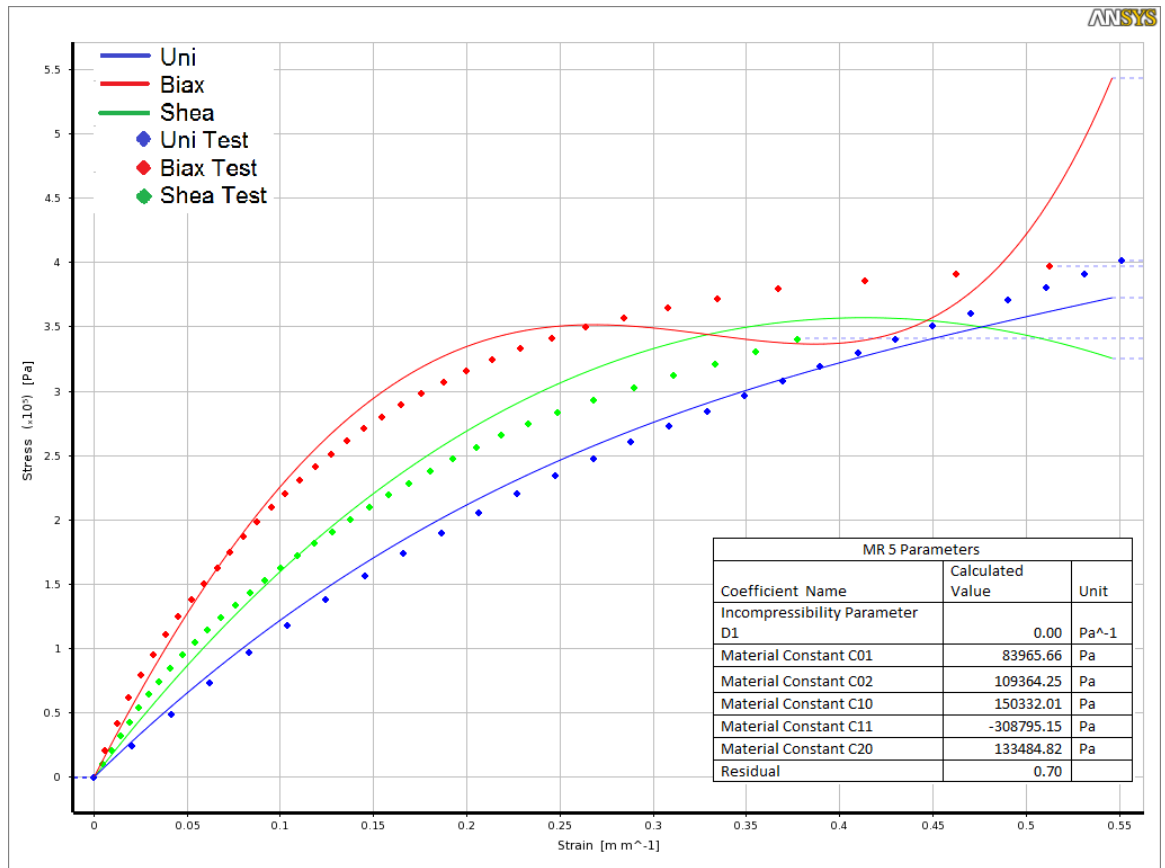


Figure B 1 Comparison of experimental and modelled stress strain data for Mooney-Rivlin 5 parameters hyperelastic model.

Table B 2 Values of Yeoh 3rd Order hyperelastic material constants.

Yeoh 3 rd Order		
Coefficient Name	Calculated Value	Unit
Incompressibility Parameter D1	0.00	Pa ⁻¹
Incompressibility Parameter D2	0.00	Pa ⁻¹
Incompressibility Parameter D3	0.00	Pa ⁻¹
Material Constant C10	236319.99	Pa
Material Constant C20	-72085.06	Pa
Material Constant C30	19003.29	Pa
Residual	0.83	

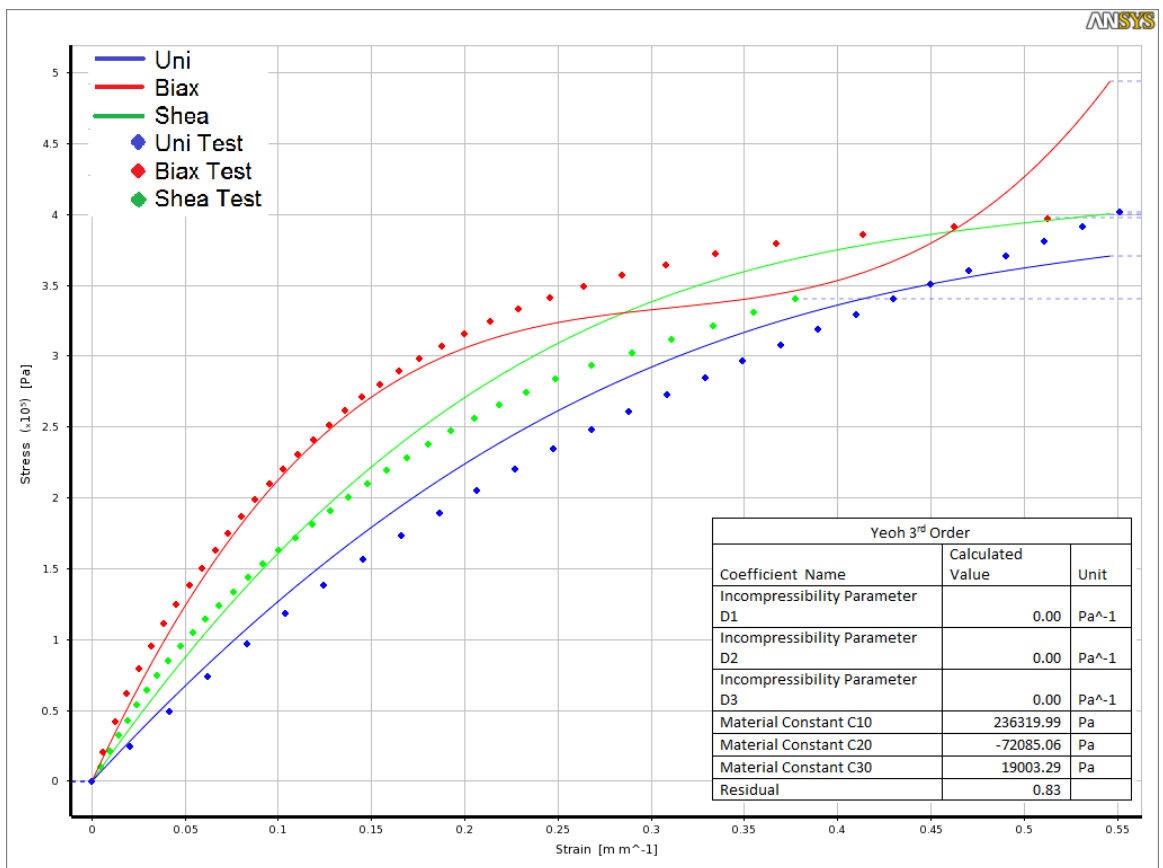


Figure B 2 Comparison of experimental and modelled stress strain data for Yeoh 3rd order hyperelastic model.

Table B 3 Values of the Mooney-Rivlin 3 parameters hyperelastic model constants.

MR 3 Parameters		
Coefficient Name	Calculated Value	Unit
Incompressibility Parameter D1	0.00	Pa ⁻¹
Material Constant C01	55804.41	Pa
Material Constant C10	164594.56	Pa
Material Constant C11	-26306.49	Pa
Residual	1.23	

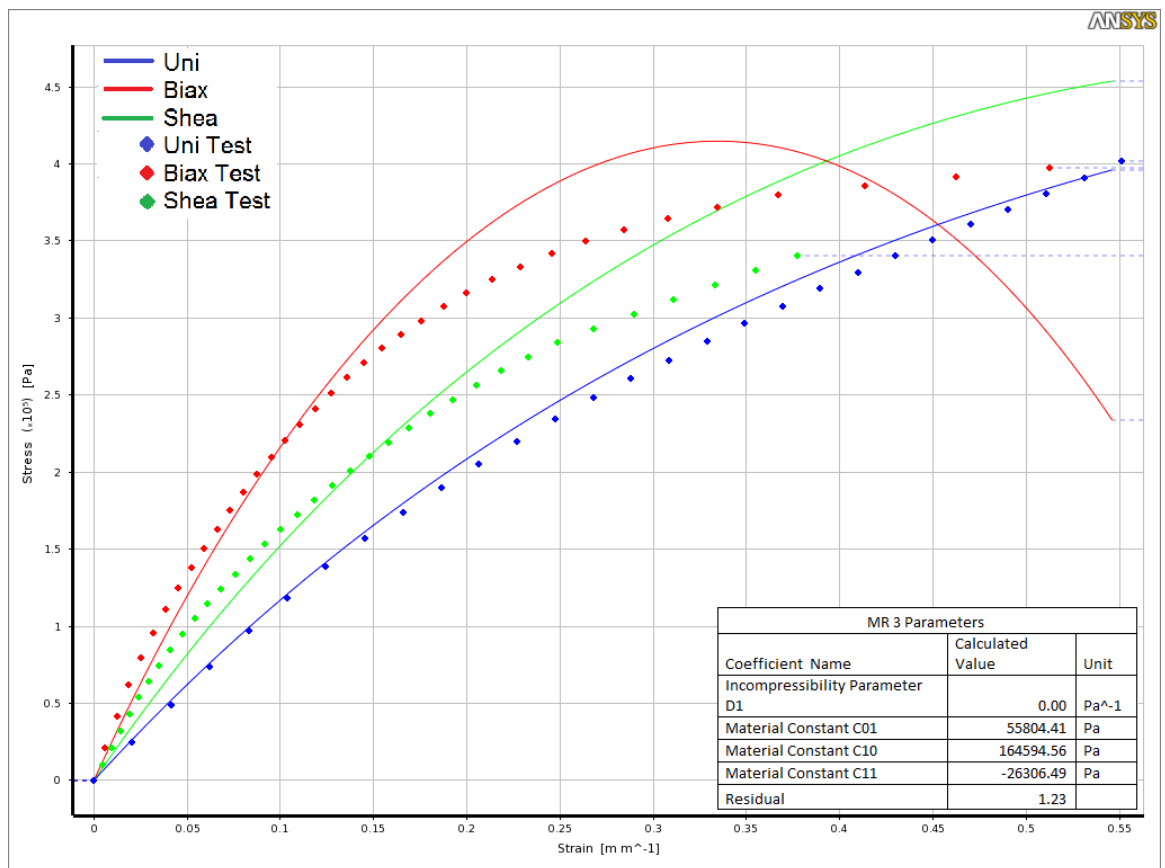


Figure B 3 Comparison of experimental and modelled stress strain data for Mooney-Rivlin 3 parameters hyperelastic model.

Table B 4 Values of Yeoh 2nd Order hyperelastic material constants.

Yeoh 2 nd Order		
Coefficient Name	Calculated Value	Unit
Incompressibility Parameter D1	0.00	Pa ⁻¹
Incompressibility Parameter D2	0.00	Pa ⁻¹
Material Constant C10	224504.79	Pa
Material Constant C20	-31801.77	Pa
Residual	1.16	

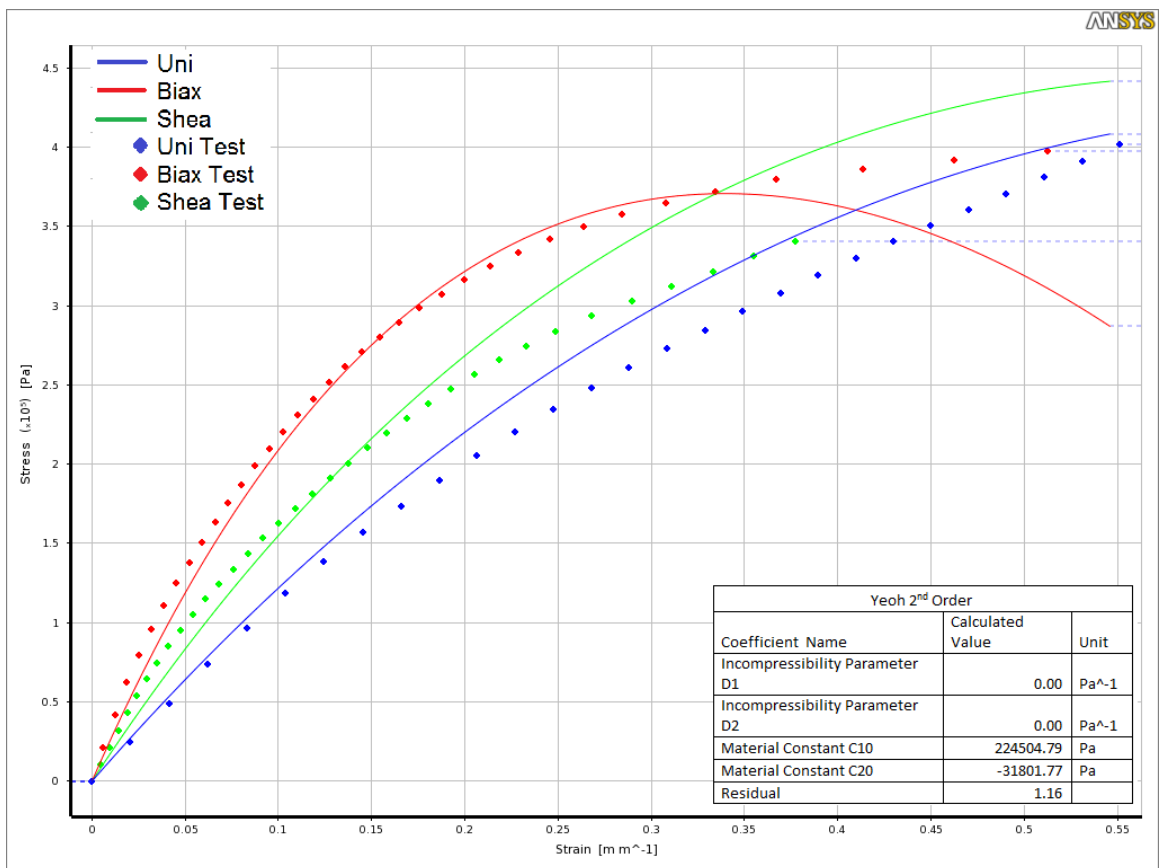


Figure B 4 Comparison of experimental and modelled stress strain data Yeoh 2nd order hyperelastic model.

Table B 5 Values of Ogden 1st Order hyperelastic material constants.

Ogden 1 st Order		
Coefficient Name	Calculated Value	Unit
Incompressibility Parameter D1	0.00	Pa ⁻¹
Material Constant A1	1.43	
Material Constant MU1	577086.46	Pa
Residual	2.31	

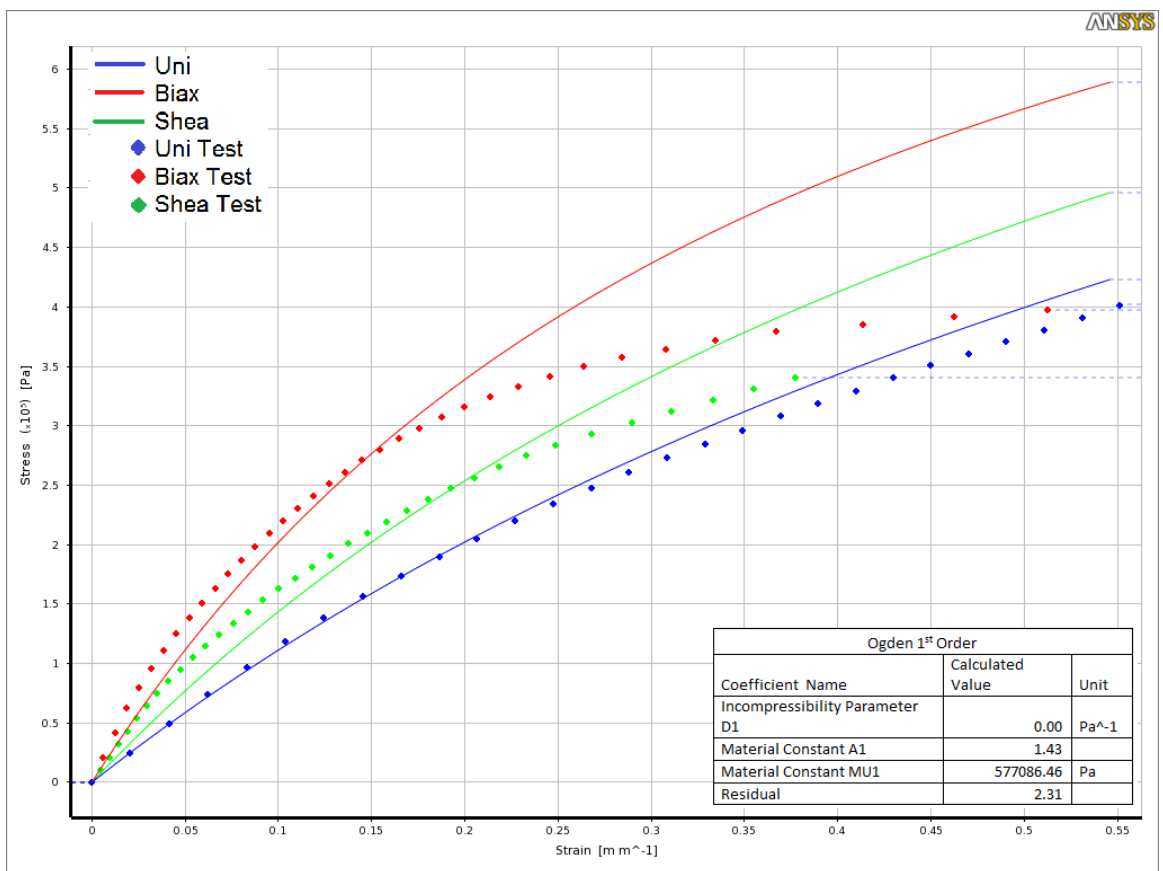


Figure B 5 Comparison of experimental and modelled stress strain data Ogden 1st order hyperelastic model.

Table B 6 Values of Mooney-Rivlin 2 Parameters hyperelastic material constants.

MR 2 Parameters		
Coefficient Name	Calculated Value	Unit
Incompressibility Parameter D1	0.00	Pa ⁻¹
Material Constant C01	-25278.68	Pa
Material Constant C10	231941.76	Pa
Residual	2.30	

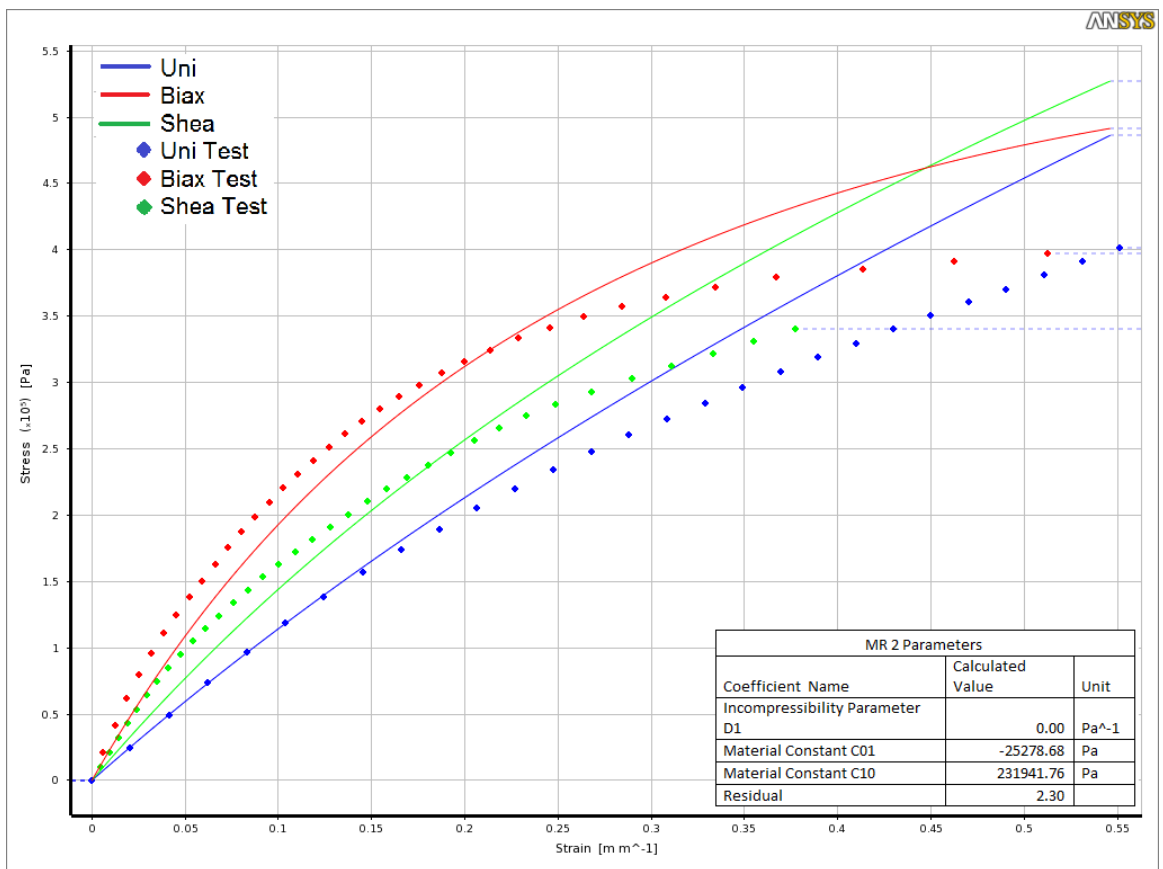


Figure B 6 Comparison of experimental and modelled stress strain data for Mooney-Rivlin 2 parameters hyperelastic model.

Table B 7 Values of Neo Hookean hyperelastic material constants.

Neo Hookean		
Coefficient Name	Calculated Value	Unit
Incompressibility Parameter D1	0.00	Pa ⁻¹
Initial Shear Modulus Mu	407663.41	Pa
Residual	2.52	

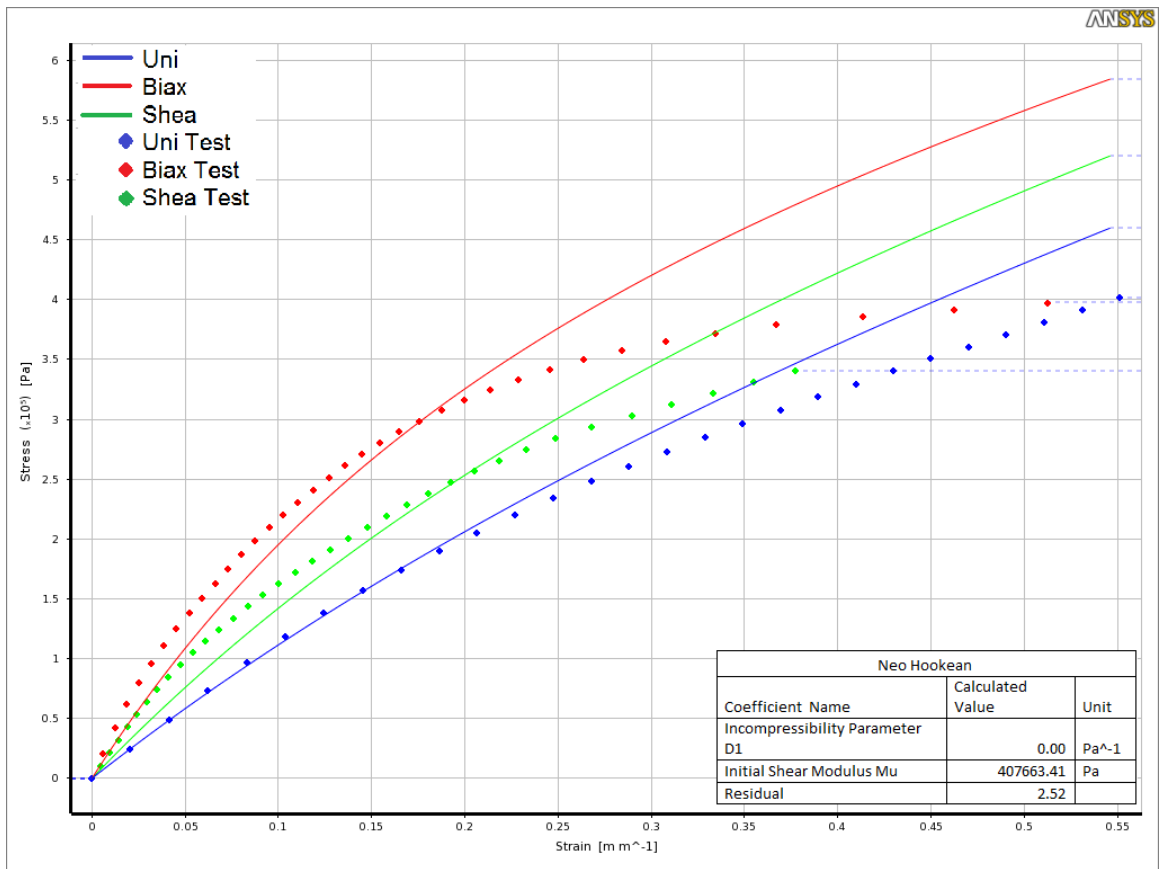


Figure B 7 Comparison of experimental and modelled stress strain data for Neo-Hookean hyperelastic model.

Table B 8 Values of Yeoh 1st Order hyperelastic material constants.

Yeoh 1 st Order		
Coefficient Name	Calculated Value	Unit
Incompressibility Parameter D1	0.00	Pa ⁻¹
Material Constant C10	203831.71	Pa
Residual	2.52	

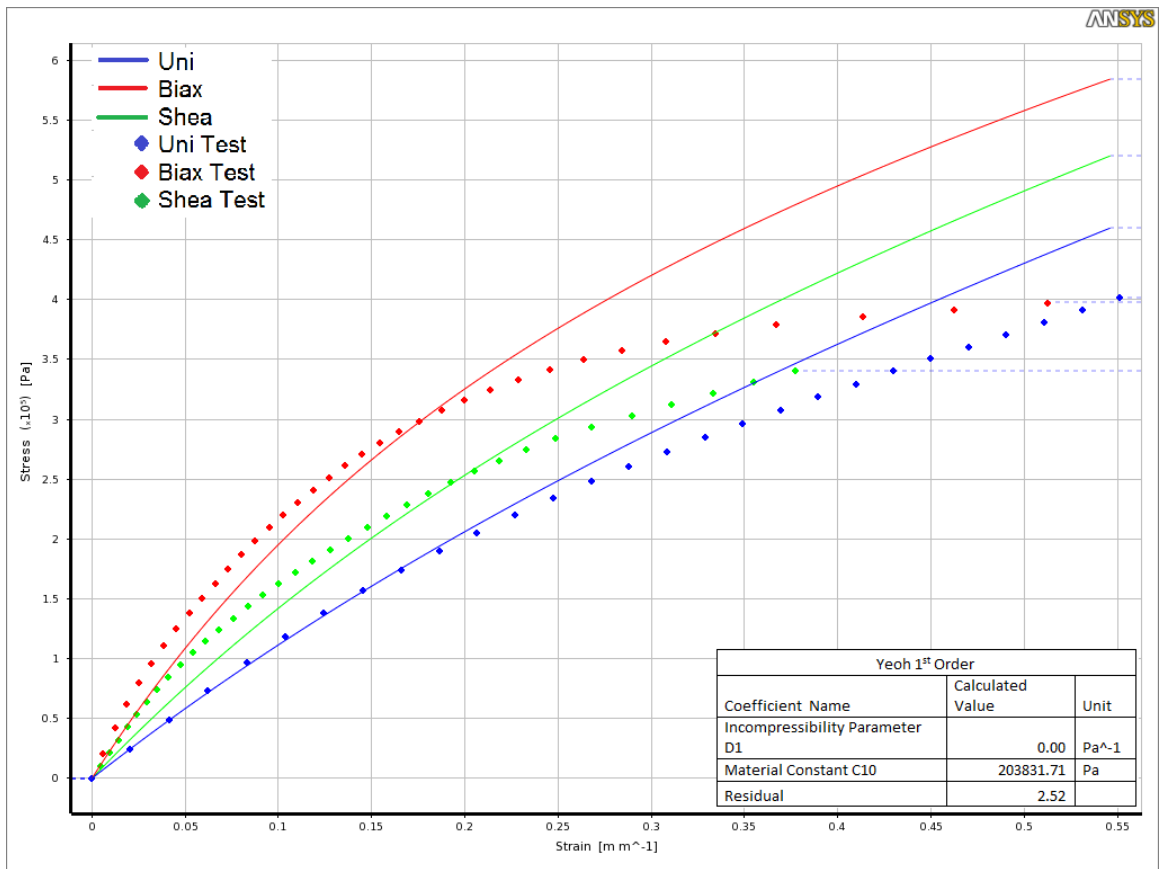


Figure B 8 Comparison of experimental and modelled stress strain data for Yeoh 1st order hyperelastic model.

Table B 9 Values of Arruda-Boyce hyperelastic material constants.

Arruda-Boyce		
Coefficient Name	Calculated Value	Unit
Incompressibility Parameter D1	0.00	Pa ⁻¹
Initial Shear Modulus Mu	407663.41	Pa
Limiting Network Stretch	-68815754.45	
Residual	2.52	

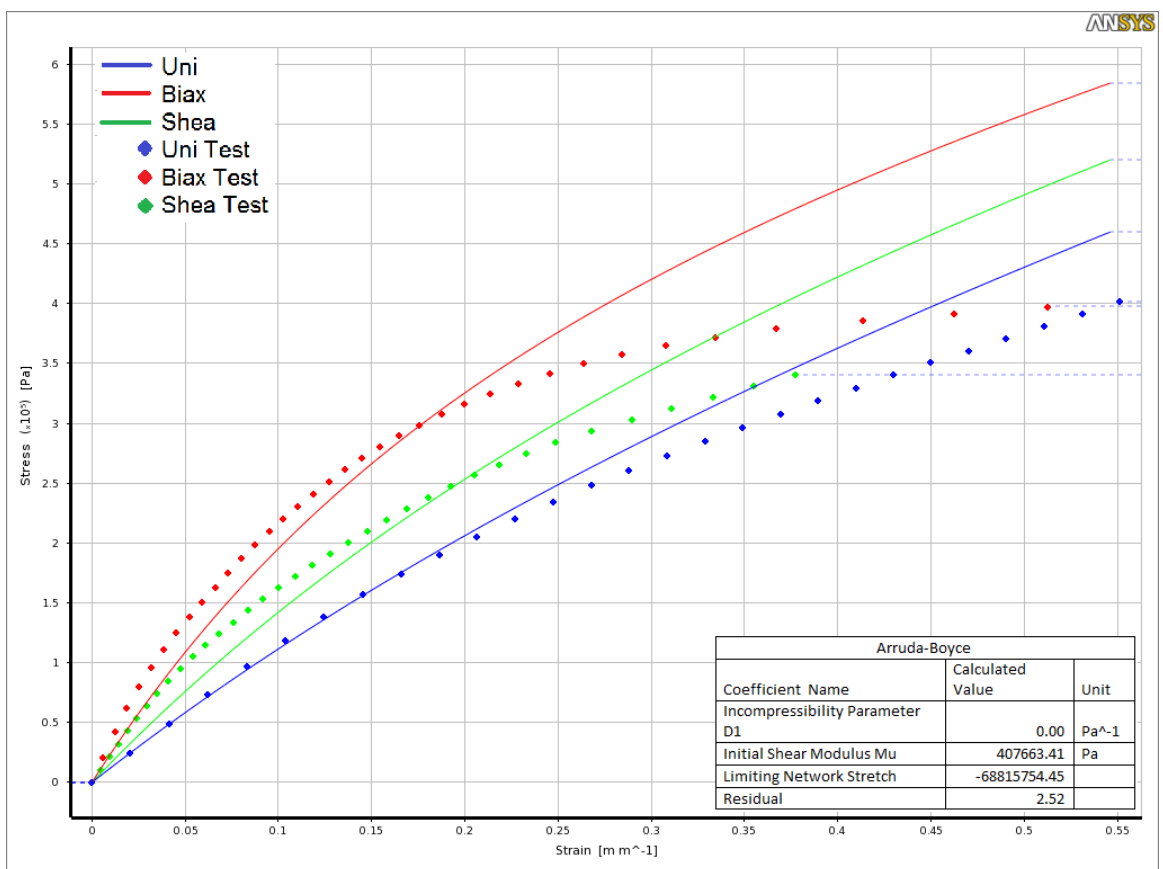


Figure B 9 Comparison of experimental and modelled stress strain data data for Arruda-Boyce hyperelastic model.

Table B 10 Values of Ogden 3rd Order hyperelastic material constants.

Ogden 3 rd Order		
Coefficient Name	Calculated Value	Unit
Incompressibility Parameter D1	0.00	Pa ⁻¹
Incompressibility Parameter D2	0.00	Pa ⁻¹
Incompressibility Parameter D3	0.00	Pa ⁻¹
Material Constant A1	16.23	
Material Constant A2	16.25	
Material Constant A3	16.25	
Material Constant MU1	316.28	Pa
Material Constant MU2	316.28	Pa
Material Constant MU3	316.28	Pa
Residual	77.50	

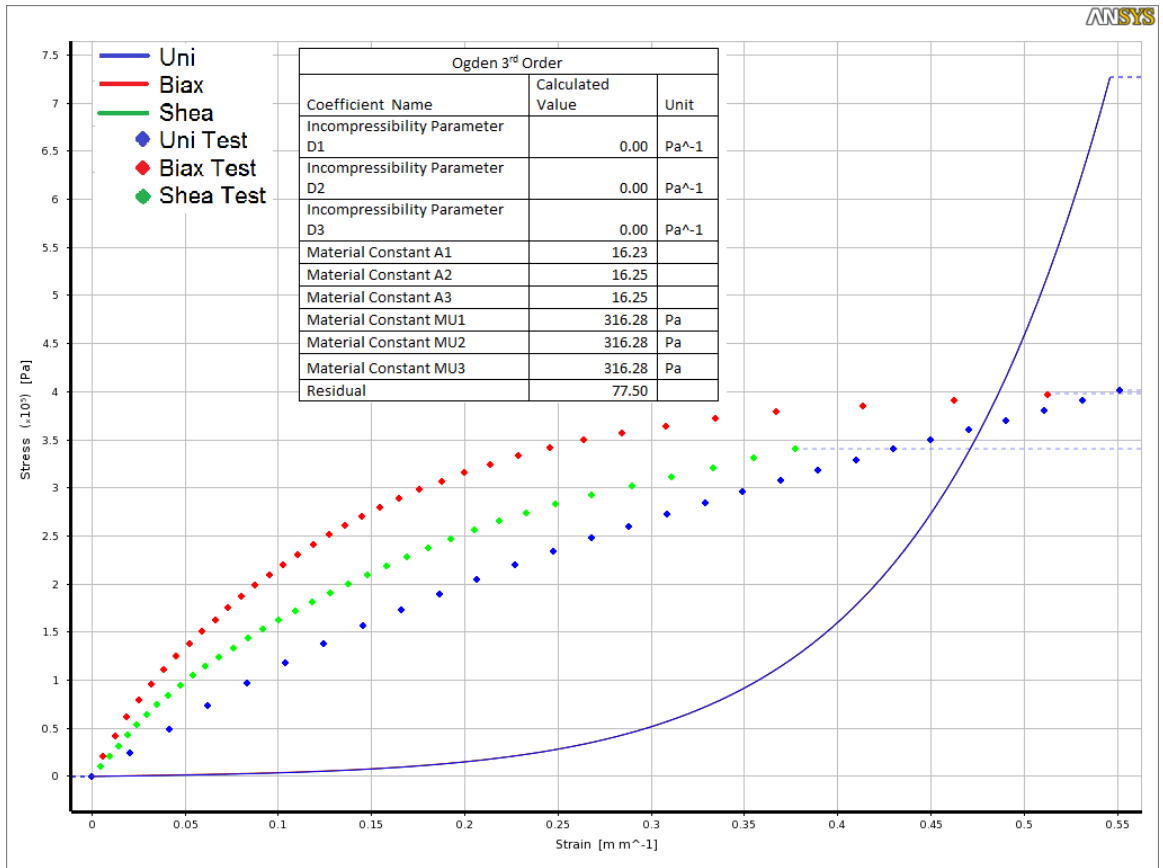


Figure B 10 Comparison of experimental and modelled stress strain data for Ogden 3rd order hyperelastic model.

Table B 11 Values of Ogden 2nd Order hyperelastic material constants.

Ogden 2 nd Order		
Coefficient Name	Calculated Value	Unit
Incompressibility Parameter D1	0.00	Pa ⁻¹
Incompressibility Parameter D2	0.00	Pa ⁻¹
Material Constant A1	16.13	
Material Constant A2	16.09	
Material Constant MU1	502.58	Pa
Material Constant MU2	502.58	Pa
Residual	77.20	

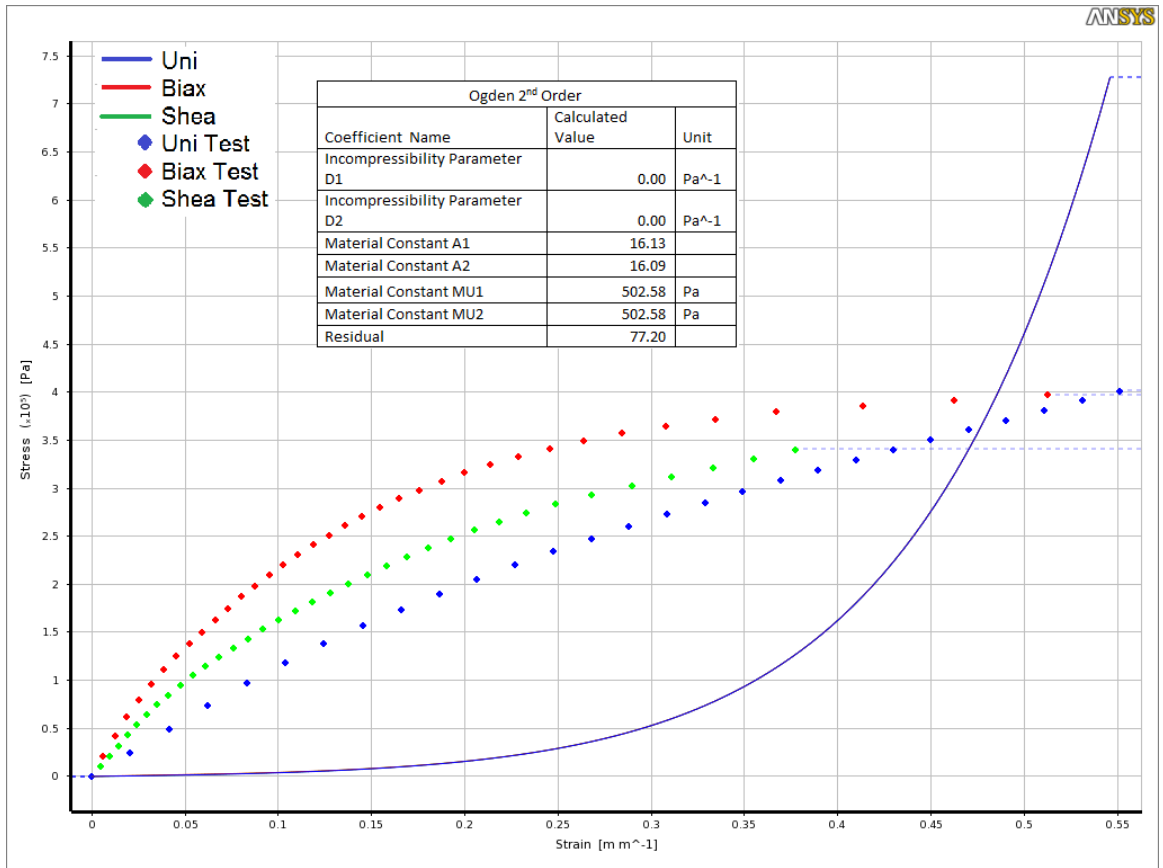


Figure B 11 Comparison of experimental and modelled stress strain data for Ogden 2nd order hyperelastic model.

Table B 12 Values of Gent hyperelastic material constants.

Gent		
Coefficient Name	Calculated Value	Unit
Incompressibility Parameter D1	0	Pa ⁻¹
Initial Shear Modulus Mu	54845.09	Pa
Limiting Value	0.8098698	
Residual	79.38	

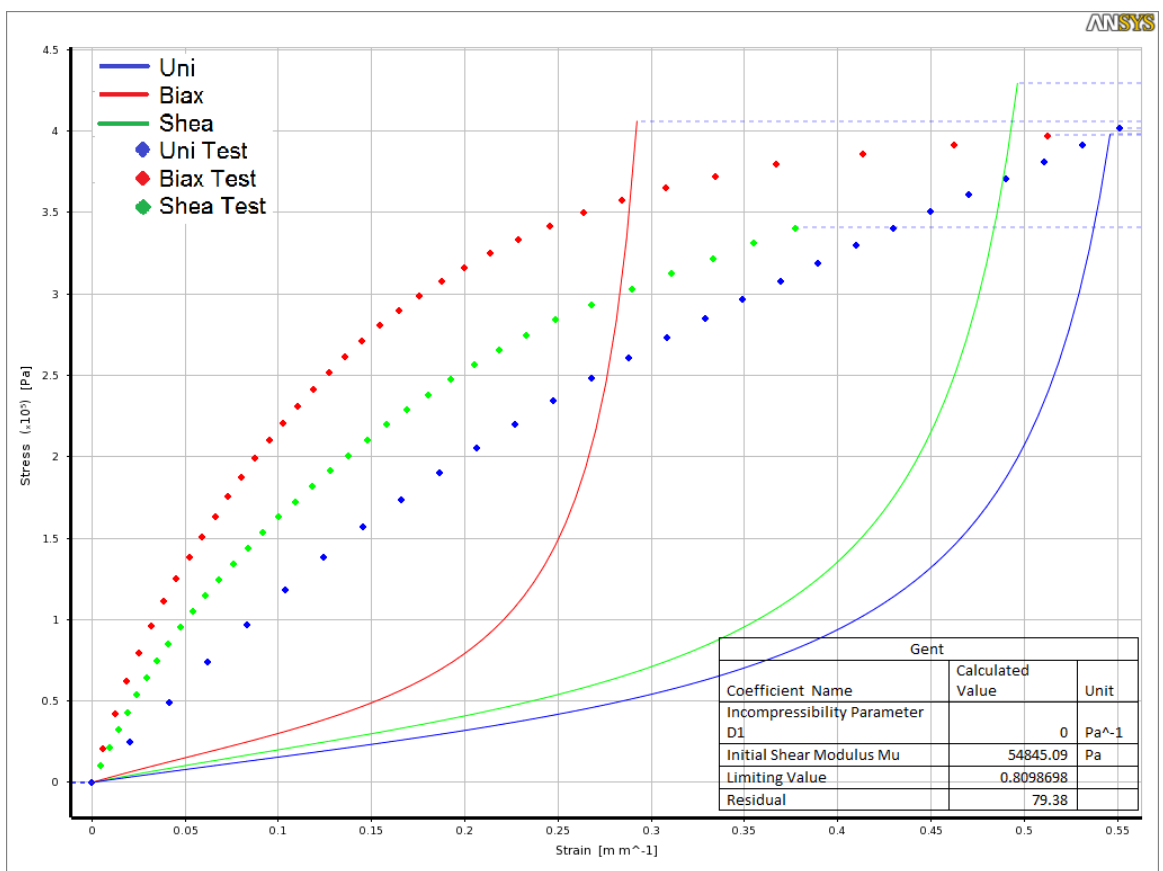


Figure B 12 Comparison of experimental and modelled stress strain data for Gent's hyperelastic model.

Appendix C. Key Plots of Data

1. Bulge Linearization plots

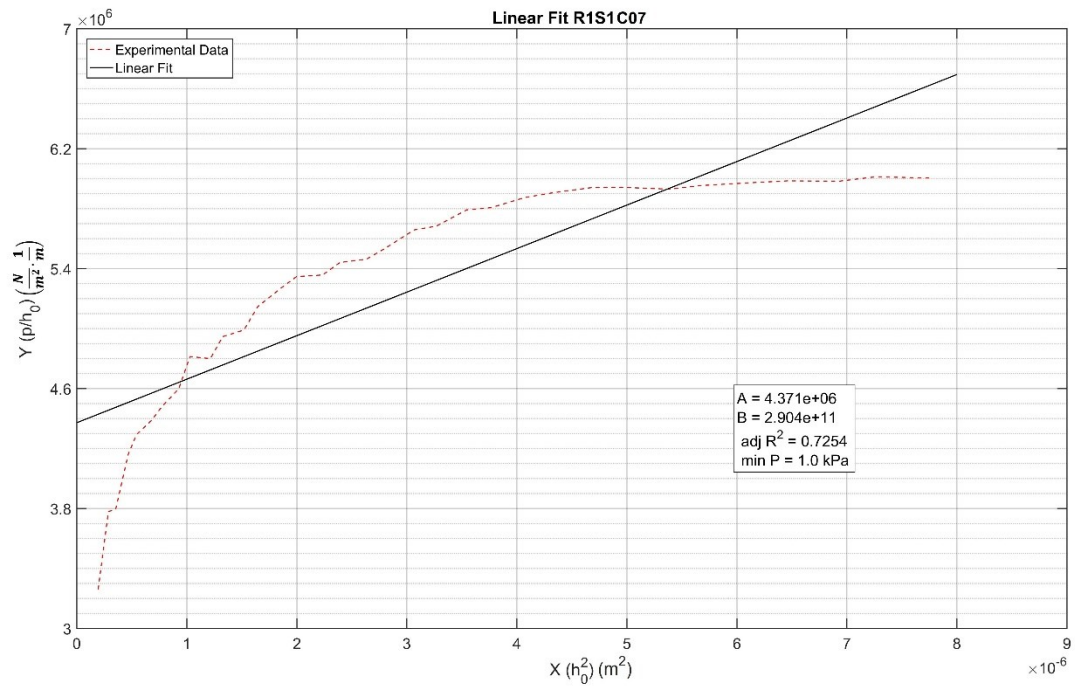


Figure C 1 Linearization result of R1S1 showing a 73% fit to the experimental data

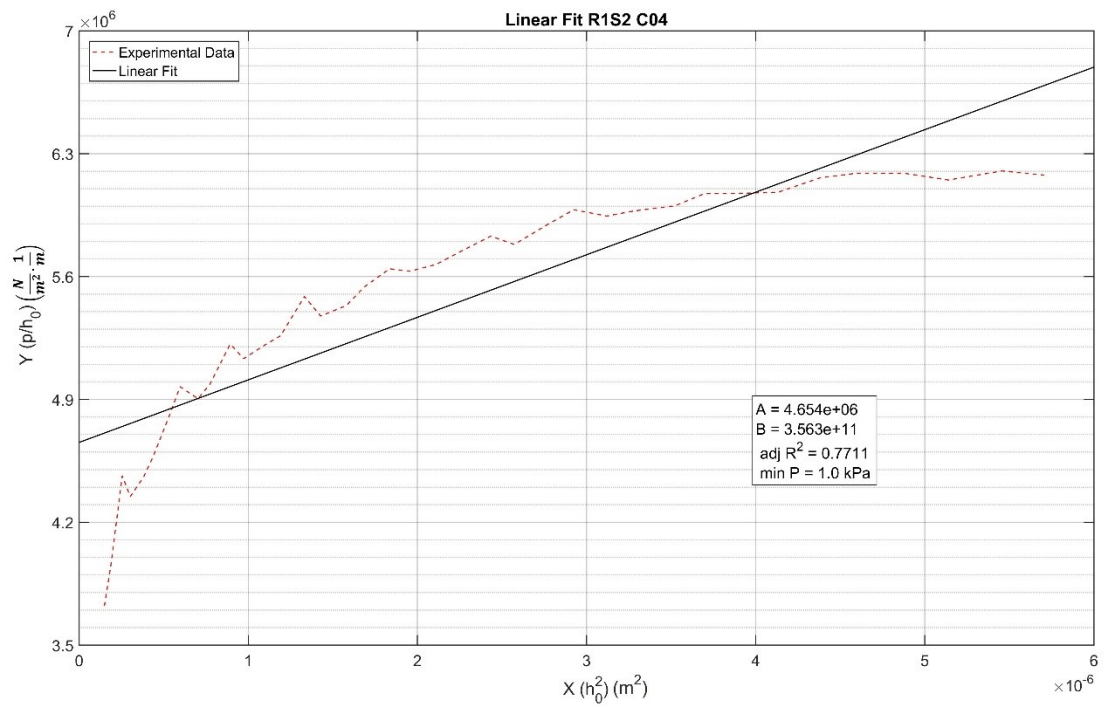


Figure C 2 Linearization result of R1S2 showing a 77% fit to the experimental data

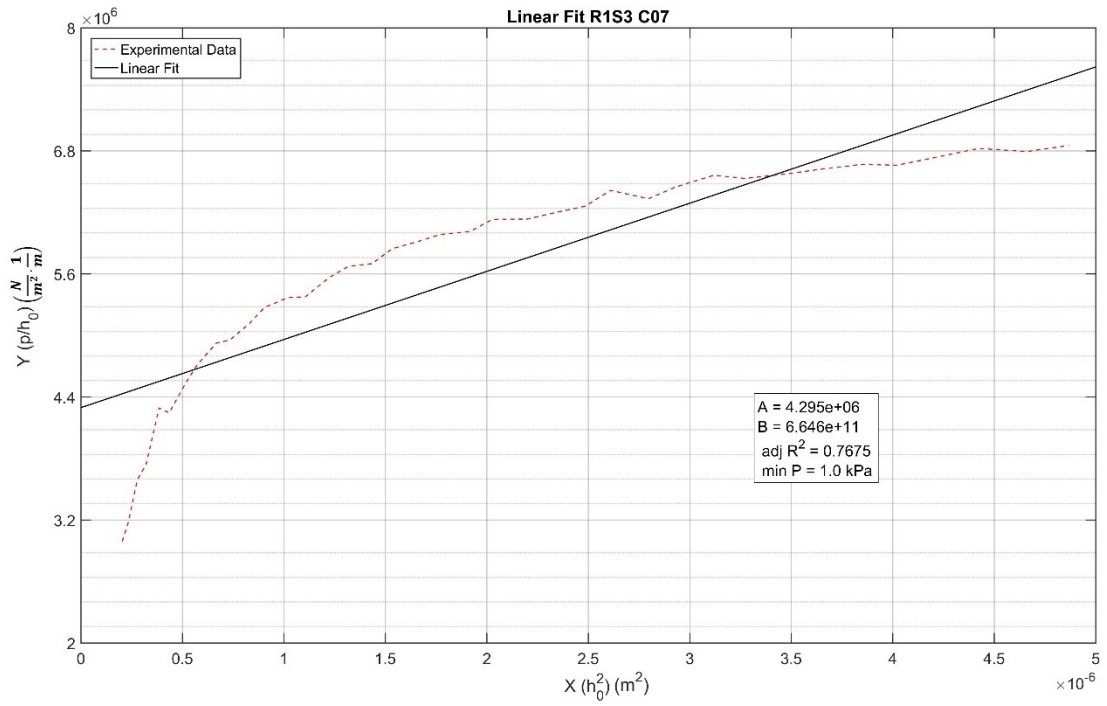


Figure C 3 Linearizatton result of R1S3 showing a 77% fit to the experimental data

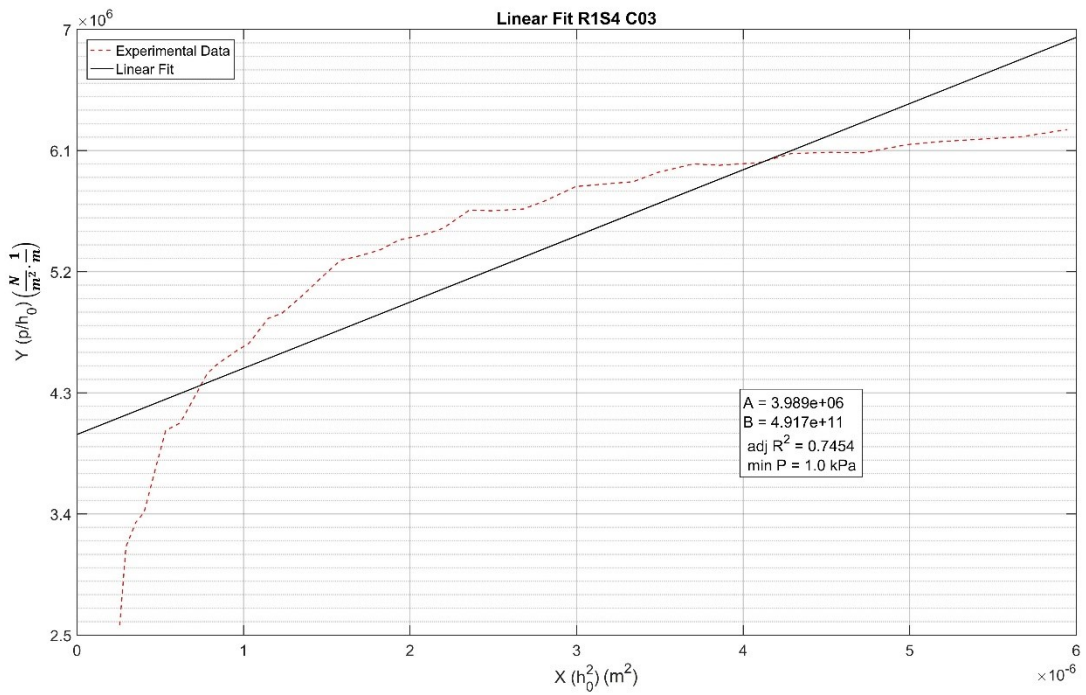


Figure C 4 Linearizatton result of R1S4 showing a 75% fit to the experimental data

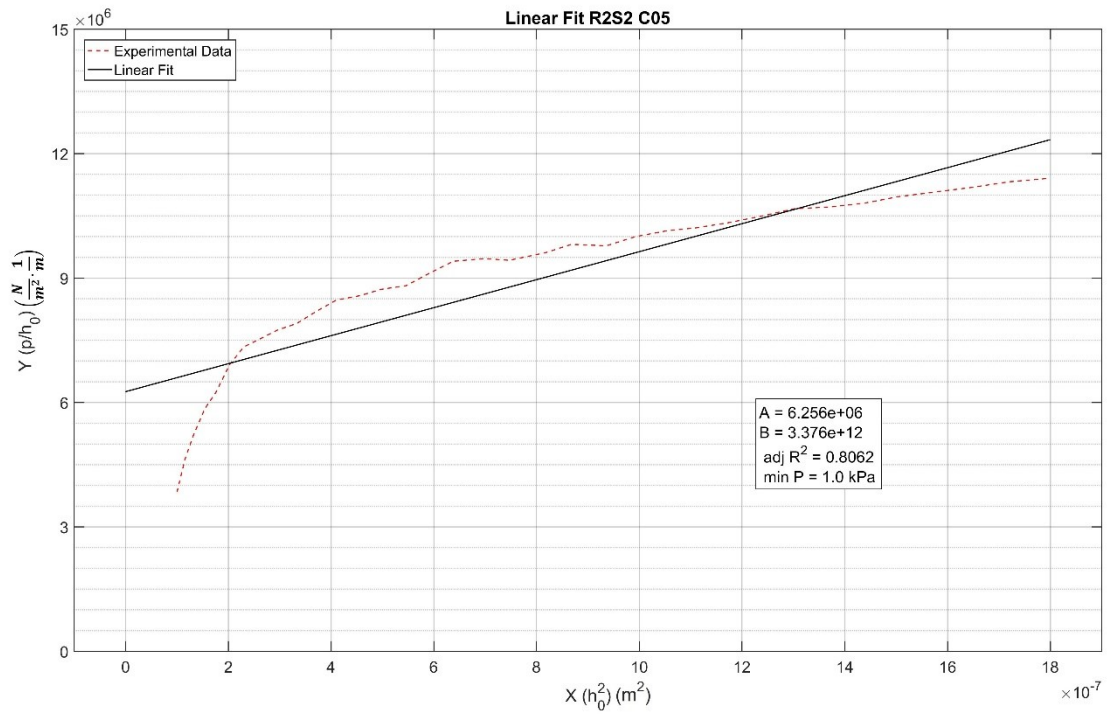


Figure C 5 Linearizatton result of R2S2 showing a 81% fit to the experimental data

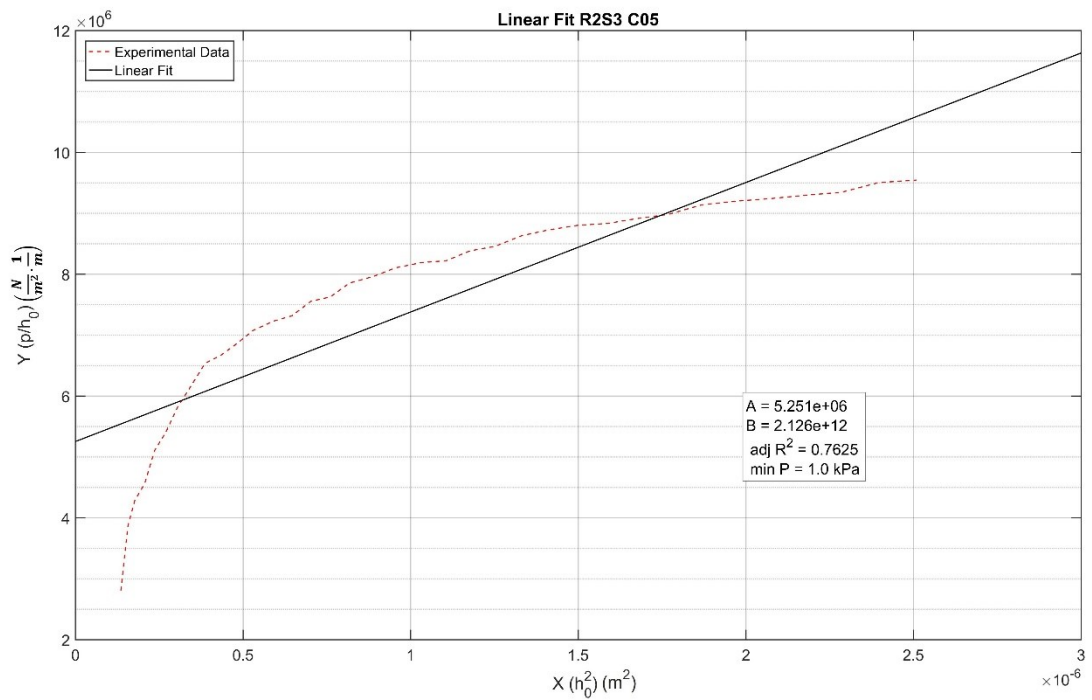


Figure C 6 Linearizatton result of R2S3 showing a 76% fit to the experimental data

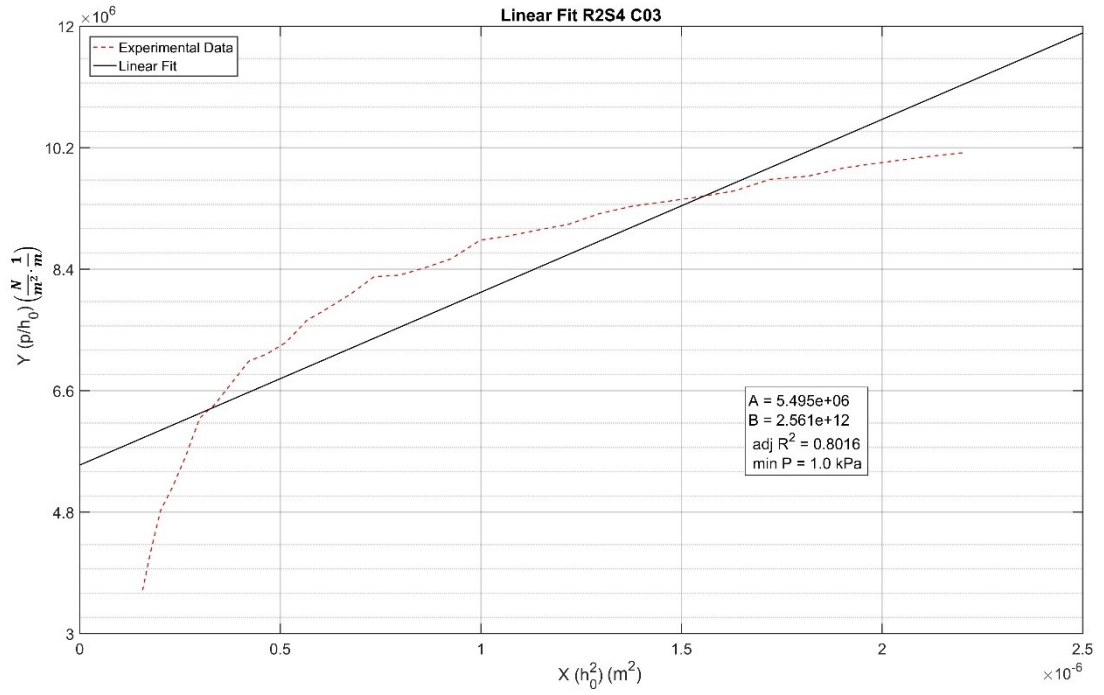


Figure C 7 Linearizatton result of R2S4 showing a 80% fit to the experimental data

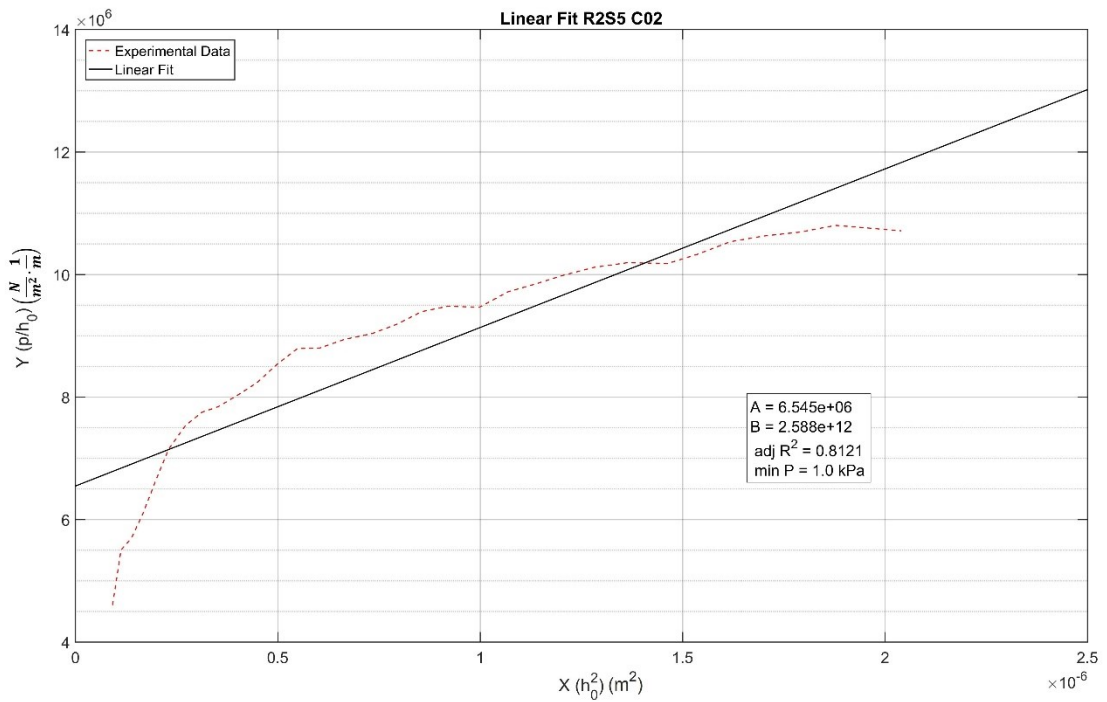


Figure C 8 Linearizatton result of R2S5 showing a 81% fit to the experimental data

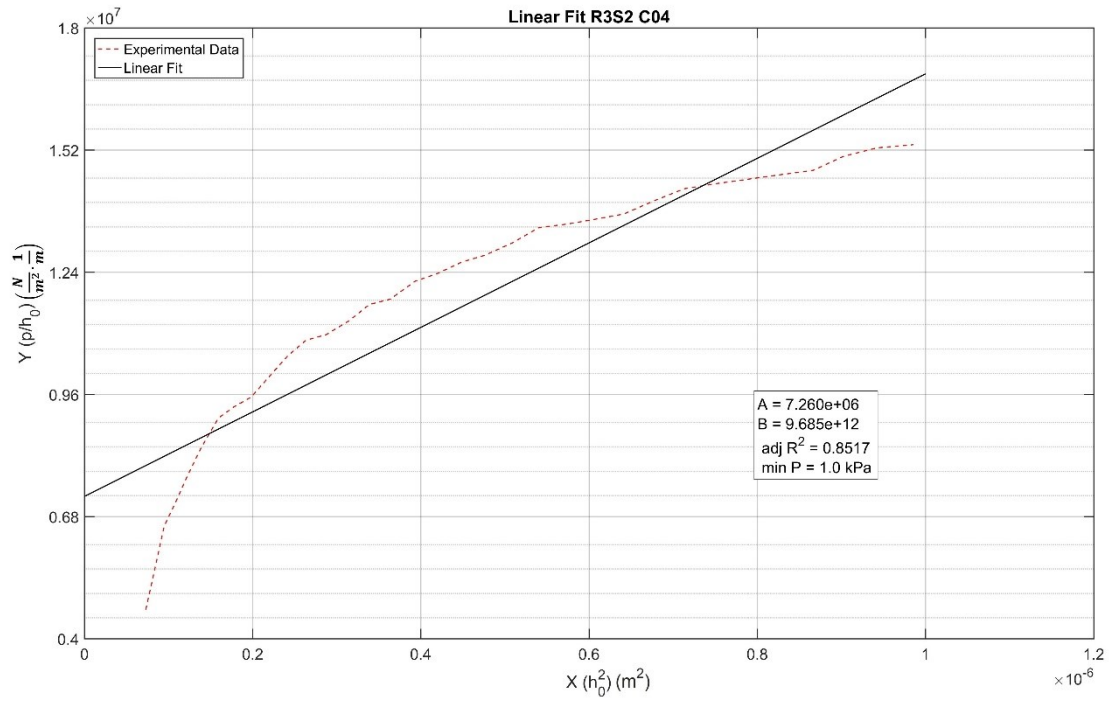


Figure C 9 Linearizatton result of R3S2 showing a 85% fit to the experimental data

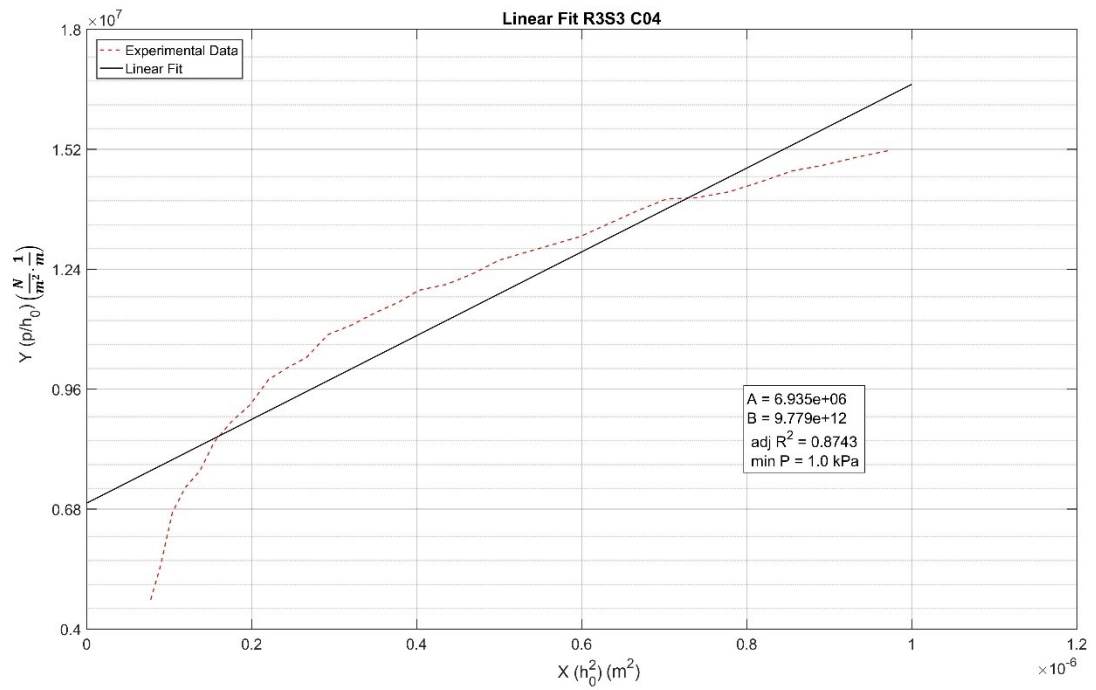


Figure C 10 Linearizatton result of R3S3 showing a 87% fit to the experimental data

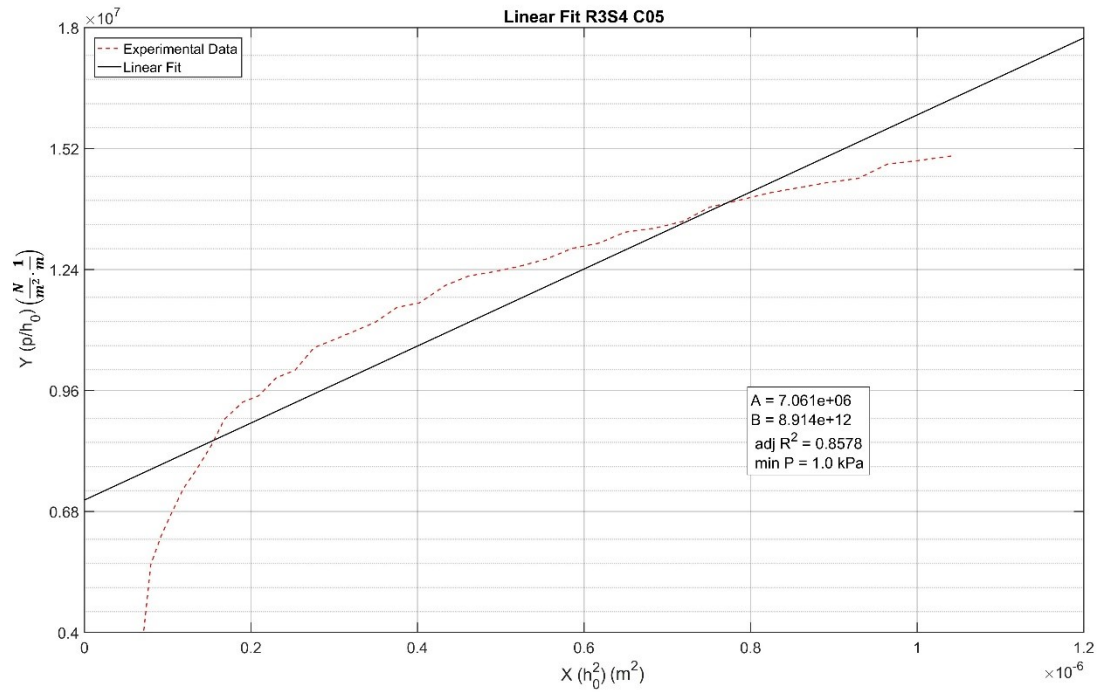


Figure C 11 Linearizatton result of R3S4 showing a 86% fit to the experimental data

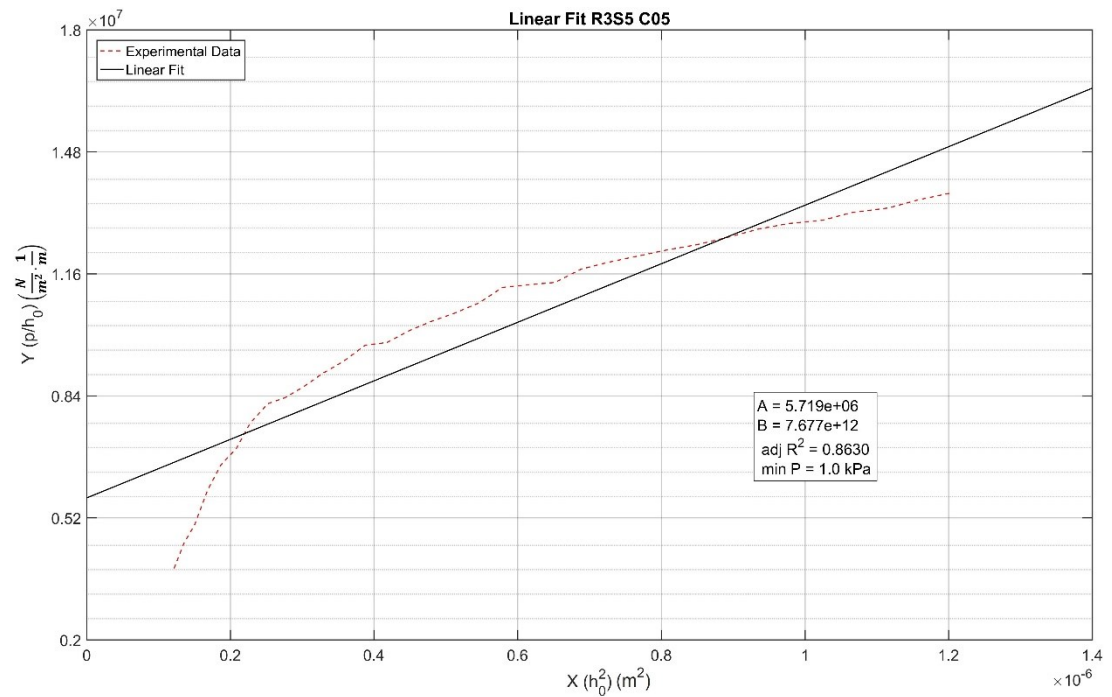


Figure C 12 Linearizatton result of R3S5 showing a 86% fit to the experimental data

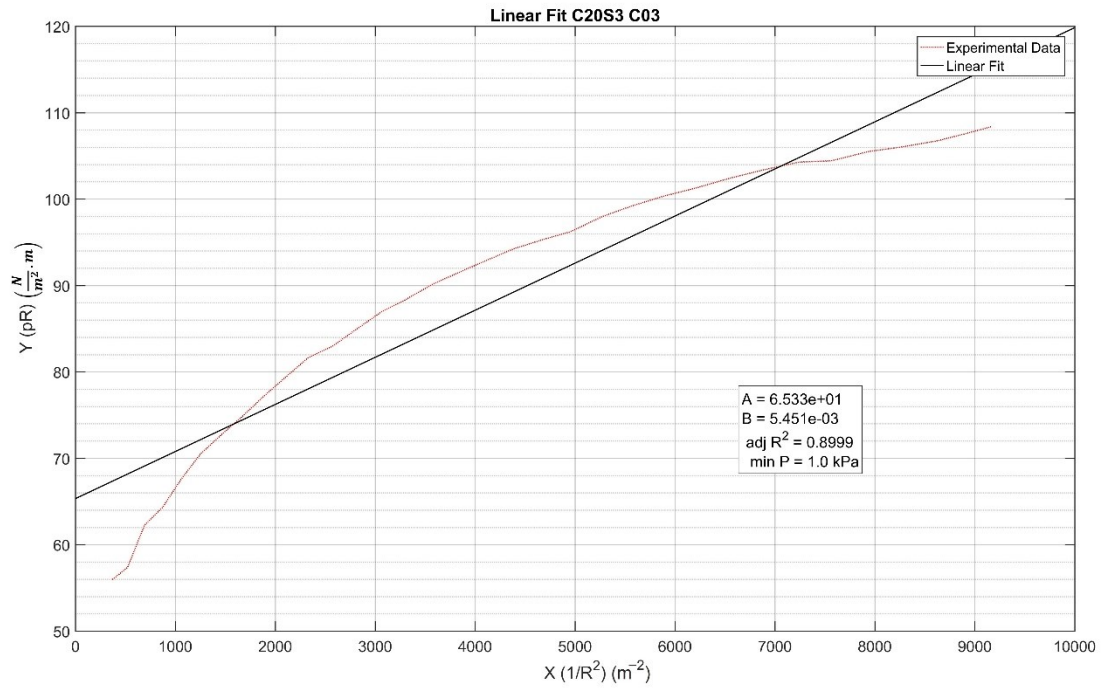


Figure C 13 Linearizatton result of C20S3 showing a 90% fit to the experimental data

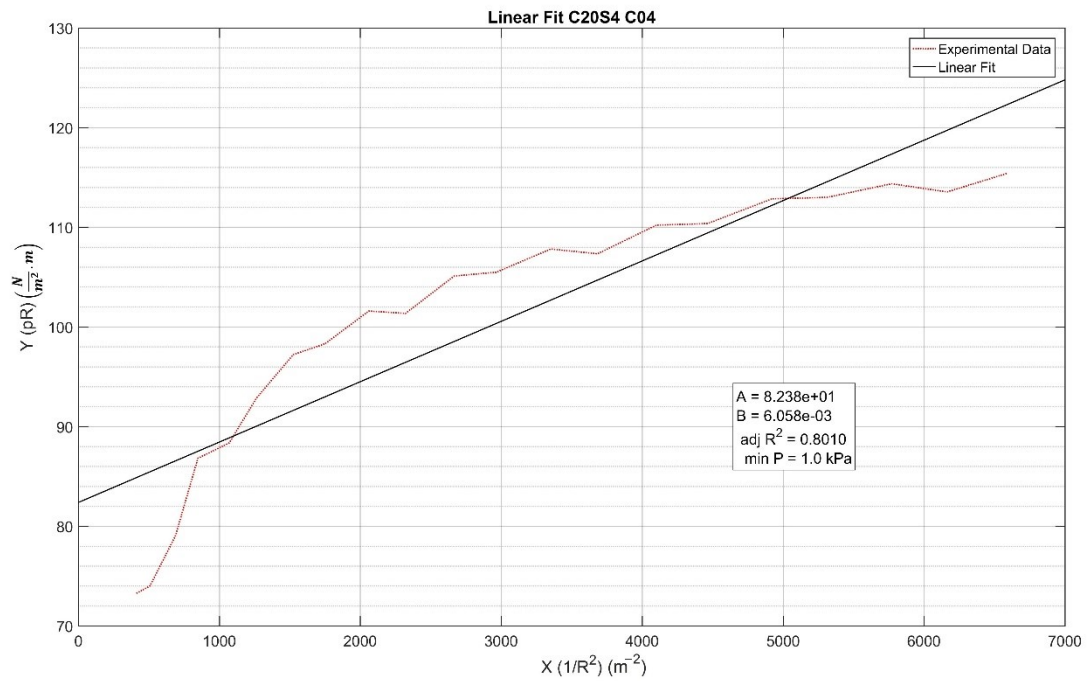


Figure C 14 Linearizatton result of C20S4 showing a 80% fit to the experimental data

2. Tensile Test key plots of Poisson's ratio

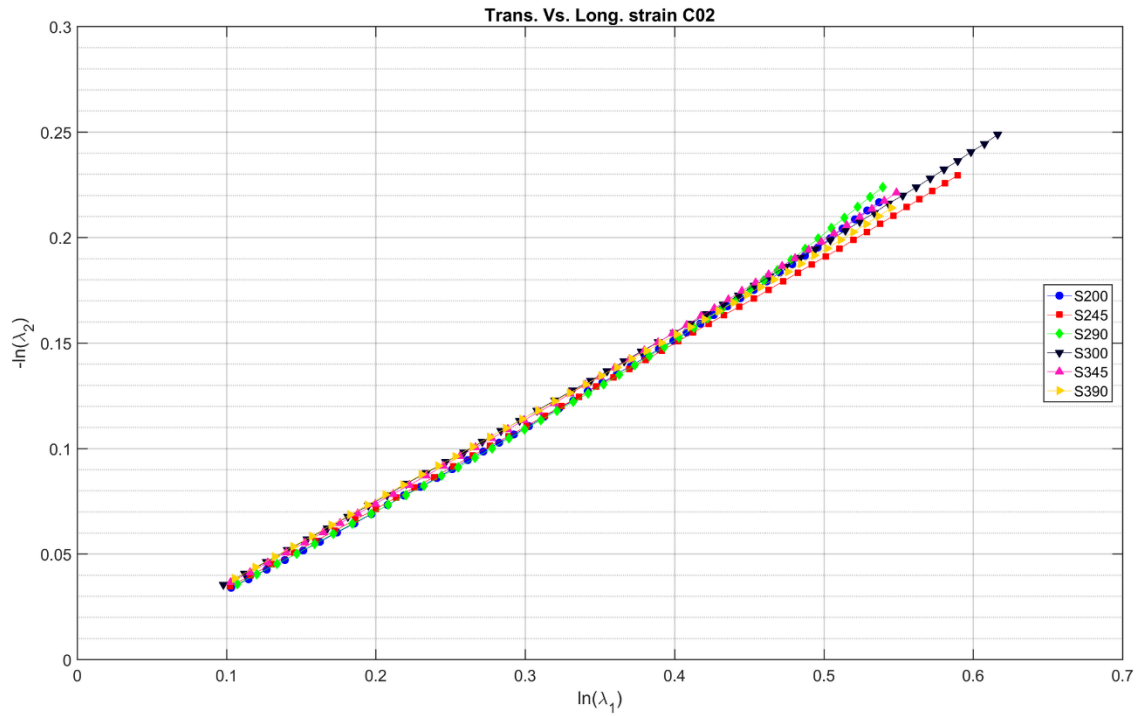


Figure C 15 The transverse strain vs. longitudinal strain for 2nd cycle for two samples (S2 and S3)

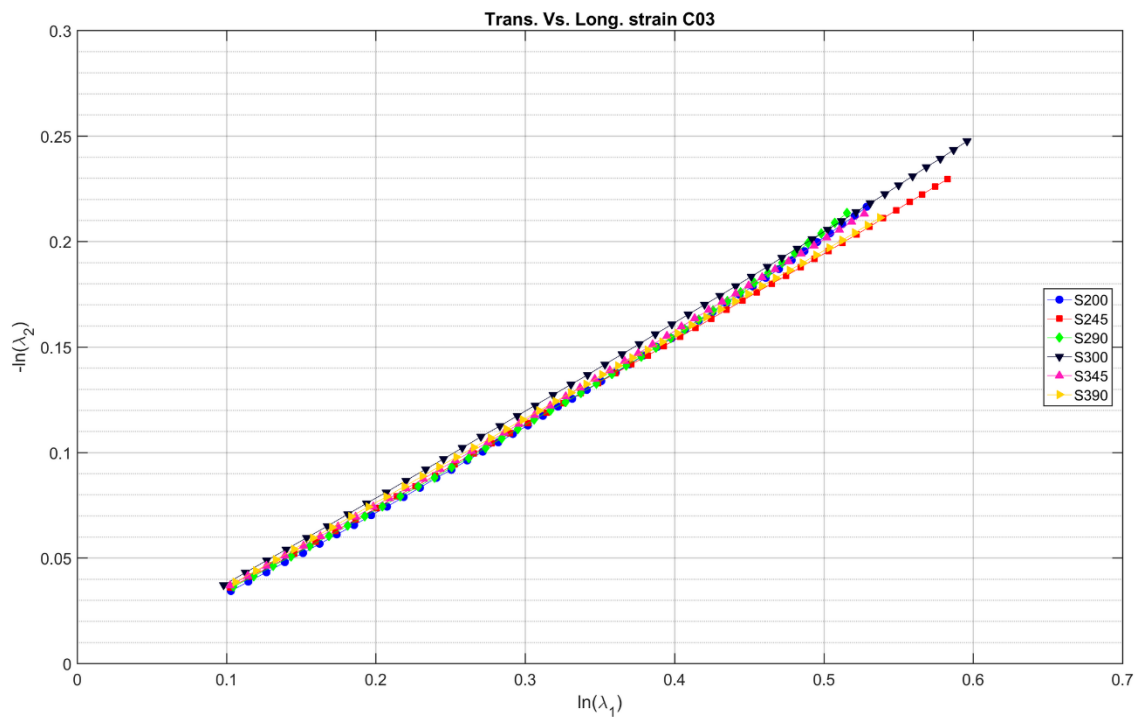


Figure C 16 The transverse strain vs. longitudinal strain for 3rd cycle for two samples (S2 and S3)

3. Tensile Test key plots of Young's Modulus

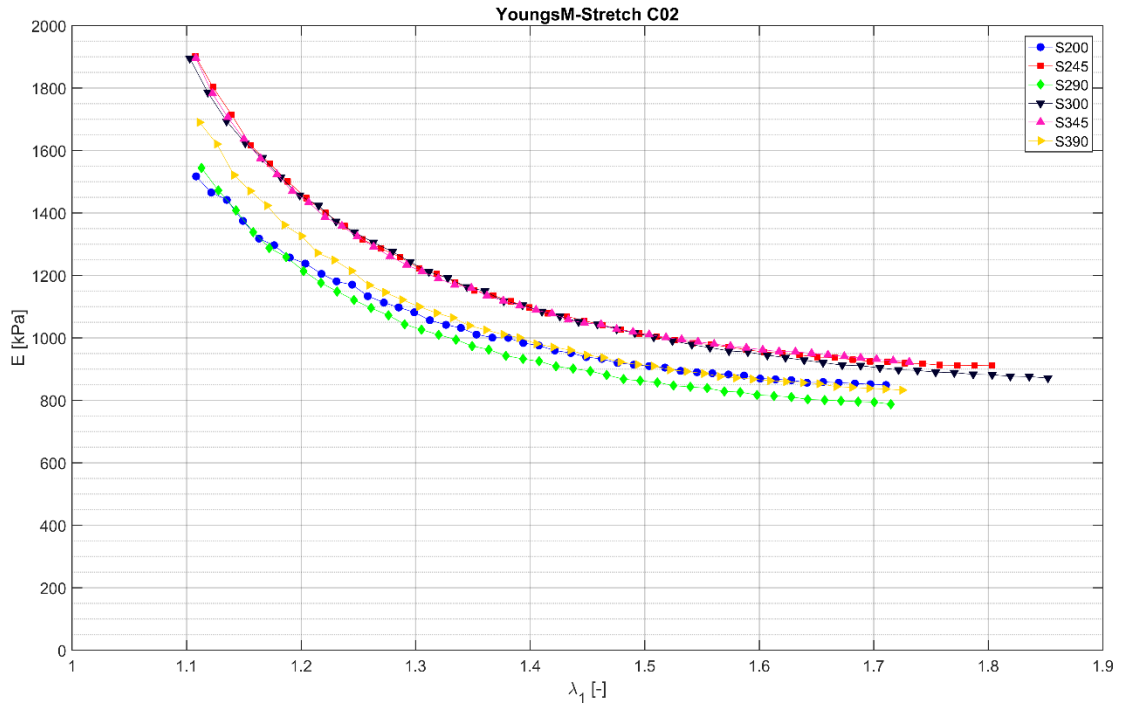


Figure C 17 Variation of Young's Modulus with longitudinal stretch for the two samples and three orientations (00°, 45°, and 90°) for 2nd stretching cycle.

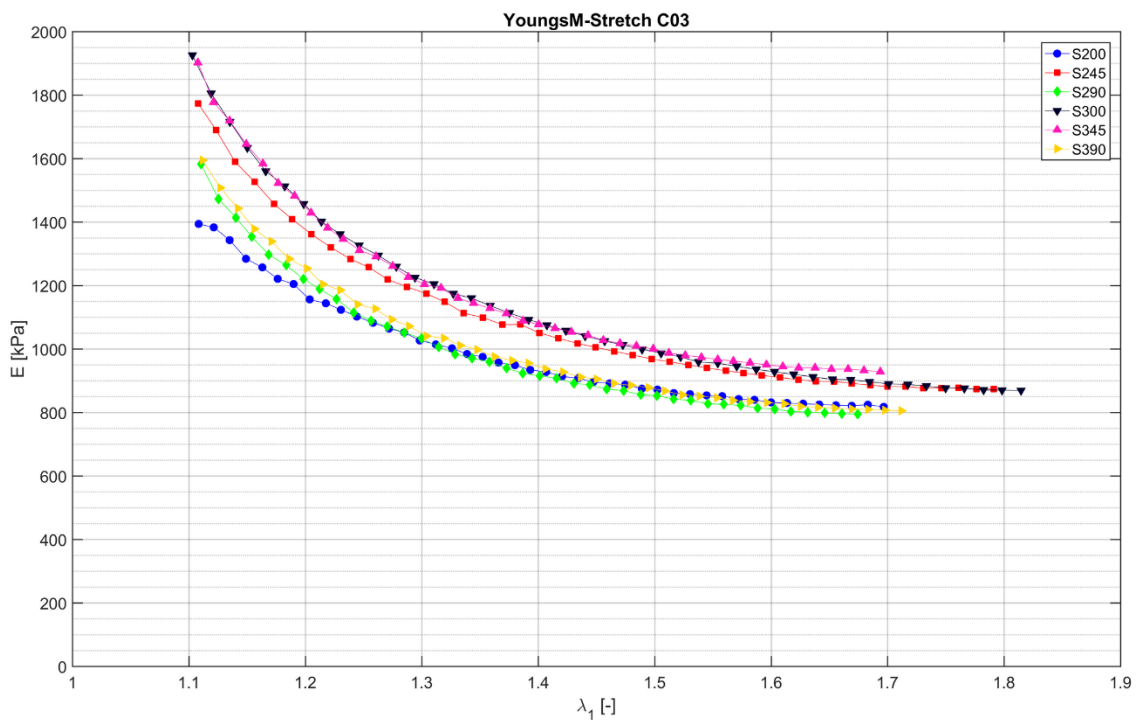
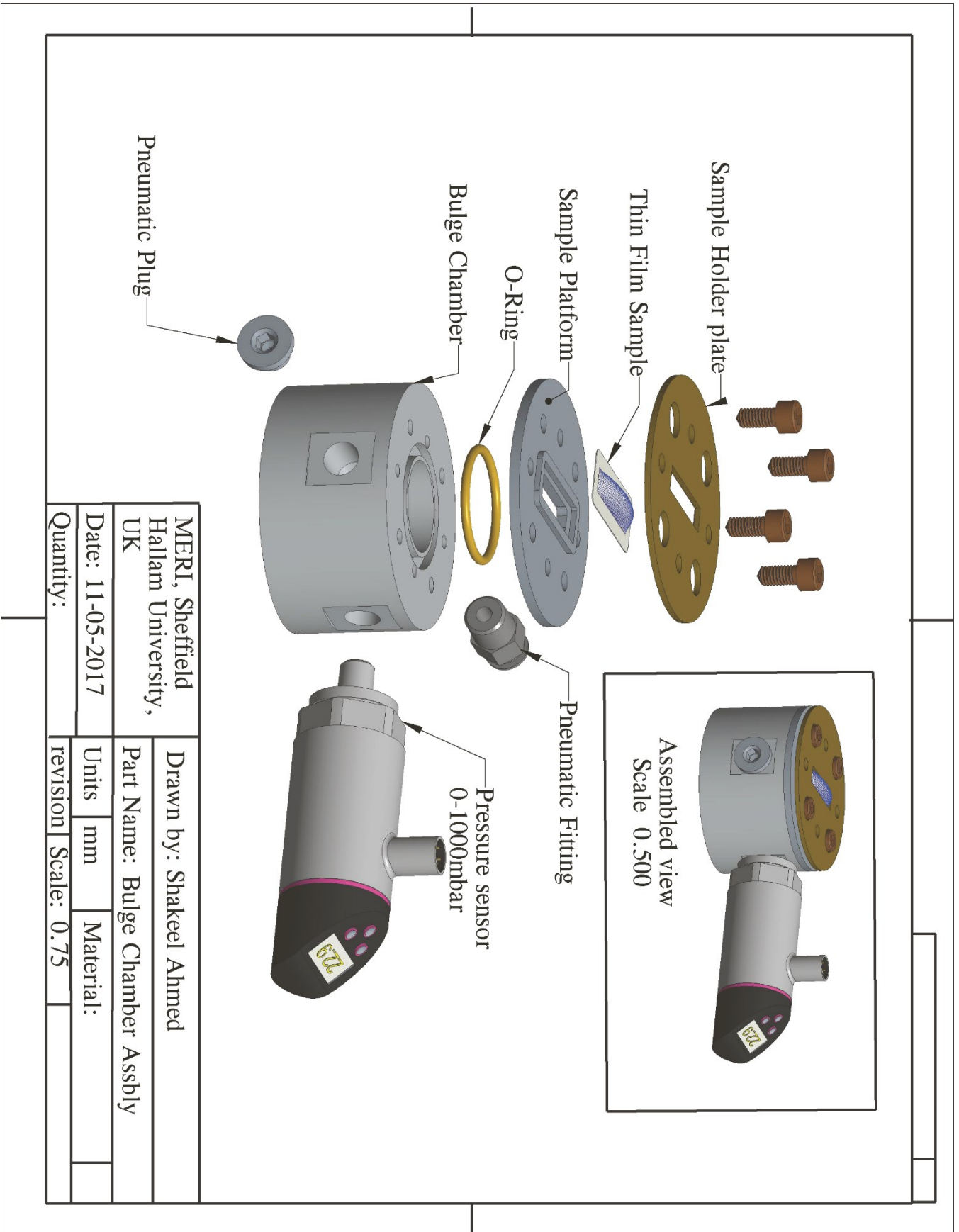
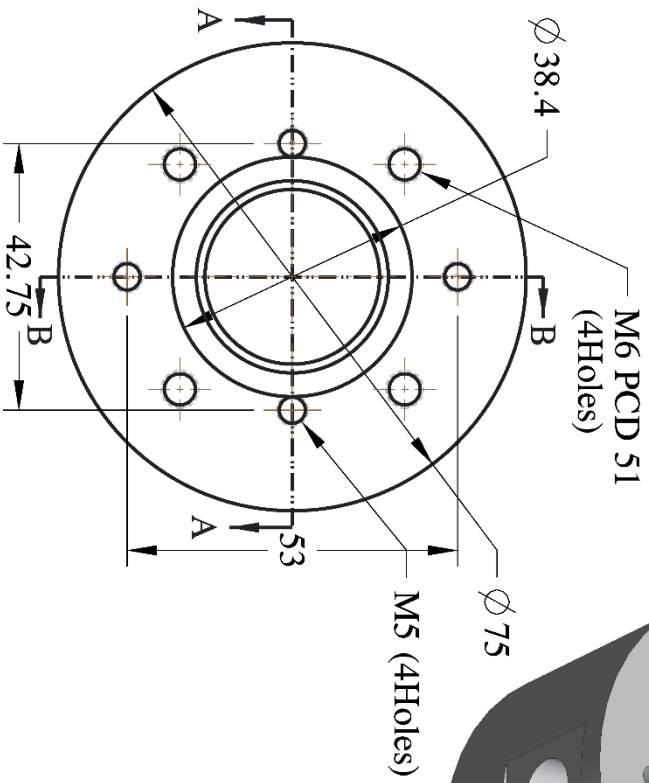
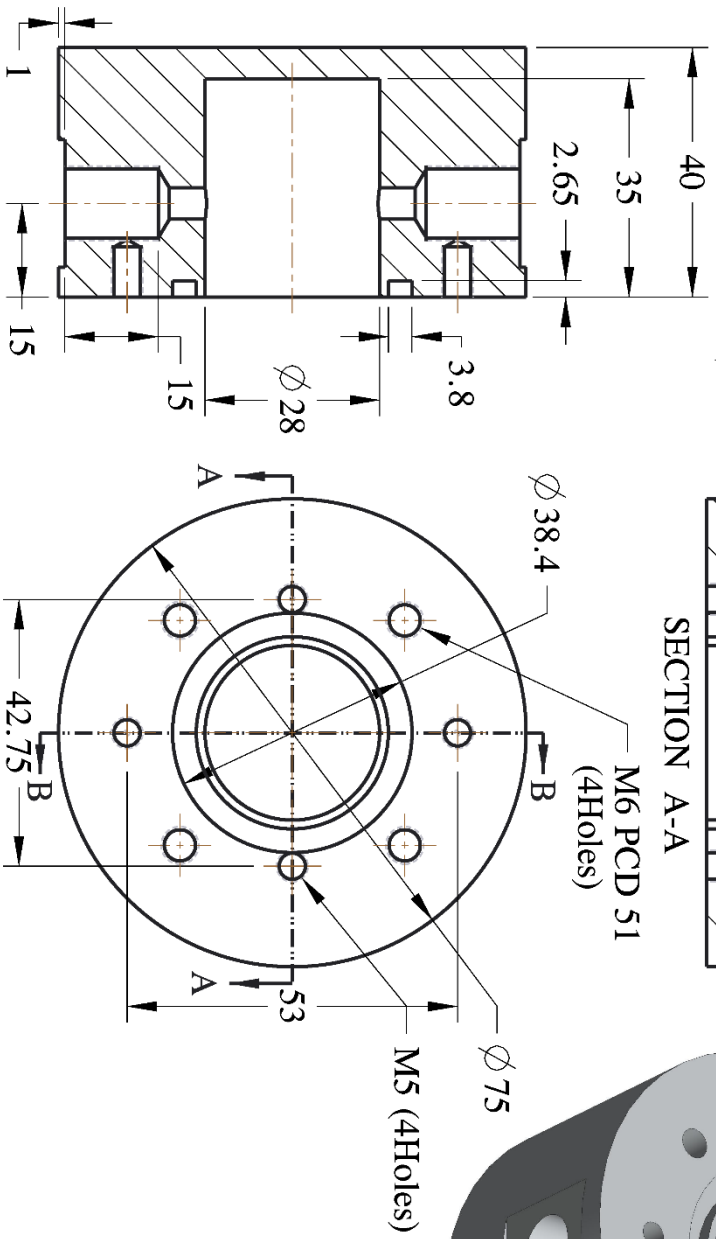
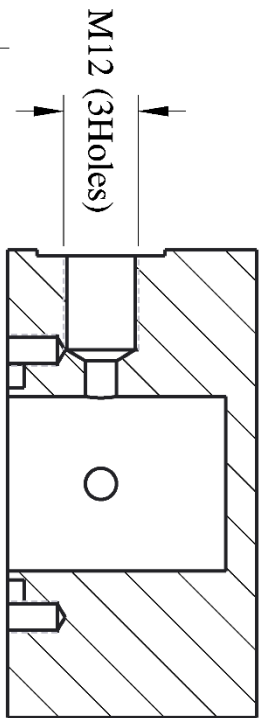
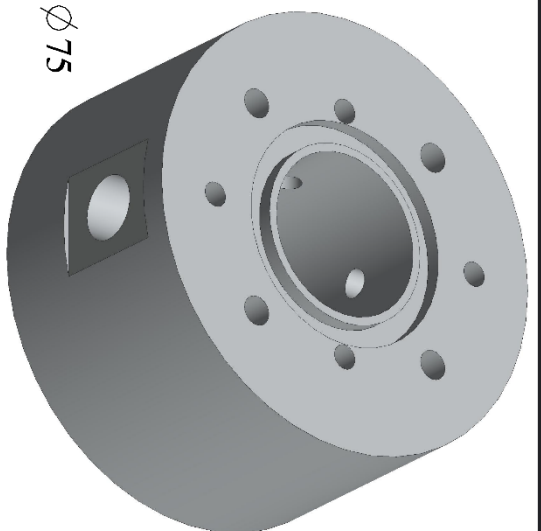


Figure C 18 Variation of Young's Modulus with longitudinal stretch for the two samples and three orientations (00°, 45°, and 90°) for 3rd stretching cycle

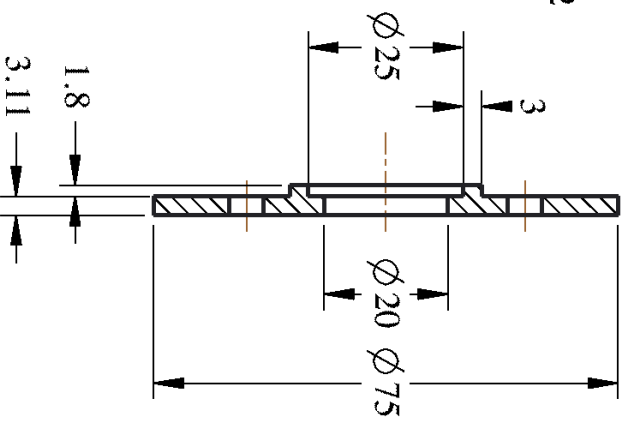
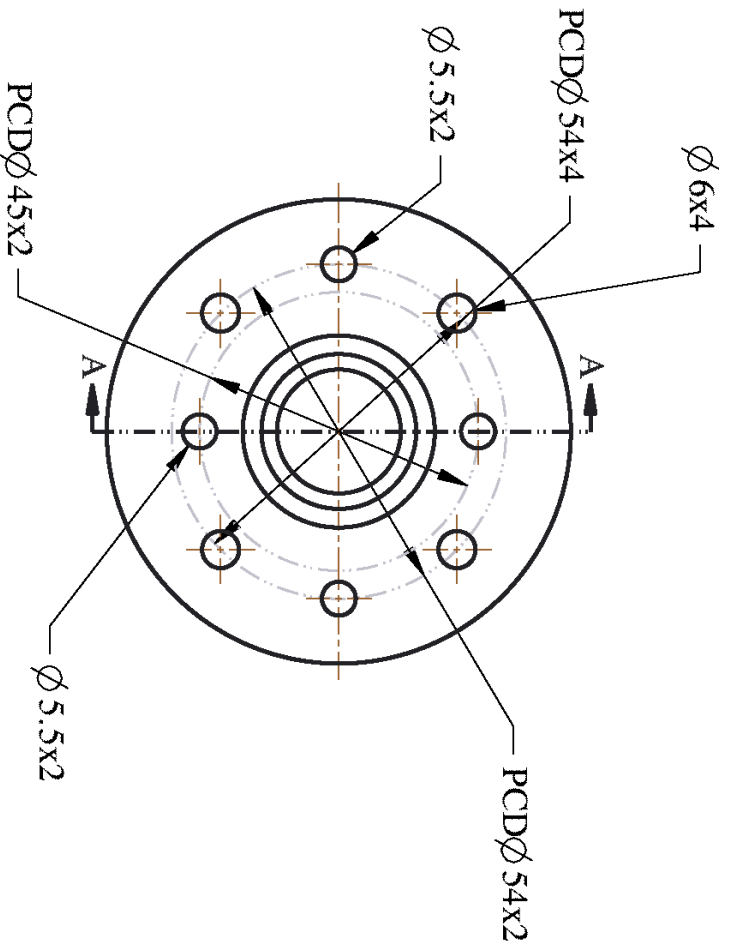
Appendix D. Engineering Drawings of Fixtures



MERL, Sheffield Hallam University, UK		Drawn by: Shakeel Ahmed	
Date: 11-05-2017		Part Name: Bulge Chamber Assbly	
Units: mm	Material:	revision:	Scale: 0.75
Quantity:			



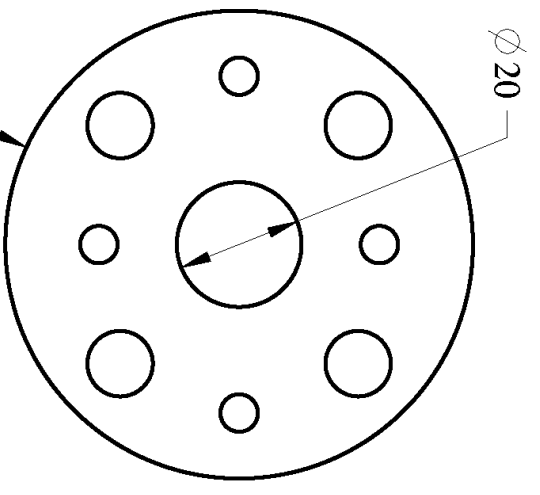
MERI, Sheffield Hallam University, UK		Drawn by: Shakeel Ahmed	
Date: 11-05-2017		Part Name: Bulge-Chamber Body	
Quantity: 01		Units	Material: MS
		revision	Scale: 1.00



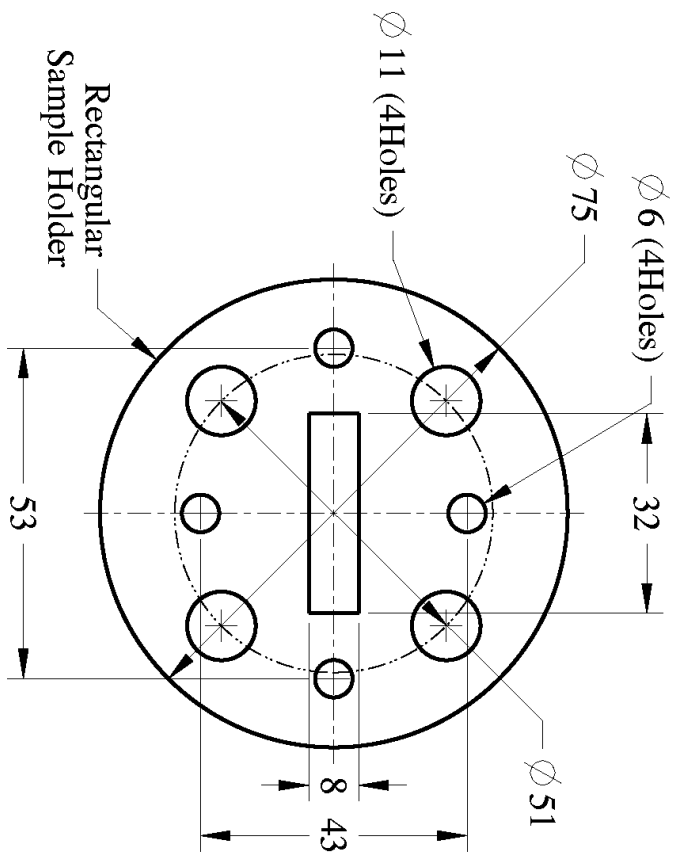
Note:
1. Remove sharp edges

MERL, Sheffield Hallam University, UK		Drawn by	Shakeel Ahmed		
Part Name:		Sample Platform (Circular)			
Date	11-05-2017	Units	mm	Material	Mild Steel
Quantity	01	revision			

Circular Sample Holder

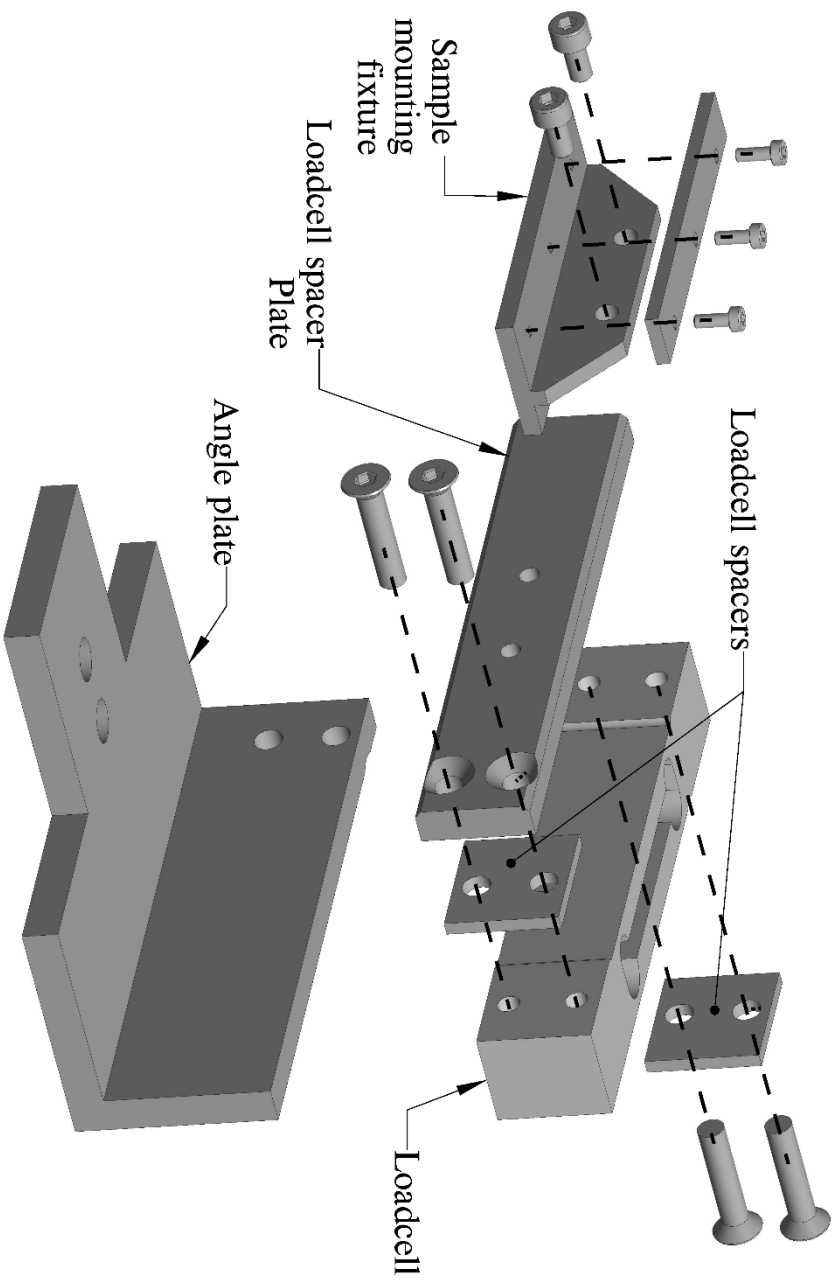


Rectangular Sample Holder

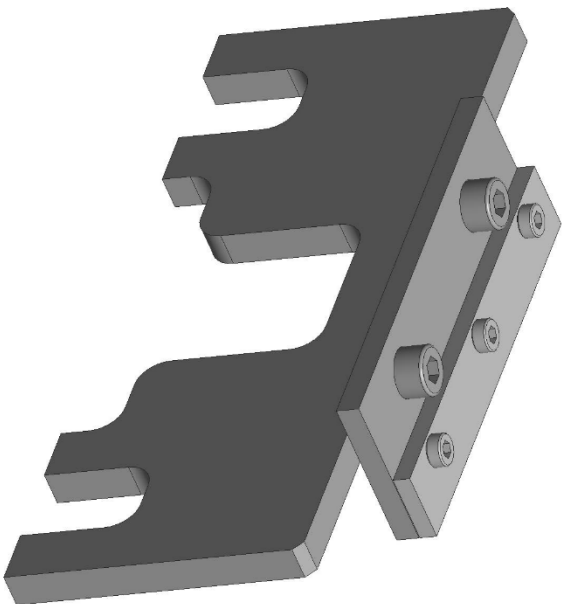
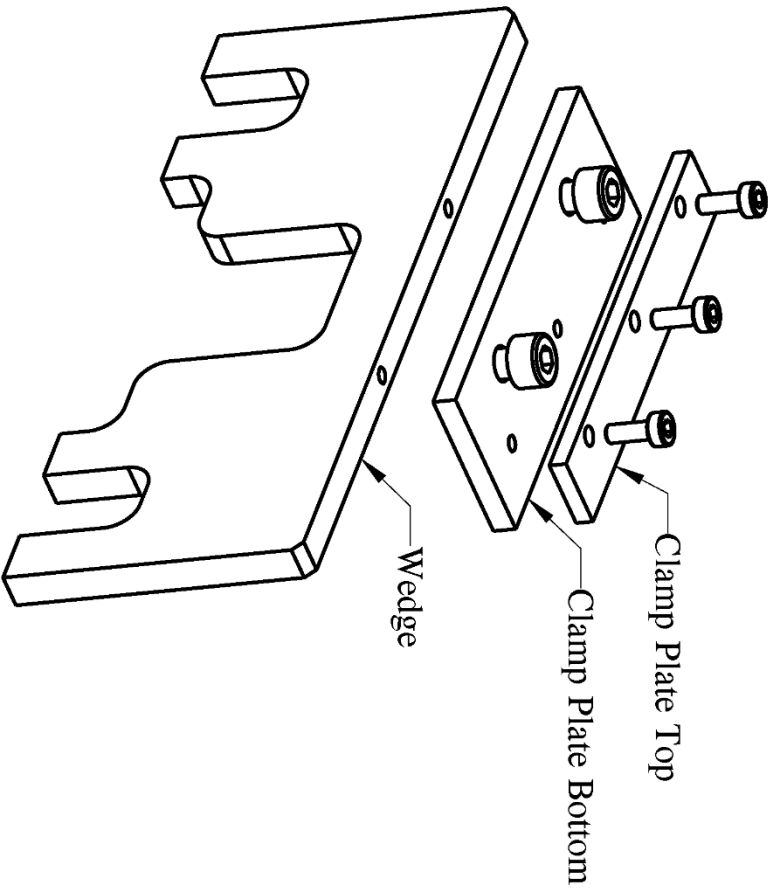


- Note:
1. Thickness of plates is 2mm
 2. Both plates are otherwise the same

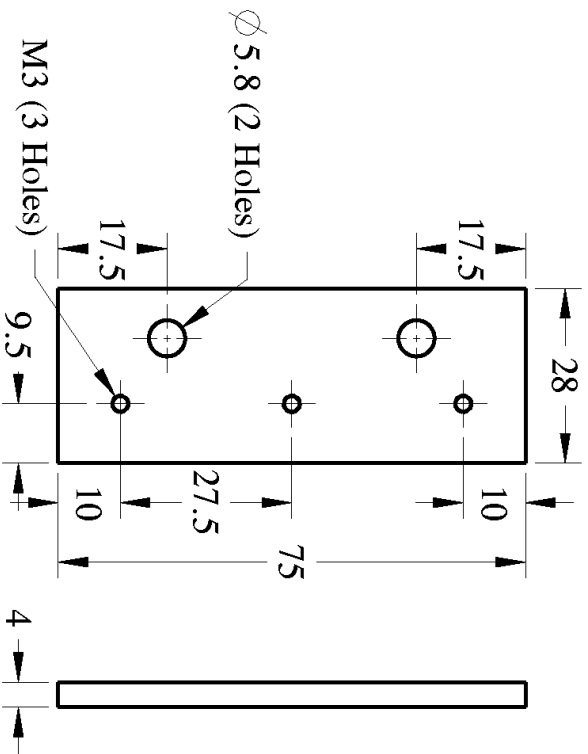
MERI, Sheffield Hallam University, UK		Drawn by: Shakeel Ahmed	
Date: 11-05-2017		Part Name: Sample Holder Plates	
Quantity:	Units	mm	Material: MS
	revision	Scale: 1.00	



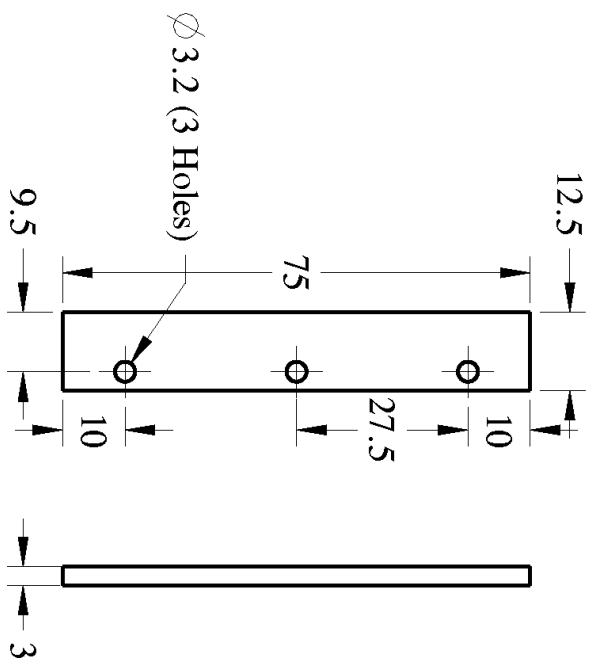
MERI, Sheffield Hallam University, UK		Drawn by: Shakeel Ahmed	
Date: 11-05-2017		Part Name: Loadcell assembly	
Quantity:	Units	mm	Material:
revision	Scale:		



MERL, Sheffield Hallam University, UK		Drawn by: Shakeel Ahmed	
Date: 11-05-2017		Part Name: Sample Clamp - Moving side	
Quantity:	Units: mm	Material: MS	
	revision	Scale: 1.00	

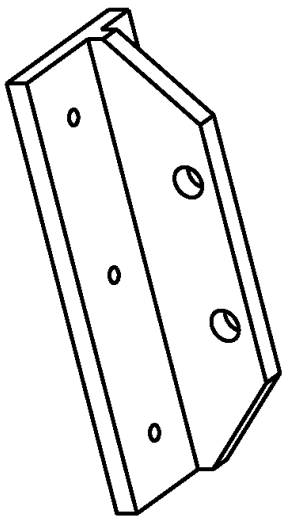
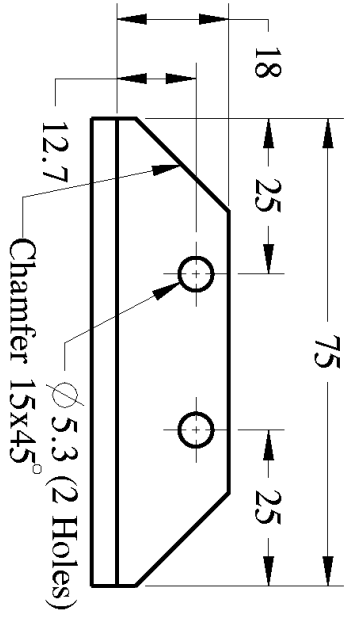
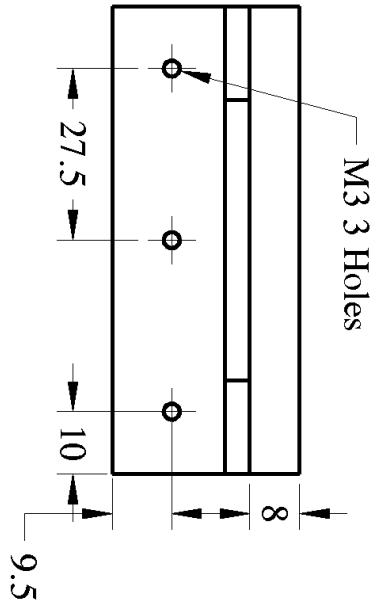


Clamp Plate Bottom
Quantity: 01

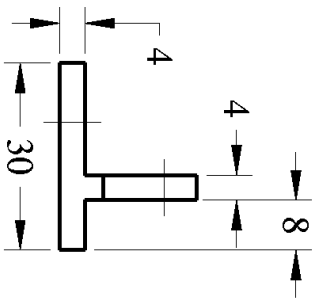


Clamp Plate Top
Quantity: 02

MERRI, Sheffield Hallam University, UK		Drawn by: Shakeel Ahmed	
Date: 11-05-2017		Part Name: Clamp Plates - Moving side	
Units	mm	Material:	MS
Quantity:	revision	Scale:	1.00



SCALE 1.000



MERI, Sheffield Hallam University, UK		Drawn by: Shakeel Ahmed	
Date: 11-05-2017		Part Name: Sample Mounting Fixture	
Quantity: 01	Units: mm	Material: Al	revision: 01
Date: 11-05-2017		Scale: 1.00	

Appendix E. Matlab Codes

1. Reading raw data from DIC experiment (Rectangular bulge)

% This script will read n number of *.dat files and store the result in data array variables.

```
clear, clc, close all
Export_path = fullfile(pwd,'Export');
Cycles_D = dir([Export_path, '*W*']);
nCycles = numel(Cycles_D);
%% Reading data from DAT files
for cycle = 1:nCycles
    Cycles_path = fullfile(Export_path,Cycles_D(cycle).name);
    D = dir([Cycles_path, '*.Dat*']);
    RawData = cell(1, 1);
    t_profiles = length(D(not([D.isdir])));
    for p = 1:t_profiles
        fid = fopen(fullfile(Cycles_path,sprintf('%s', D(p).name)));
        n = 1;
        tLine = fgetl(fid);
        while ischar(tLine) % checks if end has already reached
            RawData(n,p) = {tLine};
            tLine = fgetl(fid);
            n = n + 1;
        end
        [~,] = fclose(fid);
        n = n - 1;
    end
    clear D fid Cycles_path tLine
    %% Converting and storing RawData into another variable
    for p = 1:t_profiles
        A = zeros(1,1);
        for r = 4:n % three header lines
            A(r-3, 1:3) = str2num(RawData{r,p});
        end
        if p == 1
            B = A;
            B(:,2) = [];
        else
            B(:, p+1) = A(:,3);
        end
    end
    end
    DataLines = n-3;
    while ~any((B(:,end)))
        B(:,end) = [];
    end
    [~,t_profiles] = size(B);
    t_profiles = t_profiles - 1;
    clear A n p RawData
```

```

%% copy non zero values of height.
start_idx = zeros(t_profiles,1);
end_idx = zeros(t_profiles,1);
for p = 2:t_profiles+1
    heights = B(:,p);
    for r = 1:DataLines
        if (~heights(r)==0)
            start_idx(p-1) = r;
            break
        end
    end
    for r = 1:DataLines-1
        if (~heights(end-r)==0)
            end_idx(p-1) = DataLines - r;
            break
        end
    end
end
start_idx = min(start_idx);
end_idx = max(end_idx);
% Invert signs, if necessary.
B = B(start_idx:end_idx,:);
eval(sprintf('%s = B;', Cycles_D(cycle).name))
end
clear B cycle* Cycle* t_* Data* Exp* end* heights n* r start_idx p
% save a_HX_W

```

2. Processing the bulge height data

```

% this script will set noise (negative heights) to
% zero, smooth the data and find max bulge heights.
clear, clc, close all
load('a_HX_W');
W_names = who('*W');
nCycles = length(W_names);
profiles = 251;
%% Processing all cycles in W (X)
max_bulge_heights = zeros(1,1);
% for cycle = 1:nCycles
for cycle = 1:nCycles
    eval(sprintf('HX = %s;', W_names{cycle}))
    [row,col] =size(HX);
    A = zeros(1,1);
    %% setting negative values to zeros and smoothing length data
    for c = 2:col
        HX(:,c) = smooth(HX(:,c), 0.2, 'lowess');
        for r = 1:row
            if(HX(r,c)<0)
                HX(r,c) = 0;
            end
        end
    end
end

```

```

end
trim = 4; % to trim a quarter from each end
row_ll = round(row/trim);
row_ul = round((1-1/trim)*row);
if any(HX(:,c))
    A(c-1,:) = max(HX(row_ll:row_ul,c));
end
end
clear row* trim
eval(sprintf('%s = HX;',W_names{cycle}));
clear HX
%% read max bulge heights from width data
for c = 1:length(A)-1
    if abs(A(c)-A(c+1))>2
        break
    end
end
if c~=length(A)-1
    A(c+1:end)=[];
end
max_bulge_heights(1:length(A),cycle) = A;
end
clear A c* del_col HX_W i PinC profiles_in_cycles
clear r row W_names P_start P_end
%% check if 'Figures' folder exists, if not create one
if ~(exist('Figures')==7)
    mkdir('Figures')
end
%% Aligning the peaks of max bulge heights and plotting
fig = figure('units', 'Normalized', 'OuterPosition', [0 0 1 1]);
hold on
temp_array = zeros(profiles,nCycles);
% for cycle = 1:nCycles
for cycle = 1:nCycles
    array1 = zeros(profiles,1);
    Temp = max_bulge_heights(:,cycle);
    [~, idx] = max(Temp);
    start_idx = round(profiles/2)-idx;
    end_idx = start_idx + length(Temp)-1;
    array1(start_idx:end_idx) = Temp;
    plot(array1, '-*')
    temp_array(:,cycle) = array1;
    grid on
end
hold off
xlabel('Profiles (L/U)')
ylabel('Max. Bulge Height [mm]')
legend('C1','C2','C3','C4','C5','C6','C7')
figurepath = fullfile(pwd,'\Figures', 'Heights (L_U) raw');
print(fig,figurepath,'-dtiff', '-r300')
saveas(fig, figurepath);

```

```

%% Delete all the empty rows
while(~any(temp_array(1,:)))
    temp_array(1,:) = [];
end
while(~any(temp_array(end,:)))
    temp_array(end,:) = [];
end
max_bulge_heights = temp_array;
clear array1 cycle end_idx fig* idx nCycles profiles start_idx Temp temp_array
% save d_max_bulge_heights max_bulge_heights
% clear max_bulge_heights
% save e_clean_cycles C*

```

3. Reading pressure data

```

% This script will read n number of *.dat files and store the result in data array
variables.
clear, clc, close all
FileName = '20161212194429R2S2.dat';
f_ard = strcat('C:\Users\b2039788\Documents\MEGA\Mega local\_PhD Docs',...
    '\_Results with Matlab\Rectangular_Samples');
ard_cal_path = fullfile(f_ard, 'f_Arduino_ADC_Cal_new');
load(ard_cal_path);
clear f_ard ard_cal_path
%% Fit a linear relation to ADC calibration
x = Arduino_ADC_Cal_new.ADC(1:62);
y = Arduino_ADC_Cal_new.mVdc(1:62);
[fof_adc, GOF] = fit( x, y, 'poly1' );
clear Arduino_ADC_Cal_new x y y_pred fit GOF
%% Reading data from DAT files
fid = fopen(FileName,'r');
RawData = cell(1,1);
n = 1;
tLine = fgetl(fid);
while ischar(tLine) % checks if end has already reached
    RawData(n,1) = {tLine};
    tLine = fgetl(fid);
    n = n + 1;
end
[~] = fclose(fid);
n = n - 1;
clear fid FileName tLine
%% Converting and storing RawData into double values
A = zeros(1,1);
i = 1;
for row = 1:n
    temp = str2num(RawData{row});
    if (~isempty(temp))
        A(i,1:3) = temp;
        i = i + 1;
    end
end

```

```

    end
end
A = A(:,2);
clear RawData temp
%% sorting data into cycles
profiles = length(A);
col = 1;
i = 1;
profiles_in_cycles = zeros(1);
for row = 1:profiles
    Cycles_ADC(i,col) = A(row);
    i = i + 1;
    if (row > 1 && row < profiles - 2)
        diff1 = A(row) - A(row-1);
        diff2 = A(row+1) - A(row);
        if (diff1 < 0 && diff2 >= 0 )
            profiles_in_cycles(col) = i-1;
            col = col + 1;
            i = 1;
        end
    end
end
end
while(~any(Cycles_ADC(:,end)))
    Cycles_ADC(:,end) = [];
end
end
[~, nCycles] = size(Cycles_ADC);
if (nCycles ~= length(profiles_in_cycles))
    profiles_in_cycles(col) = i-1;
end
end

clear A col diff1 diff2 i n profiles row
%% Aligning the ADC peaks with same number of profiles in each
rows = 251; % a large odd number
figure('units', 'Normalized', 'OuterPosition', [0 0 1 1]);
hold on
Array1 = zeros(rows,nCycles);
for cycle = 1:nCycles
    temp_array1 = zeros(rows,1);
    Temp = Cycles_ADC(:,cycle);
    [~, idx] = max(Temp);
    idx = idx;
    start_idx = round(rows/2)-idx;
    end_idx = start_idx + length(Temp)-1;
    temp_array1(start_idx:end_idx) = Temp;
    plot(temp_array1)
    xlabel('Profiles')
    ylabel('Pressure ADC')
    grid on
    Array1(:,cycle) = temp_array1;
    Temp = zeros(1);
end
end

```

```

hold off
grid on
%% Delete all the empty rows
while(~any(Array1(1,:)))
    Array1(1,:) = [];
end
while(~any(Array1(end,:)))
    Array1(end,:) = [];
end
Cycles_ADC = Array1;
clear Array1 end_idx idx m n start_idx Temp temp_array1
%% Bulge pressure data file names and calculating Pressure [kPa]
for cycle = 1:nCycles
    BP_names{cycle} = sprintf('BP_C%d',cycle);
end
[rows, ~] = size(Cycles_ADC);
P_kPa = zeros(rows,1);
for cycle = 1:nCycles
    ADC = Cycles_ADC(:,cycle);
    for row = 1:rows
        if any(ADC(row))
            P_kPa(row) = fof_adc(ADC(row))*1e-2;
        end
    end
    BP_Data(:,cycle) = P_kPa;
    eval(sprintf('%s = P_kPa;', BP_names{cycle}))
    P_kPa = zeros(rows,1);
end
figure('units', 'Normalized', 'OuterPosition', [0 0 1 1]);
hold on
for cycle = 1:nCycles
    plot(BP_Data(:,cycle))
    xlabel('Profiles')
    ylabel('Pressure [kPa]')
    grid on
end
legend('C1', 'C2','C3','C4','C5','C6','C7')
clear ADC BP_names cycle Cycles_ADC fof_adc nCycles P_kPa row rows
% save c_Pressure_cycles

```

4. Synchronizing bulge heights and pressure

```

clc, clear, close all
load('c_Pressure_cycles', 'BP_Data');
load('d_max_bulge_heights');
[p_profiles, nCycles] = size(BP_Data);
[h_profiles, ~] = size(max_bulge_heights);
temp_p = BP_Data;
temp_h = max_bulge_heights;
temp_size = 251;

```

```

BP_Data = zeros(temp_size, nCycles);
max_bulge_heights = zeros(temp_size, nCycles);
ph_cycles = struct;
height_corrected = zeros(temp_size, nCycles);
max_p = ceil(max(max(temp_p)));
%% Adjusting pressure values to a new size array
[~, p_idx] = max(temp_p(:,1));
p_start = round(temp_size/2) - p_idx+1;
p_end = round(temp_size/2) + (p_profiles-p_idx);
BP_Data(p_start:p_end, :) = temp_p;
clear p_*
%% Adjusting height values to a new size array
[~, h_idx] = max(temp_h(:,1));
h_start = round(temp_size/2) - h_idx+1;
h_end = round(temp_size/2) + (h_profiles-h_idx);
max_bulge_heights(h_start:h_end, :) = temp_h;
clear h_* temp*
%% Correcting heights with reference to data
for cycle = 1:nCycles
    p = BP_Data(:,cycle);
    h = max_bulge_heights(:,cycle);
    if cycle == 1
        for row_p = 1:length(p)
            if any(p(row_p))
                break
            end
        end
        for row_h = 1:length(h)
            if any(h(row_h))
                break
            end
        end
        row = max([row_p row_h]);
        h0 = h(row-1);
    end
    clear row_*
    h = h - h0;
    % setting negative h values to zero
    for row = 1:length(h)
        if h(row) < 0
            h(row) = 0;
        end
    end
    % setting negative p values to zero
    for row = 1:length(p)
        if p(row) < 0
            p(row) = 0;
        end
    end
    height_corrected(:,cycle) = h;
    temp_p(:,cycle) = p;
end

```

```

end
BP_Data = temp_p;
max_h = ceil(max(max(height_corrected)));
clear h0 max_bulge* temp*
%% delete leading and trailing zero rows
while(~any(height_corrected(1,:)))
    height_corrected(1,:) = [];
    BP_Data(1,:) = [];
end
while(~any(height_corrected(end,:)))
    height_corrected(end,:) = [];
    BP_Data(end,:) = [];
end
%% Plotting styles and other configuration
n = 1; % to plot set n = 1;
if(n)
plot_style = [{'-ko'}, {'-bx'}, {'-g*'}, {'-rs'}, {'-c^'}, {'-mv'},...
    {'-kd'}, {'-bx'}, {'-g*'}, {'-rs'}, {'-c^'}, {'-mv'}];
MarkerFaceColor = [{'k'}, {'b'}, {'g'}, {'r'}, {'c'}, {'m'}, {'k'},...
    {'b'}, {'g'}, {'r'}, {'c'}, {'m'}];
markersize = 4.0;
%% Plotting the cycles
figurename = 'PH Cycles';
figure('FileName', figurename,'units', 'Normalized', 'OuterPosition', [0 0 1 1],...
    'PaperPositionMode','auto');
hold on
for cycle = 1:nCycles
    x = BP_Data(:,cycle);
    y = height_corrected(:, cycle);
    plot(x,y,plot_style{cycle},'markersize',markersize,'MarkerFaceColor',Marker-
FaceColor{cycle},...
        'LineWidth', 1.13)
    xlabel('Pressure [kPa]')
    ylabel('Max. Bulge Heights [mm]')
    grid on
    ph_data = [x, y];
    string1 = sprintf('ph_cycles.ph_C%d = ph_data;', cycle);
    eval(string1)

end
hold off
legend('C1', 'C2','C3','C4','C5','C6','C7')
axis([0 max_p+1 0 max_h-0.5]);
figurepath_save = fullfile(pwd,'\Figures', 'PH_Cycles');
figurepath_print = fullfile(pwd,'\Figures', figurename);
% print(figurepath_print,'-dtiff', '-r300')
saveas(gcf, figurepath_save)
magnify;
end
% clear BP_Data cycle figure* h* M* m* n* p ph_data plot* row string1 x y
% save g_ph_cycles ph_cycles

```

5. Fit curve and read material parameters

```
clear, clc, close all
load('g_ph_cycles');
cycle_names = fields(ph_cycles);
nCycles = numel(cycle_names);
rect = 'R2';
sample = 'S2';
Mat_Para = zeros(nCycles,3);
save_path = strcat('C:\Users\b2039788\Documents\MEGA\Mega local\_PhD
Docs\_Results',...
' with Matlab\Rectangular_Samples');
min_p = 1.0; % pressure in kPa
%% most important: change a
% R1: 2a = 7.93e-3
% R2: 2a = 5.85e-3
% R3: 2a = 4.83e-3
if strcmp(rect, 'R1')
    a = (7.93e-3)/2;
elseif strcmp(rect, 'R2')
    a = 5.85e-3/2;
else
    a = 4.83e-3/2;
end
t = 125e-6; % thickness of the thicker samples
for cycle = 1:nCycles
    eval(sprintf('ph_data = ph_cycles.%s;', cycle_names{cycle}));
    [~, max_idx] = max(ph_data(:,1));
    for r = 1:max_idx
        if (ph_data(r,1)>min_p)
            break
        end
    end
    loading = ph_data(r:max_idx,:);
    p = loading(:,1); % Pressure in kPa
    p = p.*1000; % Pressure in Pa.
    h = loading(:,2); % Max. Bulge height
    h = h./1000; % Bulge height meters
    X = h.^2;
    Y = p./h;
    [Linear_ph, GOF_Linear]=PolyFit(X,Y,1);
    A = Linear_ph.p2;
    B = Linear_ph.p1;
    adjRsqr = GOF_Linear.adjrsquare;
    p_pred = A*h+B*h.^3;
    clear G* idx l* L* ph_data X Y
    %% Pressure and Height back in kPa and mm for plot
    p = p/1000;
```

```

h = h*1000;
p_pred = p_pred/1000;
FigureName = sprintf('Ph_0 Fit Cycle %d', cycle);
h1(cycle) = figure('FileName', FigureName, 'units', 'Normalized', 'OuterPosition', [0 0 1 1],...
    'PaperPositionMode', 'Auto');
plot(h,p,'r--', 'LineWidth',1.15);
hold on
plot(h,p_pred,'k','LineWidth',1.15);
hold off
grid on
legend('Experimental Data', 'Curve Fit','Location','NW');
xlabel('h_0 [mm]');
ylabel('P [kPa]');
title(FigureName);
clear p p_* h
sigma_not = A*a^2/(2*t); % residual stress
M = 3*B*a^4/(4*t); % Plain-strain modulus
p_text = sprintf(' \sigma_0 = %5.3e\n M = %5.3e\n adj R^2 = %5.4f',...
    sigma_not, M, adjRsqr);
Mat_Para(cycle,:) = [sigma_not, M, adjRsqr];
% Text position on diagram
x_lim = xlim; y_lim = ylim;
x_pos = x_lim(1)+2/3*(x_lim(2)-x_lim(1)); y_pos = y_lim(1)+1/3*(y_lim(2)-
y_lim(1));
text(x_pos, y_pos, p_text);
clear A B p_text x* y*
figurepath_print = fullfile(pwd, 'Figures', FigureName);
print(h1(cycle),figurepath_print, '-dtiff', '-r300')
end
figurepath_save = fullfile(pwd, 'Figures', 'PH0_cubic_fit_cycles');
saveas(h1, figurepath_save);
clear a* c* f* F* h1 M p* sig* t
data_file_name = sprintf('z_Mat_Para_%s%s', rect, sample);
eval(sprintf('save %s Mat_Para', data_file_name)) % save to the current directory
filesave_path = fullfile(save_path,data_file_name);
save(filesave_path, 'Mat_Para'); % save to Rectangular_Samples dir
%% plot the variation of parameters and fit quality
clc, close all
sigma_not = Mat_Para(:,1)/1e6; % units MPa
M = Mat_Para(:,2)/1e6; % units MPa
adjRsqr = Mat_Para(:,3);
%% plot variation of sigma_not
FigureName = sprintf('Variation of rasidual stress (%s%s)', rect, sample);
h1 = figure('FileName', FigureName, 'units', 'Normalized', 'OuterPosition', [0 0 1
1],...
    'PaperPositionMode', 'Auto');
plot(sigma_not, '-k*');
xlabel('cycles (loading)');
ylabel('\sigma_0 [MPa]');

```

```

grid on
title(FigureName);
figurepath_print = fullfile(pwd, '\Figures', FigureName);
print(h1, figurepath_print, '-dtiff', '-r300')
%% plot variation of sigma_not
FigureName = sprintf('Variation of Plain-strain Modulus (%s%s)', rect, sample);
h1 = figure('FileName', FigureName, 'units', 'Normalized', 'OuterPosition', [0 0 1
1],...
'PaperPositionMode', 'Auto');
plot(M, '-k*');
xlabel('cycles (loading)');
ylabel('M [MPa]');
grid on
title(FigureName);
figurepath_print = fullfile(pwd, '\Figures', FigureName);
print(h1, figurepath_print, '-dtiff', '-r300')
close all
%% plot variation of sigma_not
FigureName = sprintf('Variation of Adj R^2 (%s%s)', rect, sample);
h1 = figure('FileName', FigureName, 'units', 'Normalized', 'OuterPosition', [0 0 1
1],...
'PaperPositionMode', 'Auto');
plot(adjRsqr, '-k*');
xlabel('cycles (loading)');
ylabel('Adj R^2');
grid on
axis([1 nCycles 0 1]);
title(FigureName);
figurepath_print = fullfile(pwd, '\Figures', FigureName);
print(h1, figurepath_print, '-dtiff', '-r300')

```

6. Fit curve and read material parameters

```

clear, clc, close all
sample_desig = 'R1S1';
FileName = sprintf('e_clean_cycles_%s', sample_desig); % Rename these two
names if needed
eval(sprintf('load("c_Pressure_cycles_%s", "BP_Data")', sample_desig));
new_size = 251;
%% Load Bulge Height data into Data_Files
Height_Data_cycles = load(FileName);
HX_names = fieldnames(Height_Data_cycles);
nCycles = numel(HX_names);
for cycle = 1:nCycles
    eval(sprintf('Height_Data = Height_Data_cycles.%s;', HX_names{cycle}));
    %% Load Bulge Height data into Data_Files
    Pressure = BP_Data(:, cycle);
    % Get rid of extra zeros from start and end of Pressure
    while(Pressure(1)==0)

```

```

    Pressure(1) = [];
end
while(Pressure(end)==0)
    Pressure(end) = [];
end
%% Prepare row and column headings for the final FitCircle table
[~, col] = size(Height_Data);
% Height_Data = Height_Data(Height_Data(:,1)>=-10.5 &
Height_Data(:,1)<=8.5,:);
ColHeaders = {'P_kPa', 'X_mm', 'Y_mm', 'R_mm', 'Adj_Rsq'};
%% Call CircleFit function (By Pratt, based upon Least squares)
temp_array = zeros(col-1,5); % will contain pressure, fit circle data(x,y,r) and
RMSE
if size(Pressure) >= col-1
    temp_array(:,1) = Pressure(1:col-1);
else
    temp_array(1:size(Pressure),1) = Pressure(:);
end
clear FileName Heights Pressure
for Profile = 1:col-1
    Pxx = Height_Data(:,[1 Profile+1]);
    if any(Pxx(:,2))
        % calling CircleFit function
        CFP = CircleFit(Pxx); % CFD=Circle Fit Parameters
        temp_array(Profile,2:4) = CFP;
        [~, Adj_Rsquare] = RMSE(Pxx, CFP); % rmse is being ignored
        temp_array(Profile,end) = Adj_Rsquare;
    end
end
%% Align the Pressure to new size
FitCircle_Data = zeros(new_size,5);
temp_p = temp_array(:,1);
 [~, p_idx] = max(temp_p(:,1));
p_start = round(new_size/2) - p_idx+1;
p_end = round(new_size/2) + (Profile-p_idx);
FitCircle_Data(p_start:p_end, 1) = temp_p;
clear p_*
%% Align the Radius to new size
temp_R = temp_array(:,2:end);
 [~, r_idx] = min(temp_R(:,3));
r_start = round(new_size/2) - r_idx+1;
r_end = round(new_size/2) + (Profile-r_idx);
FitCircle_Data(r_start:r_end, 2:end) = temp_R;
clear r_*
FitCircle_Data = array2table(FitCircle_Data, 'VariableNames',...
    ColHeaders);
eval(sprintf('FitCircle_%s=FitCircle_Data;', HX_names{cycle}))
clear FitCircle_Data temp*
end
clear BP_* CFP col Col* cycle h0 Height* HD_* index Profile Pressure_Data
clear new_* Pxx RowHeaders sIndex Adj_Rsquare rmse_val

```

```

save d_FitCircle_Data Fit*
%% Plotting circular fit
vector_names = who('FitC*');
for cycle = 1:nCycles
    eval(sprintf('FitCircle = %s;', vector_names{cycle}))
    R = FitCircle.R_mm;
    Adj_Rsqr = FitCircle.Adj_Rsqr;
    pressure = FitCircle.P_kPa;
    clear d_FitCircle_Data curvature string1 c row noise
    %% radius plot figure 1
    FigureName = sprintf('R-plot (C%02.0f)', cycle);
    h1 = figure('FileName', FigureName, 'units', 'Normalized', 'OuterPosition', [0 0
1 1],...
    'PaperPositionMode', 'Auto'); % Figure 1
    plot(R, '-pk', 'MarkerFaceColor', 'k');
    grid on
    xlabel('Profiles')
    ylabel('Bulge Radius (R) [mm]')
    title(FigureName);
    figurepath_print = fullfile(pwd, '\Figures', FigureName);
    % print(h1, figurepath_print, '-dtiff', '-r300')
    % saveas(h1, figurepath_print);
    clear Figure* figure* h1 r
    %% Pressure vs Adjusted R^2
    FigureName = sprintf('adjRsqr-plot (C%02.0f)', cycle);
    h2 = figure('FileName', FigureName, 'units', 'Normalized', 'OuterPosition', [0 0
1 1],...
    'PaperPositionMode', 'Auto'); % Figure 2
    plot(Adj_Rsqr, '-pk', 'MarkerFaceColor', 'k');
    xlabel('Profiles')
    ylabel('Adjusted R^2')
    title(FigureName);
    axis([0 length(Adj_Rsqr) 0 1.05])
    grid on
    figurepath_print = fullfile(pwd, '\Figures', FigureName);
    % print(h2, figurepath_print, '-dtiff', '-r300')
    % saveas(h2, figurepath_print);
end
% clear, close all

```

7. Compare all results

```

clear, clc, close all
Samples_Data = dir([pwd, '\z_*']);
for t_s = 1:length(Samples_Data)
    Sample_names = Samples_Data(t_s).name;
    load(sprintf('%s', Sample_names))
    name1 = strsplit(Sample_names, '.');
    legends_str(t_s,:) = strsplit(name1{1}, '_');
    eval(sprintf('sigma.sigma_%s = Mat_Para(:,1)/1e6;', legends_str{t_s,4}))

```

```

eval(sprintf('M.M_%s = Mat_Para(:,2)/1e6;', legends_str{t_s,4}))
eval(sprintf('Rsqr.adjRsqr_%s = Mat_Para(:,3);', legends_str{t_s,4}))
eval('clear Mat_Para')
end
clear legends_str
clear name1 S*
%% Delete values whose R^2 is below threshold
threshold = 0.25;
adjRsqr_names = fieldnames(Rsqr);
for t_s = 1:length(adjRsqr_names)
    eval(sprintf('tempR = Rsqr.%s;', adjRsqr_names{t_s}))
    for i = 1:length(tempR)
        if ~isempty(find(tempR(i)<threshold,1))
            good_fit(i,t_s) = 1;    % The fit is not so good
        else
            good_fit(i,t_s) = 2;    % the fit is within acceptable range
        end
    end
end
end
%% Delete Good fit for the first cycle
good_fit(1,:) = [];
clear adjRsqr_names Rsqr temp* threshold
%% Deleting the values below the threshold R^2 and negatives
M_names = fieldnames(M);
sigma_names = fieldnames(sigma);
M_avg = zeros(length(M_names),2);
sigma_avg = zeros(length(M_names),2);
for t_s = 1:length(M_names)
    %% -----copy values leaving first cycle values-----
    eval(sprintf('tempSigma = sigma.%s(2:end);', sigma_names{t_s}))
    eval(sprintf('tempM = M.%s(2:end);', M_names{t_s}))
    GoodSigma = zeros(1);
    GoodM = zeros(1);
    ii = 1;
    for i = 1:length(tempSigma)
        if (good_fit(i,t_s) == 2 && (tempSigma(i)>0 && tempM(i)>0))
            if (good_fit(i,t_s) == 2)
                GoodSigma(ii) = tempSigma(i);
                GoodM(ii) = tempM(i);
                ii = ii + 1;
            end
        end
    end
    eval(sprintf('sigma.%s = GoodSigma;', sigma_names{t_s}))
    eval(sprintf('M.%s = GoodM;', M_names{t_s}))
end
clear good* Good* i* temp*
%% Calculate averages of sigma and M data
for t_s = 1:length(M_names)
    eval(sprintf('M_avg(t_s, 1) = mean(M.%s);', M_names{t_s}))
    eval(sprintf('M_avg(t_s, 2) = std(M.%s);', M_names{t_s}))
    eval(sprintf('sigma_avg(t_s, 1) = mean(sigma.%s);', sigma_names{t_s}))
end

```

```

    eval(sprintf('sigma_avg(t_s, 2) = std(sigma.%s);', sigma_names{t_s}))
end
%% remove any empty fields
% For M
field_names = fieldnames(M);
for index = 1: numel(field_names)
    if (M.(field_names{index}) == 0)
        M = rmfield(M, field_names{index});
    end
end
% For sigma
field_names = fieldnames(sigma);
for index = 1: numel(field_names)
    if (sigma.(field_names{index}) == 0)
        sigma = rmfield(sigma, field_names{index});
    end
end
% For Averages
ii = 1;
del_row = zeros(1);
for index = 1: numel(field_names)
    if (M_avg(index)==0)
        del_row(ii) = index;
        ii = ii + 1;
    end
end
if any(del_row)
    M_avg(del_row,:)= [];
    sigma_avg(del_row,:)= [];
end
sigma_names = fieldnames(sigma);
M_names = fieldnames(M);
% t_s = numel(M_names);
for index = 1: numel(M_names)
    legends_str(index,:) = strsplit(M_names{index}, '_');
end
legends_str = legends_str(:,2);
clear del_row field* ii index *_names t_s
save Final_results_All M* sigma* legends*
clear legends_str
%% -----Important-----
% plot_results_all
%% Delete any identified outlier/s
OutLiers = {'R2S1','R3S1'}; % add names of the OL samples
for t_s = 1:length(OutLiers)
    % Rsqr_OL = strcat('adjRsqr_',OutLiers{t_s});
    M_OL = strcat('M_',OutLiers{t_s});
    sigma_OL = strcat('sigma_',OutLiers{t_s});
% Rsqr = rmfield(Rsqr, Rsqr_OL);
M = rmfield(M, M_OL);
sigma = rmfield(sigma, sigma_OL);

```

```

end
clear Out* *OL * _avg
%% Calculate averages of sigma and M data
M_names = fieldnames(M);
sigma_names = fieldnames(sigma);
for t_s = 1:length(M_names)
    eval(sprintf('M_avg(t_s, 1) = mean(M.%.s);', M_names{t_s}))
    eval(sprintf('M_avg(t_s, 2) = std(M.%.s);', M_names{t_s}))
    eval(sprintf('sigma_avg(t_s, 1) = mean(sigma.%.s);', sigma_names{t_s}))
    eval(sprintf('sigma_avg(t_s, 2) = std(sigma.%.s);', sigma_names{t_s}))
end
%% legends_str
for index = 1:numel(M_names)
    legends_str(index,:) = strsplit(M_names{index}, '_');
end
legends_str = legends_str(:,2);
%% Calculate averages of sigma and M data all samples
c20 = 1; R1 = 1; R2 = 2; R3 = 3;
for t_s = 1:length(M_names)
    if ~isempty(regexpi(legends_str{index}, 'C\w*', 'match'))
        eval(sprintf('M_avg2(c20, 1) = mean(M.%.s);', M_names{t_s}))
        eval(sprintf('M_avg(t_s, 2) = std(M.%.s);', M_names{t_s}))
        eval(sprintf('sigma_avg(t_s, 1) = mean(sigma.%.s);', sigma_names{t_s}))
        eval(sprintf('sigma_avg(t_s, 2) = std(sigma.%.s);', sigma_names{t_s}))
    end
end
end
%% calculate mean of M
Mc = [M.M_C20S3 M.M_C20S4];
Mc = mean(Mc);
clear del_row field* ii index *_names t_s
save Final_results M* sigma* legends*
%% Plot all the results from two script files
% plot_results
% plot_results_aspect_ratio

```

Appendix F. Publications and Posters

Publications:

1. Shakeel A. and David T. Asquith, "Strain measurement of a thin hyperelastic polymer sheet using 3D-Digital Image Correlation and Bulge Test", The British Society for Strain Measurement

11th International Conference on Advances in Experimental Mechanics

29th - 31st August, 2017 University of Exeter, UK

Abstract: A bulge test is commonly used to analyse equibiaxial tensile stress and strain usually at the pole of an inflated thin sheet. Using three dimensional digital image correlation (3D-DIC) technique, three dimensional surface displacements can be measured and hence the corresponding strain fields. In this paper, strain is measured in a rectangular polymer sample with aspect ratio of four. The bulged profile is shown to take a 4th degree polynomial shape. Hysteresis is present in polymer material and pressure vs. bulge height profile stabilizes after few cycles of loading-unloading. Since digitally image correlated results are usually noisy, different methods of extracting the results are discussed. An analytical (Vlassak & Nix, 1992) model is compared with measured strain.

Posters:

1. Shakeel Ahmed, Prof Jacques Penders and Dr. David Asquith, Gripping and Handling Technology for Flexible Materials. MERI Symposium, Sheffield Hallam University, Sheffield United Kingdom, December 2013.

GRIPPING AND HANDLING TECHNOLOGY FOR FLEXIBLE MATERIALS.

**Shakeel Ahmed
Prof Jacques Penders and Dr David Asquith**

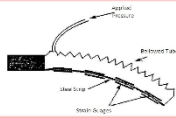
Centre for Automation & Robotics Research, Sheffield Hallam University, S1 1WB, UK. Email: Shakeel.Ahmed2@student.shu.ac.uk

Background
As a result of research and development in elastomeric materials engineering, flexible materials are used extensively in a wide range of industrial applications including the manufacture and assembly of garment and footwear products, the packaging industry and aircraft manufacturing. These applications are often extremely labour intensive requiring fast and accurate manipulation of materials by skilled human operators. The proposed output of this research will be a novel concept of end effector design assembling an LED unit inside a balloon.

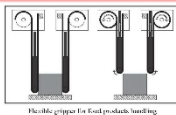


Current State of the Art:
Many designs exist to deal with flexible materials but none of them can solve this specific problem, few common solutions are mentioned below.

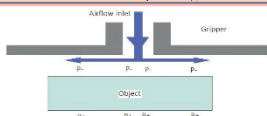
1. Pneumatic Actuator. Stone, R.S.W., Brit. Pat. (1965), "A flexible pneumatic actuator for gripping soft irregular shaped objects" IEE Colloquium (Digest) Flexible Pneumatic Actuator for Gripping, Vol. 170, pp.131-132



2. Flexible Gripper. SAM, Rosdiah, et al. (2008), Design and development of flexible robotic gripper for handling food products, In: IEEE, 1884-1888.



3. Bernoulli principle gripper. Anders Pettersson, et al. (2010), A Bernoulli principle gripper for handling of planar and 3D (food) products, Industrial robot: An international journal, 37 (6), 518-526.



Design Basis

1. Time:
One complete assembly every 30 sec. (½ Min)

2. Opening: for safe assembly balloon mouth should be open like fig. below. (All dimensions are in mm)



Open Mouth for assembly Balloon Mouth

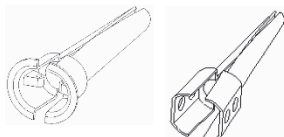
3. Reliability: Process should be very reliable and should be able to detect any missing components before next assembly station.

4. Light Weight: The whole assembly should be light weight; to facilitate fast movements.

5. Low Friction: To facilitate easy insert into the balloons, mouth inserts should offer least friction to balloon latex.

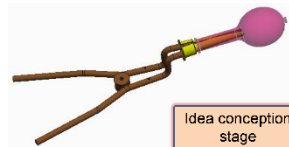
Gripper Design

1. Mouth Inserts Design:



Initial Design Design for Manufacturing (DFM)

2. Scissors Opener: Different Design Phases



Idea conception stage

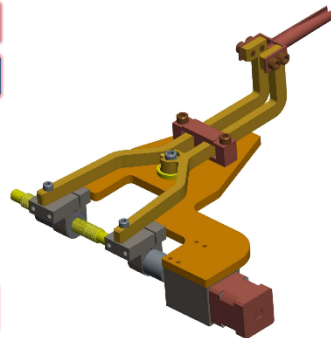


After applying current manufacturing constraints



Distance between fulcrum and inserts is optimised for nearly parallel opening of the balloon.

3. Complete Mouth Opener Assembly: (First Prototype)



1. Shakeel Ahmed, Prof Jacques Penders and Dr. David Asquith, Gripping and Handling Technology for Flexible Materials. MERI Symposium, Sheffield Hallam University, Sheffield United Kingdom, May 2015.



GRIPPING AND HANDLING TECHNOLOGY FOR FLEXIBLE MATERIALS.

**Shakeel Ahmed
Prof Jacques Penders and Dr David Asquith**

Centre for Automation & Robotics Research, Sheffield Hallam University, S1 1WB, UK. Email: Shakeel.Ahmed2@student.shu.ac.uk

BACKGROUND & OBJECTIVES

An LED unit with pull strap is to be assembled in a balloon at the rate 120 units per minute. Currently they are being assembled manually (Slow) hence not meeting the market demands. The objective of this study is design a Machine/Gripper that does the job un-manned, reliably and quickly.



KEY STAGES OF THE PROCESS

1. SINGULATE THE BALLOON FROM A PILE.
Balloons are put into a Bowl Feeder which will separate them.



2. FEED THE BALLOON ONE AT A TIME.
Balloons should be fed at a controlled rate and with certainty ready to be picked-up for next operation.



3. HOLD THE BALLOON FOR ASSEMBLY.
Balloon should be held suitably for inserts to go into the balloon. Balloon should be quickly released as soon as its mouth starts to expand by the action of Inserts.



4. OPEN THE BALLOON MOUTH
Open the Mouth of the balloon min. dia. 25mm for LED unit to be assembled through it.



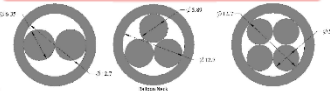
5. PUT THE LED UNIT IN THE BALLOON AND PUT AN O-RING.
Finally, move the Led Unit into the balloon and put an O-ring that holds it with balloon firmly.

MOUTH INSERTS DESIGN

1. SEMI-CYLINDRICAL PAIR:



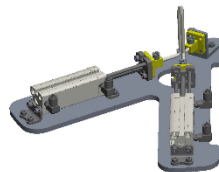
2. SEVERAL PRONG INSERTS:



Given length of Neck is ~60mm, three prongs will just do the job.

HOW TO PULL THESE PRONGS OPEN?

1. USE TWO CYLINDERS WITH ONE PRONG FIXED
 > Total weight of this assembly is 895.6 g.
 > Foot Print area is 747 cm².
 > Very compact design and fewer moving parts

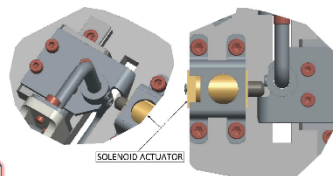
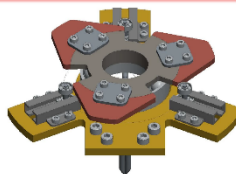


3. USE VERTICAL CAM TO OPEN THREE PRONGS
 > Total weight of the this assembly is 672 g.
 > Foot Print area is 141 cm².
 > Cam is not fixed to the assembly hence stays at only one assembly station.
 > Latching mechanism is required keep the prongs as
 > Too many moving parts with three miniature slides (expensive)



How to keep the Balloon stretched while the cam is removed?

2. USE HORIZONTAL CAM TO OPEN THREE PRONGS
 > Total weight of this assembly is 881g.
 > Foot Print area is 152 cm².
 > Cam is fixed to the assembly hence moves to every assembly station.

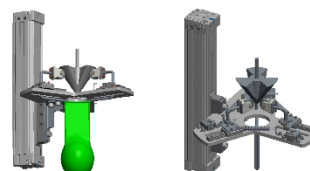


How to make prongs more stable?

COMPLETE ASSEMBLY WITH VERTICAL SLIDE



COMPLETE ASSEMBLY WITH VERTICAL SLIDE



Appendix G. Pressure Sensor Data Sheet

PN3097



Pressure sensor with display

PN-001BRER14-MFRKG/US/ IV

Response times	
Response time [ms]	< 3
Delay time programmable dS, dr [s]	0...50
Damping for the switching output dAP [s]	0...4
Damping for the analogue output dAA [s]	0...4
Max. response time analogue output [ms]	3
Software / programming	
Parameter setting options	hysteresis / window; normally open / normally closed; switch-on/ switch-off delay; Damping; Display unit; current/voltage output
Interfaces	
Communication interface	IO-Link
Transmission type	COM2
IO-Link revision	1.1
SDCI standard	IEC 61131-9
IO-Link device ID	433 d / 00 01 b1 h
Profiles	Smart Sensor: Process Data Variable; Device Identification, Device Diagnosis
SIO mode	yes
Required master port type	A
Process data analogue	1
Process data binary	1
Min. process cycle time [ms]	2.3
Operating conditions	
Ambient temperature [°C]	-25...80
Storage temperature [°C]	-40...100
Protection	IP 65; IP 67
Tests / approvals	
EMC	DIN EN 61000-6-2
	DIN EN 61000-6-3
Shock resistance	DIN EN 60068-2-27
	50 g (11 ms)
Vibration resistance	DIN EN 60068-2-6
	20 g (10...2000 Hz)
MTTF [years]	181
UL approval	UL Approval no.
	J004
Pressure Equipment Directive	Sound Engineering Practice; can be used for group 2 fluids; group 1 fluids on request
Mechanical data	
Weight [g]	234.5
Materials	stainless steel (1.4404 / 316L); PBT+PC-GF30; PBT-GF20; PC
Materials (wetted parts)	stainless steel (1.4404 / 316L); Al2O3 (ceramics); FKM
Min. pressure cycles	100 million
Tightening torque [Nm]	25...35; (recommended tightening torque; depends on lubrication, seal and pressure rating)
Process connection	threaded connection G 1/4 internal thread M6 I
Restrictor element integrated	no (can be retrofitted)

PN3097



Pressure sensor with display

PN-001BRER14-MFRKG/US/ /V

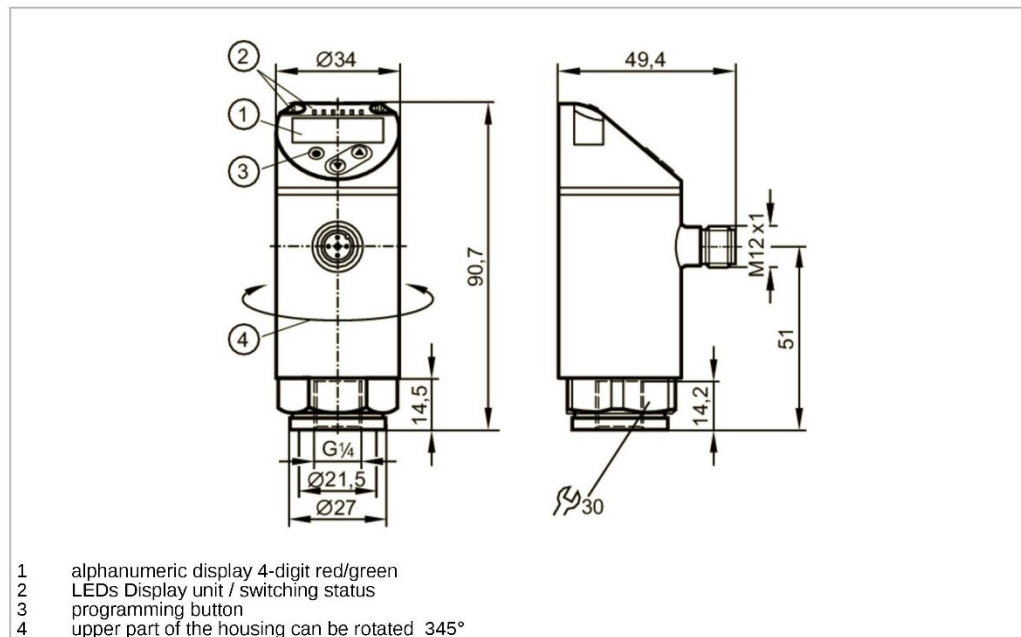
Outputs				
Total number of outputs	2			
Output signal	switching signal; analogue signal; IO-Link; (configurable)			
Electrical design	PNP			
Number of digital outputs	1			
Output function	normally open / normally closed; (parameterisable)			
Max. voltage drop switching output DC [V]	2.5			
Permanent current rating of switching output DC [mA]	150; (200 (...60 °C) 250 (...40 °C))			
Switching frequency DC [Hz]	< 170			
Number of analogue outputs	1			
Analogue current output [mA]	4...20			
Max. load [Ω]	500			
Analogue voltage output [V]	0...10			
Min. load resistance [Ω]	2000			
Short-circuit protection	yes			
Type of short-circuit protection	pulsed			
Overload protection	yes			
Measuring/setting range				
Measuring range	0...1000 mbar	0...14.5 psi	0...29.5 inHg	0...100 kPa
Set point SP	10...1000 mbar	0.1...14.5 psi	0.2...29.5 inHg	1...100 kPa
Reset point rP	5...995 mbar	0.05...14.45 psi	0.1...29.4 inHg	0.5...99.5 kPa
In steps of	5 mbar	0.05 psi	0.1 inHg	0.5 kPa
Accuracy / deviations				
Switch point accuracy [% of the span]	< ± 0,5			
Repeatability [% of the span]	< ± 0,1; (with temperature fluctuations < 10 K)			
Characteristics deviation [% of the span]	< ± 0,25 (BFSL) / < ± 0,5 (LS); (BFSL = Best Fit Straight Line; LS = limit value setting)			
Hysteresis deviation [% of the span]	< ± 0,25			
Long-term stability [% of the span]	< ± 0,05; (per 6 months)			
Temperature coefficient zero point [% of the span / 10 K]	0,2; (-25...80 °C)			
Temperature coefficient span [% of the span / 10 K]	0,2; (-25...80 °C)			

PN3097



Pressure sensor with display

PN-001BRER14-MFRKG/US/ IV



Application				
Measuring element	ceramic-capacitive pressure measuring cell			
Application	for industrial applications			
Media	liquids and gases			
Medium temperature [°C]	-25...80			
Pressure rating	10000 mbar	145 psi	290 inHg	1000 kPa
Min. bursting pressure	30000 mbar	450 psi	880 inHg	3000 kPa
Vacuum resistance [mbar]	-1000			
Type of pressure	relative pressure			
Electrical data				
Operating voltage [V]	18...30 DC; (according to EN 50178 SELV/PELV)			
Current consumption [mA]	< 35			
Min. insulation resistance [MΩ]	100; (500 V DC)			
Protection class	III			
Reverse polarity protection	yes			
Power-on delay time [s]	0.3			
Integrated watchdog	yes			
Inputs / outputs				
Number of inputs and outputs	Number of digital outputs: 1; Number of analogue outputs: 1			

PN3097



Pressure sensor with display

PN-001BRER14-MFRKG/US/ IV

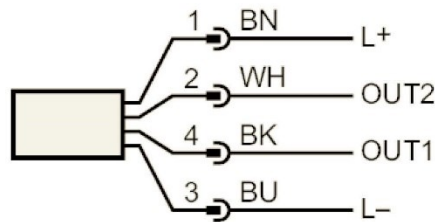
Displays / operating elements		
Display	Display unit	4 x LED, green (bar, psi, kPa, inHg)
	switching status	1 x LED, yellow
	measured values	alphanumeric display, red/green 4-digit
Remarks		
Pack quantity	1 pcs.	

Electrical connection

Connector: 1 x M12; Contacts: gold-plated



Connection



- OUT1 switching output
- OUT2 analogue output
- Core colours :
- BK = black
- BN = brown
- BU = blue
- WH = white